Design and Development of a Novel Soft Inflatable Multi-Filament Actuator

By

Mohammad Holdar

Submitted in accordance with the requirements for the degree of Doctor of Philosophy

The University of Leeds

School of Mechanical Engineering

August 2024

Acknowledgements

I would like to express my deepest gratitude to my exceptional supervisors, Dr. Ali Alazmani and Dr. Peter Culmer, for their continuous support and guidance throughout my research journey. Their knowledge and encouragement have been crucial in helping me complete this work. I am especially thankful for their support during the difficulties and challenges I faced throughout my PhD journey. I am truly grateful for their support.

I would also like to extend my thanks to the government of Saudi Arabia for providing full funding for my studies. Their support has been fundamental in allowing me to pursue this research.

I am also thankful to the members of the Healthcare Mechatronics Group, both past and present, for creating such a collaborative and supportive environment. Working with this group has been a rewarding experience, and I want to specifically acknowledge my colleagues Majed Melibary, Sina Najjari, Ahmet Colakoglu, Dominic Jones, Jun Know, Ian Waters, and Mark Zhang. Majed, my best friend since 2006, your support has been invaluable. You have always been there, never hesitating to help and guide me. I am lucky to have you in my life, and I grateful to share this journey with.

I am incredibly thankful to all my friends in Leeds, who have been a great source of strength and joy. Waleed, thank you for all the time we've spent together, helping me disconnect from the stress of study. Youssef Elsayed, you are a wonderful friend. Your integrity, kindness, and consistent support have made a difference during my time in the UK.

Finally, to my amazing mum and my dear brothers and sisters, without whom none of this would have been possible. Your love and constant support have been my greatest source of strength. To my wonderful kids Yusuf and Ibrahim, you are my inspiration and motivation, reminding me every day why I strive to achieve my best. You all mean the world to me.

Abstract

Soft Artificial Muscles (SAMs) are a type of soft actuator designed to contract and expand in a manner similar to natural muscles. These actuators play a crucial role in enabling flexible and adaptable movement in soft robots, which are often inspired by biological organisms. SAMs consist of a soft inflatable component that generates expansion when pressurized, and a braided sleeve that acts as a strain-limiting component, directing the contraction motion of the actuator. SAMs have a wide range of applications, including healthcare, wearable technology, and robotics. However, a key challenge lies in optimizing the performance of SAMs, as there has been limited progress in improving the design of the soft components. Specifically, advancements in the geometry and structures used could lead to improve strength and responsiveness during actuation.

This research addresses these challenges by introducing a novel approach to SAM development, inspired by the biomechanical efficiency of human muscles. A multi-filament SAM design (Model-1), along with two comparative models, was developed and evaluated through rigorous experimental testing. Model-1 introduces a circular bundle comprised of multiple soft filaments, representing the innovative soft actuator proposed in this research. Model-2 features a single cylindrical soft body containing an equivalent number of small cylindrical cavities as Model-1. Lastly, Model-3 features a single cylindrical soft body with a simple lone cavity, resembling the traditional structure found in McKibben muscles. The methodology involved the implementation of fabrication techniques to produce consistent and reliable SAM models. These models were subjected to detailed block force and displacement tests. Model-2 consistently generated the highest force output, with an 8% higher force than Model-1 and 35% higher force than Model-3. However, displacement tests did not reveal a significant effect of changing the SAM model on displacement performance. In terms of response to pressure, Model-1 demonstrated higher actuation speed, outperforming Model-2 by 25% and Model-3 by 35%. These results highlight the significant impact that improvements in the design of the soft components can have on enhancing the force generation and response to pressure performance of SAMs.

A case study confirmed the real-world potential of SAMs in dynamic systems, aligning with the results from main tests. Finally, preliminary Finite Element (FE) simulations were used to predict the behaviour of SAM models, providing an initial framework for future improvement.

Table of Contents

List of Figures

List of Tables

Chapter 1 : Introduction

This chapter serves as the introduction to the research, aiming to present the general concept of soft robotics and muscle-like actuators. It provides an overview of the PhD research topic and details how this work will contribute to the field. The chapter outlines the significance of the study, presents the research questions, and defines the scope and objectives of the research. Additionally, it offers an overview of the forthcoming chapters and sections to guide the reader through the thesis.

1.1 Soft Robotics and Muscle-like Actuators

Soft robotics is a developing field that uses soft elastomers to enhance robotic capabilities by constructing actuators or sensors from deformable, compliant materials. These materials display nonlinear hyperelastic behaviours, making soft robots more adaptable and safer for interaction, especially in environments where conventional rigid robots are impractical.

The flexibility and compliance of soft robots enable them to endure collisions, absorb shocks, and interact delicately, making them well-suited for unpredictable environments and close human-robot collaborations. This shift towards more adaptable robotics is relevant in healthcare and collaborative settings. Additionally, the use of biomimicry in soft robotics, replicating biological movement patterns, highlights its potential for innovative functionality.

Soft robotics also focuses on developing muscle-like actuators, termed "Soft Artificial Muscles" (SAM), designed to mimic natural muscles. These actuators, resembling models such as the McKibben muscle or Pneumatic Artificial Muscles (PAM), made of specific components to enable more natural movements. The study of these SAMs is crucial due to their lightness and efficiency, and optimizing their performance is essential to fully realize their potential across various applications. Additionally, the application of biomimicry in soft robotics, replicating biological movement patterns, underscores its potential for enhancing robot functionality.

1.2 Scope of the Research

This thesis is considered to discover critical aspects of SAM. The research aims to get inspiration from biology and the way muscles are formed in the body and enhance the performance of SAMs by using multi filaments instead of a large single soft component. This involves proposing conceptual designs to study and compare different configurations of SAMs, developing SAMs based on these designs, and implementing a robust testing methodology to evaluate and compare the performance of these configurations. SAM, as a soft actuator, comprises two main components: the soft component and the strain limiting component, termed “braid”. The soft component is the soft part in SAM that inflates and expands when pressurized with air, while the braid restricts the soft component's motion and translates its expansion into linear contraction.

Designing the structure of SAM involves considering the configuration of soft components and overall geometry. Recent advancements in soft robotics have led to various designs of SAMs. However, to our knowledge, despite these actuators are inspired by human muscles none have considered the biological mechanism of human muscles. Observing that human muscles gain strength from the repetition of muscle fibers, we hypothesize that a similar principle can enhance SAM performance. Specifically, bundling multiple filaments within the soft component, similar to the repeating sections in muscle’s fibers, is expected to improve SAM's capabilities compared to a single tube design.

To evaluate the validity of creating bundle of soft filament, it is essential to compare this conceptual design with other SAM counterparts. Three different conceptual designs (referred to in this thesis as Model-1, Model-2, and Model-3) are designed, fabricated, and evaluated to compare their performance and determine the effectiveness of using multi-filaments to enhance SAM performance. The processes of designing, fabricating, and evaluating the SAM models involve several refining and improvement trials to ensure high methodological quality. The research focuses on evaluating SAM's performance primarily through two key metrics: the generated force by SAM and its range of contraction. Each metric is assessed separately through single-variable tests and presented in a separate chapter in order to allow for a focused examination of specific metric.

Despite the main focus of this research being on the development evaluation of new concept of SAM, it also addresses other relevant key concepts in the field of soft robotics. For instance, soft material characterization is covered as part of this research.

Understanding the properties of soft materials is essential for customizing them to meet the specific needs of SAM. Properties like ultimate tensile strength, stiffness, and shore-hardness impact how effective the actuators are at a desired function. These materials should match the needed characteristics to enable the required deformations and movements.

Furthermore, the thesis investigates the capability of Finite Element (FE) simulation methods in evaluating and predicting the performance of SAMs. This involves an exploration of the accuracy of FE simulation methods in modelling SAM behaviour, with a focus on providing detailed information on processes, parameters, and results. The FE simulation of SAM includes the generation of a CAD model that accurately represents the complex geometry of the braid within SAM, along with the modelling of various configurations of SAM's models.

1.3 Aim and Objectives

1.3.1 Aim

Despite recent advancements in the design of Soft Artificial Muscles (SAMs), current approaches have yet to fully incorporate the biological mechanisms found in human muscles. Notably, while human muscles derive their strength from being composed of a multitude of muscle fibres, this principle has not been widely applied in SAM design.

This research aims to draw inspiration from biology, specifically the structure of muscles in the body, to enhance the performance of SAMs by using multiple filaments instead of a single large tube.

1.3.2 Objectives

To accomplish the research aim, the following objectives are set:

1. To identify existing SAM designs to address the research gap.
    - Provide a comprehensive literature review about SAM.
    - Analyse the findings from the literature review to identify gaps and critical aspects related to SAM in soft robotics field.

2. To characterize various soft materials suitable for SAM fabrication.

- Develop methodology and procedures for fabricating test specimens from soft materials.
- Conduct standardized tensile and compression tests on several soft materials.
- Generate hyperelastic models by using the collected data from the experiments.

3. To design and fabricate a SAM.
    - Develop and propose conceptual designs for various models of SAM's.
    - Design and fabricate soft component that can be effectively assembled to create SAM.
    - Establish an optimal protocol for fabricating the SAM.

4. To investigate the performance of various models of SAM through experimental studies to enhance our understanding of their behaviour.
    - Develop a testing methodology for determining specific metrics.
    - Implement experiments to measure SAM range of capabilities under particular testing conditions.
    - Collect and analyse data from experimental tests to assess and compare the performance of various SAM models.

5. To investigate a case study of SAM by designing a robust real-world application.
    - Create a dynamic system that effectively showcases the application of SAM in real-world scenarios.
    - Develop testing methodology specifically suitable to assess SAM's capabilities within the designed case study.
    - Measure specific metrics within SAM and the case study systems to gather meaningful data for analysis.
    - Conduct a thorough assessment, analysis, and comparison of the performance of various SAM models within the designed case study.

6. To employ FE modelling and simulation techniques to enhance the understanding of SAM.
    - Develop and simulate a FE model for a single soft component to analyse its hyperelastic behaviour.
    - Create a CAD model to represent the complex geometry of the braided sleeve that serve as the strain limiting component within SAM.

- Conduct FE simulation on the assembled model of SAM, integrating the soft component with the braid, to analyse and predict the complex behaviour of the complete SAM actuator.
- Validate the reliability of the FE simulations of SAM against experimental findings.

1.4 Thesis Structure

Chapter 1: Introduction

The chapter of introduction provides an overview of the field of Soft Robotics and Soft Artificial Muscle (SAM) with emphasizing the scope of the research, research key concepts, and gap identification. The aim and objectives of the study and the structure of the thesis are presented.

Chapter 2: Literature Review

In the Literature Review chapter, the existing current knowledge on Soft Robotics and muscle-like actuator is explored. It covers fundamental concepts such as Soft Material Characterization, the conceptual design of SAM, and soft material fabrication. The chapter also explores the experimental examination and simulation of SAM that offer a comprehensive understanding of the literature ground.

Chapter 3: Soft Material Characterization

This chapter focuses on characterizing soft materials by detailing the fabrication of tensile and compression specimens. It provides standardized experiments that determine hyperelastic material properties, employing hyperelastic models for precise data fitting. Additionally, validation is performed using the Finite Element Method (FEM), and the results and discussions contribute to a deeper understanding of the soft material characteristics utilized in soft robotics applications.

Chapter 4: Design and Fabrication of SAM

This chapter introduces SAM with detailing its conceptual design and fabrication techniques. It sets the foundation for the subsequent chapters by providing a comprehensive understanding of SAM's structure and development.

Chapter 5: Experimental Evaluation of SAM

This chapter presents a comprehensive experimental evaluation of SAM through both block force and displacement tests. The block force test aims to assess SAM's ability to generate force through cyclic and static tests. These tests provide insights into SAM's performance under a range of conditions, contributing to a better understanding of how different SAM models respond to these conditions. The displacement test evaluates the range of motion and displacement characteristics of SAM. This section details the development of the test setup, the experimental procedures, and the methods used for data processing. The findings from these tests provide a significant contribution to understanding SAM performance in terms of movement and actuation efficiency.

Chapter 6: Case Study: SAM in Practical Application

This chapter explores a case study to investigate how SAM is practically applied in real-world situations. SAM's capabilities are tested and evaluated using specific metrics within a dynamic system. The results provide insights into the performance of different SAM models in the designed case study.

Chapter 7: FE Simulation of SAM

The simulation chapter introduces Finite Element (FE) modelling and simulation for SAM using hyperelastic material. Procedures for FE modelling and simulation are detailed, followed by the evaluation of SAM models (Model-1, Model-2, and Model-3). The chapter concludes with a summary of the FE simulation findings and validating simulations against experimental findings.

Chapter 8: Discussion and Conclusions

This chapter provides a comprehensive discussion of the key findings of the research, focusing on the critical analysis of the literature, material characterization, SAM

development, experimental evaluations, the case study, and FE simulations. It critically assesses the implications of these findings for the advancement of SAMs. The chapter concludes by summarising the main contributions of the research and offers recommendations for future work, highlighting potential areas for further development in this field.

1.5 Flowchart of Methodologies Employed Across the Thesis

The flowchart below illustrates the methodologies employed throughout this research to fulfil its aim and objectives:

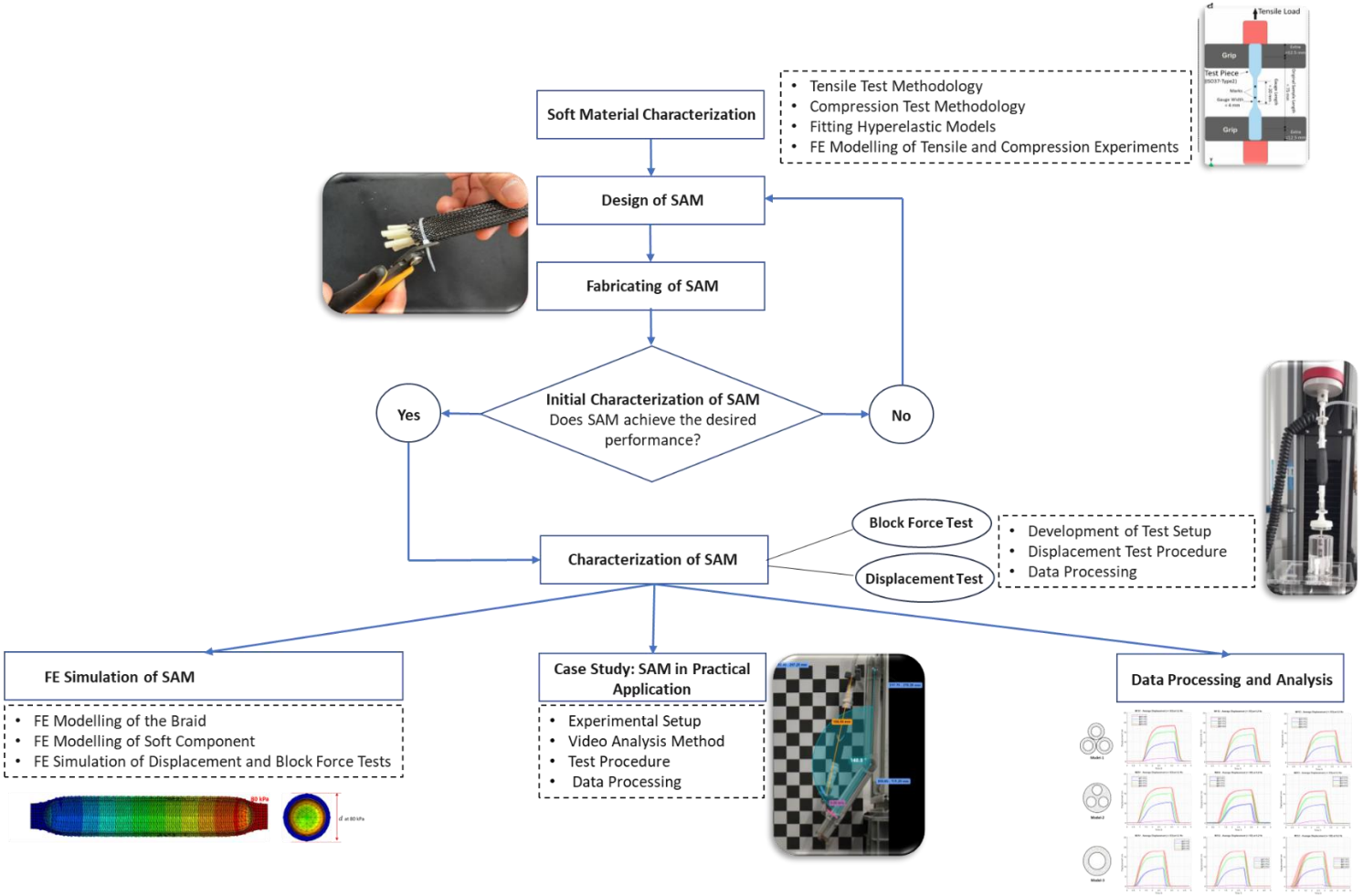

Figure 1-1: Flowchart illustrating the methodologies employed throughout the thesis.

Chapter 2 : Literature Review

2.1 Introduction

In this chapter, a study of the current knowledge surrounding soft robotics and muscle-like actuators is carried out. The focus is on presenting the basic concepts, methods, and advancements within this field. The literature review aims to provide a wide overview of soft material characterization, the basic design principles of SAM, and the techniques involved in fabricating soft materials. Additionally, the review covers an exploration of testing and simulating SAM, aiming to give a full understanding of the related literature.

Introducing Soft Pneumatic Actuators (SPAs) is important in the literature review about SAM development because SAMs are a type of SPA. By discussing SPAs, including their designs, fabrication techniques, and examples, we provide context and background information relevant to understanding SAMs. This allows readers to comprehend the broader category of SPAs, of which SAMs are a specific subset.

The structure of the chapter is organized to guide readers through the various aspects of soft robotics. A thorough look at current research and developments about SAM is provided, showing the findings and identifying the challenges within the field. It also identifies research gaps and compares different methods in the design, fabrication, and characterization of soft actuators, particularly muscle-like actuators, showing the diversity in research practices.

2.2 Objectives

The aim of this chapter is to present the essential related aspects of soft robotics with an emphasis on SAM. To achieve this, the following objectives are set:

Objective 1: To introduce the field of Soft Robotics, focusing on SAM and discuss the importance of material characterization in developing these actuators.

Objective 2: Explore various designs and fabrication methods of SAM, aiming to highlight innovation within the field and identify gaps in current research that could lead to advancements in soft robotics technologies.

Objective 3: Examine the role of Finite Element Analysis (FEA) in simulating SPAs and SAM, assessing how these simulations contribute to the optimization and practical application of soft robotics technologies.

2.3 Soft Robotics

Conventional robots, typically constructed from rigid materials like plastic and metal and powered by regular motors, contrast with the soft and flexible nature of the human body and biological creatures. This difference has encouraged the rise of soft robotics, a growing field focused on designing robots from elastic materials and actuated by soft actuators [1][2]. The concept of soft robotics beginnings its origins back to the early 2000s, with foundational research exploring the potential of soft structures to produce complex motions [3]. Using inspiration from living organisms, researchers have developed soft actuators and sensors, leading to significant advancements in bio-inspired robotics [4]. By leveraging elastomeric materials, soft robotics offers the potential to mimic the behaviours of various biological organisms, such as fish [5], jellyfish [6], squid [7], octopus, and earthworms [8]. These advancements hold promise for developing robots capable of navigating diverse environments and performing tasks with enhanced flexibility and adaptability. Additionally, compliant materials offer the flexibility to perform functions similar to traditional robotics while having properties that allow them to absorb hard impacts without damage, making them suitable for some harsh environments.

Soft actuators have unique capabilities that make them ideal for interacting with humans and navigating unstructured environments. The key capability is their inherent compliance, which allows them to deform to the shape of objects they interact with. This compliance reduces the risk of damage or injury when handling fragile objects, making soft actuators safer for human interaction compared to traditional rigid actuators [9].

Soft robotics is a multidisciplinary field that merge different areas like biomedical engineering, biomechanics, chemistry, programming, and tissue engineering [10]. This multidisciplinary approach is important for the development and innovation within soft robotics. The applications of soft robotics are diverse. In healthcare, soft robotic devices assist in surgeries and rehabilitation, offering safer interaction with patients [11][2]. In manufacturing, soft grippers handle fragile items, improving efficiency while reducing damage [12]. Environmental exploration benefits from soft robots' ability to adapt to

various conditions, from deep-sea floors to rough landscapes, enabling studies in previously inaccessible areas [13][14].

2.4 Soft Material

Soft materials are a large category of substances known for their flexibility, deformability, and compliance. They include a wide range of polymers, elastomers, and certain biological materials. These materials can easily change shape under external forces or environmental conditions but return to their original state once these forces are removed or conditions are normalized [15]. Key characteristics of soft materials include low Young's modulus and high elasticity. Soft material characteristics fundamentally define the applicability of soft robotics, distinguishing them significantly from their rigid counterparts.

Various companies offer a range of products suitable for fabricating soft robots, among which Smooth-On, Inc. (http://www.smooth-on.com) is notable for its extensive selection of silicone rubbers. Originally designed for creating skin effects in movies, these products have been discovered to be well-suited for soft robotics fabrication. Their products include platinum-catalysed silicones known as the Ecoflex series and the Dragon Skin series. The Ecoflex series comprises silicone materials with different ratings of shore-hardness that range from 00-10 to 00-50, while the Dragon Skin series offers materials with shore-hardness ratings from A10 to A30. Shore-hardness scale is depicted in Figure 2-1. Another widely used material is Elastosil M 4601 (a silicone produced by Wacker Chemie AG; https://www.wacker.com), which possesses characteristics such as low shore-hardness and high tear strength. Table 2-1 provides a comparison of properties among various materials, including Ecoflex 10-00, Ecoflex 20-00, Ecoflex 30-00, Ecoflex 50-00, Dragon Skin Silicon 10, Dragon Skin Silicon 20, Dragon Skin Silicon 30 medium, and Elastosil M 4601. These soft materials have Young’s modulus in the order of 10^5 to 10^6 Pa, while natural organisms, such as skin or muscle tissue, have a Young's modulus ranging from 10^4 to 10^9 Pa [18]. The selection of these eight materials was based on their widespread use in the field of soft robotics [1][16][17], where they have proven to be reliable for creating soft actuators.

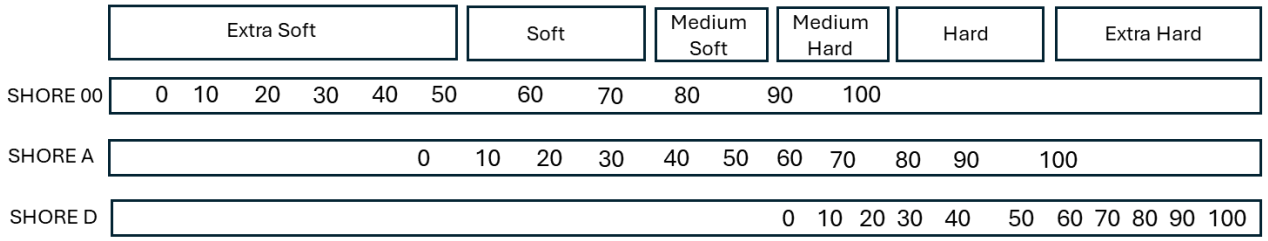

Figure 2-1: Shore-hardness scales and everyday items to express the sense of hardness.

Table 2-1 summary of the elastomers data from the manufacturer [19][20]**.**

PROPERTIES	ECOFLEX 10-00	ECOFLEX 20-00	ECOFLEX 30-00	ECOFLEX 50-00	DREGON SKIN 10	DREGON SKIN 20	DREGON SKIN 30	ELASTOSIL
SPECIFIC GRAVITY G/CM^3	1.04	1.07	1.07	1.07	1.07	1.08	1.08	1.13
POT LIFE (MIN.)	30	30	45	18	20	25	45	90
CURE TIME (H)	4	4	4	3	5	4	16	12
SHORE HARDNESS	OO-10	OO-20	OO-30	OO-50	10A	20A	30A	28A
TENSILE STRENGTH (MPA)	0.8273	1.1031	1.3789	2.1718	3.2750	3.7921	3.7921	6.5
ELONGATION @ BREAK (%)	800	845	900	980	1,000	1,000	1,000	700
MIX RATIO BY WEIGHT	1A:1B	1A:1B	1A:1B	1A:1B	1A:1B	1A:1B	1A:1B	9A:1B
COLOR	Translucent	Translucent	Translucent	Translucent	Translucent	Translucent	Translucent	Reddish brown

2.4.1 Soft Material Characterization

Soft materials are notable for their ability to undergo substantial deformation without failing, attributed to their low Young's modulus [21]. They can adapt to the shapes of contacting surfaces under stress, and they typically return to their original form and size unless stretched beyond their breaking point.

The mechanical behaviours of hyperelastic materials can be tested in several ways, including uniaxial test (tension and compression), biaxial test (tension and compression), planar test (tension and compression) [22]. For instance, Moseley *et al.* [17] conducted a study to understand the properties of Ecoflex 00-30 by uniaxial tension, biaxial tension, and planar tension tests [17]. Schumacher *et al.* [23] have described two ways to create models for this kind of hyperelastic material: one using data from uniaxial tension and another using data from both uniaxial tension and biaxial tension. They discovered that the accuracy of the models created from both methods was nearly the same. This approach is considered reliable even for very soft silicone materials when they are stretched or compressed significantly.

It is important to utilize suitable standard methods appropriate for soft materials. Standards such as ASTM D412 and ASTM D575 specify procedures for tensile and compression tests, respectively, on soft material samples. These standards provide detailed guidelines on how to perform tests, including specimen preparation, testing machine setup, and the execution of the test. This consistency ensures that tests conducted by different operators or laboratories are comparable, making results more reliable and reproducible. Some papers, such as that by P. Moseley *et al.* [17] have presented testing methods for testing soft materials by using ASTM D412.

Another set of standards for tensile and compression tests are ISO 37:2017(E) [24] and ISO 7743:2017(E) [25], respectively. These standards outline methods for determining the tensile and compression stress-strain properties of vulcanized and thermoplastic rubbers. They specify the shapes and dimensions of specimens, test procedures, and result calculations. For tensile tests, the two main shapes provided are dumb-bell and ring. The dumb-bell shape is the most commonly used for tensile tests. Figure 2-2 depicts the dimensions of a dumb-bell specimens, illustrating the detailed dimensions of type 2 as an example. On the other hand, the compression tests standard, ISO 7743:2017(E), provides four test methods (A, B, C, and D) as well as two cylindrical specimens. Figure 2-3 shows typical force-displacement curve for an elastomer and shape of the specimen under tensile and compression tests.

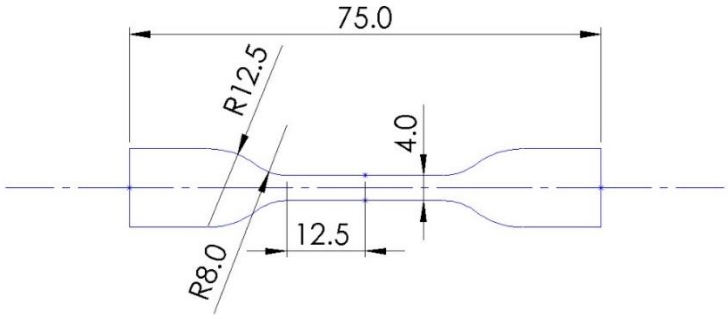

Figure 2-2: Dumb-bell specimens' dimensions [24]**.**

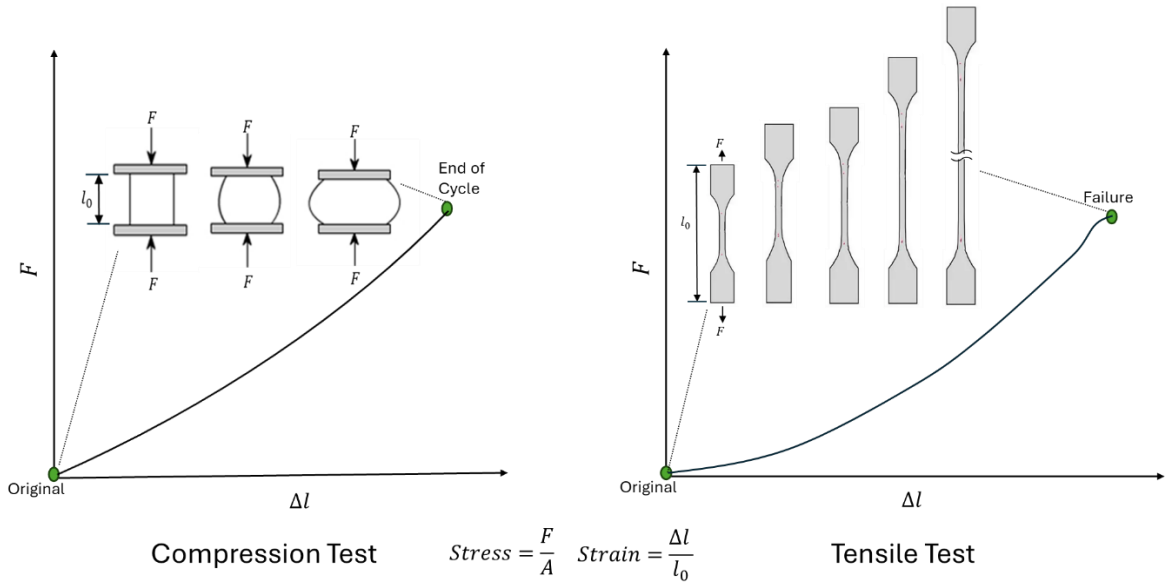

Figure 2-3: Typical force-elongation curve for an elastomer and shape of the specimen under tensile and compression tests.

For compression tests, they are conducted to assess the compression stress and strain characteristics of various soft materials. In compression tests, a specimen is positioned between two flat plates within a testing apparatus and is then exposed to compressive force. The stress applied to the specimen is determined by dividing the force exerted by the initial surface area of the specimen. The standard ISO 7743:2017(E) provides procedures for conducting these compression tests adhere to the guidelines set. Table 2-2 provides a systematic categorization of the standard testing methods and their corresponding specimen types.

Table 2-2 classification for the standard test methods and the related specimens or product [25]**.**

Methods	Specimens	Compression Plates	Results
Method A	**Specimen A** Cylindrical piece with diameter of 29 ± 0.5 mm and height of 12.5 ± 0.5	Two lubricated metal plates. At least one of the two plates should be highly polished.	Dependent on the modulus of the material. Independent of the specimen shape. Slip conditions are achieved.
Method B	**Specimen A**	Two metal plates bonded to the specimen. At least one of the two plates are intended for bonding.	Dependent on the modulus of the material. Dependent on the specimen shape. No Slip conditions.
Method C	**Specimen B** Cylindrical piece with diameter of 17.8 ± 0.25 mm and height of 25 ± 0.25	Two metal plates lubricated or not. The surface finish of the plates is not important.	Independent on the specimen shape. Independent on the lubricant conditions.
Method D	Product or part of a product. The length of the specimen should be between 50 mm and 100 mm.	Two lubricated metal plates. At least one of the two plates should be highly polished.	Dependent on the product shape.

Each method utilized in the compression tests shares a similar setup, with variations only in how the specimens are assembled between the compression plates. These differences can lead to varying outcomes, necessitating careful selection of the most appropriate method based on several criteria: the desired outcomes of the compression tests, the availability of suitable moulds for specimen fabrication, and the capabilities of the compression-testing machine. A compression-testing machine

must meet specific requirements to be considered adequate for these tests, including:

1. The ability to measure deformation with an accuracy of ±0.02 mm.
2. The capacity to operate at a compression rate of 10 ± 2 mm/min.
3. The capability to align the compression plates in parallel.

2.4.2 Hyperelastic Models

Unlike traditional robots whose movements can be predicted with standard movement equations, the flexible movements of soft robots are too complex for this method. To deal with this difficulty, FE simulation can be used to predict the complicated mechanical actions of soft robots by breaking down their shape into small, finite parts. Importantly, accurately simulating these soft robots relies on having a precise and strong understanding of the soft materials, which can be captured through a mathematical model and its specific values [18].

The materials most often used in soft robotics are known as hyperelastic materials that exhibits large elastic deformations. These materials can undergo significant stretching or compressing and still return to their original shape once the applied load is removed [26]. Because these materials can deform a lot and their force-displacement relationship isn't linear, the traditional theory of small strains does not work well for understanding the complicated behaviours of soft materials [22]. In 1940, M. Mooney introduced a mathematical formula to describe the energy stored in a material when it's stretched significantly [21]. Other researchers have suggested different mathematical formulas to explain how these hyperelastic materials behave, including the Neo-Hookean model, Polynomial model, Yeoh model, Ogden model, and Arruda-Boyce model [22][17][27]. These models have been used to define soft materials properties and have found applications in diverse movement systems, including actuators employed in robotic surgery [28] and actuators that move in straight or bending ways [17].

The hyperelastic properties of soft materials can be characterized through a strain energy function employed in FE modelling. This function is based on invariants (I_1, I_2, I_3) of the Green deformation tensor and invariants functions related to the principal stretch ratios $(\lambda_1, \lambda_2, \lambda_3)$ The strain energy function is expressed as:

$$W = f(I_1, I_3, I_3) \qquad \text{Equation 1}$$

Here, the invariants are defined as $I_1 = \lambda_1^2 + \lambda_2^2 + \lambda_3^2$, $I_2 = \lambda_1^2\,\lambda_2^2 + \lambda_2^2\,\lambda_3^2 + \lambda_1^2\,\lambda_3^2$, and $I_3 = \lambda_1^2\,\lambda_2^2\,\lambda_3^2$ [26][29].The strain energy equation (W) can be further expressed as:

$$W = \underbrace{\sum_{i+j=1}^{N} C_{ijk}\,(I_1 - 3)^i \,.\, (I_2 - 3)^j}_{\text{Deviatoric Term}} + \underbrace{\sum_{i=1}^{N} \frac{1}{D_i}\,(J_l - 1)^{2i}}_{\text{Volumetric Term}} \qquad \text{Equation 2}$$

In continuum mechanics, stress tensors are categorized into hydrostatic (volumetric) and deviatoric stresses. The deviatoric term influences the change in the shape of hyperelastic materials, while the volumetric term affects the volume change [30][31]. For incompressible materials like elastomers, where the volume remains constant during deformation, the equation simplifies to [32]:

$$W = \sum_{i+j=1}^{N} C_{ij}\,(I_1 - 3)^i \,.\, (I_2 - 3)^j \qquad \text{Equation 3}$$

Here, C_{ij} represents a material constant, and N defines the order of the term [26].

The FE software Abaqus (Simulia, Dassault Systems) offers a feature to fit curves to test data based on the strain energy potential form. Mooney-Rivlin and Polynomial N2 models utilize the full form Equation 3 known as Polynomial models, while Neo-Hookean and Yeoh adopt the reduced form, referred to as Reduced Polynomial models [17].

2.5 Soft Pneumatic Actuator (SPA)

The soft actuator serves as the active component in a soft robot, generating movement. Research communities focus on the development of high-capacity soft actuators to enhance the robot's ability to perform various tasks. These actuators are typically made from soft materials such as silicone rubber [33] and polymers [7], enabling flexible and continous motion [16]. Furthermore, they can be designed with different configurations to achieve desired amount of force, type of motion, and speed outputs [33]. The efficiency of soft actuators is often evaluated based on two main outputs: generated force [34] and end effector speed [33].

Soft actuators find applications in diverse fields such as medical assistance [2] and gripping objects in rough environments [35][36]. Soft actuators for soft robotics can be categorized based on the stimulus that generates the actuation response. These stimuli include pneumatic, thermal, magnetic, and electric fields [37]. For example, some researchers in this field utilize shape memory alloy (SMA) to generate movement through electric current and heating [38]. SMA actuators offer high deformation and force with simple mechanical operation. However, soft actuators actuated by pneumatic inflation provide larger amplitude of motion with higher flexibility. Moreover, SPAs are interesting due to their affordability and ease of fabrication. Both the design and the fabrication process of soft actuators are challenging and require careful consideration to achieve high efficiency [28].

Researchers in the field of soft robotics have proposed various configurations of SPAs, including PneuNets Bending Actuators [1], Fiber-Reinforced Actuators [35], Multi-directional soft manipulators [7][39], McKibben Air Muscles [40], and Thin McKibben Air Muscles [41]. Numerous papers have been published on these soft actuators and their applications. Figure 2-4 shows various configurations of SPAs in soft robotics. Researchers continue to explore the development of novel SPA to expand the applications of soft robotics [42]. Depending on the conceptual design, SPAs can implement specific types of movement, such as bending, elongating, twisting, contracting, or combining multiple types of movement in one actuator [42]. The following section provides various examples of the SPAs in order to reveal insights into how different designs influence actuator performance. This knowledge can guide the selection of structural designs for specific applications.

2.5.1 PneuNets Bending Actuators

PneuNets Bending Actuators are a type of SPA that implements movement via pressurized embedded channels, leading to bending motion [1]. The desired amount of bending motion is achieved by modifying the properties of the chambers. After pressurization, the elastomeric structure expands. This expansion is more clear in areas of the bladder where the walls exhibit lower stiffness or reduced thickness, leading to the actuator's bending [43]. Figure 2-4a illustrates the structure of the PneuNets Bending Actuator, which consists of two layers: the extensible layer and the inextensible layer [33]. The series of chambers form the extensible layer, while the function of the inextensible layer is to constrain the inflation from the bottom, thereby bending the actuator body when inflated.

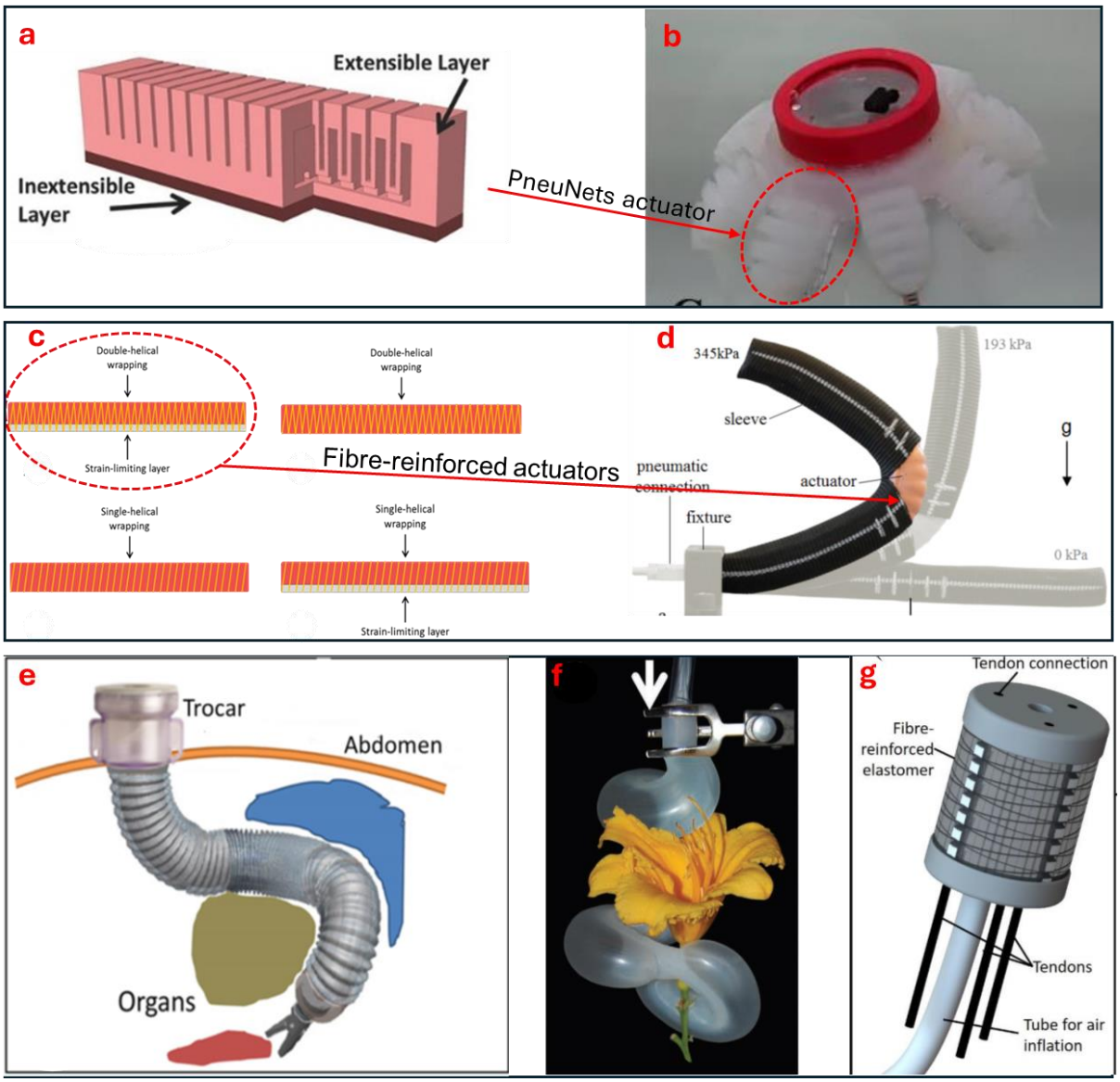

Figure 2-4: Various configurations of SPAs in soft robotics: (a) Schematic for PneuNets actuator [33]**, (b) Jellyfish robot achieving propulsion using PneuNets actuators** [6]**, (c) Motion configurations of fibre-reinforced actuators** [44]**, (d) Case study of the double helical fiber-reinforced actuator** [35]**, (e) High dexterity and flexibility of STIFF-FLOP in surgical environments** [45]**, (f) Robotics Tentacles** [46]**, and (g) 3 DOFs Mini Variable Stiffness actuator** [47]**.**

PneuNets Bending Actuators are versatile and can be utilized in various applications, enabling soft robots to operate in multiple modes of actuation. For instance, the Bio-Robotics Lab at Florida Atlantic University has developed a free-swimming soft robot inspired by jellyfish (see Figure 2-4b) [6]. The robot achieves propulsion using eight PneuNets Bending Actuators arranged around an electronic housing. Each group of four PneuNets Bending Actuators is actuated by separate impeller pumps, allowing

for control over the direction of movement. Additionally, each individual actuator is equipped with resistive flex sensors to monitor its position.

2.5.2 Fibre-Reinforced Actuators

The Fiber-Reinforced Actuator is a famous type of SPA consisting of a soft bladder and fibers surrounding the outer surface to restrict radial expansion [35]. The soft bladder inflates like a balloon in all directions. For different types of motion such as bending, twisting, or elongation, there are typical configurations involving strain limiting with fibers [44]. To achieve bending motion, fibers are helically wrapped multiple times around the outer surface, and an inextensible layer is added to the bottom of the soft actuator. For elongating motion, the same fiber wrapping configuration is used without adding an inextensible layer. For twisting and extending motion, fibers are wrapped helically around the outer surface once without adding an inextensible layer. Another configuration involves wrapping fibers helically around the outer surface once and adding an inextensible layer to achieve twisting and bending motion. Figure 2-4c illustrates these four configurations. The range of motion for each configuration can be controlled by modifying the structure of the soft actuator.

For example, K. C. Galloway *et al.* [35] demonstrate a methodology for adjusting the magnitude of the desired range of bending motion in the fiber-reinforced actuator by enveloping the actuator with an inextensible sleeve and leaving a small portion without strain limiting. Figure 2-4d shows the impact of changing the sleeve spacing on the range of bending. The ability of performing various types of motion enables the use of fiber-reinforced actuators in various applications, such as holding objects [35] and in rehabilitation devices [48].

2.5.3 Multi-Direction Soft Manipulators

Some papers have discussed various strategies for enabling soft actuators to move in multiple directions. Among the most popular actuators are the STIFF-FLOP Surgical Manipulator [39][7] and Robotic Tentacles with Three-Dimensional Mobility [46], 3 DOFs Mini Variable Stiffness [47], all which are actuated by pressurized air. Although the designs of the STIFF-FLOP and Robotic Tentacles with Three-Dimensional Mobility differ in aspects such as dimensions and fabrication techniques, they share a similar conceptual design. Specifically, both utilize three

independent chambers within a single cylindrical actuator to achieve movement with multiple degrees of freedom.

STIFF-FLOP allows for high dexterity and flexibility in surgical environments while the Robotics Tentacles are more suitable for applications requiring high adaptability and the ability to handle various objects. The end effector of surgical robots is typically made of rigid materials such as laparoscopic tools or needles and is usually driven by motorized links. STIFF-FLOP manipulator has the ability to perform bending and elongation [39][45]. The actuator consists of a sequence of three modules attached to each other, with each module containing three chambers to facilitate movement in multiple degrees of freedom. Additionally, a central cavity is used to control the stiffening of the modules by employing the granular jamming technique. The actuator is then enclosed within a mesh structure that amplifies angular movement and prevents lateral expansion when the actuator is inflated (see Figure 2-4e). On the other hand, Robotic Tentacles with Three-Dimensional Mobility draws inspiration from flexible organisms such as lizards or octopuses by mimicking the active parts in their bodies. It is capable of gripping and handling patchy and rough items. The structure is constructed of elastomeric material that expands to bend, and it can be shaped according to the object that the robot intends to grip (see Figure 2-4f).

2.6 Soft Actuators Fabrications

One of the most crucial steps in developing soft actuation systems is the fabrication process [48]. The fabrication of soft actuators differs significantly from that of rigid actuators due to the soft materials used and the methods of fabrication. The methods used to fabricate soft components often requiring specific techniques unlike rigid components that are usually fabricated through traditional techniques. Additionally, fabricating the soft robots' complex designs from flexible materials adds a layer of complexity.

Several techniques are utilized in soft actuator fabrication, including moulding and 3D printing. Moulding involves pouring or injecting a pre-polymer, in liquid state, into a predefined mould and letting it cure, while 3D printing allows for layer-by-layer construction of soft object. The process of fabricating soft actuation system [49] typically begins with design and material selection, followed by the creation of moulds or models for 3D printing. After fabrication, actuators undergo post-processing, which may include curing, cutting, and assembly with other components like sensors or control units.

2.6.1 Fabrication by Moulding

Traditionally, soft actuators are fabricated by casting liquid elastomer into moulds. When casting soft material, it is important to consider properties of the liquid elastomer such as viscosity, curing time, and pot life, as they require specific conditions for fabrication. Many papers proposing fabrication techniques for soft actuation systems have utilized moulds made of 3D-printed materials [43][16]. Figure 2-5 shows fabrication process by moulding from several papers.

The common fabrication processes by moulding include designing and fabricating the mould. The components of the elastomer liquid are mixed, initially often done manually in a cup [43][46], but now frequently performed using centrifugal mixers [16]. Next, the mixture is degassed to remove air, achieved either by using a vacuum pump [43][50] or centrifugal vacuum. The elastomer liquid is then cast into the mould [6][16][43][46], followed by allowing the material to cure at the required temperature.

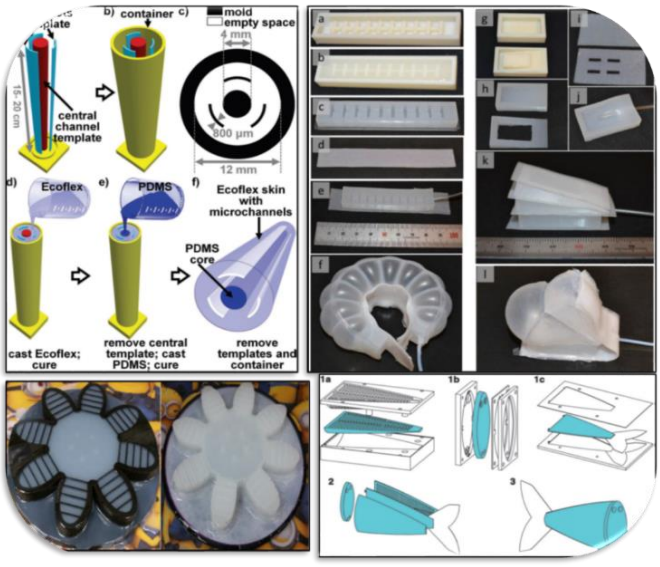

Figure 2-5: Fabrication process by casting [5][43][46]**.**

2.6.2 Fabrication by 3D Printing

3D printing technology offers significant advantages for fabricating soft actuators, including the ability to create complex geometries, customize designs for specific applications, and rapidly iterate prototypes. This capabilities makes 3D printing an increasingly popular choice for researchers working in the field of soft robotics [51].

Fabricating soft actuators using 3D printing technology involves the creation of elastomeric structures of the soft actuator. Depending on the design, the printer may also create channels or cavities within the actuator to accommodate pneumatic or hydraulic fluid for actuation purposes [52]. This process typically begins with the design of the actuator using CAD software [53]. Some advanced 3D printers allow for the incorporation of multiple materials in a single print such as Polyjet printers [53], enabling the creation of complex structures with varying degrees of flexibility.

Once the printing is complete, the fabricated actuator may undergo post-processing steps such as curing to enhance its mechanical properties and ensure dimensional stability. After post-processing, the actuator is ready for integration into a soft robotics system. For instance, in a single-step fabrication, a gripper is created from Shape Memory Polymer (SMP) using 3D FDM technology [54].

Researchers have also developed soft actuation systems using adaptable fabrication techniques, including Shape Deposition Manufacturing (SDM) and multilateral 3D printing [55]. Both technologies facilitate the manufacturing of soft actuation systems and bringing unique advantages. The SDM technique provides a layer manufacturing method that enables the fabrication of 3D parts through cycles of layer deposition. In the context of fabricating soft actuation systems, SDM is particularly useful because it enables the integration of soft and rigid materials within the same component. On the other hand, Multilateral 3D printing capable of handling multiple materials within a single manufacturing process. It is interesting technology for fabricating soft actuation system because it allows for the direct fabrication of soft actuators with integrated functionalities.

2.7 Overview of SAM

The McKibben air muscles, initially innovated in the 1960s, are alternatively referred to as Pneumatic Artificial Muscles in some research contexts [40]. However, in this thesis, they are denoted as SAMs. They have since found applications due to their flexibility, ease of fabrication, and ability to provide contraction motion similar to human muscles. These artificial muscles consist of an soft component surrounded by strain-limiting component (braid) [56]. The braid is contractible but not stretchable, so the radial expansion of the soft component causes the artificial muscles to contract [57].

Despite its simple appearance, understanding the SAMs operational mechanism involves considering two phenomena [58]. Firstly, there is a non-linear relationship between stress and strain within the soft component, coupled with a complex

relationship between the muscle's outputs and its input pressure range. Secondly, the braid, which functions as a 'flexible joint structure,' deforms during contraction to accommodate the muscle's increasing radius.

2.7.1 Bundle of SAMs

Discussing the creation of bundle of SAMs is crucial in this literature because the conceptual design of the soft actuator in this research draws inspiration from human skeletal muscles. Initially, it is essential to simply understand the components of skeletal muscles from an anatomical perspective. Skeletal muscles consist of bundles of muscle fibers, which are long cylindrical cells that contract or relax upon receiving signals from the nervous system [59]. These muscles contain muscle bundles composed of repeating sections of muscle fibers Figure 2-6. The more repeating sections of muscle fibers present, the stronger the muscle will be. The muscle fiber shortens due to an internal chemical reaction, leading to the shortening of the entire muscle and generating the force required to move the body.

Using a bundle of SAMs, inspired by the biomechanical efficiency of the human muscular system, offers a strategic approach in soft actuator design for enhanced force output and modularity. This inspiration from human muscles, which consist of multiple fibers working together to produce force, suggests that a collective of SPAs can similarly achieve higher force outputs than a single unit. Such an arrangement not only mimics the strength found in natural muscle but also introduces modularity into the soft actuator’s design.

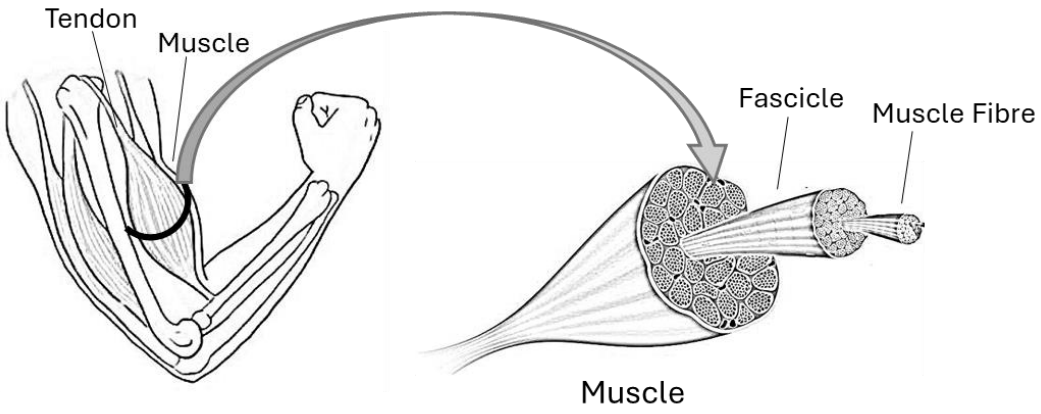

Figure 2-6: The structure of skeletal muscle.

S. Kurumaya *et al.* [41] developed bundles of thinner McKibben air muscles, each with a diameter of 1.8 mm. By bundling these muscles together, they achieved a multifilament muscle that possesses the required shape and flexibility. Traditional McKibben air muscles typically have diameters ranging from 10 to 40 mm, which limits their flexibility in tight spaces. Figure 2-7a illustrates the structure of the thin McKibben muscle, consisting of a thin rubber tube surrounded by a braided sleeve of 1.8 mm. When the bundle is inflated with air, they contracted and curve outward due to their lateral inflation (see Figure 2-7b).

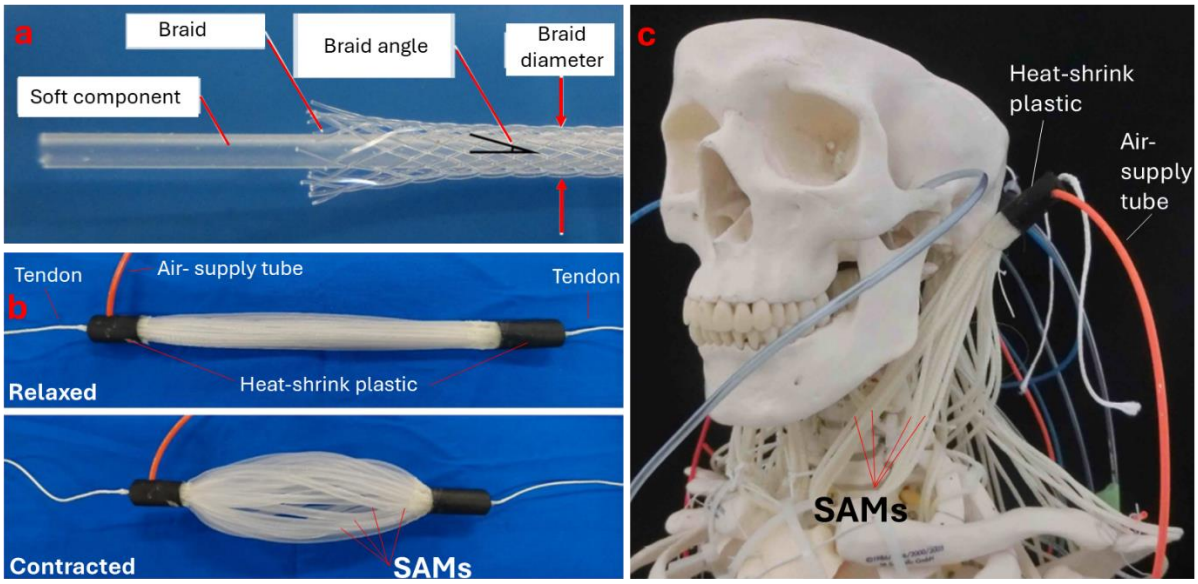

Figure 2-7: (a) structure of a single thin SAM [41]**, (b) linear actuator of 30 thin SAM rest at the upper figure and contracted in the lower** [41]**, (c) Thin SAMs integrated on an artificial human neck included bones and ligaments** [60]**.**

The advantages of thin McKibben muscles have encouraged researchers to explore potential applications, such as multifilament McKibben muscles, which aim to mimic the mechanics of the human neck [61]. A. Garriga-Casanovas *et al.* [61] introduced thin McKibben muscles integrated into an artificial human neck, complete with simulated bones and ligaments (Figure 2-7c). This artificial neck replicates the complex structure of the human neck, including its muscles, bones, and ligaments. Another application of thin McKibben muscles is evident in the development of a musculoskeletal lower-limb robot [60]. Given the nature of human lower-limb muscles, a considerable number of multifilament muscles are required. The resulting motion achieved by this artificial limb closely resembles that of a human.

2.7.2 SAM Fabrication

Fabrication techniques for SAMs typically involve fabricating and assembling soft component and a braid [58]. Common methods include moulding the soft component or using commercial materials often made from latex or silicone. Various types of commercial braids with different properties are used, as explored in the literature. The soft component is chosen for its flexibility, while the braid, composed of materials like nylon or polyester, provides reinforcement [62]. Careful integration of these components is essential to ensure proper functionality. Key requirements include compatibility of materials to ensure precision in the fabrication process to achieve consistent actuator performance. The design must also consider the ease of integration with pneumatic activation systems and the final application's specific requirements [63].

The fabrication process of SAMs involves several sequential steps. It begins with the selection of appropriate materials of the soft component and braid. Following material selection, the rubber tube is prepared to the desired length, and the braided sleeve is trimmed accordingly [64][65]. Subsequently, the rubber tube is inserted into the braided sleeve, ensuring a secure fit, and the ends of the sleeve are typically fastened to prevent unravelling. Connectors are then attached to the end of the assembly to facilitate pneumatic connections. After assembly, the ends of the rubber tube are sealed with the connectors to prevent air leakage, employing adhesive bonding.

2.7.3 SAM Characterization

SAMs characterization have been the focus of several research projects over the past decades [66]. The literature review highlighted the importance of precise and thorough testing methods to understand the capabilities and limitations of these actuators [56][65][67][68]. Due to the unique properties of soft actuators like SAMs, researchers in the field of soft robotics have been developing specialized methods to measure their mechanical performance. SAM characterization methods found in literature vary. The level of variation can be clearly observed in some papers such as between the test that conducted by C. Kothera *et al.* [68] and N. Goulbourne *et al.* [69].

The literature review shows varying objectives and methodologies in SAM characterization. While N. Goulbourne *et al.* [69] acknowledged the load as an input factor, they did not perform separate tests to evaluate the SAM's force generation capabilities, unlike C. Kothera *et al.* [68] The literature mostly focuses on two

parameters: force generation and the range of contraction adopting different testing approaches. These enable the system to perform a variety of conditions, including constant pressure testing, isometric testing, and isotonic testing [56][70][71]. Figure 2-8 shows methods of testing SAMs: a) testing SAM's range of contraction freely without tension effect to observe contraction behavior without any load effect, b) testing SAM's range of contraction under tension effect to evaluate performance under specific load, and c) testing SAM's generated force in a block force test.

Furthermore, characterization often includes assessing the muscles' response to different operating parameters, such as varying levels of pneumatic pressures or actuation frequencies. This helps determine optimal operating conditions for achieving desired performance characteristics, such as force output, speed, and energy efficiency [72]. Accurate characterization requires precise control over testing conditions, such as the use of calibrated sensors to measure forces, pressures, and displacements accurately [73].

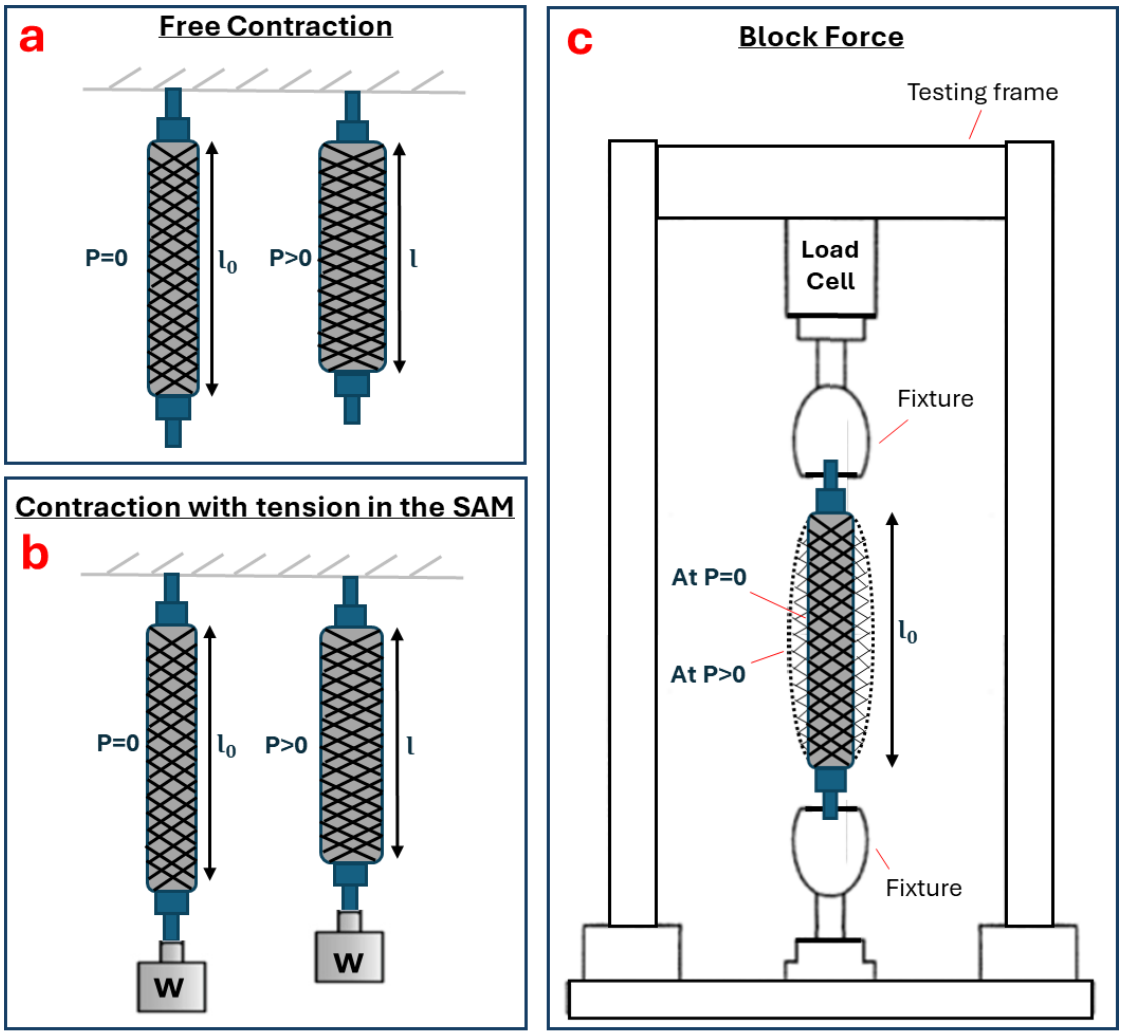

Figure 2-8: Methods of testing SAMs: (a) testing SAM's range of contraction freely without tension effect, b) testing SAM's range of contraction under tension effect, and c) testing SAM's generated force in a block force test.

2.7.4 SAM Applications

In the field of robotics, the utilization of SAMs has been extensively investigated. Researchers present various types of SAMs documented in the literature [63] and explore their application as actuators that facilitate precise and flexible movement similar to human muscles [74]. The compliance and adaptability of SAMs make them suitable for applications requiring delicate and responsive robotic motions.

SAMs have been used in various applications instead of piston cylinders because they have low friction, are lighter, and do not require critical actuator alignment. However, compared to piston cylinders, SAM produce smaller magnitudes of force [58]. Figure 2-9a presents the renewed version of the SAM designed by Bridgestone

in the 1990s. The Bridgestone version, also known as a "rubbertuator," marked a significant advancement in the development of SAMs, showcasing the industry's interest in developing more human-friendly robots that offer natural skeletal muscle compliance. Figure 2-9b illustrates the original use of the SAM as a prosthetic actuator in the 1960s. This application demonstrates the muscle's early adoption in prosthetics, where it acted as a pneumatic actuator to simulate natural muscle movements. Figure 2-9c depicts the use of the SAM up to the paper date (2012) in soft actuation for service robotics. This configuration highlights the muscle's versatility and its application in modern robotics, providing soft actuation that mimics the compliance and flexibility of biological muscles. The setup in this figure could represent how SAMs are integrated into robotic systems to achieve manipulation tasks, adaptive gripping, or movements that require a gentle touch, underscoring the evolution of the muscle's applications from medical devices to robotic components.

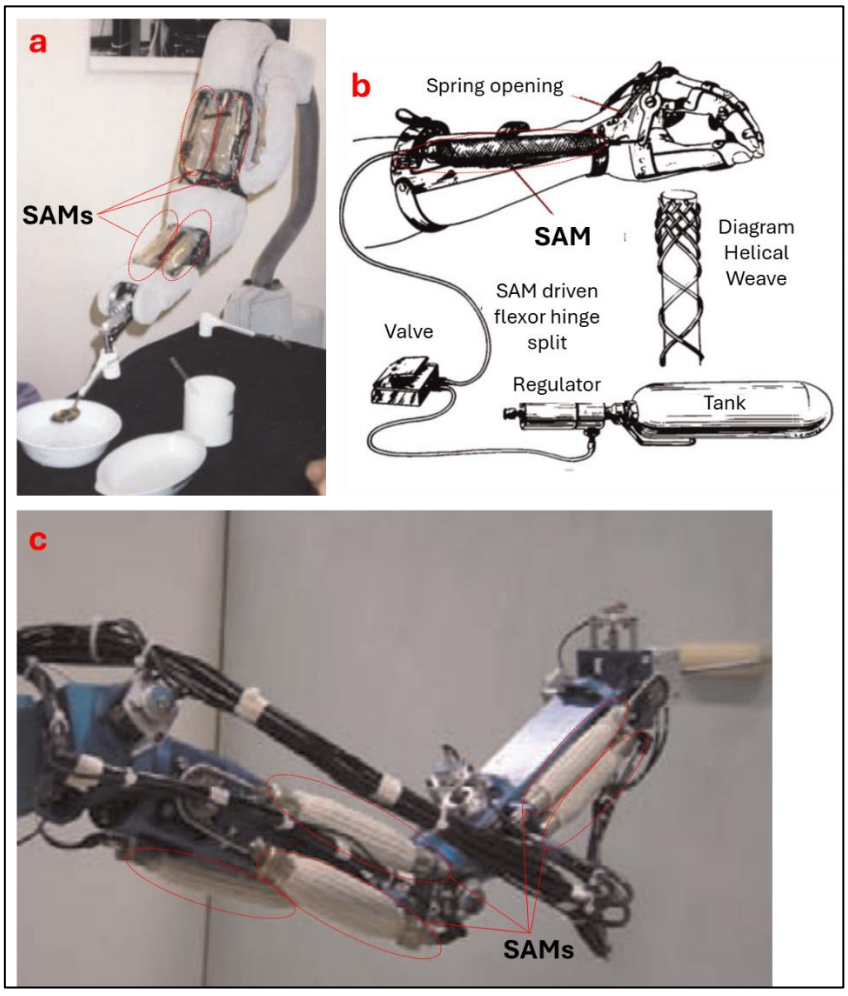

Figure 2-9: SAM applications: (a) robots mimicking human muscle in 1993, (b) the first use in 1960s as a prosthetic actuator, and (c) service robotics in 2012 [58]**.**

G. Nikolakopoulos *et al.* [63] presents a comprehensive overview of the applications of SAM across biorobotics, medical, and industrial fields. In biorobotics, SAMs are good for developing biologically inspired robots, mimicking human muscles movements in robots such as humanoid robots [75][76] and robotic limbs [77]. These applications demonstrate SAMs' ability to emulate organic muscle movements, offering compliant structures for robots that interact safely in human environments.

Medical applications of SAMs are particularly notable for rehabilitation and assistive devices [78], where their compliance and muscle-like action support the development of exoskeletons, prosthetic limbs, and devices aiding in the recovery of motor functions. One notable case study discussed is a soft robotic prosthetic hand for amputees [79], featuring an actuated thumb with three pneumatic artificial muscles arranged to achieve multiple degrees of freedom similar to a human thumb. Furthermore, the potential of PAMs in developing medical robots that assist in delicate surgeries, such as microsurgery, and rehabilitation robots that help patients regain mobility and independence.

In the industrial sector, SAMs contribute to the advancement of robotics by offering a range of actuators suited for various manufacturing applications, emphasizing safety, affordability, and ease of maintenance. For example, Ichim *et al.* [80] presented a simple gripper that is lightweight and mechanically straightforward, designed for powerful gripping actions. SAM is positioned close to the rotation centre of the finger to executes clamping motions. Another example by Ichim *et al.*, the positioning systems utilize SAMs for enabling workpieces to be raised or lowered as required, through the application or release of pressure in the SAMs, controlled by a hand-operated lever valve.

2.8 Simulation using FE Analysis (FEA)

2.8.1 Simulation of SPAs using FEA

Once the conceptual design for the soft actuation system is established, numerical tools such as CAD and FEA can be employed to facilitate modifications, improvements, and evaluations of the design. FEA allows for the prediction of the deformation pattern of the design and provides insight into its performance before fabricating a physical prototype and in other cases after fabricating and testing a physical prototype to validate the performance of the actuator. These advantages

have led to widespread adoption of FEA within the research community for soft robotics applications [81][82].

Predicting the behaviour of soft actuators using FEA requires incorporating several key components. These include accurate characterization of the material properties, precise modelling of the soft actuator's geometry, proper meshing of the soft actuator geometry, application of realistic loading conditions, and proper configuration of the FEA solver settings. For example, Y. Elsayed *et al.* [28] utilized FEA to simulate the deformation pattern of an existing soft actuator and optimize the material to prevent undesirable effects such as high pressure that could lead to bursting. The analysis identifies design parameters that minimize the module's ballooning effect during inflation and reduce the required actuation pressure.

2.8.2 Simulation of SAM using FEA

Simulation of SAMs using FE builds upon the foundational understanding established regarding the simulation of SPAs using FE generally. The link between the FE simulation of SAMs and the other types of SPAs lies in their common structure, where all comprise a soft inflatable structure. However, it's crucial to note that the braid in SAMs is significantly complex, requiring special consideration to model the complex interactions between the soft component and the braid. By incorporating the unique structural characteristics and material properties of SAM into the FEA model, researchers work on predicting their mechanical behaviour using various solving approach [71][83][84].

Several challenges were presented about simulating SAMs using FEA, particularly in accurately representing the braid and its interaction with the soft component. The braided sleeve's structure consists of interwoven fibers, which can be challenging to replicate accurately in a CAD model due to its complex geometry. Additionally, accurately modelling the interaction between the soft component and the braid presents challenges in FEA simulations.

FEA of SAMs has been conducted in various research papers, utilizing specialized software for FE simulation such as Ansys and Abaqus. These tools enable detailed modelling and analysis of the complex behaviours exhibited by SAMs under various conditions. Additionally, to accurately represent the structural intricacies of SAMs, some studies have employed separate software solutions to design the braided sleeve component. This design process is often facilitated through the use of CAD software or by developing custom coding scripts.

FEA methods for SAMs can be simplified using different approaches. Antonelli *et al.* [71] used axisymmetric geometry and assumed that the braid is rigidly locked with the soft component during contraction. Their model geometry is generated through a specialized algorithm that produces a script file for FE code input. Similarly, Tu *et al.* [83] applied a simplified FEA method by treating the braid as part of the rubber tube (soft component) and representing each thread as a singular element. In their approach, the thread model is created separately, then imported, duplicated, and embedded into the rubber tube model in the simulation software.

While Antonelli *et al.* [71] integrated the braid directly within the soft component's geometry, Tu *et al.* [83] modelled the threads separately before incorporating them into the overall design. Both methods aim to simplify the FEA process, but they differ in their treatment and integration of the braid with the soft component model.

Unlike previous researches that oversimplified the braid model, T. Hassan *et al.* [84] developed a comprehensive 3D model of the interlaced braided sleeve using software "Pyformex." This software employs Python scripts to create detailed 3D geometrical models, making it more suitable for modelling SAMs with soft components that are not in a regular tube shape. However, this process is more complex and time-consuming.

The simplified methods used by M. G. Antonelli *et al.* [71] and Tu *et al.* [83] streamline the modelling process. However, they can still be complex because the model's geometry is generated through a specialized script file, which may be less accessible for other researchers. Despite these differences, both comprehensive and simplified methods provide accurate FE modelling approaches. This is evident when comparing the agreement between experimental and simulation results in the three papers, where all presented a high level of agreement.

2.9 Discussion

The discussion highlights research gaps identified in the literature and shows the need for further exploration to advance the field. Key areas of focus include the characterization of soft materials, the design of SPAs, and the development of SAM designs. Additionally, the chapter examines the methodologies of SAM FE modelling. By addressing these gaps, this discussion aims to present development opportunities in soft robotics, with an emphasis on SAM.

2.9.1 Soft Pneumatic Actuators (SPAs)

Research gaps identified in the literature on SPAs that show the field's innovation potential. Among these gaps, two critical areas stand out: control and feedback mechanisms, and force output and efficiency optimization.

Firstly, it has been observed that the flexible structure of SPAs introduces complexities in control and feedback systems. The need for research into more advanced control systems is emphasized by the requirement to accommodate the non-linear behaviour of soft materials, enabling precise and predictable performance from the actuators.

Secondly, challenges in the force output and efficiency of SPAs, especially when compared to their rigid counterparts, are highlighted as significant research opportunities. Efforts aimed at optimizing both the design and material composition to improve force output and operational efficiency are seen as vital for expanding the scope of SPA applications. In this research, focus is placed on improving force output and efficiency due to its significant impact on advancing the field of soft robotics. Improving force output in SPAs enables them to perform a wider range of tasks, including those requiring more strength, such as lifting heavier objects or executing more powerful movements.

2.9.2 Soft Material Characterization

Despite significant efforts in the field of soft materials characterization, notable research gaps have been identified, underscoring the need for further exploration and innovation. A primary observation is the absence of comprehensive characterizations that encompass both tensile and compression experiments across a variety of soft materials. It has been observed that most research predominantly focuses on tensile testing [17][85], with a limited number of studies addressing compression testing [86], and even no one providing analyses of both within the same study. The inclusion of both types of testing is deemed essential for a thorough understanding of material behaviours under varied conditions.

Furthermore, a clear deficiency has been recognized in the existence of comprehensive and standardized methodologies for the characterization of soft materials, covering all aspects from fabrication to examination. This deficiency leads to inconsistencies in data and complicates the comparison of results across different studies. The following of standardized, universally recognized testing protocols is seen as important for the advancement of the field. Such standardization would

ensure consistency and reliability in material characterization, facilitating a more collaborative and accumulative knowledge base within the soft robotics community.

2.9.3 SAM Design

SAMs demonstrate unique actuation capabilities by expanding and contracting in response to pneumatic pressure. Despite their potential, the literature shows specific areas where knowledge is notably limited, particularly concerning design innovation. A significant research gap exists in the development of new designs for McKibben muscles, especially regarding the soft component and the braid. The current literature does not sufficiently address how innovative designs and advanced materials could enhance the efficiency and performance of these muscles. This gap suggests a pressing need for comprehensive studies focused on exploring novel configurations and materials to improve the overall functionality of McKibben muscles.

2.9.4 SAM Fabrication

The section of fabrication methods of soft actuators outlines techniques like moulding and 3D printing, which are essential understand for constructing soft pneumatic systems. Exploring the literature indicates a need for innovation in areas such as power sources development. The development of portable power sources is identified as a significant research gap in soft robotics for several reasons. Soft robots require power sources that can maintain functionality under deformation to match the inherent flexibility and compliance of their structures. All the current power sources are rigid and do not meet these criteria, limiting the potential applications of independent soft robots in environments requiring high flexibility or where robots need to undergo significant shape changes [18].

2.9.5 SAM Characterization

The study of previous research work on SAM characterization has shown a research gap that need to be addressed to advance the field. There exists a noticeable lack of comprehensive studies focusing on the static and dynamic response of various models of SAM. This includes their behaviour under conditions of pressure changes and variable load scenarios. A deeper understanding of these responses is essential

for developing SAM suited for applications that demand high precision control and quick actuation capabilities.

Another research gap, there is a notable absence of robust methodologies for accurately measuring the displacement or contraction exhibited by SAM during operation. The ability to precisely determine the extent of SAM contraction is vital for effectively designing and implementing these actuators in various soft robotic applications. Establishing reliable methods for displacement measurement would greatly enhance the predictability and repeatability of SAM performance, contributing significantly to their practical utility and advancement in soft robotics.

2.9.6 FE Simulation

Finally, the chapter concludes with presenting the use of FEA in the simulation of SPAs and SAMs, providing crucial insights into the actuators' deformation patterns and performance and demonstrating the utility of FEA in enhancing the design of soft robotic systems.

This chapter closely relates to the research aim and objectives by covering key aspects of soft robotics, especially SAMs, introducing essential concepts, material characterization, and techniques needed to understand and develop SAMs. Additionally, it explores different designs, fabrication methods, and the use of FEA to validate the design and performance.

Chapter 3 : Soft Material Characterization

This chapter presents a methodology crucial for defining the material properties of eight elastomers, pivotal in the field of soft robotics. The experiments conducted adhere to ISO standards, focusing on the characterization of both tensile and compression properties. Processing and FE analysis are applied to the acquired test data. Importantly, this chapter lays the groundwork for subsequent chapters by contributing to an understanding of various aspects of soft systems.

3.1 Introduction

Soft pneumatic actuators, designed to achieve desired movements through inflation and deformation, are exposed to various load tensions and compressions. Understanding the soft material behaviour under these loads is important for proper material selection. Soft material characterization involves determining the stress-strain properties of elastomers, including tensile strength, elasticity, and stiffness, through compression and pull-to-failure tensile tests according to specific standards. Furthermore, FE analyses are utilized to expect stress-strain curves, and their corresponding mathematical coefficients are documented. This approach facilitates the development of highly accurate FE models for robotic design.

The advantage of this characterization is its repeatable method, which can be used on many different soft elastomeric materials, setting a particular approach for characterizing materials in soft robotics. Despite valuable efforts in the literature [17]-[87], where researchers have focused on tensile tests, there is a clear lack of comprehensive studies that include both tensile and compression tests. Specifically, only a few researchers such as Sparks *et al.* [88] have conducted compression tests on soft materials. This chapter fills the gap by conducting both tensile and compression tests on various soft materials, adhering to ISO standards. It recognizes that in soft robotics, materials face different types of tension and compression.

This chapter outlines an experimental investigation for eight soft materials across a spectrum of hardness levels. The chapter details the design and fabrication of specimens for both tensile and compression tests, including the evolution of specimen moulds and optimal fabrication techniques. It then describes the procedures for conducting tensile and compression tests on soft materials. The results from these experimental characterizations are presented, followed by the development and validation of FE models.

3.2 Objectives

The objectives of this chapter are set up to guide the study of how various soft materials behave, ensuring a look into their mechanical properties. The chapter follows a clear set of objectives, aiming to:

Objective 1: Develop methodology and procedures for fabricating test specimens from soft materials.

Objective 2: Conduct standardized tensile and compression tests on several soft materials.

Objective 3: Generate hyperelastic models by using the collected data from the experiments.

Objective 4: Validate the accuracy of the developed hyperelastic models through FE simulation.

3.3 Methodology

The soft materials characterization procedures encompassed both tensile and compression tests, conducted on the eight distinct elastomers: Ecoflex 00-10, Ecoflex 00-20, Ecoflex 00-30, Ecoflex 00-50, Dragon Skin 10, Dragon Skin 20, Dragon Skin 30, and Elastosil M 4601. These tests were performed using the Instron 5943 machine, a device specifically designed for assessing the tensile and compression stress-strain properties of elastomeric materials. Adhering to the ISO 37:2017(E) and ISO 7743:2017(E) standards, the procedures provided a standardized method for evaluating the mechanical behaviour of elastomers under tensile and compressive forces. The ISO standard for tensile testing is preferred over ASTM for use with specific machines that can pull materials until they break (for example, elongating up to 1123mm with an Instron 5943 machine).

Rigid test specimens can be manufactured using traditional machining processes, whereas soft specimens require specialized techniques that can handle the nature of pre-silicone (liquid), the formation of the desired shape, and specific curing requirements. Various methods have been employed to fabricate the tensile compression specimens. With every attempt, modifications were made to either the design of the mould or the fabrication process itself. The aim of developing an optimal mould for specimens is to produce repeatable pieces with precise geometries.

Detailing soft materials characterization procedures is very important, as it ensures consistency in conducting tests across different laboratories. Additionally, it makes it easier to share methods among researchers, reflecting the significant advancements in these procedures. The creation of soft test specimens involves several key steps: designing the moulds using CAD software, moulds fabrication, soft materials preparation, material casting, and demoulding.

3.3.1 Tensile Test Methodology

Tensile tests are conducted to measure mechanical properties of materials, such as tensile strength, tensile strength at break, and tensile strain. During these tests, the testing machine applies stress to stretch (strain) the specimens, enabling the determination of their tensile stress-strain characteristics. ISO 37:2017 standard offers various shapes of dumb-bell specimens. Dumb-bell specimen type 2 was chosen for its dimensions, which are compatible with the Instron 5943 testing machine. The standard measurements for the narrow section of dumb-bell specimen type 2 are 12 mm in length, 4 mm in width, and 2 mm in thickness. Figure 2-2 in Chapter 2, illustrates the detailed dimensions of dumb-bell specimens type 2. Marks to indicate reference points for measuring strain are placed on the narrow part (gauge region) of the specimen. The distance between these marks, known as the test length or gauge length, for dumb-bell specimen type 2 is 20 mm, as shown in Figure 3-1. According to ISO 37:2017, a minimum of three specimens shall be tested. In this characterization, 5 specimens were tested to ensure more reliable results.

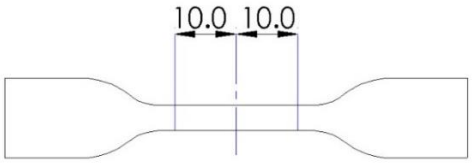

Figure 3-1: Gauge length in mm of the dumb-bells specimen.

3.3.2 Compression Test Methodology

In the literature review presented in chapter 2, Table 2-2 offers a systematic breakdown of the standard testing methods alongside their respective specimen types, serving as a guide for method selection. Among these, Method C was specifically chosen for its superior ability to show the intrinsic properties of the material, highlighting the importance of amplifying uniaxial stress while minimizing biaxial stress. This is particularly relevant when the slenderness ratio (the ratio of length (l) to diameter (d)) is equal to or greater than 1, which helps in avoiding biaxial stress across a broad strain range. For Method C, the chosen standard specimen is Type B, characterized by a cylindrical diameter of 17.8 ± 0.5 mm and a length of 25 ± 0.25 mm, resulting in a slenderness ratio (l/d) of 1.40. This is compared to Type A's slenderness ratio of 0.43, which is below 1, making Type B more suitable due to its favourable slenderness ratio.

A minimum of four specimens is required for compression tests; however, in this study, six specimens of each material were tested. Post-fabrication, all specimens must be stored under laboratory conditions and shielded from any form of load compressive, tensile, or shear that might affect their mechanical properties. Prior to testing, the dimensions of each specimen should be verified to confirm match the standard geometries, ensuring the reliability of the test results.

3.3.3 Fitting Hyperelastic Models

The data obtained from uniaxial tensile and compression tests underwent resampling through linear interpolation, followed by averaging in MATLAB (MathWorks Inc, USA). In Abaqus (Dassault Systèmes, USA), hyperelastic models were applied to the averaged stress-strain data encompassing the entire strain range (from initiating the test till the failure). The fitting process utilized the processed data from both tensile and compression stress-strain tests, as well as the combined data from both sets. The attention was directed towards six hyperelastic models, each exhibiting distinct levels of stability and fitting quality. These models include Polynomial 1st order (Mooney-Rivlin), Polynomial 2nd order, Ogden 2nd order, Ogden 3rd order, Reduced Polynomial 1st Order (Neo-Hookean), and Reduced Polynomial 3rd Order (Yeoh) [22].

After deriving the coefficients for the material models, the stress-strain curves for each model were exported from Abaqus for the computation of the root mean square

error (RMSE). The RMSE serves as an indicator of the accuracy of the fitted curve when compared to the experimental curve, aiding in the selection of the most appropriate hyperelastic model [32]. Optimal model selection involves not only achieving a low RMSE but also establishing a stability limit to assess the quality of the fit. In this context, a stability limit was determined based on the Drucker criterion within a specified strain range where the infinitesimal strain energy should only exhibit an increase. Any material under examination failing to meet this criterion at any strain range would be deemed unstable.

3.3.4 FE Modelling of Tensile and Compression Experiments

To verify the test outcomes, the three-dimensional configuration of both tensile and compression specimens was created in Abaqus. Defining the hyperelastic material model derived from the most stable fitted coefficients. Boundary conditions (BC) were established at the upper and lower ends of the specimens for accurate simulation. In the case of the tensile test, the lower gripper was configured as Encastre (fully fixed), while the upper gripper assumed a "Displacement BC" with displacement in the Y-direction. To simulate the compression experiment, the cylindrical specimen was simplified to a quarter to simplify the solution process for analysis. The bottom surface was fully fixed, and the upper surface was subjected to a "Displacement BC" in the Y-direction. Hexahedral elements were selected to mesh both models efficiently.

The analysis of the tensile test results focuses on the gauge region of the specimen, while the compression test analysis is applied on an element located on the upper surface of the specimen. Strain and stress values are recorded for the identified elements in both the tensile and compression specimens' 3D models.

3.4 Fabrication of Tensile and Compression Specimens

3.4.1 Fabrication of Tensile Test Specimens

In previous material characterization projects, specimens were typically made by pouring the material into moulds shaped for dumb-bell specimens. However, this method often resulted in specimens with imprecise thickness due to the potential for underfilling or overfilling the mould cavities with silicone. Additionally, some specimens would end up having convex or concave surfaces due to surface tension

effect. To address these issues, we refined our approach by sealing the top of the mould and injecting the soft material through an inlet port.

All moulds used in the development process to fabricate tensile test specimens consisted of three acrylic sheets, all of the same length and width, bonded together with bolts and nuts. The middle sheet, matching the thickness of the desired specimen, was cut into the ISO 37 type 2 dumb-bell shape as shown in Figure 3-2. To ensure uniform fabrication conditions, the mould was designed to produce multiple specimens simultaneously. The top and bottom sheets were uncut except for holes for the bolts and nuts. Optimal fabrication processes and mould designs were achieved after several trials, each incorporating slight modifications, as detailed in Appendix 2.

This method produced air bubble-free specimens with accurate geometries according to ISO 37 type 2 standards. A key improvement from previous trials was relocating the injection port from the mould's side sheet to the front of the top sheet. The injection port featured a hole and a groove that securely accommodated the syringe's luer tip, ensuring a stable and leak-proof connection (as shown in Figure 3-2).

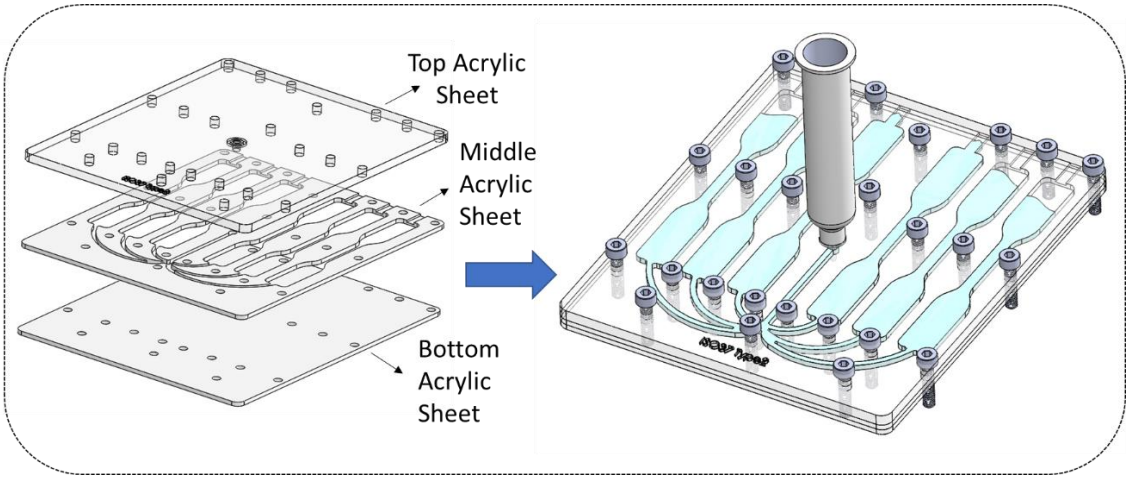

Figure 3-2: Mould assembly and fabrication process of tensile specimen.

The process for fabricating tensile specimens from soft materials begins with the design and preparation of three acrylic sheets of the mould using CAD software. The design is transferred to a laser cutting machine (VLS3.50 Universal Laser Systems, USA).

Next, the three acrylic sheets are manually assembled using nuts and bolts, ensuring the bolts are not tight to allow air to escape during the injection process. Pre-silicone,

such as Ecoflex or Dragon Skin from Smooth-On Company, is mixed according to the manufacturer's instructions in a 1A:1B ratio by weight. The mixture is thoroughly mixed and vacuum degassed using a centrifugal mixer at 2000 rpm for 1:30 minutes. After mixing, the pre-silicone is transferred into the injecting syringe, ensuring a smooth flow to avoid air bubbles formation, and sealed with a flat-base tip cap to prevent leaks (as shown in Figure 3-3a).

The mould is then placed horizontally on a flat surface. The injection syringe tip is inserted into the mould's injection port, and constant force is applied until the pre-silicon fill the mould and flows from the vent slots (as shown in Figure 3-3b).

Once the soft material has been fully injected, it is allowed to cure at room temperature. After curing the mould is carefully disassembled. Excess material is trimmed, and the specimens are slowly peeled off the mould to avoid changing their mechanical properties. This process ensures the production of high-quality soft tensile specimens.

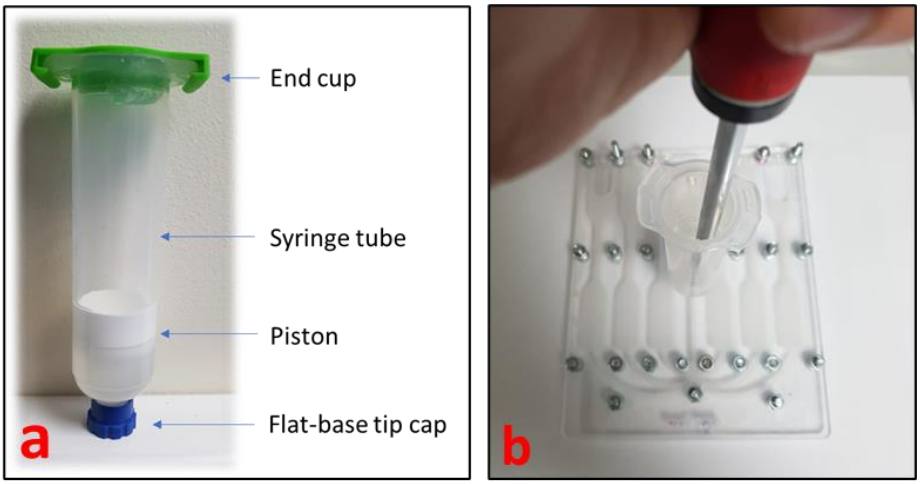

Figure 3-3: (a) Injection syringe with accessories and (b) Manual injection for the pre-silicon into the tensile specimens' mould.

3.4.2 Fabrication of Compression Test Specimens

The optimal fabrication processes and mould designs were developed through multiple trials, each involving minor adjustments, as outlined in Appendix 2. The goal of this was to create a mould capable of simultaneously filling pre-silicon into six cavities to produce specimens with accurately flat surfaces from top and bottom. Ensuring flatness required the mould to be sealed on all sides. Figure 3-4 illustrates a circular aluminium mould with cylindrical cavities, each 17.8 mm in diameter and

25 mm high. The bottom was sealed with an acrylic sheet featuring three holes for screw attachment. The top was covered with two acrylic sheets: one with six runners for pre-silicone flow and small ventilation holes, and the most top sheet with a central injection port and additional ventilation holes aligned with those on the second sheet (Figure 3-4a). This method led to the development of an optimal mould design, capable of producing high-quality, soft specimens from various materials.

A release agent is applied to the main aluminium die to facilitate the demoulding process. The main die is then assembled with the acrylic sheets using screws and bolts, ensuring a sealed mould ready for pre-silicone injection. The prepared mould is placed on a flat surface for even distribution during injection. The syringe tip is inserted into the mould's injection port, and pre-silicone is injected with constant force until it fills the mould and exits through the ventilation holes.

After injection, the pre-silicone is allowed to cure at room temperature. Once cured, the mould is disassembled by removing the screws, and the specimens are carefully extracted. The demoulding process can be challenging, particularly with high Shore hardness soft materials, often requiring additional tools like a metal-working vice and a C-clamp vice for gentle and safe ejection. The detailed method for the safe ejection of the specimen from the aluminium die through a sequence of steps can be found in the Appendix 2. This thorough process ensures the production of high-quality specimens suitable for soft materials characterization.

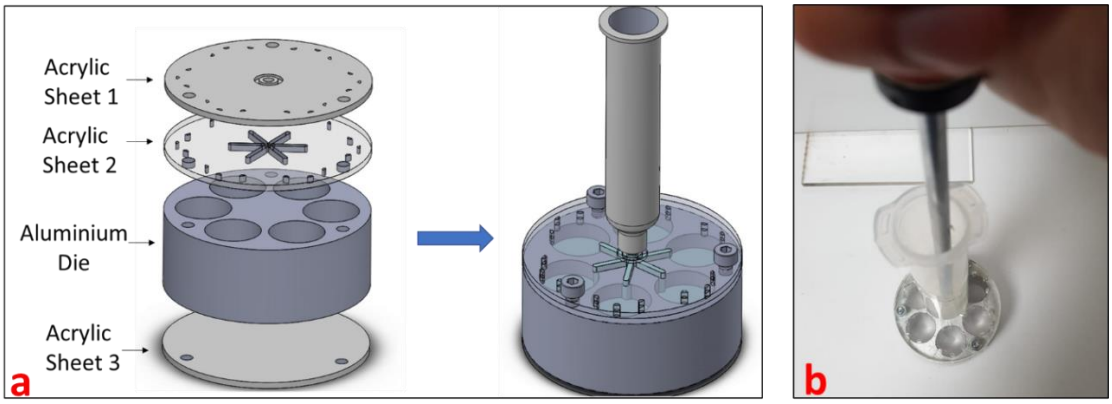

Figure 3-4: Mould assembly and fabrication process of compression specimens.

3.5 Soft Materials Characterization Procedures

3.5.1 Tensile Tests Procedures

The procedure presented here is important for characterizing the material properties under tensile stress and involves several steps. The characterization setup for tensile tests is shown in Figure 3-5a. The stress-strain behaviour of each elastomer was recorded at strain rates of 100, 200, and 500 mm / min. While the ISO 37:2017(E) standard recommends a strain rate of 500 mm / min, our investigation extended to lower speeds to mimic the slower strain rates encountered in certain soft robotics applications. A minimum of three samples were tested at the 100 mm / min rate, whereas one to two samples used for the 200 and 500 mm / min rates.

By following a standardized approach, the procedure aims to minimize variability and enhance the precision of the measurements. The steps provide detailed instructions for preparation, specimen collection, precise marking, and system calibration. Full details about the steps of the tensile testing procedure are provided in the Appendix 2.

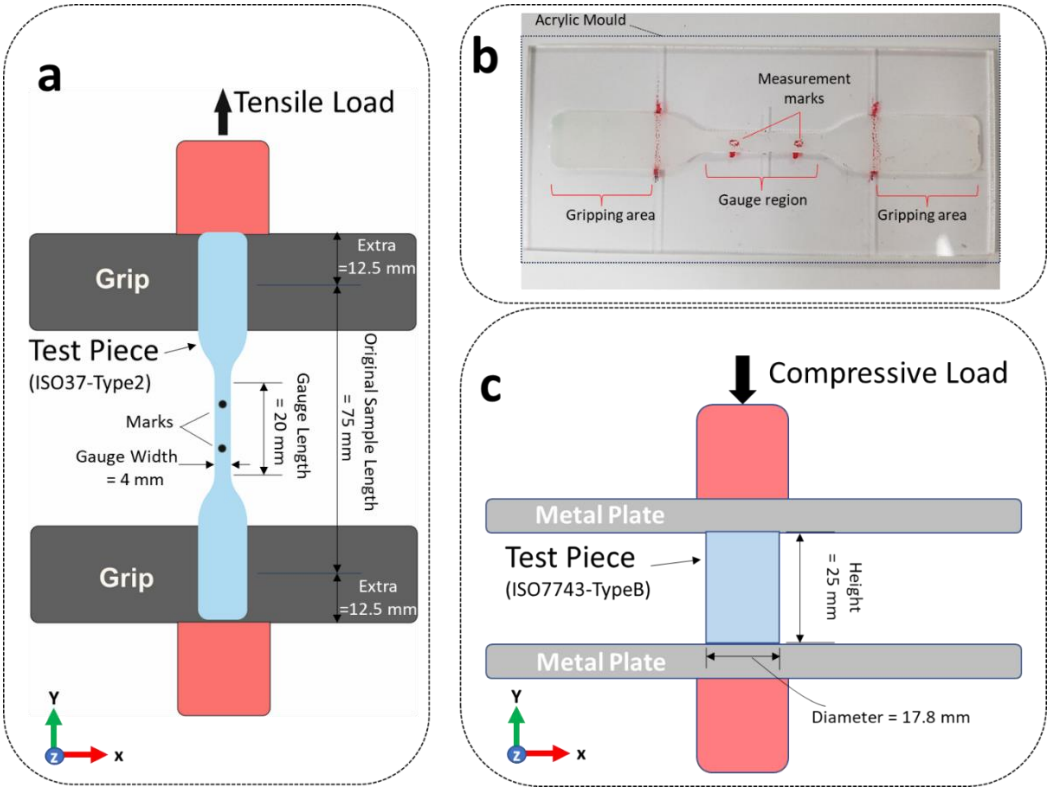

Figure 3-5: (a) Characterization setup for tensile tests, (b) acrylic mould for remarking the tensile specimen, and (c) Characterization setup for compression tests.

3.5.2 Compression Tests Procedures

Following the outline of the tensile tests protocol, we transition into the compression tests protocol, applying a similar approach while focusing on the unique aspects of compression testing. In the compression tests, the methodology followed ISO 7734:2017(E) with test method C. The Bluehill Universal Software was configured to control the compression machine, operating at a speed of 10 mm / min until a deformation of 25% was achieved over four sequential compression cycles. Each cycle is comprised of two phases: compression (loading) and release (unloading). Force-strain curves were recorded following the standard's guidelines to extract measurements of stiffness and compression modulus at 10% and 20% strain during the compression phase of the fourth cycle. The compression modulus (MPa) is defined by the equation:

$$\text{Compression Modulus (MPa)} = \frac{F}{A\varepsilon} \qquad \text{Equation 4}$$

Where F is the applied force (N), A is the cross-sectional area (mm²), and ε is the strain. Specifically, the Compression Modulus at 10% strain is calculated using the equation:

$$\text{Compression Modulus at } 10\% \text{ strain} = \frac{F_{at\ 10\%}}{A\ \varepsilon_{at\ 10\%}} \qquad \text{Equation 5}$$

Similarly, the Compression Modulus at 20% strain is determined with the equation:

$$\text{Compression Modulus at } 20\% \text{ strain} = \frac{F_{at\ 20\%}}{A\ \varepsilon_{at\ 20\%}} \qquad \text{Equation 6}$$

The same load cell utilized in the tensile tests is employed for the compression tests, ensuring consistency across testing modalities. Compression testing simplifies certain measurements, as the displacement does not depend on the video extensometer but is directly measured by the movement of the Instron machine's crosshead. The characterization setup for compression tests is shown in Figure 3-5c. Full details about the steps of the compression testing procedure are provided in the Appendix 2.

3.6 Results from Experimental Characterization

3.6.1 Tensile Tests Results

Figure 3-6 displays the combined stress-strain curves for all tested samples. Notably, the elastomers demonstrated greater elongation at break as the strain rate increased. Specifically, the majority of the samples displayed their peak tensile strength and maximum elongation at break at a strain rate of 500 mm / min. Examination of the stress-strain curves shows occasional slips are noticeable as fluctuations within the end of the curve, particularly in materials with lower shore hardness, such as Ecoflex 00-10, Ecoflex 00-20, Ecoflex 00-30, and Ecoflex 00-50.

Table 3-1 and the corresponding bar chart in Figure 3-7 and Figure 3-8 illustrate the average maximum tensile strength and average elongation at break for strain rates of 100, 200, and 500 mm / min, respectively. For instance, Ecoflex 00-10, the softest among the tested materials, shows the highest elongation at break with an average of 8.95, 8.99, and 10.14 at strain rates of 100, 200, and 500 mm / min, respectively. It also presented the lowest tensile strength, with recorded values of 0.4633, 0.4811, and 0.5757 MPa at these strain rates. Due to its low shore hardness, Ecoflex 00-10 was expected to achieve the highest elongation at break and the lowest tensile strength, underscoring a clear relationship between a material's softness (low shore hardness) and its ability to undergo extensive elongation.

Following Ecoflex 00-10 in softness based on the shore hardness scale are Ecoflex 00-20 and Ecoflex 00-30, with their performance in stress-strain tests aligning with the expected relationship between shore hardness, tensile strength, and elongation at break. However, breaking this pattern, Ecoflex 00-50 exhibits a greater elongation at break compared to Ecoflex 00-30, suggesting that a lower shore hardness does not always result in higher elongation at break. This characteristic makes Ecoflex 00-50 more suitable for actuators that require significant stretching, as well as its ability to withstand higher stress before breaking.

When selecting materials for soft actuators that inflate under high pressure, using a material with higher tensile strength, like Ecoflex 00-50, is preferable because it can withstand greater stress than Ecoflex 00-30 without bursting, making it safer for high-pressure applications. On the other hand, materials with relatively high shore hardness, such as Dragon Skin 30, are less suitable when the available pressure source is limited. This is because stiffer materials require more pressure to achieve the same level of deformation, which may not be ideal in some soft robotics applications where pneumatic pressure is typically kept lower to maintain the soft and adaptable nature of the systems.

Another illustration involves Elastosil M 4601, with a shore hardness of 28A, and Dragon Skin 30, with a shore hardness of 30A. As expected, Elastosil M 4601 exhibits a higher elongation at break due to its softer shore hardness. However, it also shows greater tensile strength, emphasising that shore hardness is not the sole factor influencing the tensile strength of elastomers.

Given that the samples were produced using the same method and conditions, the variability observed in the experimental results among the samples is likely indicative of the variability that can be expected in practical applications. For instance, six samples of Dragon Skin 20 were tested at various strain rates, with the average tensile strength ranging between 2.664 and 3.822 MPa. This range provides designers with a realistic expectation of the tensile strength for their projects.

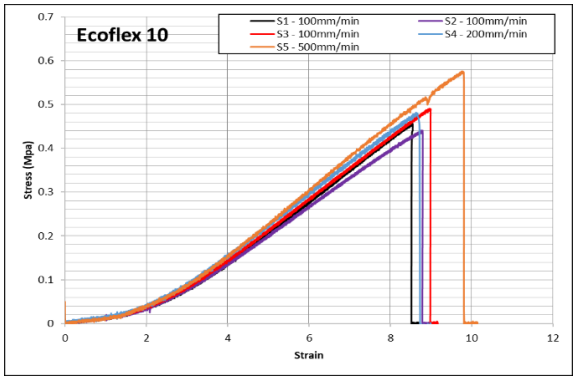

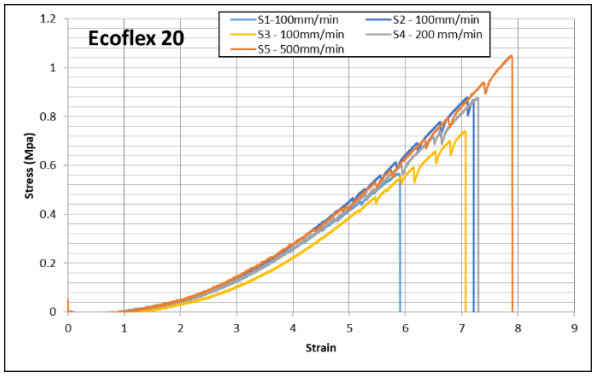

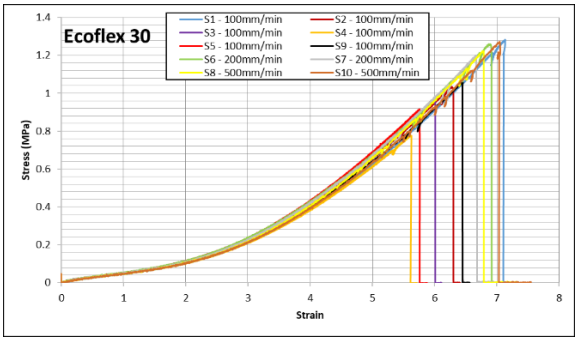

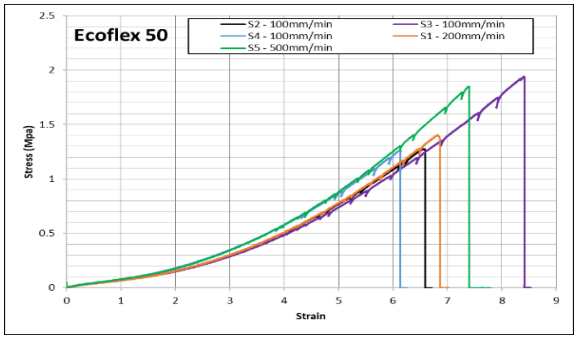

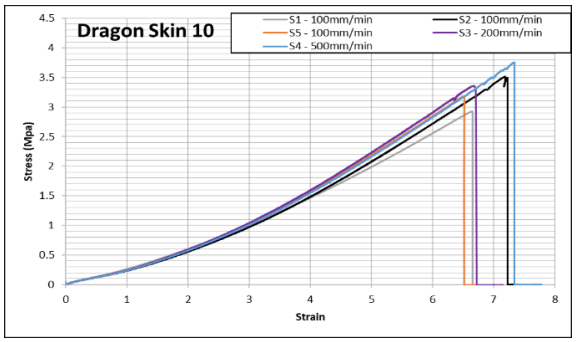

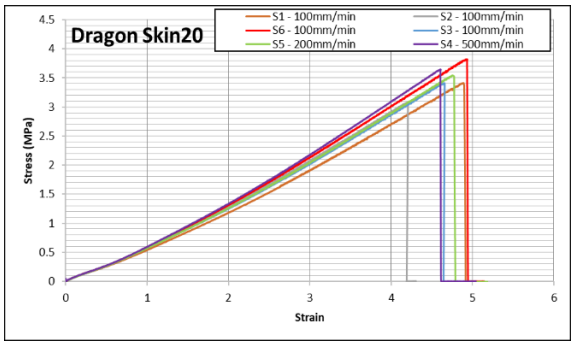

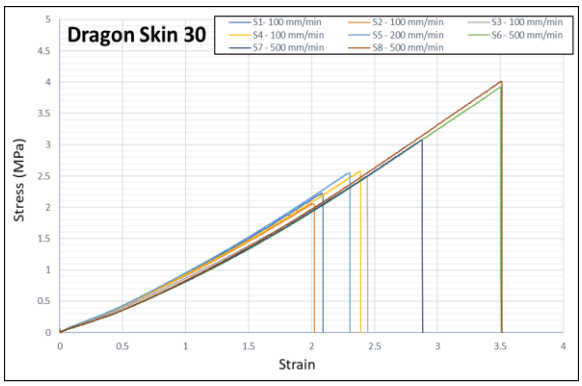

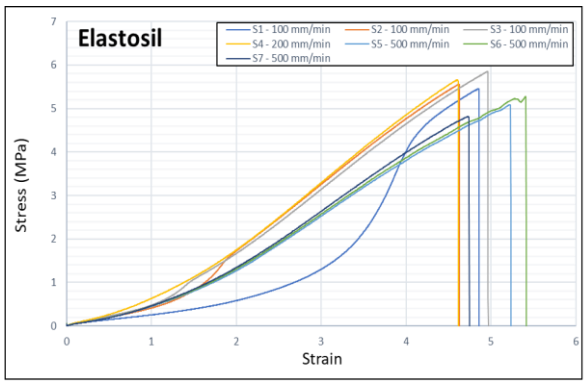

Figure 3-6: Stress-strain curves at strain rates of 100, 200, and 500 mm/min for the eight elastomers.

Table 3-1: Average tensile strength and average elongation at break at strain rates of 100, 200, and 500 mm/min.

Material	*Avg. Tensile Strength (MPa)*				*Avg. Elongation at break*			
	Avg at 100 mm / min	STD at 100 mm /min	at 200 mm / min	at 500 mm / min	Avg at 100 mm / min	Avg at 100 mm / min	at 200 mm / min	at 500 mm / min
Ecoflex 10	0.4633	0.0252	0.4811	0.5757	8.9422	0.2372	8.9910	10.1404
Ecoflex 20	0.7293	0.1564	0.8794	1.0010	7.0503	0.7202	7.6145	8.3595
Ecoflex 30	0.9938	0.0647	1.2298	1.2477	6.2388	0.6344	5.7165	5.8765
Ecoflex 50	1.4938	0.3896	1.4040	1.8522	7.1674	1.2051	7.0212	7.7983
Dragon Skin 10	3.2106	0.2961	3.3582	3.7535	6.9004	0.3358	7.1475	7.7830
Dragon Skin 20	3.2444	0.2368	3.5449	3.6458	4.5446	0.3388	5.1828	5.0402
Dragon Skin 30	2.3372	0.2370	2.5558	3.6693	2.2368	0.2120	2.3052	3.2988
Elastosil M 4601	5.6236	0.2078	5.6612	5.0603	4.8187	0.1715	4.6143	5.1299

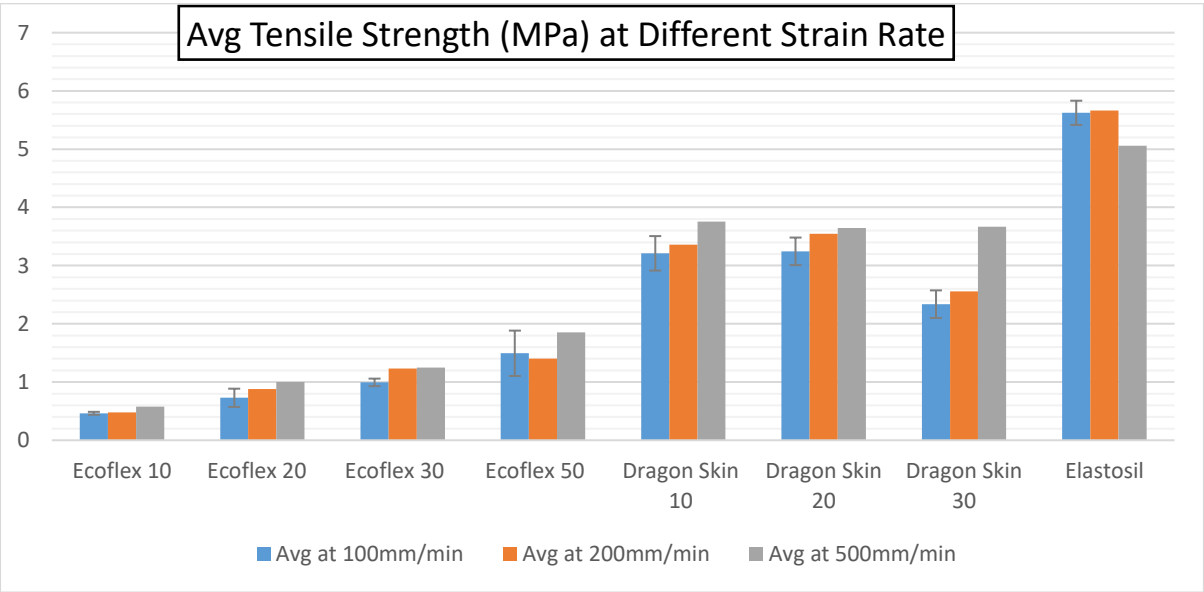

Figure 3-7: Average maximum tensile strength at strain rates of 100, 200, and 500 mm/min.

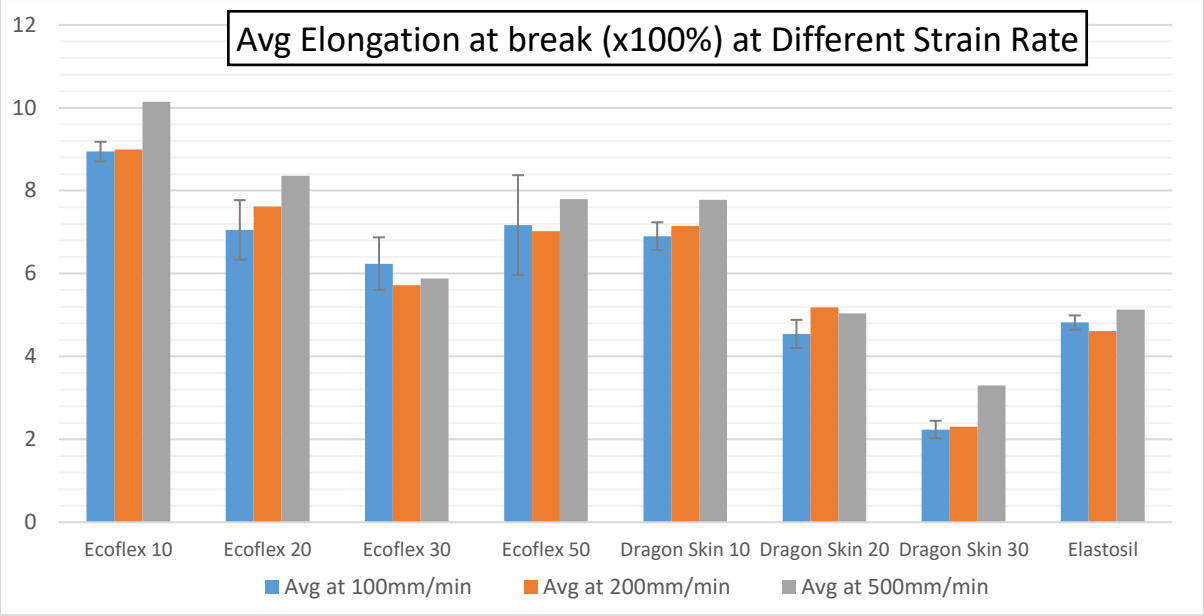

Figure 3-8: Average elongation at break at strain rates of 100, 200, and 500 mm / min.

3.6.2 Compression Tests Results

Figure 3-9 presents the force-strain curves for a single sample as an example of each material. It is evident that as strain increases, so does the force. The cumulative curves of the compression (loading) and release (unloading) from all four cycles largely coincide, indicative of the force-strain data recording similar values across the cycles. The hysteresis effect is also evident, characterized by a slight gap between the compression of the material and its return to the original shape. This effect is seen as a loop in the curves, where the paths of compression and release differ.

Table 3-2 along with the bar chart in Figure 3-10, details the average compression modulus and the standard deviations for the samples at 10% and 20% strain. For instance, the average compression modulus for the softest material, Ecoflex 00-10, was measured at 0.01059 MPa and 0.01263 MPa at 10% and 20% strain, respectively. Conversely, Dragon Skin 30, an elastomer with a higher shore hardness, exhibited an average compression modulus of 0.4239 MPa and 0.5055 MPa at 10% and 20% strain, respectively. Although the standard protocol requires testing a minimum of three specimens, six were tested in this instance to enhance the reliability of the results.

The bar chart in Figure 3-10 allows us to observe the compression modulus increase with shore hardness. It is noteworthy that the results from the compression tests demonstrate reduced variability among samples when compared to the tensile tests. This discrepancy is attributed to the significant difference in the range of strain applied to the materials during these tests.

Table 3-2: Average maximum values for the compression modulus (MPa).

Material	*Strain %*	*Avg. modulus*	*Standard dev.*
Ecoflex 10	10%	0.010598726	0.000911518
	20%	0.012636943	0.000558189
Ecoflex 20	10%	0.028127389	0.000911518
	20%	0.032407643	0.000455759
Ecoflex 30	10%	0.051464968	0.001019108
	20%	0.058343949	0.000509554
Ecoflex 50	10%	0.067770701	0.005854331
	20%	0.099617834	0.041072087
Dragon Skin 10	10%	0.12555414	0.004226536
	20%	0.146140127	0.002346163
Dragon Skin 20	10%	0.227261146	0.008237354
	20%	0.287770701	0.004804873
Dragon Skin 30	10%	0.423949045	0.025489933
	20%	0.505562633	0.015887688
Elastosil	10%	0.301995754	0.011577836
	20%	0.378768577	0.006909424

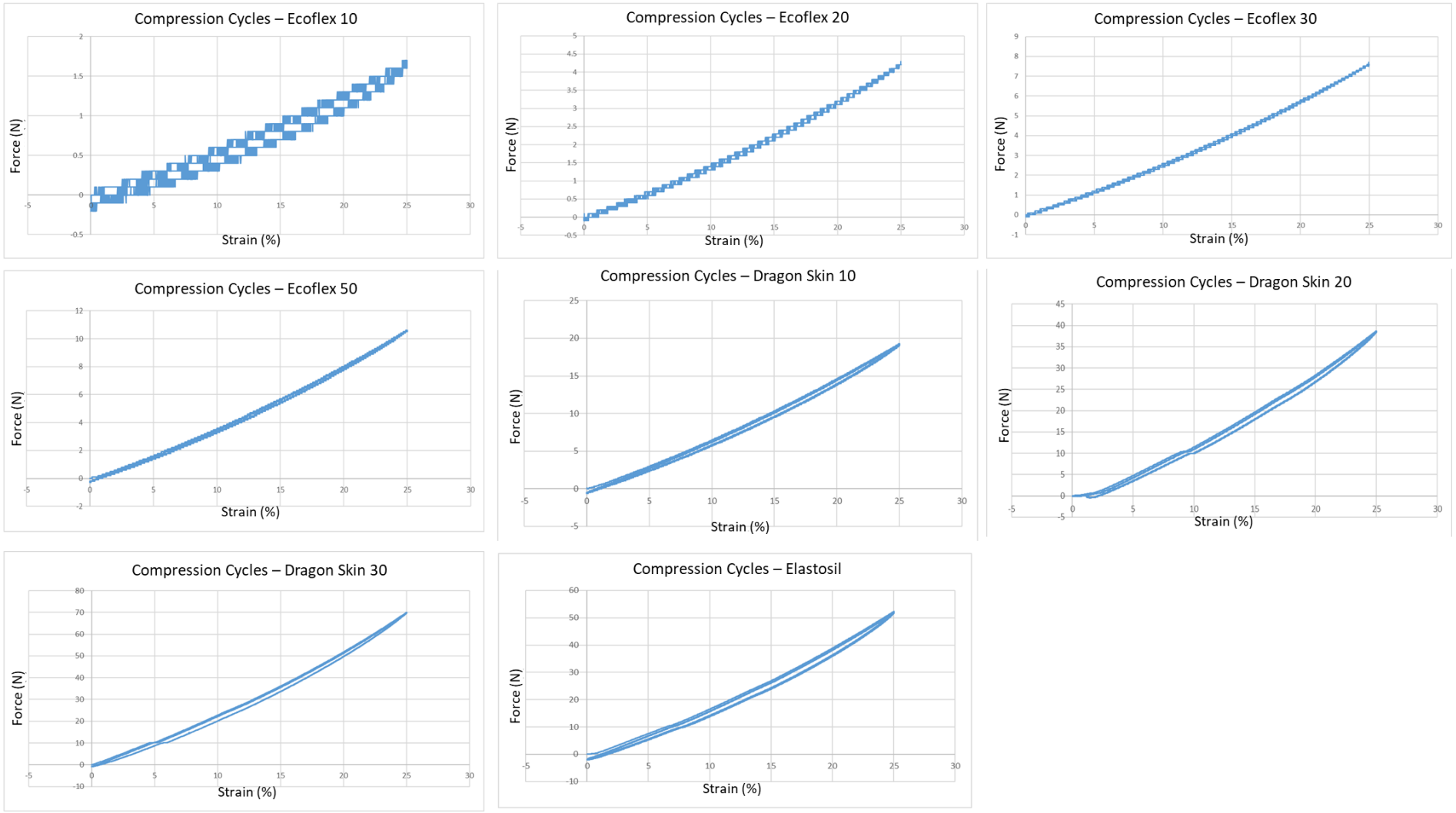

Figure 3-9: Force-strain curves of the compression test for the eight elastomers.

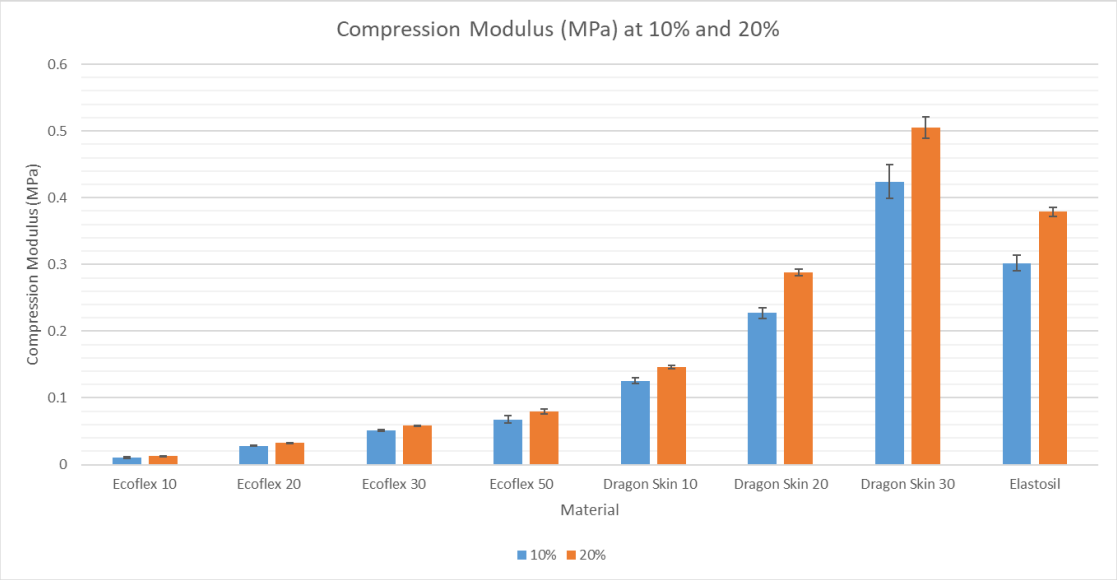

Figure 3-10: Average modulus stiffness values for the eight elastomers.

3.7 FE Modelling

In this section, the focus is placed on modelling and simulation for the characterization tests, focusing on both tensile and compression tests of the soft elastomers. The data extracted from these uniaxial tests undergoes processing and analysis through FE modelling techniques. Ecoflex 00-30 has been specifically chosen as the representative material for the eight characterized soft materials. This selection allows for a detailed examination of its behaviour and responses in the subsequent modelling and simulation analyses.

3.7.1 Results of Fitting Hyperelastic Models

Table 3-3 displays the coefficients obtained through fitting for all six hyperelastic models concerning the average curves derived from tensile, compression, and combined experimental data. The table also provides relevant stability limit details and RMSE values. In general, the RMSE values suggest that the model exhibits reduced accuracy when combining both tensile and compression data. This discrepancy occurs due to the high strain range in the tensile data, resulting in higher RMSE values compared to the compression data. However, the inclusion of a representation of higher strain facilitates a more comprehensive understanding of the soft material's behaviour.

The determination of coefficients and the evaluation of fit performance across various hyperelastic models for this soft elastomeric material offer valuable insights for researchers in the field of soft robotics. Figure 3-11 provides a visual representation of each hyperelastic model's performance. However, for a more precise selection of the optimal hyperelastic model, reference can be made to the RMSE values and stability limit information in Table 3-3. For instance, stability is maintained across all strain ranges by the Neo-Hookean model, yet it displays the least accurate fit. In contrast, the Ogden 2nd order and Reduced Polynomial 3rd order (Yeoh) models remain stable throughout all strain ranges for both tensile and combined data, but within a restricted range for compression data. Furthermore, their minimal RMSE values represent the high-quality fit achieved by both models.

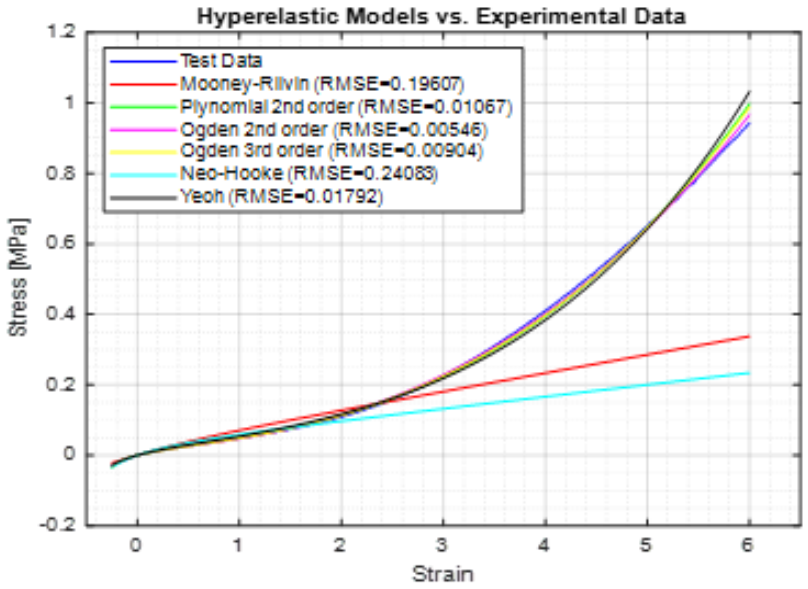

Figure 3-11: Hyperelastic models Polynomial N1 (Mooney-Rivlin), Polynomial N2, Ogden N2, Ogden N3, Reduced Polynomial N1 and Reduced Polynomial N3 (Yeoh) – combined data fit of Ecoflex 00-30.

Table 3-3: Material's constants of hyperelastic models for tensile, compression, and combined data of Ecoflex 00-30.

Hyperelastic Model	*Parameter name*	*Tensile data*	*Compression data*	*Combined data*
Polynomial, N=1 (Mooney- Rivlin)	Material Constant C10 (Pa)	0.034832065	1.03E-02	0.025765897
	Material Constant C01 (Pa)	-0.031902435	4.04E-03	-1.12E-02
	Uniaxial Tension Stability	UANS >0.05	STABLE	UANS >0.52
	Uniaxial Compression Stability	UANS <0.0574	STABLE	UANS <-0.36
	RMSE	0.192481696	0.000513709	0.196071568
Polynomial, N=2	Material Constant C10 (Pa)	7.76E-02	-0.186557262	7.23E-03
	Material Constant C20 (Pa)	-2.80E-04	-5.33308191	7.00E-04
	Material Constant C01 (Pa)	-0.072834162	0.196996418	5.93E-03
	Material Constant C11 (Pa)	7.63E-03	8.10728302	-3.39E-04
	Material Constant C02 (Pa)	-3.45E-02	-3.16851986	0.001418935
	Uniaxial Tension Stability	UANS >0.04	UANS >0.02	STABLE
	Uniaxial Compression Stability	UANS <-0.0388	UANS <-0.0388	UANS <-0.9023
	RMSE	0.002006865	0.000427438	0.010676136
Ogden, N=2	Material Constant A1	4.31548842	-5.34952146	3.68305334
	Material Constant A2	2.3768293	-6.70233043	-1.7365599
	Material Constant MU1 (Pa)	2.63E-03	0.084440173	0.009453153
	Material Constant MU2 (Pa)	1.84E-02	-0.056997769	0.017379757
	Uniaxial Tension Stability	STABLE	UANS >0.79	STABLE
	Uniaxial Compression Stability	STABLE	UANS <-0.2695	STABLE
	RMSE	0.005467699	0.000368602	0.005467699
Ogden, N=3	Material Constant A1	-3.03212873	21.0882637	1.10327885
	Material Constant A2	3.14967679	24.992827	3.91855593
	Material Constant A3	-3.53883734	-15.631644	-4.93713491
	Material Constant MU1 (Pa)	0.624400748	0.231791901	0.013890708
	Material Constant MU2 (Pa)	0.035947803	-0.230564767	0.006112413
	Material Constant MU3 (Pa)	-0.649941832	0.020900664	0.006405646
	Uniaxial Tension Stability	UANS >0.04	UANS >0.03	STABLE
	Uniaxial Compression Stability	UANS <-0.0388	UANS <-0.0388	STABLE
	RMSE	0.008719893	0.000380951	0.009045024
Reduced Polynomial, N=1 (Neo-Hookean)	Material Constant C10 (Pa)	0.0181821	0.014973221	0.02
	Uniaxial Tension Stability	STABLE	STABLE	STABLE
	Uniaxial Compression Stability	STABLE	STABLE	STABLE
	RMSE	0.275610389	0.000297578	0.240831661
Reduced Polynomial, N=3 (Yeoh)	Material Constant C10 (Pa)	0.011038152	0.0143230	1.34E-02
	Material Constant C20 (Pa)	6.61E-04	0.011278102	4.81E-04
	Material Constant C30 (Pa)	-3.29E-07	-0.032997499	2.48E-06
	Uniaxial Tension Stability	STABLE	UANS >0.33	STABLE
	Uniaxial Compression Stability	STABLE	UANS <-0.2695	STABLE
	RMSE	0.009025158	0.000364509	0.017927428

*UANS: unstable at nominal strain, stable with small RMSE, stable with big RMSE, and unstable.

3.7.2 Results of FE Simulation

The hyperelastic material model defined by the most stable fitted coefficients: Ogden 2nd order. Engineering stress-strain data for the tensile and compression experiments are presented in Figure 3-12, compared to their FE simulation. A favourable agreement between the experimental and FE results is observed across the entire strain range. These outcomes affirm the validity of employing the hyperelastic models presented here to characterize the mechanical behaviour of Ecoflex 00-30 in real-world applications.

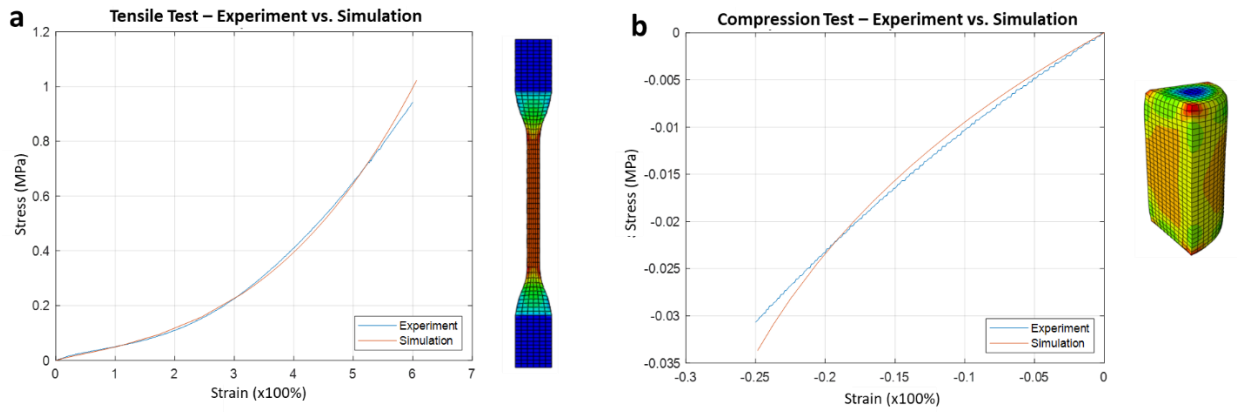

Figure 3-12: Tests' simulation using Ogden 2nd order model – tensile data fit of Ecoflex 00-30.

3.8 Discussion

The study successfully developed a methodology for fabricating test specimens, conducted standardized mechanical tests, generated accurate hyperelastic models, and validated these models through FE simulation, achieving all the chapter's objectives. Since this characterization aimed to test a range of soft materials with various shore-hardness levels, creating a reliable and repeatable methodology for fabricating the soft specimens was crucial. The optimized fabrication processes led to greater characterization efficiency. By reducing the number of failed specimens, this approach saved time, materials, and costs associated with re-fabrication and re-testing.

Within the existing body of literature, researchers have conducted tensile tests on similar soft materials, showing discrepancies in the reported outcomes. For example, studies by Jennifer *et al.* [22] and Marechal *et al.* [89] have investigated the tensile properties of Ecoflex 00-30. In Jennifer's paper, the maximum tensile strength and elongation at break for Ecoflex 00-30 were reported to be approximately 7.25 MPa and 650%, respectively. Similarly, in Marechal's paper, the values for maximum tensile strength and elongation at break for Ecoflex 00-30 were approximately 23 MPa and 1650%, respectively. In comparison, the obtained results from our study on the tensile properties of Ecoflex 00-30 revealed a maximum tensile strength of around 1 MPa and an elongation at break of 623%. This presents a notable deviation from the literature findings.

These variations could result from differences in testing conditions and equipment, as well as the geometry of the specimens. Additionally, the testing methodology, including variables such as strain rates, the degree of pre-strain, and the number of

cycles applied during testing, can significantly influence outcomes. A crucial aspect is also found in sample preparation; the process of creating specimens from soft materials presents considerably more complexity than that for rigid materials, leading to noticeable variations among the specimens produced.

In the existing literature, researchers have conducted compression tests on similar soft materials, yielding variations in reported results. For instance, unconfined compression experiments performed by Sparks *et al.* [88] on three distinct soft materials recorded peak stresses. Dragon Skin, Ecoflex 00-10, and Ecoflex 00-30 exhibited measured peak stresses of 73.0, 12.1, and 24.0 kPa in their study, whereas the obtained results in this investigation for the same materials were 57.4, 2.4, and 11.6 kPa, respectively. It is noteworthy that these values denote force data converted into engineering stress by dividing them by only the initial cross-sectional area of the specimen to ease the comparison with the literature, while the modulus in Table 3-3 was determined using the equation $F/A\varepsilon$.

3.9 Summary

A rigorous methodology has been presented for determining the material properties of eight elastomers: Ecoflex 00-10, Ecoflex 00-20, Ecoflex 00-30, Ecoflex 00-50, Dragon Skin 10, Dragon Skin 20, Dragon Skin 30 and Elastosil M 4601, which can be employed for other commonly used materials in soft robotics. A robust and repeatable fabrication process was developed to manufacture specimens for tensile and compression testing. The experiments were conducted in accordance with ISO standards to ascertain the intrinsic characterization of the tensile and compression properties of the elastomers. The data derived from these uniaxial tests undergoes processing and analysis through FE modelling techniques. The material Ecoflex 00-30 has been selected to represent the characteristics of the eight soft materials under consideration.

The experimental data of Ecoflex 00-30 were input into Abaqus to generate several hyperelastic models, and the best model was chosen based on stability and RMSE factors. Among six hyperelastic models, Ogden 2nd order was identified as the most suitable model for predicting the behaviour of Ecoflex 00-30 in FE simulation. This study offers a comprehensive experimental and computational method for characterizing hyperelastic materials. The methodology can be further applied to characterize additional soft materials used in soft robotics, as well as for characterizing these materials under cyclic, fatigue, and biaxial test conditions.

Chapter 4 : Design and Fabrication of SAM

This chapter is dedicated to advancing the SAM, with a specific focus on the design, development, and optimization of SAM. The primary objectives include proposing conceptual designs for various SAM models, designing and fabricating soft component, and establishing an optimal protocol for SAM fabrication. This chapter sets the stage for detailed SAM characterizations, introducing fresh concepts and stimulating innovation in soft actuator development.

4.1 Introduction

The significance of SAM lies in their ability to mimic natural muscle movements and in their potential to address specific challenges within the domain of soft robotics development. The limited force output of soft actuators is a considerable challenge in the field of soft robotics. Many soft actuators struggle to produce high forces, which can constrain their applications, particularly in tasks requiring higher levels of force. However, the design of the proposed actuator in this research aims to address this challenge by offering an actuator that distinguishes itself in this regard, showing the ability to produce comparatively increased forces when compared to other counterpart soft actuators.

This chapter contributes to the advancement of soft robotics by proposing conceptual designs for various SAM models, each designed to address specific challenges and improve the efficiency of SAM. This involves introducing new concepts and improved functionality, drawing inspiration from biomimicry to mimic the natural movement of biological muscles. In fabricating the soft component integral to SAM, part of this research focuses on optimizing the manufacturing process through a process of iterative refinements to ensure quality and repeatability. This objective aligns with establishing a standardized fabrication protocol, helping in providing a consistent production method of SAM.

In the context of soft component development, the focus is on the utilization of moulding techniques. This involves shaping the pre-silicon, in its liquid state, to create desired soft structures using moulds. Various moulding techniques, including those involving acrylic sheets and tube, as well as 3D printed moulds, were employed within the development iterations.

Within this chapter, the selection of materials becomes a crucial aspect of SAM development, connected to the outcomes derived from the soft material characterization explored in Chapter 3. The choice of soft materials directly influences SAM's performance, durability, and response to input power. The properties of each tested soft material undergo examination, facilitating the decisions on their effectiveness in fabricating SAM.

4.2 Objectives

This chapter aims to present the development of SAMs, focusing on both the design and fabrication processes. The specific objectives of this chapter are as follows::

Objective 1: Develop and propose conceptual designs for various models of SAMs. This objective involves creating three conceptual designs for SAMs. The primary model will be inspired by the structure of muscle cells. The other two counterpart models will be developed to facilitate performance comparison.

Objective 2: Design and fabricate soft components that can be effectively assembled to create SAM. This component is the main part in SAMs. The design and fabrication of these soft components will undergo a development process to ensure that they can effectively actuate SAM.

Objective 3: Establish a repeatable protocol for fabricating the SAM. This includes identifying appropriate manufacturing processes and assembly methods.

4.3 Conceptual Design of SAM

The conceptual design of SAM in this research is inspired by the biomechanical efficiency of the human muscular system, particularly its ability to generate high force through the integration of numerous minor muscle fibers. This design approach introduces a novel method of replicating this strength in an artificial system. By emphasizing repeated sections of muscle fibers, the design aims to enhance the force output of SAM, offering a new perspective on efficient actuator design.To bring this concept to reality, a novel approach is adopted: the creation of a thin soft filament comprised of soft material that extends to the manufacturing of a bundle of these soft filaments, designed to inflate when pressurized. This approach sets the stage for the subsequent exploration of SAM's foundational aspects and the creation of innovative conceptual designs.

Figure 4-1 illustrates the distinct components utilized in SAM actuators, including soft components in three variations, soft component of Model-1, soft component of Model-2, soft component of Model-3. Additionally, it highlights the consistent “braid” (braided sleeve) across all models. Notably, in the figure, Model-1 incorporates the soft filament, which bundle of it integral to soft component of Model-1.

4.3.1 Foundational Aspects

The soft component mirrors the behaviour of an expanding balloon, determining its path of motion through the interplay of two critical factors: the geometry of the elastomer and embedded chambers, and the specific configuration of the braid. The braid, tailored for the soft component, serves as an inextensible element that can govern inflation direction, steering the actuator toward a contraction motion. In alignment with the imitation of muscle fibers, the soft filament takes the form of a soft, thin tube. The uncontrolled inflation of this soft filament, without a strain-limiting component, leads to significant longitudinal and lateral expansion.

In the field of soft robotics, researchers have proposed various braid, with a popular choice being a braided sleeve (a Nylon mesh translating radial expansion into linear contraction). The braid must exhibit compatibility and flexibility to contract with the expansion of the soft component. Despite the wide scope, this research excludes the development of braid within SAM due to their complexity. Commercial braided sleeves, similar to those in existing literature, are used instead.

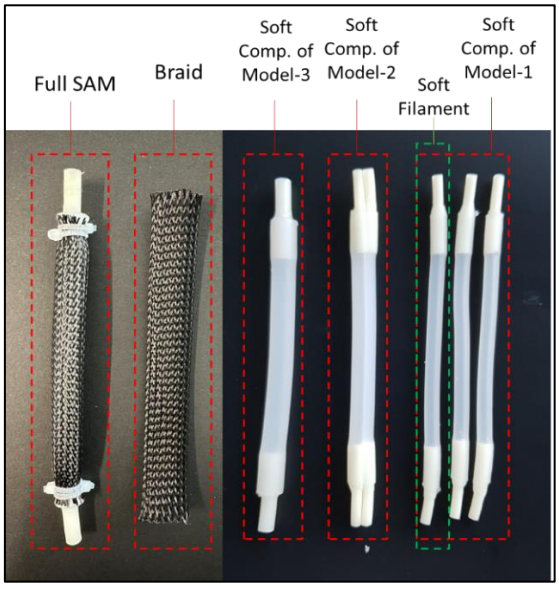

Figure 4-1: Key components of SAM's design, including the soft components of each model, the braided sleeve, and the fully integrated SAM.

4.3.2 SAMs' Models

To assess the viability of the proposed multi-filament actuator concept, a comparative exploration with other soft actuator counterparts is essential. The various conceptual designs will undergo testing in following chapters, with output variables such as the force generated by each model and the necessary pressure for inflation serving as key metrics for evaluation. Expectation suggests that the interaction between bundled soft filaments in the multi-filament actuator will lead to a higher force output. Another critical aspect to be investigated is the impact of creating a bundle of soft filaments on the range of movement in terms of contraction motions.

Figure 4-2 provides 3D CAD drawing of the soft components of three distinct SAM's models. Model-1 introduces a circular bundle comprised of multiple soft filaments, representing the innovative soft actuator proposed in this research. Model-2 features a single cylindrical soft body containing an equivalent number of small cylindrical cavities as Model-1. Lastly, Model-3 features a single cylindrical soft body with a simple lone cavity, resembling the traditional structure found in Mckibben muscles. To ensure a fair comparison, the sectional areas of the cavities and walls in all three models are equal. This equalizes the volumes of cavities and soft materials across the soft component of the models.

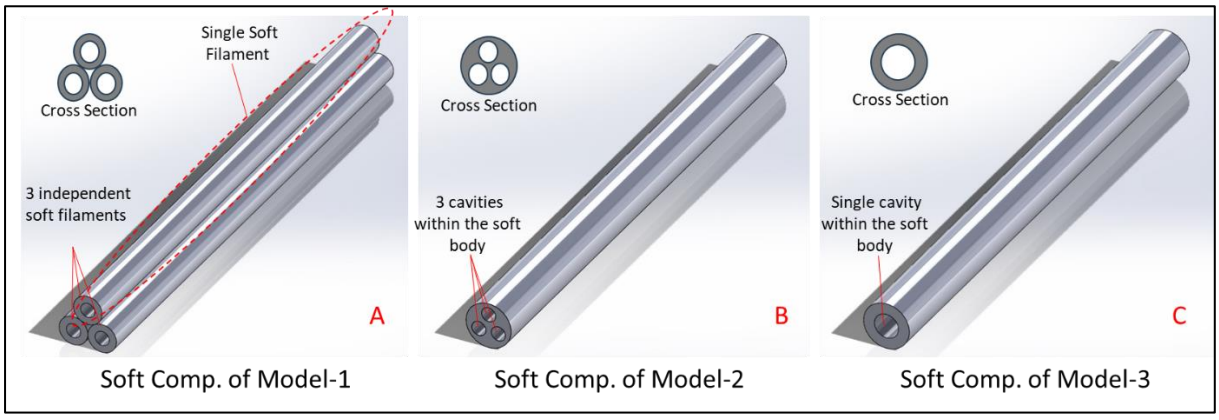

Figure 4-2: 3D CAD model of the soft components of Model-1, 2 and 3.

The structure of the Model-1, as depicted in Figure 4-2, incorporates three soft filaments that can fit into an outer larger circle. The assembly of these circles minimizes free space between soft filaments by estimating the maximum number of small circles that can fit into the larger circle. The foundational form of the soft inflatable multi-filaments actuator (Model-1) necessitates a minimum of three soft

filaments. The concept of circle packing in a circle involves the two-dimensional packing of unit circles into the smallest possible larger circle. Figure 4-3 provides solutions for finding optimal packing of 2-6 circles in a circle. The density represents the fraction of the area covered by the unit small circles relative to the enclosing circle. The concept involves finding arrangements that minimize the radius of the enclosing circle while accommodating the specified number of unit circles. For 1, 2, 3, 4, 5, and 6 unit circles, the corresponding densities are 1.00, 0.50, 0.6466, 0.6864, 0.6854, and 0.6666, respectively. The optimality of the packing has been proven by Graham (1968) [90].

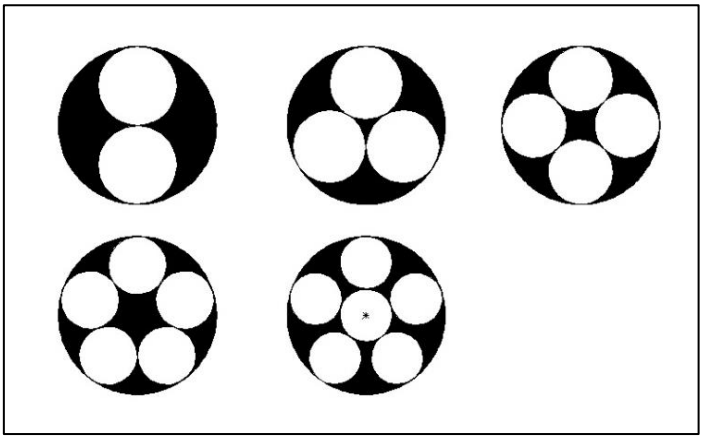

Figure 4-3: Dense packing of congruent circles in a circle

In the early trails, the soft filaments of Model-1 were created with inner and outer diameters approximately 1 mm and 3 mm, respectively. However, it was observed that larger soft filaments offered a more favourable option. The decision of selecting bigger soft filaments was driven by their ability to provide a clearer and more observable representation of deformations, movements, and interactions. Additionally, the utilization of larger soft components was found to simplify the fabrication process and experimental setup.

Model-1 represents a soft structure incorporating three soft filaments arranged in accordance with the optimality of packing principles proposed by Graham (Figure 4-3) [90]. Each individual soft filament within the model has an outer diameter of 6 mm and an inner diameter (cavity diameter) of 3 mm. The arrangement of these three soft filaments results in an imaginary outer circle with a diameter of 12.93 mm, determined by applying the optimized packing configuration in a CAD drawing. Understanding the characteristics of the imaginary outer circle in Model-1 serves as an important parameter for selecting the diameter of the braided sleeve in the overall

SAM's models' design. This consideration ensures that the diameter of the braided sleeve is slightly larger to provide clearance, allowing for the insertion of the soft component inside the braided sleeve.

The geometries of Model-2 and Model-3 (Figure 4-2b and c) are derived from the foundational geometry of Model-1, as previously mentioned. To determine the diameter of Model-2, the first step involves summing the cross-sectional areas of the soft filaments in Model-1. The calculation conducted by using MATLAB to determine the relative geometry of the soft component for Model-1, Model-2, and Model-3. This determination is achieved by calculating the dimensions of the diameter of the solid area (wall thickness) and the cavity for each model. The mathematical expressions for volume involve:

$$\mathrm{Vc}_{\,\mathrm{M1}} = \mathrm{Vc}_{\,\mathrm{M2}} = \mathrm{Vc}_{\,\mathrm{M3}} \qquad \text{Equation 7}$$

$$\mathrm{Vw}_{\,\mathrm{M1}} = \mathrm{Vw}_{\,\mathrm{M2}} = \mathrm{Vw}_{\,\mathrm{M3}} \qquad \text{Equation 8}$$

Where in $\mathrm{Vc}_{\,\mathrm{M1}}$, V represents volume, c represents cavity, w represents wall thickness, and $\mathrm{M1}$ represents Model-1. The volume is computed using the formula $Volume = Sectional\ Area \times length$, with the length being constant for all models. Therefore, the focus of the calculations will be on the sectional area as following:

$$A_{\mathrm{SF,wall}} = \pi \frac{{OD_{SIF}}^2 - {ID_{SIF}}^2}{4} \qquad \text{Equation 9}$$

$$A_{\mathrm{tot-wall\,M1}} = n * A_{\mathrm{SOFT\ FILAMENT-w}} \qquad \text{Equation 10}$$

$$A_{\mathrm{SF,cavity}} = \pi \frac{{ID_{SIF}}^2}{4} \qquad \text{Equation 11}$$

$$A_{\mathrm{tot-c\,M1}} = n * A_{\mathrm{SOFT\ FILAMENT-c}} \qquad \text{Equation 12}$$

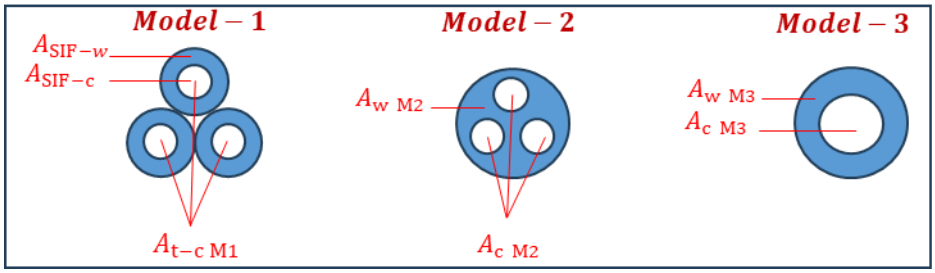

Figure 4-4: Illustration for the cross-sectional area of the wall thickness and cavity/ies for Model-1, Model-2, and Model-3.

Where $A_{\mathrm{SF,wall}}$ is the cross-sectional area of the wall thickness of a single soft filament, $A_{\mathrm{t,wall}}$ is the total cross-sectional area of the wall thickness for *n* soft filaments, and OD_{SIF} and ID_{SIF} are the outer and inner diameter of the soft filament, respectively. Similarly, $A_{\mathrm{SF-cavity}}$ represents the cross-sectional area of the cavity of a single soft filament and $A_{\mathrm{t-cavity}}$ is the total cross-sectional area of the cavity for *n* soft filaments. Figure 4-4 illustrate the cross-sectional area of the wall thickness and cavity/ies for Model-1, Model-2, and Model-3.

Since $\mathrm{Vc}_{\mathrm{M1}} = \mathrm{Vc}_{\mathrm{M2}} = \mathrm{Vc}_{\mathrm{M3}}$ and $\mathrm{Vw}_{\mathrm{M1}} = \mathrm{Vw}_{\mathrm{M2}} = \mathrm{Vw}_{\mathrm{M3}}$, it follows that, $A_{\mathrm{t-c\ M1}} = A_{\mathrm{c\ M2}} = A_{\mathrm{c\ M3}}$ and $A_{\mathrm{t-w\ M1}} = A_{\mathrm{w\ M2}} = A_{\mathrm{w\ M3}}$. To define the total area of the soft component of Model-2 and Model-3, the cross-sectional area of the wall thickness is summed with the cross-sectional area of the cavity:

$$A_{\mathrm{t\ M2}} = A_{\mathrm{c\ M2}} + A_{\mathrm{w\ M2}} \qquad \text{Equation 13}$$

$$A_{\mathrm{t\ M3}} = A_{\mathrm{c\ M3}} + A_{\mathrm{w\ M3}} \qquad \text{Equation 14}$$

The outer diameter ($OD_{t\ \mathrm{M2}}$) for Model-2 is calculated as $2 * \sqrt{A_{\mathrm{t\ M2}}/\pi}$, resulting in approximately 10.39 mm. A similar mathematical procedure is applied to Model-3, maintaining consistency. Model-3, with an outer diameter ($OD_{t\ \mathrm{M3}}$) equal to Model-2's 10.39 mm, sets the baseline for the standardized comparison.

It is important to recall that the diameter of a soft filament's cavity is equal to a single cavity of the soft component of Model-2, while Model-3 differs as it comprises a single cavity. The inner diameter of Model-3 ($ID_{t\ \mathrm{M3}}$) is calculated using the equation $2 * \sqrt{A_{\mathrm{c\ M3}}/\pi}$, resulting in 5.19 mm, which is rounded later to be 5 mm.

The length of the Soft Artificial Muscles (SAM) is standardized across all models, with each soft component measuring 110 mm in length. $A_{Int-\mathrm{c\ M1}}$

is the internal area of the cavity, and l is the length of the soft filament/soft component. While defining the internal area of the cavity is not essential for determining the geometries of Model-2 and Model-3, it is crucial to consider in exploring its potential effects on performance or behaviour.

This uniformity in soft component length, aligned with the specified geometries and dimensions of the SAM models, forms the basis for the subsequent fabrication process. The fabrication process will be meticulously applied to fulfil the design requirements with precision, ensuring consistency in the construction of SAM models.

4.3.3 Strain-Limiting Components (Braid)

Creating a 3D model in CAD for a braided sleeve proves challenging due to the intricate geometric structure and the multi-layered composition of the braiding pattern. The same braid will be used for the three models. Understanding the dynamic response of the soft component to various types of strain-limiting components is essential for designing effective SAM.

The literature review in Chapter 2 carefully outlined various configurations of strain-limiting component, each showing distinct constraints on the soft component and influencing the resulting motion. Figure 4-5 provides a visual representation of different strain-limiting component configurations and their corresponding effects on motion types. Wrapping the fiber reinforcement in a double-helix configuration symmetrically restricts radial expansion, forcing the actuator to expand axially. Including a strain-limiting sheet of inextensible material on one side of the actuator stops radial expansion on that side, inducing an overall bending motion. This configuration creates a controlled bending response, crucial for certain applications. The single-helical fiber wrapping induces twisting and axial expansion in the actuator, resulting in a unique twisting motion that allows flexibility in achieving rotational and extensional forms of movement.

Utilizing a braided sleeve introduces a scissor-like linkage effect, where the mesh geometry translates radial expansion into linear displacement, showing the flexibility of this configuration in achieving linear contraction motions. These configurations exemplify how the choice of the braid intricately determines the motion characteristics of the actuator. By strategically selecting and implementing the final design of the braided sleeve, the SAM can be customized to fulfil the aimed functional requirements in mimicking the muscle movement.

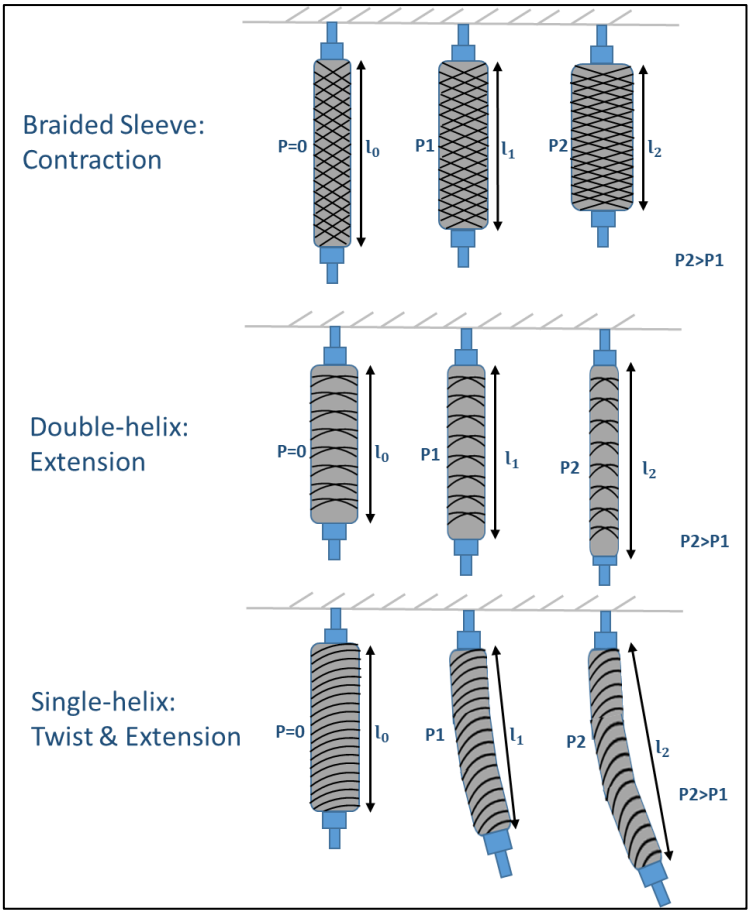

Figure 4-5: Different braid configurations and their corresponding effects on motion types.

4.4 Fabrication Techniques

4.4.1 Materials Selection

In the process of fabricating the soft component for SAM, careful consideration is given to the selection of soft materials, guided by specific criteria aimed at achieving desired properties. The primary criteria included: 1) a soft material characterized by higher elongation at break to response to the low level of input pressure, and 2) a soft material characterized by partially high tensile strength to withstand high deformation. These criteria are essential as they allow for optimal performance within the constraints of the utilized pneumatic system that produce the input pressure, which operates within a maximum pressure of 80 kPa. From the previous chapter, among the elastomers evaluated were Dragon Skin 10, Dragon Skin 20, Dragon Skin 30, and Elastosil M 4601, which characterised with high tensile strength, were not recommended because they require high pressure for expansion.

In contrast, Ecoflex 00-50 emerged as a promising candidate to be used due to its properties. This material exhibits both a high elongation at break, allowing for significant extension, and partially high tensile strength, ensuring it can withstand the maximum input pressure without failing. Additionally, the consideration of Ecoflex 30 as a candidate material revealed similar elongation at break but lower tensile strength compared to Ecoflex 00-50, suggesting it may fail under lower pressure, reinforcing our decision to prioritize Ecoflex 00-50 for the fabrication of the soft components.

4.4.2 Fabrication Techniques for Soft Components

In the development of the soft component of SAM, various fabrication techniques are utilized, each playing an important role in refining the overall fabrication procedure. The focus was on optimizing the fabrication of individual soft filaments for Model-1. Once an effective fabrication technique for the soft filament was established, this approach was then extended to create the other soft components for both Model-2 and Model-3. The methods developed in this research primarily focused on moulding techniques. While other fabrication methods, such as using commercial silicon tubes, were considered, they were not extensively detailed due to their limited contribution to advancing the development process (see Appendix 3.1 for more details about this method).

4.4.2.1 Fabrication Trial of a Soft Filament by Moulding in Steel Tubes

This technique is not the final method for fabricating a single soft filament, but it is included to show the iterative nature of the development process and to highlight the method's advantages and disadvantages. It involves moulding a single soft filament using steel tubes. The next iteration (described in Appendix 3.2) expands the fabrication technique to include multiple soft filaments within the same mould.

In an initial novel attempt to fabricate soft filament through a moulding technique using a stainless-steel tube, certain limitations and areas for improvement have been identified. The method involves injecting pre-silicon (in liquid state) into a closed mould designed to precisely produce a single soft filament. The mould setup includes two stainless-steel tubes of different gauges (8 and 18), along with five thin acrylic sheets, four steel shafts for stabilization, and the requisite bolts and nuts for assembly. The primary objective is to inject the pre-silicone into the larger tube (S-Steel tube-1), which then cures and adheres to the inner surface of the tube, while

the smaller tube (S-Steel tube-2) is cantered within to create the soft filament's internal cavity. Figure 4-6 shows the assembly of the mould, where the stainless-steel tubes are positioned between upper and lower groups of acrylic plates. Bolts and nuts secure the acrylic plates, and balancing shafts align the components.

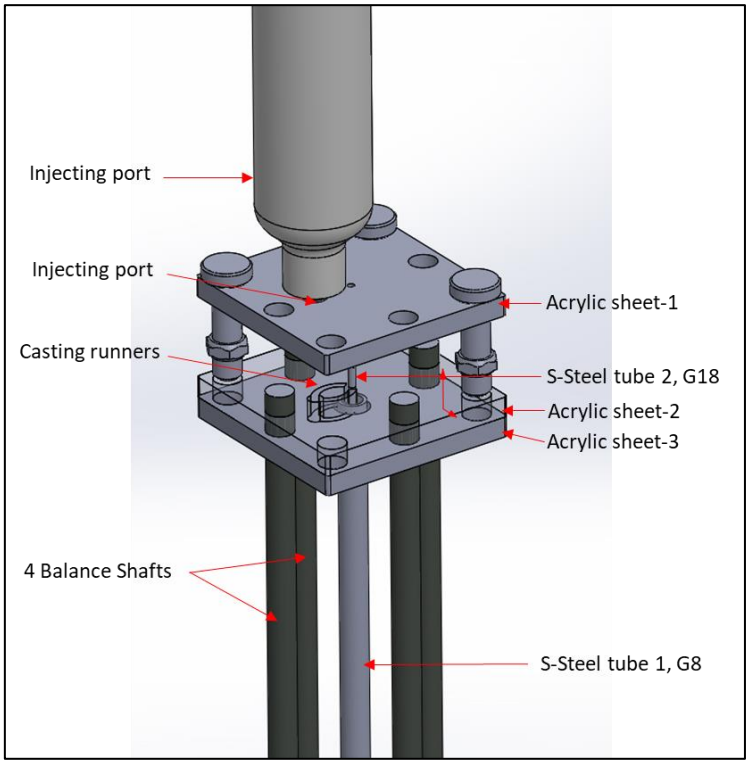

Figure 4-6: The assembled mould that designed to produce a single soft filament.

The spacing between the upper and lower groups of acrylic layers is set equal to the length of S-Steel tube-1. Acrylic sheets 3 and 4 have holes in the centre matching the outer diameter of S-Steel tube-1, while acrylic sheets 1, 2, and 5 have holes matching the outer diameter of S-Steel tube-2. Figure 4-6 depicts the casting runners in acrylic plate 2 and the injection port in acrylic sheet 1. To decrease viscosity, Ecoflex 00-50 is mixed with a thinner additive before injection into the mould. Although this method produced a soft tube with a smooth exterior, aligning the inner cavity poses a challenge. Even slight misalignments in stainless-steel tube-2 can significantly impact the internal cavity's formation, significantly affecting the motion and performance of the soft filament. Areas for improvement include refining the mould design to enhance alignment, addressing the challenges associated with S-Steel tube-2 buckling, and exploring alternatives to achieve a more accurate and reliable production of soft filaments.

4.4.2.2 Fabrication of Soft Components by Using 3D Printed Moulds (Finalized)

This fabrication technique involves utilizing 3D printed moulds to create soft components. This method excels in producing soft components with high accuracy and repeatable geometry, showing the consistency of the overall manufacturing process. The improvement of soft component production applied through an approach that include the development of 3D printed moulds for moulding soft components and refining fabrication techniques for soft components and subsequently for SAMs.

1. Developing 3D Printed Moulds for Soft Components' Models

The development of a design for the 3D printed moulds of soft components involves the determination of dimensions of the soft component's diameter of the solid area (wall thickness) and the cavity for each model. Subsequently, design and fabrication for the moulds' components are created using CAD software then translated into real 3D printed moulds. The manufacturing process employs three different 3D printers, namely FDM, PolyJet, and Formlabs, with the Formlabs 3D printers being the preferred choice due to their ability to produce moulds with a smoother internal surface finish and finer creation for small circles within the moulds. As part of the optimization process for developing a suitable 3D printed mould compatible with moulding Ecoflex 50, careful consideration is given to the type of resins used in Formlabs 3D printers. It is notable that Grey Pro Resin offers the highest precision and a smooth surface finish for moulds, facilitating the demoulding process and producing soft component with smooth surface.

Figure 4-7 depicts the 3D CAD model of the moulds, showing the mould designed for fabricating the soft components of the three models and the way of the injection syringe insertion. It's important to recall that a bundle of three soft filaments represents the soft components of Model-1. Each mould comprises three essential components: the main body, the end closer, and steel rods. In Figure 4-7, the main body is evident with its cylindrical shape, featuring a chamber to accommodate the injected pre-silicon. The top surface of the main body incorporates a hole, serving as an injection port for the precise fitting of the injection syringe tip. Additionally, other small holes are positioned on the top surface, which serve as vents during the injection process to allow any trapped air to be released. Figure 4-7 also shows the end closer, a thin circular 3D printed part with two circular grooves on its top surface. These grooves serve the purposes of securely holding the main body in place and

tightly accommodating the steel rods that form the cavity. The choice of a steel rod is deliberate, as it offers superior surface finish and straightness compared to a 3D printed rod, ensuring a cavity with high quality inside the soft component.

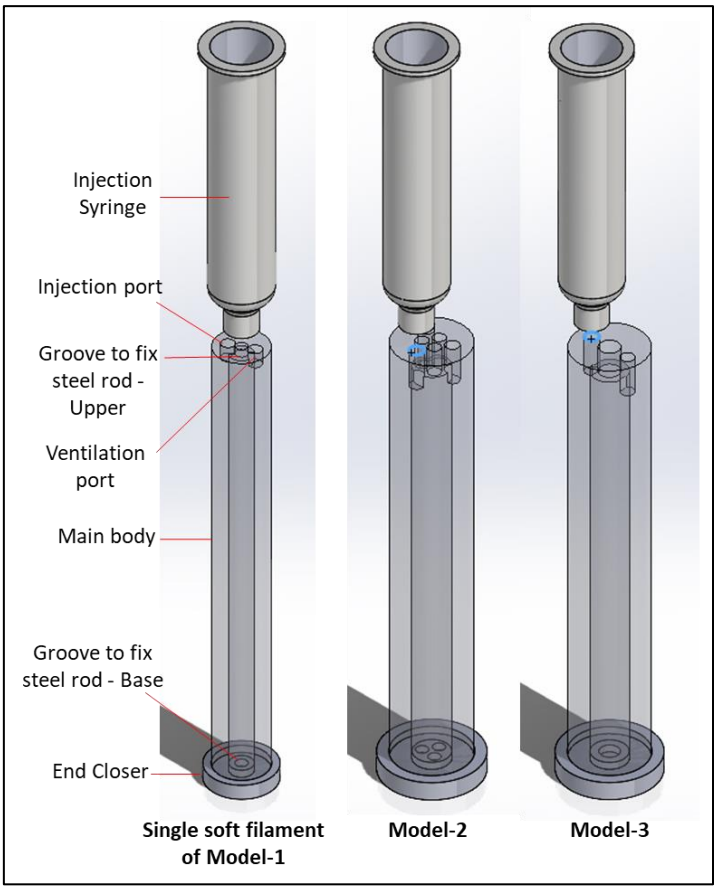

Figure 4-7: The 3D CAD model of the moulds for fabricating a single soft filament of Model-1, the soft component of Model-2, and the soft component of Model-3.

In addition to the initial mould designed for fabricating the original set of SAMs, where the soft component of Model-1 consists of only three filaments, an advanced mould has been created with the ability to produce an augmented set of soft components, following the same conceptual design principles. the soft components in this set are crafted based on optimal circle packing principles established by Graham (1968) for six circles [1]. In this augmented soft component set, Model-1 comprises six soft filaments, Model-2 includes six cavities, and Model-3 features a single cavity equivalent in cross-sectional area to the six cavities in Model-1/Model-2. Figure 4-8 presents these augmented innovative moulds as 3D CAD models and real 3D printed models.

In the Model-3 mould, the same conceptual design is implemented as in the original set. For the Model-1 mould, an advanced version has been developed to simultaneously produce four soft filaments that employ the same conceptual design principles to enhance productivity. In the Model-2 mould, a distinctive advancement is made by strategically relocating the injection port from the top surface of the main body to the side. This modification addresses a significant challenge encountered with the original mould, preventing the early escape of the pre-silicon material through the ventilation holes, especially when dealing with high-viscosity material, before fully filling the main chamber.

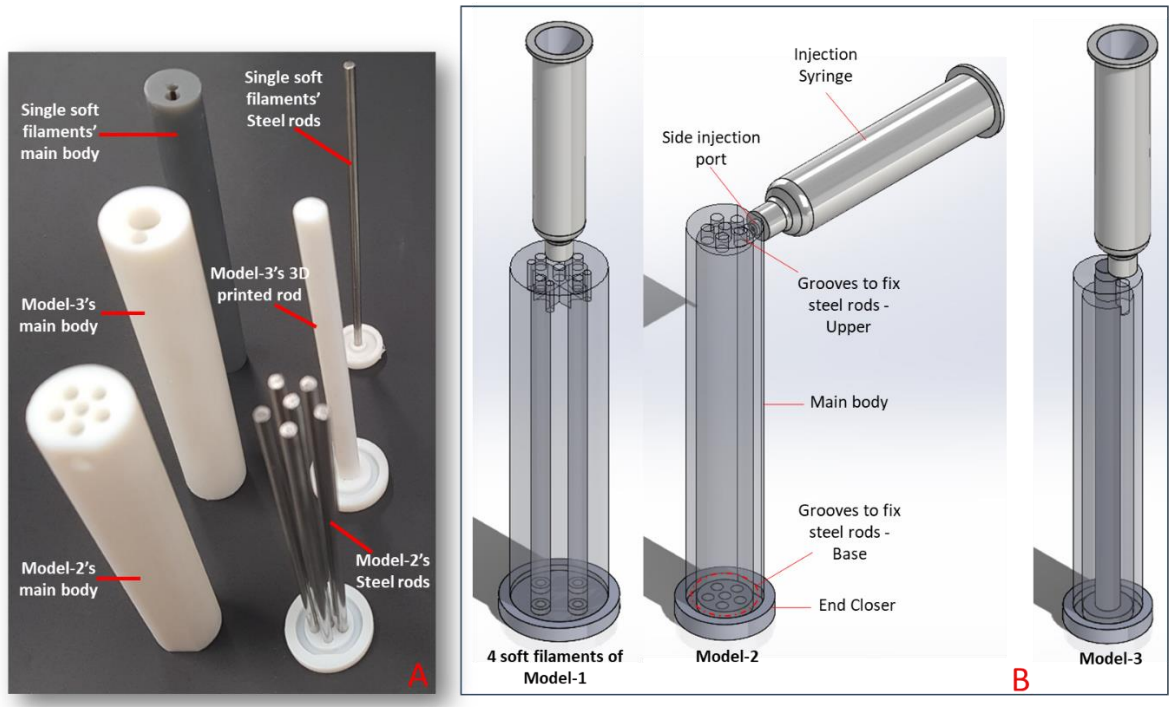

Figure 4-8: A) real models of the moulds and B) CAD model depicting the moulds designed for the fabrication of four soft filaments of Model-1, the mould of Model-2 with six cavities and the mould of Model-3 featuring a single cavity equivalent in cross-sectional area to six cavities.

2. Developing Fabrication Techniques for soft components' Models

Developing an optimal fabrication technique for manufacturing the soft components of Model-1, Model-2, and Model-3 involving several key procedures. Figure 4-9 presents flow chart of the key fabrication processes of SAM. Firstly, accurate manufacturing of the moulds is essential to ensure their cleanliness to avoid defects resulting from uneven internal surface of the mould's main body or imprecise creation of small circles used for ventilation and injection ports. The internal surface

of the mould's main body is sprayed with release agent (Universal Mold Release, Smooth-On, Inc, USA) to facilitate the easy release of cured soft material from the moulds.

The assembly of the steel rod or rods, used to create the cavity within the soft material, is a crucial step (shown Figure 4-8A). Subsequently, the cup-part (main body) and end closer are assembled as shown in Figure 4-7 and Figure 4-8, requiring precise placement to ensure the steel rod is correctly positioned at the end-part and passes through the hole in the cup-part. To prevent leakage from the bottom of the mould, the parting edges are carefully glued.

The next step involves weighing, mixing, and degassing the pre-silicon in a specially designed container using a mixing machine. Illustrated in Figure 4-10A, the container is equipped with two lids, each featuring a centrally positioned hole, facilitating the release of air during the mixing process. The removal of air bubbles from the pre-silicon is addressed through various experimental methods. Two mixing machines are used in the optimization process for the mixing and degassing techniques: centrifugal mixer (THINKY ARE-250) and centrifugal mixer (THINKY ARV-310P). The THINKY ARE-250, a planetary centrifugal mixer, is designed for mixing and degassing materials. However, its use was not sufficient with all types of pre-silicon due to some material properties like high viscosity. The most effective method identified for removing air bubbles is vacuuming the air from the material while it is being mixed, a technique applied by the THINKY ARV-310P, which combines vacuum pressure reduction with rotation and revolution mixing. This method has proven to be highly efficient in preventing air bubble-related issues during the fabrication process.

The pre-silicon is discharged from the container into an injection syringe, which is closed by an end-cup before injection into the mould. A pushing-piston is then inserted into the injection syringe and manually pushed to ensure the release of air bubbles. Manual injection of the pre-silicon is carried out with caution, maintaining a low and consistent speed and keeping the barrel tip in the mould's injection port (as shown in Figure 4-10B). The amount of resin consumed is determined based on the mould's cavity volume, with a 20% increase to account for waste during the fabrication process. Extra details about where the pre-silicon/soft material is being wasted are provided in Appendix 3.

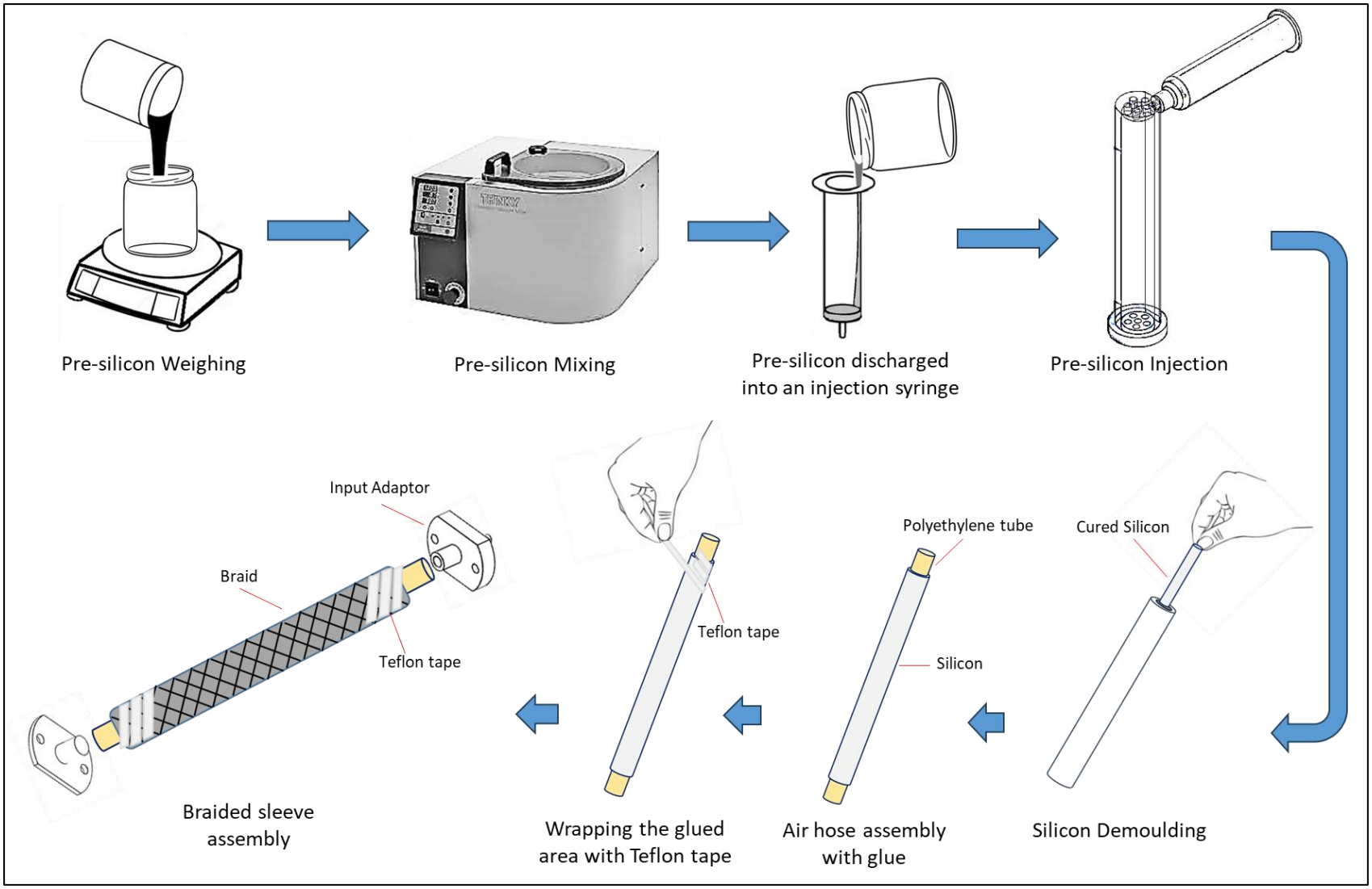

Figure 4-9: Flow chart of the key fabrication processes of SAM.

Figure 4-10: Fabrication process for soft component. A) a container covered with two lids for the pre-silicon miximg, each featuring a centrally located hole, B) injecting the pre-silicon into the augmented mould of Model-2, and C) the demoulding process, showing the extraction of a cured soft filament from its mould.

The filled mould with pre-silicon is left at room temperature until the material becomes fully cured soft material. Subsequent steps involve disassembling the mould, carefully pulling the steel rod first and then pulling soft material from the main mould cup. The cured soft material is pulled with an oscillated gradual movement from side to side (Figure 4-10C). Straight pulling for soft material or one-time pulling is not recommended during the disassembling process to avoid cutting or tearing it. The final step includes checking the condition and geometry of the fabricated soft component, where the diameter of the soft cylinders is accurate due to the high precision of the 3D printed mould. However, the length of the produced soft component may need adjustment (trimming) according to the required size (110 mm).

4.4.3 Fabrication Techniques for SAM

For an ideal fabrication technique for SAMs across Model-1, Model-2, and Model-3, a careful process takes place. This involves material preparation, precise bonding methods, and strategic assembly steps to ensure the SAMs meet desired specifications. Each model demands unique components, from Polyethylene tubing and braided sleeves to 3D printed adaptors. The following explains the procedure in a clear manner that include specific details.

Initiating the fabrication process for SAMs of Model-1, Model-2, and Model-3 commences with the collection and preparation of all requisite tools and materials, as outlined in Table 4-1. Following this, the next step involves measuring the desired

length of Polyethylene tubing, which is then cut to serve as an air hose connected to the ends of the soft component (shown in Figure 4-9). To ensure secure attachment, the Polyethylene tubes are uniformly glued before insertion into the soft component ends. The bonding agent employed for this task is ELASTOSIL E41, a one-component silicon known for its strong adhesion to soft materials. The procedure involves applying a small quantity of ELASTOSIL E41 onto a disposable rigid surface, such as an acrylic plate, followed by the horizontal dipping and rotation of the Polyethylene tube piece. This process ensures an even layer of ELASTOSIL E41, encompassing approximately 10 mm of the tube. It is crucial to rotate the Polyethylene tube onto the ELASTOSIL E41 carefully, ensuring the hose remains clear to avoid the formation of any obstruction to the airflow. The curing time for this adhesive silicon is 12 hours at room temperature, which means the need to leave the bonded parts overnight for curing. Subsequently, the bonded region is enveloped with Teflon tape to reinforce the connection between the soft component and Polyethylene tube, ensuring its ability to withstand high pressure without leakage.

Table 4-1 inventory of components required for the fabrication of SAMs for Models 1, 2, and 3.

Component	Model	Length	Diameter(D) / Width (W)/ Inner Diameter (ID)/ Outer Diameter (OD)
SOFT COMPONENT OF MODEL-1	Model-1	110	ID= 3, 3*OD= 6
	Model-2	110	3*ID= 3, OD= 10.39
	Model-3	110	ID= 5, OD= 10.39
BREADED SLEEVE	All Models	120	D= 13
POLYETHYLENE TUBE	Model-1	20	ID= 2, OD= 4
	Model-2	20	ID= 2, OD= 4
	Model-3	20	ID= 4, OD= 6
ZIP TIE	All Models	60	W= 2
	Model-1	10	ID= 2, OD= 4
	Model-2	10	ID= 2, OD= 4

INLETS/OUTLETS 3D PRINTED ADAPTORS FOR MODEL-1 AND MODEL-2	Model-3 (inlet)	10	ID= 2, OD= 4
	Model-3 (outlet)	10	ID= 4, OD= 6
SILICON TUBES FOR CONNECTION	Model-1	12	ID= 3, OD= 5
	Model-2	12	ID= 3, OD= 5
	Model-3	12	ID= 5, OD= 7

After ensuring a secure attachment of the Polyethylene tubes to the soft component with ELASTOSIL E41 and Teflon tape, the fabrication process for SAM advances to the preparation of the braided sleeve, integral to all three models. This phase begins with measuring the required length of the braided sleeve, using a white marker to accurately mark the exact point for cutting. With precision, the marked section is then trimmed using scissors to achieve the desired length. To prevent unravelling and ensure the quality of the braided sleeve ends, a torch lighter is employed in the next step. The end of the braided sleeve is brought close to the flame (approximately 2 cm apart), and the sleeve is rotated slowly in a circular motion. This heat treatment causes the loose strands at the end of the sleeve to fuse together. This process is repeated for the second end.

The subsequent stage involves integrating the soft component within the prepared braided sleeve. Figure 4-11 shows the sequence progression for integrating the soft component within the braided sleeve. For Model-2 and Model-3, this is achieved by first compressing the braided sleeve to enlarge its diameter, facilitating the insertion of one end of the soft component. This technique requires careful manipulation; the end of the soft component is held steady within the expanded sleeve, which is then allowed to contract, securing a portion of the soft component within. This process of pushing, holding, and releasing is repeated until both ends of the soft component precisely align with the two ends of the braided sleeve, ensuring a precise fit that optimizes the production of the SAM.

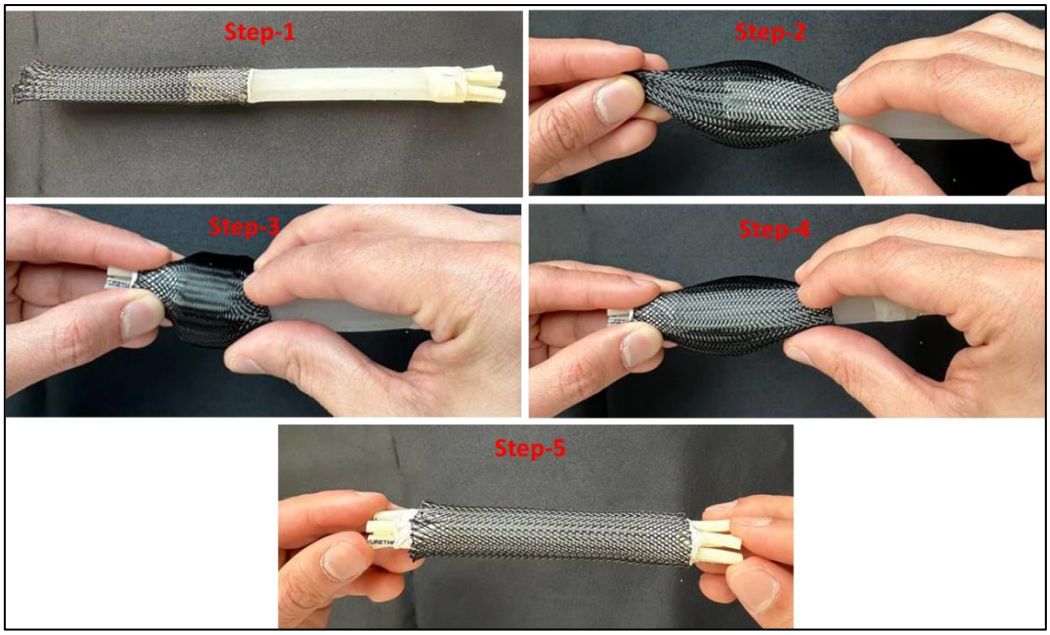

Figure 4-11: The sequence progression for integrating the soft component within the braided sleeve.

In the case of Model-1, a similar approach is taken for inserting the soft component into the braided sleeve. However, this model introduces an additional complexity due to its construction from multiple soft filaments. To maintain a constant and uniform position of the three soft filaments, a thin layer of Teflon tape is wrapped around the bonded ends of the bundle. This step is important for overcoming one of the significant challenges in manufacturing a Model-1 of SAM, requiring a high level of manual dexterity to ensure that the filaments are bound tightly together. A discussion on securing the braided sleeve to the soft component and its implications for SAM functionality, including the potential limitations of using an elastomer coating, is provided in Appendix 3.

Following the insertion of the soft component into the braided sleeves, the next step in the fabrication of SAM focuses on securing the assembly to maintain air tightness and structural integrity. This is achieved through the use of zip ties, a straightforward yet effective method for ensuring the braided sleeve remains tightly fastened to the soft component, which preventing any braid slippage which is crucial for the functionality of the SAM. To accomplish this, two zip ties are placed at each end of the SAM, specifically over the bonded areas where the Polyethylene tubes are inserted into the soft component. As shown in Figure 4-12, the application of the zip ties involves a dual-plier technique for optimal tightening. One plier is used to hold the head of the zip tie in place, while the other is used to pull the tail, ensuring the zip tie is secure around the sleeve without damaging the underlying components. After

achieving a tight fit, the excess portion of the zip tie is trimmed off to maintain a proper finish on the SAM.

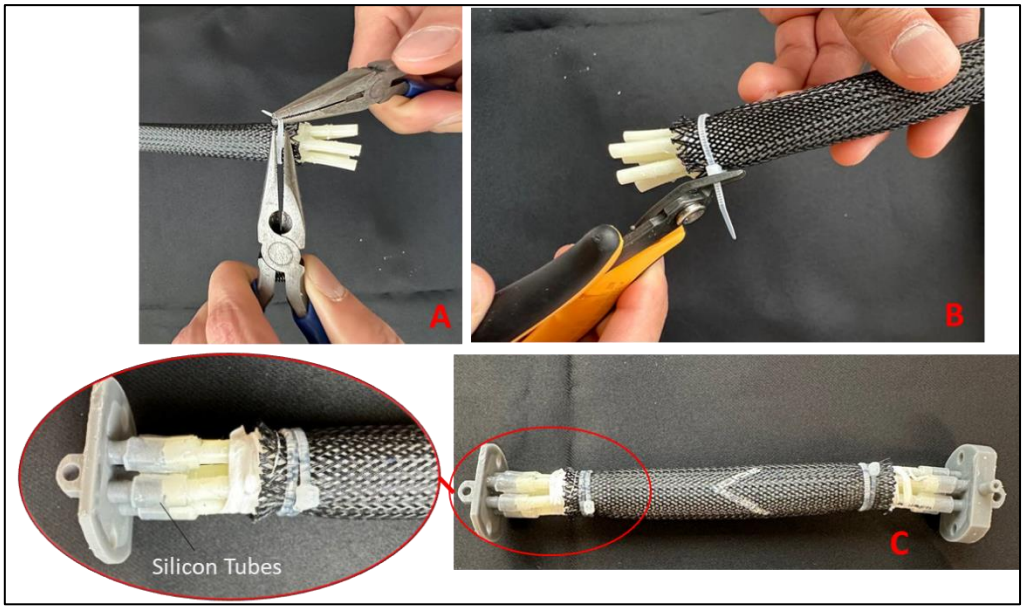

Figure 4-12: The process of applying zip ties to each end of the SAM. A) the application involves using dual pliers, B) the trimming of the excess portion of the zip tie, and C) the integration of 3D printed adaptors to both ends of the SAM, employing silicon tubes.

The next procedural step involves the integration of 3D printed adaptors to both ends of the SAM, employing silicon tubes to establish a connection as illustrated in Figure 4-12C. These adaptors play a critical role in the overall function of the SAM, serving as either air inlets from one side and air blocks from the other side. The adaptors vary by model, accommodating different numbers and sizes of air outputs to suit the unique design and operational needs of each SAM model. Figure 4-13 shows the cross-section view, top view, 3D models, and real 3D printed adaptors that used with Model-1, Model-2, and Model-3.

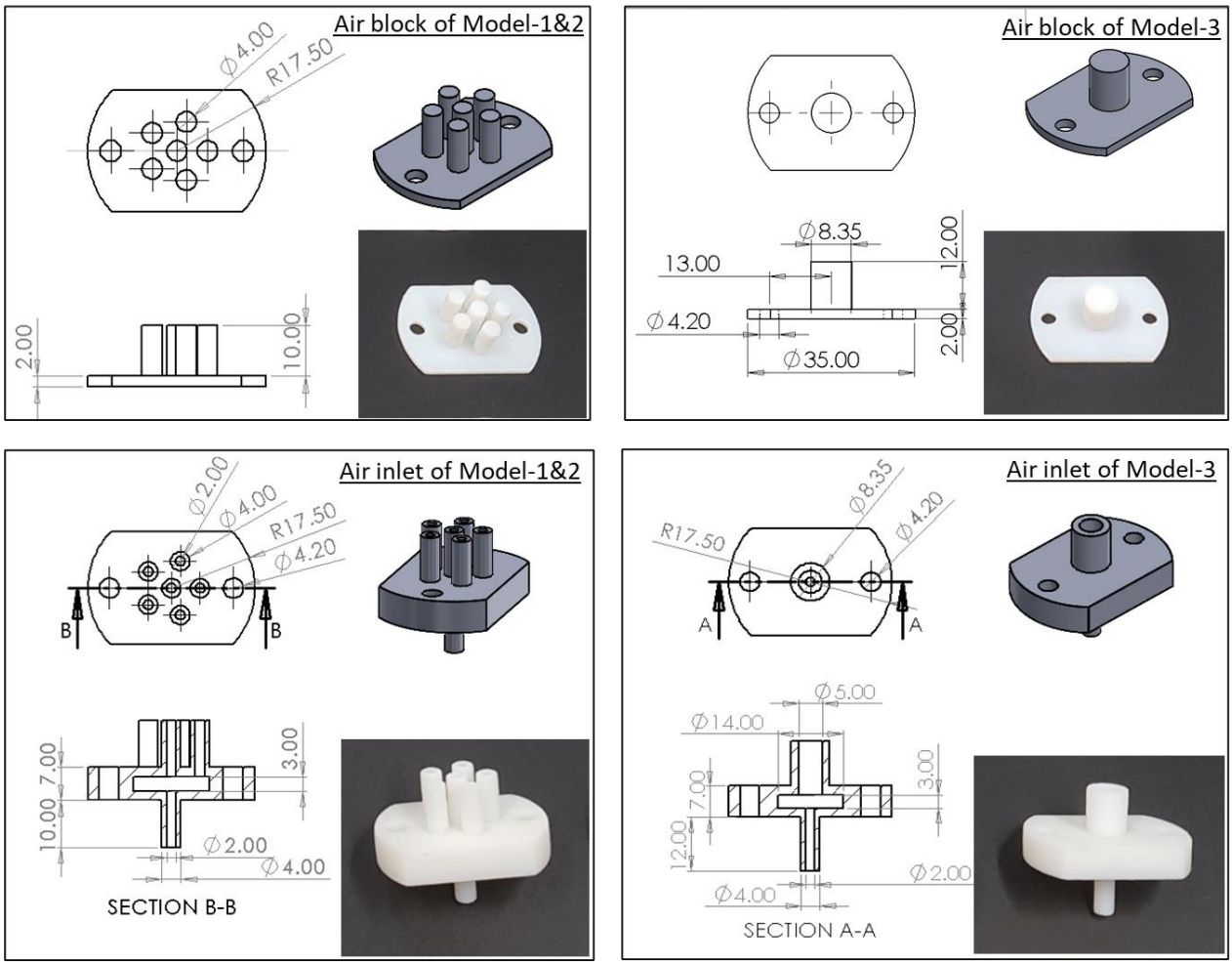

Figure 4-13: The four different types of the 3D printed adaptors.

For Models 1 and 2, the same type of 3D printed adaptors is used due to their identical requirement for multiple air outputs, illustrating the adaptors' role in managing air flow within the SAM. These adaptors are designed as pneumatic manifolds, featuring a central chamber that acts as a junction point for equal air distribution to the SAM's cavities. Conversely, Model 3 utilizes a different type of adaptor, reflecting its design for a single, with larger air output. All types of air-inlet adaptors, regardless of the model, are customized to have a common input channel at 4mm. This uniformity in the input channel ensures compatibility with the feeding tube that extends from the input pressure box, streamlining the assembly process of the SAM's during operation.

Following the secure attachment of the 3D printed adaptors and the application of zip ties, the fabrication process progresses with an additional step aimed at enhancing the structural integrity and uniformity of the assembly. This step involves the use of Teflon tape, a material chosen for its ability to provide a secure and evenly

distributed tightening around the SAM's ends. The application of Teflon tape covers the area around the inserted end of the Polyethylene tube till its end. This method ensures creating a more uniform and secure binding additional to the zip ties, which, while effective at preventing braid slippage, apply pressure evenly across the surface.

4.5 Discussion

This chapter focused on presenting comprehensive development of SAM that make a contribution to the field of soft actuators development. Through the conceptual design phase, the structural foundation of SAM is presented by taking inspiration from biomimicry to imitate the movements of biological muscles. The careful consideration of fabrication techniques and processes affected the quality and repeatability of SAM manufacturing. The choice of the appropriate soft material, based on the soft material characterization conducted in Chapter 3, follows two important criteria: elongation at break and characterized by partially high tensile strength. Applying these criteria shows that Ecoflex 00-50 was the ideal choice for fabricating the soft components.

This chapter presents the careful journey through the design and fabrication processes to illustrate the progress in development and highlight the benefits of the applied solutions for improving SAM manufacturing. The fabrication of SAM is outlined through three main phases: Mould fabrication, soft component fabrication, and SAM fabrication.

Fabricating the soft components is found to be most effective using 3D printed moulds. This technique consistently produces high-quality soft components, addressing issues encountered with other methods. Therefore, the initial phase focused on fabricating these moulds. Several 3D printers were utilized, with Formlabs 3D printers, using a resin called "Grey Pro," offering the highest precision and smooth surface finish for moulds. Subsequently, in the second phase of soft component fabrication, careful consideration was given to the fabrication process of the soft materials and the tools and equipment used. This underwent an improvement process to ensure precision and consistency in the produced soft components. Following this, the final phase focused on SAM fabrication by assembling the soft components with the braid (strain-limiting component) and other components.

The outcomes of this chapter facilitate the SAM characterizations and evaluations that will be conducted in the next chapters. Each component used in creating SAM

facilitates the testing procedures, such as creating 3D adapters that are easy to fit into various testing systems. Additionally, applying multiple bonding techniques such as glue, zip ties, and Teflon tape, ensure secure connections of the components. It is clear that the effort of enhancing SAMs involves design innovation, material exploration, and refined fabrication techniques. The foundation set here opens the door for further future exploration and improvement.

Chapter 5 : Experimental Evaluation of SAM

Having introduced the background of SAMs, this chapter investigates the methodologies for evaluating both their force generation and movement capabilities. The first section focuses on the block force test, where the SAM is assembled in a universal load tester (Instron 5943) to measure its ability to generate force. Following the block force evaluation, the chapter progresses to the displacement test, which assesses the range of contraction of SAMs. This test involves integrating the soft actuator into a finalized test frame designed to evaluate its movement capabilities. The methodology draws from earlier research but introduces refinements in measurement techniques and setup to enhance the accuracy of the performance data. Together, these experiments provide a comprehensive understanding of SAM's actuation behavior under different test conditions, contributing to the overall performance assessment.

5.1 Block Force Test

5.1.1 Introduction

In this section, the focus in investigating the mechanical behaviour of McKibben muscles by measuring the force they generate under various conditions. Force generation is a critical aspect of McKibben muscles' performance, as it directly impacts their ability to actuate and manipulate objects in robotic systems. The block force test includes assessing three different Soft Artificial Muscle (SAM) designs—Model-1, Model-2, and Model-3 (Figure 5-1). Testing for each design involved varying conditions, including four frequencies and four input pressure levels, resulting in a total of 16 test scenarios for each sample. This directly addresses one of the key research objectives: to compare the performance of the three SAM models based on the generated force. Given that these actuators mimic biological muscle performance and functionality, measuring the generated force is a logical and effective metric for comparison.

These tests can be broadly categorized into two main types. The first type, cyclic tests, involves subjecting SAM to repeated pressurizing and air releasing cycles. These cyclic tests are conducted to understand how SAM behaves under repeated pressure over time. The second type, static tests, includes applying a constant pressure to SAM over time, aiming to evaluate SAM's response under sustained pressure.

A significant outcome of these tests is the actuation time analysis, which provides valuable insights for users of soft actuators. This analysis enables users to appropriately select a SAM based on the specific application requirements. For instance, in medical rehabilitation, a SAM with a gradual speed until reaching peak force may be preferable, whereas an industrial production line setting might require a faster SAM with a quicker reach to peak force.

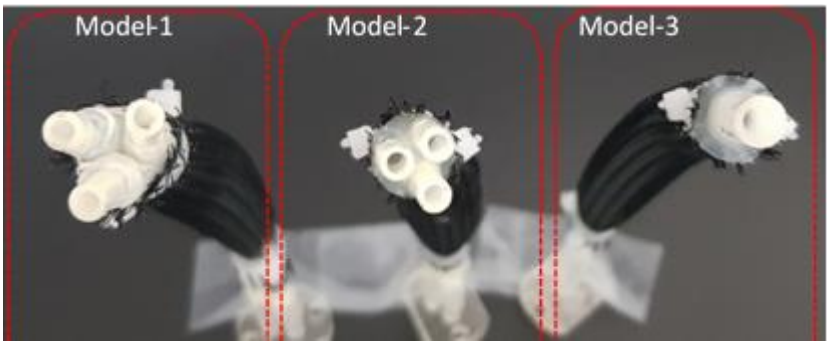

Figure 5-1: Soft Artificial Muscle (SAM) designs—Model-1, Model-2, and Model-3.

5.1.2 Objectives

This section aims to explore the details of SAM's performance by looking closely at how it generates force. A clear set of objectives is presented to guide the experiments. These objectives serve as guides for better understanding SAMs and their load capabilities and responses in various conditions.

Objective 1: To develop a detailed and replicable methodology for testing the performance of SAMs, ensuring that the testing setup is isolated from variations that could affect the measurements accuracy or consistency.

Objective 2: To measure the force generated by each SAM model under various pressure levels and actuation frequencies, using precise and repeatable testing procedures.

Objective 3: To evaluate and compare the performance of different SAM models, presenting the comprehensive output data in a format that facilitates clear comparison.

5.1.3 Methodology

5.1.3.1 Experimental Setup

5.1.3.1.1 Development History of the Test Setup

The experimental setup for the block force test has two primary requirements: to measure the generated force by SAM accurately and to provide consistent and repeatable test conditions for the various SAM samples. The development history of this experimental setup is presented in this section to provide an overview of the journey from the first version to the final setup, detailing how the versions were iteratively designed to meet the set-up requirements. Each iteration involved identifying necessary improvements, ultimately leading to a solution that met the precise measurement and consistency needs for the SAM tests.

First Version:

Version 1 of the setup, shown in Figure 5-2, was inspired by a previous research works [70][57], and it aimed to conduct the block force test using the available materials in the laboratory efficiently. This version utilized an aluminium strut structure to hold up the setup, and its main components included a load cell (LCFD-100), an amplifier (DR7DC), a data acquisition (DAQ) device (NI myDAQ), a computer equipped with DAQ software (LabVIEW, National Instruments), pressure sources (Nordson EFD Performus device), 3D printed adaptors, and connectors. More details about the electric component and connection are provided in the Appendix 4. The setup was designed with SAM and the connected load cell positioned horizontally. In Figure 5-2, the important details that demonstrate the pneumatic and electric connections are illustrated. Pneumatic components are located on the right side of the figure, while the electric circuit is on the left side.

SAM and the load cell are adopted within the aluminium structure and 3D-printed inlet and air block adaptors were designed and fabricated to connect to them. In Figure 5-2, the air inlet adaptor is magnified to illustrate its conceptual design. This design features a single air inlet on the bottom side and three air outlets on the upper side. The manifold adaptor is necessary for Model-1 and Model-2 of SAM because they contain of multiple pressurizable chambers. However, Model-3 requires a larger single air outlet due to its single cavity.

Furthermore, the setup incorporated a Nordson EFD Ultimas device, is typically used for controlled and precise fluid dispensing in various industries. Although not

originally designed for controlling actuator pressure, this lab equipment proved to be useful for controlling the level of pressure. However, it has limitations in terms of manual control and is insufficient for controlling the specific characteristics of pressure wave modes.

Version 1 of the test setup revealed some issues. Looking back at the test setup requirements, we see that it lacks the ability to provide consistent and repeatable test conditions for various SAM samples. This is because SAM is restricted between the two fixed vertical aluminium struts, preventing the adjustment of pre-tension. Therefore, an adjustable frame is needed to improve the test setup. Additionally, in this setup, the SAM is placed horizontally, which reveals two issues. Firstly, calibration was done vertically by applying weights to the load cell. To maintain consistency, it's preferable to conduct the test in the same position as the calibration. Secondly, the horizontal position led to potential deflection in SAM's body due to gravitational forces. The current test setup with these issues is insufficient and needs improvement to meet the test setup requirements.

Second Version:

In version 2 of the setup (shown in Figure 5-3), key improvements were applied while keeping the same aluminium structure and electrical components. These enhancements can be summarized as follows: vertically repositioning the SAM, replacing the Nordson EFD Performus device with a pressure controller box, and integrating a pressure sensor into the setup's system. Figure 5-4 provides a visual representation of the real configuration for the test setup. Figure 5-3 offers detailed insights into the second version, including pneumatic and electric connections. These figures offer a comprehensive visualization of the setup's design and components.

The first change in the Version 2 was the repositioning of SAM and the load cell within the aluminium structure. Instead of the horizontal setup used in the first version, the SAM and load cell were now assembled in a vertical position. This change was conducted for two primary reasons: to achieve consistency between the test and calibration positions, and to avoid potential deflection in SAM's body due to gravitational load.

The second change in the Version 2 replacing the Nordson EFD Performus device with a pressure controller box, where pressure box was introduced as a more controllable means of air pressure source. The pressure box played the role of converting high-pressure compressed air from the main source of air supplier into a

stable and controllable outlet pressure. It consisted of key components, including an Air Reservoir (CRVZS-0.1), an Electro-pneumatic Regulator (SMC ITV0010), a solenoid valve (SMC V114A), and a control unit with an embedded control panel and screen. More details about the pressure box can be found in the Appendix 4.

The third change in the Version 2 was the incorporation of a pressure sensor. The pressure sensor helps in monitoring and recording pressure data within the internal system, which includes SAM and translate them into electrical signals, with voltage levels proportional to the measured pressure. It is pneumatically connected to tubing channels responsible for supplying pressure to SAM. Also, it is electrically connected to the myDAQ device.

In Version 2 of the setup, tests were successfully conducted, and their results were recorded. However, a notable limitation in the setup was the inability to precisely adjust the vertical position of the aluminium strut that holds SAM. To ensure consistent results across samples, it is crucial to establish a unique and consistent initial positioning. In this version, the separation between the two aluminium struts can only be adjusted by loosening the joints that connecting the bottom aluminium strut with the two vertical aluminium struts and manually moving it up or down (Figure 5-4). Therefore, it is necessary to find a new test frame that allows for a more precise adjustment of the separation between the holders.

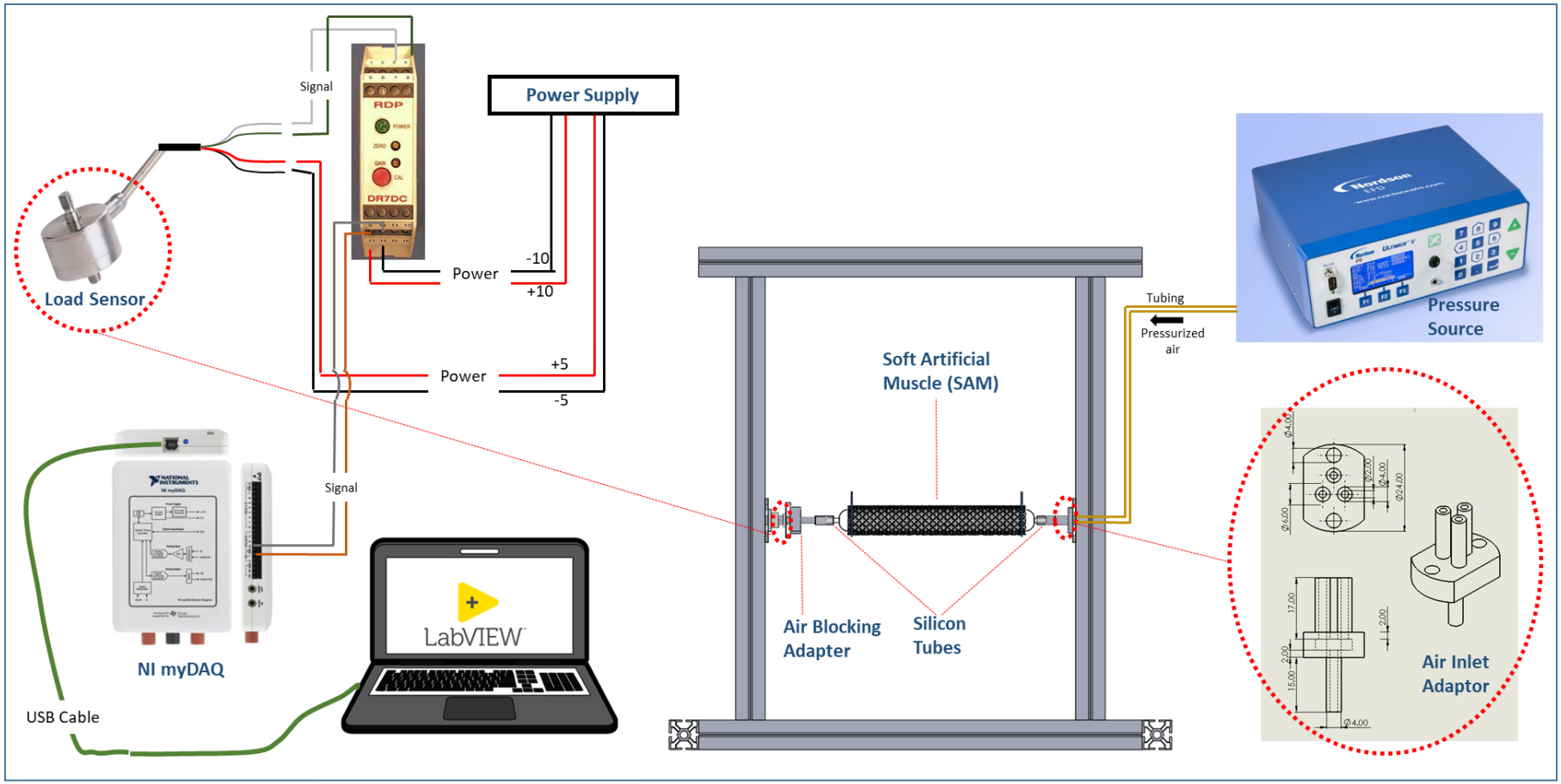

Figure 5-2: Pneumatic and electric circuits of Version 1 of the test set up.

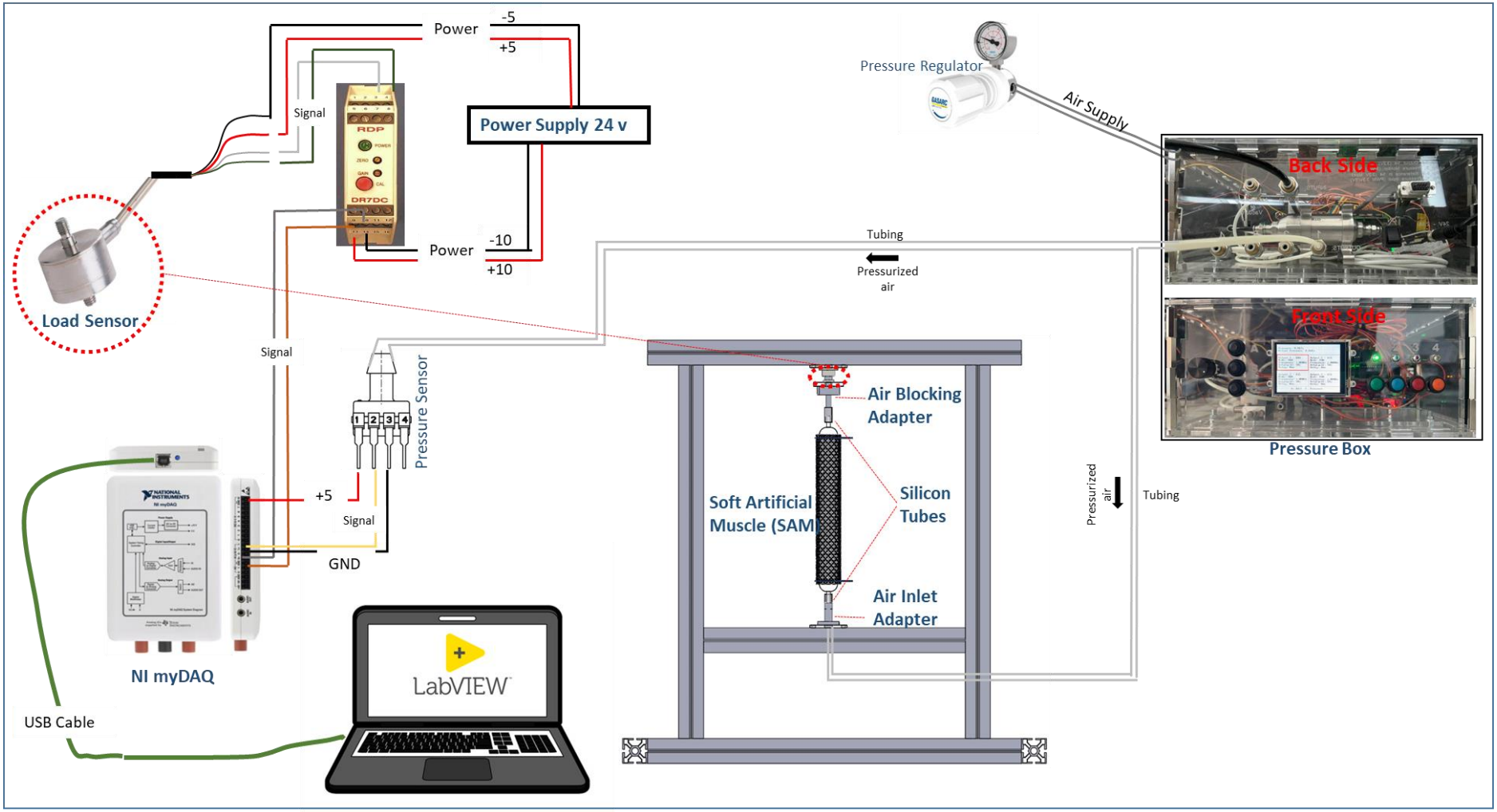

Figure 5-3: Pneumatic and electric circuit of the Version 2 of the test set up.

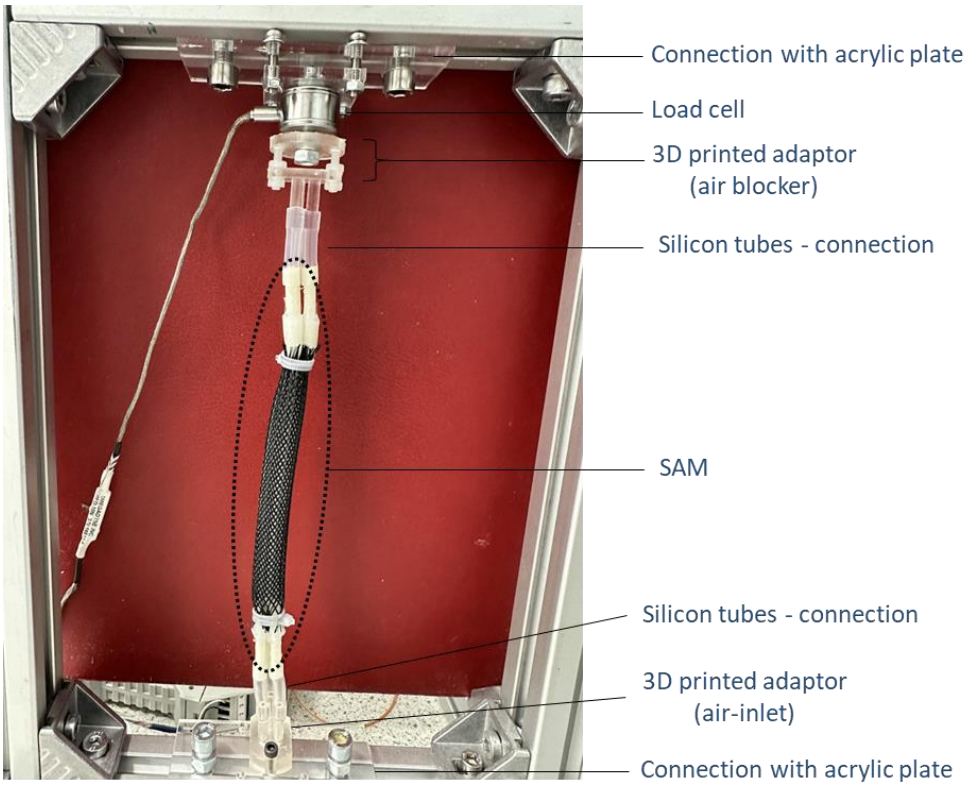

Figure 5-4: The real configuration for the test setup of Version 2.

Third Version:

In Version 3, a significant change was made by replacing the aluminium strut structure with the load testing machine. This involved assembling the upper and lower parts of SAM within the machine crosshead and the lower holder, respectively. The machine crosshead's position can be precisely adjusted to establish a uniform and consistent initial condition for all the tested samples. To provide a visual representation of this setup, Figure 5-5 displays important details that illustrate the pneumatic and electric connections.

In the SAM sample testing process, pre-tensioning is applied to ensure the even loading of the sample before the primary test begins. This pre-tensioning is controlled by adjusting the crosshead, a task that can be accomplished in two ways: manually from the load tester control unit or automatically by setting the desired pre-tension through the load tester interface software, Bluehill. To ensure a consistent starting point with zero load, an initial preload of 0.5 N is applied to all samples.

The load testing machine is equipped with a 500 N load cell. While the range of this load cell is slightly larger than needed, it was chosen as a safety factor to

accommodate the range of forces generated by SAM. A load cell with a smaller range is preferred due to its higher sensor sensitivity. However, to select an appropriate a smaller range of load cell, it first need to determine the range of forces generated by SAM.

In order to convert the input voltage signal into units of force (Newton), a calibration process for the 500 N load cell is necessary. The primary goal of calibration is to establish a linear relationship between the voltage output and the applied force. This calibration procedure involves applying known loads to the load cell for precise calibration measurements.

In this version, SAMs were subjected to testing under various conditions, with the pressure levels being adjusted to 20, 40, 60, and 80 kPa, and the actuation frequencies being varied between 1 Hz and 0.5 Hz. A total of eight different testing conditions were included, considering the four pressure levels and two frequencies.

In Version 3, two main limitations were identified. Firstly, there was an issue with the synchronization of force data received from the load tester with the control test system, resulting in unsynchronized load data (from the load tester) and pressure data (from the pressure sensor). Secondly, it was noted that the 500 N load cell used had a larger capacity than the range of the generated force. As mentioned earlier in this section, one of the experimental setup requirements for the block force test is to accurately measure the force generated by SAM. Using a 500 N load cell has limitations in detecting minor changes in load, especially when actuating within a small range of pressure. The next smaller load cell available in the lab had a capacity of 50 N, which provided an ideal range for accurately measuring the generated force.

Fourth Version (the Final):

Version 4 setup was considered ideal because it successfully addressed all the challenges in the previous setup versions. The same configuration as the third version was kept, with a focus on collecting the load tester output data with the control system and utilizing a 50 N load cell for enhanced accuracy. This setup will be presented upon in detail in the following section.

These four versions represent a process of improvement and addressing challenges, where each version learns from the previous one. The changing setups have led to the development of a more robust and precise testing configuration, enabling a consistency in the test conditions.

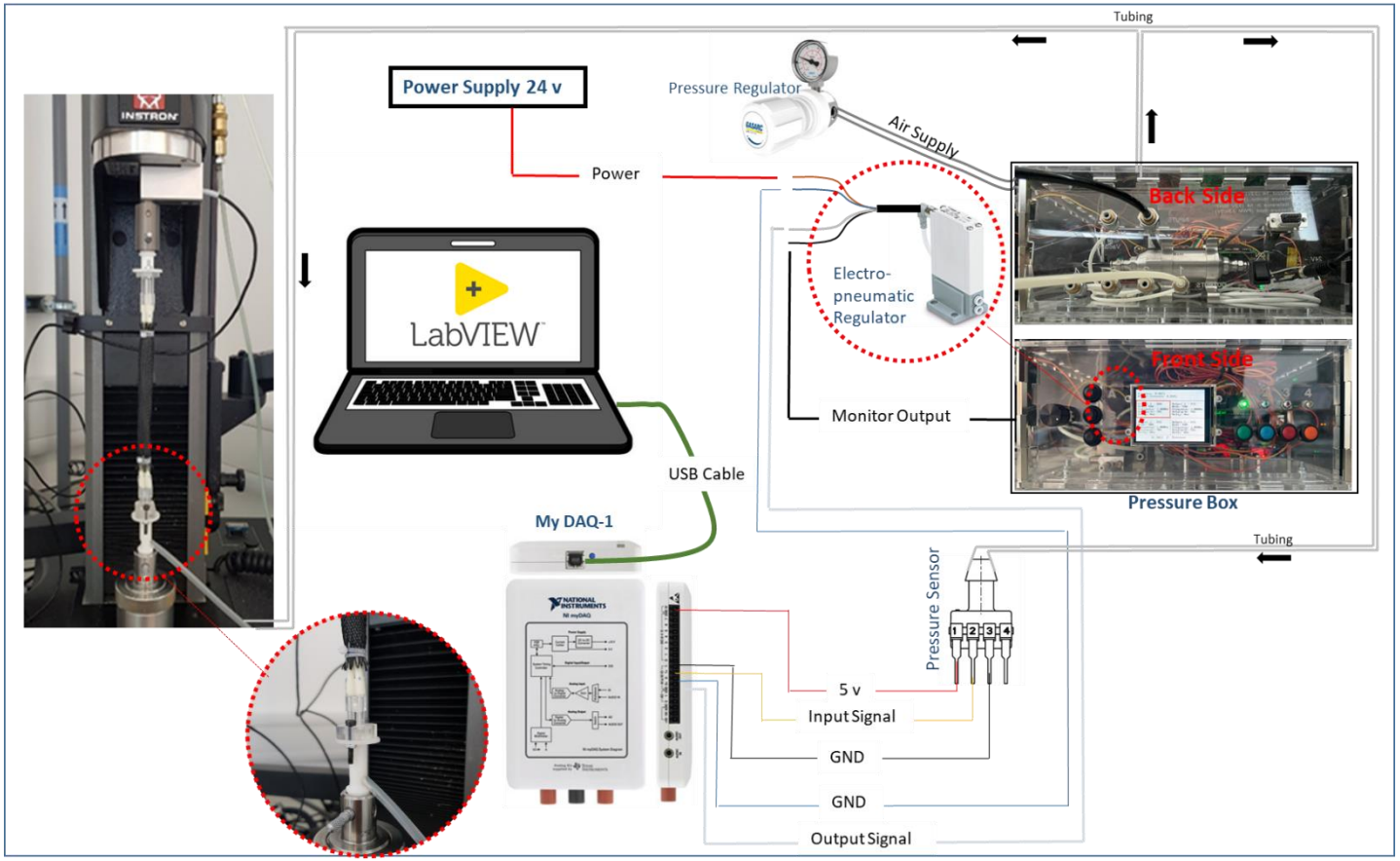

Figure 5-5: Pneumatic and electric circuit of the Version 3 of the test setup.

5.1.3.1.2 Version 4 (Final) Test Setup

Figure 5-6 illustrates the setup used for testing the generated force by SAM's models. The load testing machine utilized as an ideal platform for conducting the load test. As shown in the figure, SAM is connected from the both ends using 3-D printed adaptors that allows for pneumatic tubing connection from the bottom side. The specific details on the design and functionality of these adaptors can be found in the Appendix 4.

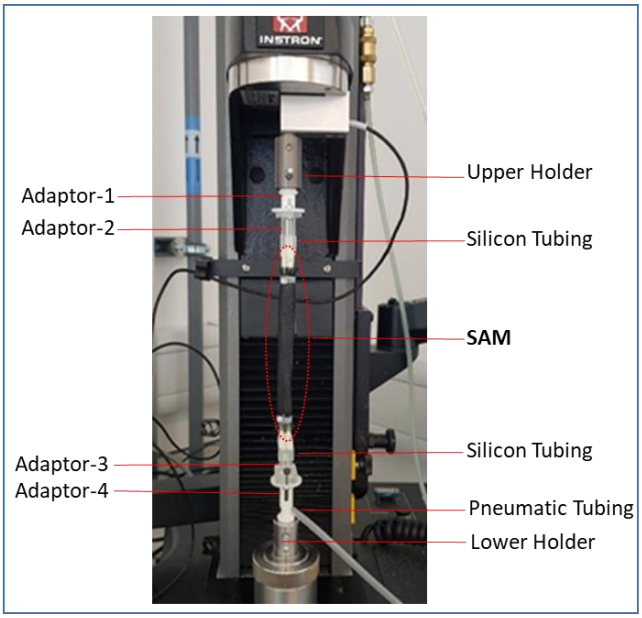

Figure 5-6: Version 4 setup for testing the generated force by SAM's models within the load tester.

During the test, the two grips of the load tester remain fixed to allow performing the block force test. SAM actuate by applying a controlled input pressure, leading to generate force that load cell records it. The conditioned signal is transmitted to the myDAQ system through direct wiring, where it is received as an analogue signal. This data is displayed on the LabVIEW software, which records and synchronizes the load data with the time and the internal pressure signal.

To convert the input voltage signal into units of force (Newton), calibration is required. The calibration's main objective is to establish a linear relationship between the voltage output and the applied force. The calibration process involves applying known loads to the load cell. Each load is applied by hanging known weights to the upper holder of the load testing machine, and more weight is added to the hanger to

increase the load. Figure 5-7 illustrates a set of load cell readings (voltage) and their corresponding hinged weight (Newton), and a calibration curve is created. This calibration curve is fitted, generating a mathematical equation that approximates the data points.

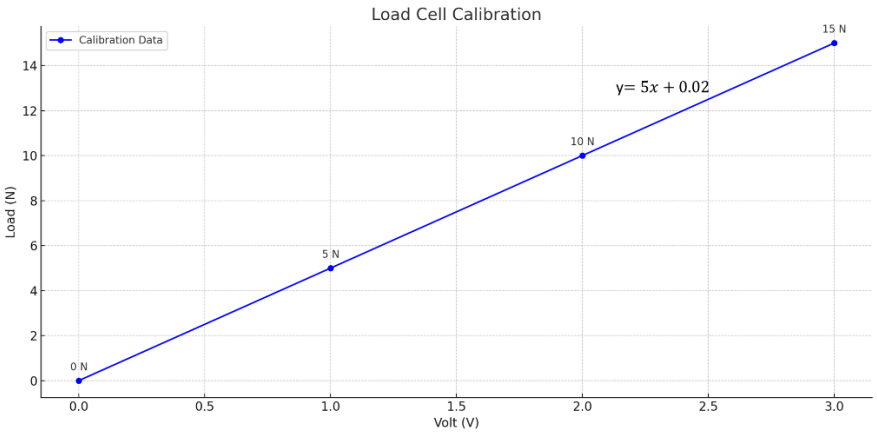

Figure 5-7: The load cell calibration data showing applied load and resultant output voltage.

Figure 5-8 provides a comprehensive illustration of both the electronic and pneumatic circuits used in the Version 4 test setup. The setup comprises key components, including two Data Acquisition (DAQ) systems, which are in charge of collecting and transmitting data. The use of two DAQ systems is necessary due to limitations in analogue pins. These DAQ systems establish connections with the pressure sensor, the Electro-pneumatic Regulator within the Pressure Box, the load cell within the load testing machine and the computer running LabVIEW. Further details about the connections are provided in the Appendix 4.

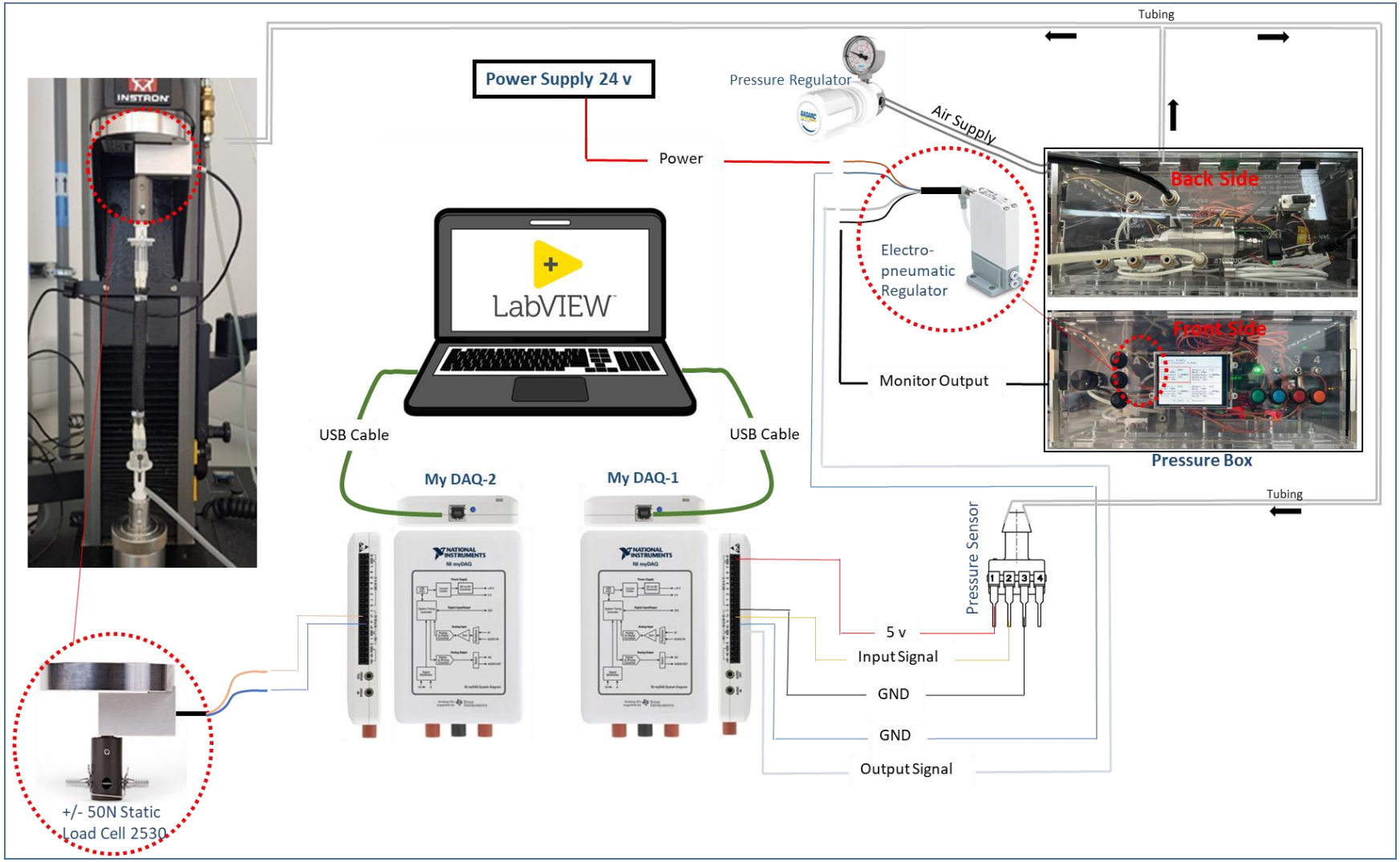

Figure 5-8: Comprehensive illustration of both the electronic and pneumatic circuits used in the optimum Block Force Test setup.

5.1.3.2 Block Force Test Procedure

This test protocol outlines the steps for conducting a block force test on SAM using an load testing machine. This protocol is important because it provides guidelines for conducting a reliable and repeatable load test for measuring the generated force by SAM. The test setup and protocol offer a robust characterization method, informed by existing work in the literature. For instance, the methodology for the block force test was developed in light of the approach presented by Takosoglu *et al.* [70], which influenced the design of our protocol. However, this test protocol provides some unique aspects of the approach such as the approach of using the 3D printed adaptor to connect SAM's samples to the testing setup. Moreover, illustrating a precise automated pre-tensioning methodology, contributing to consistent initial testing conditions. Figure 5-9 presents a flowchart that outlines the steps for conducting this block force test.

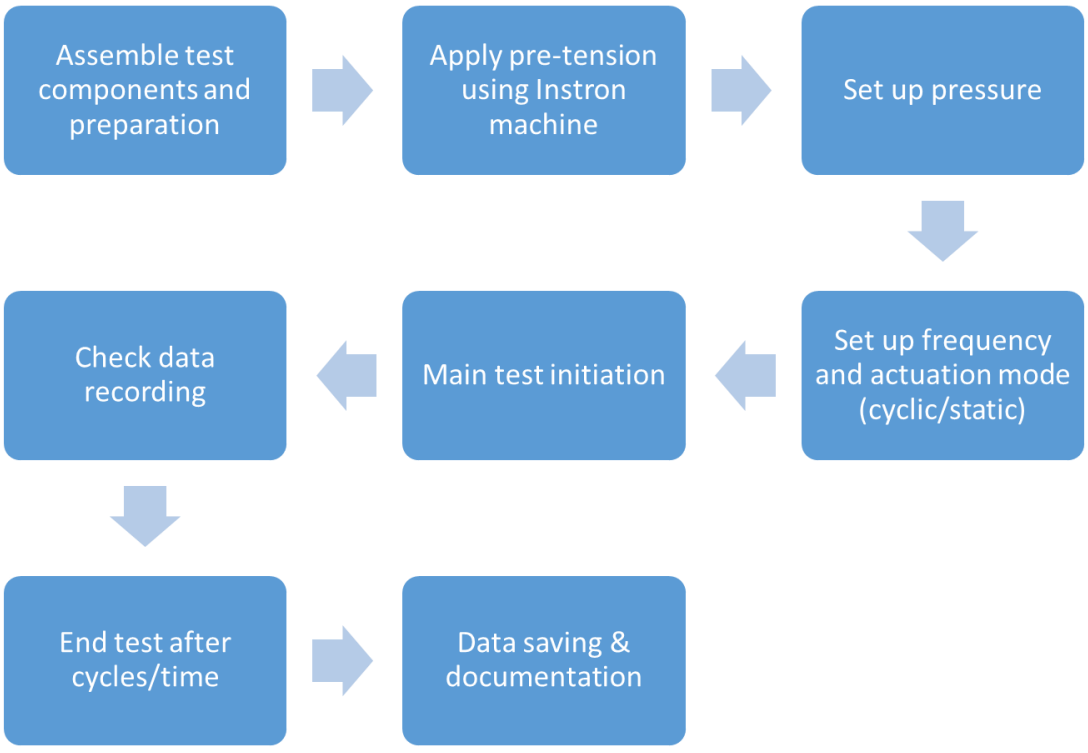

Figure 5-9: Block force test procedure flowchart.

Procedure:

1. Setup: To get ready for the testing procedure, first, SAM should be assembled in the setup within the load testing machine through joining the adaptors with screws. Once SAM is in place, the necessary tubes and connectors are connected to it. This connection ensures that the pneumatic circuit is set up correctly. Finally, before starting the testing, all components within the setup are checked in order to be functioning properly and ready to record data.
2. Pre-Tension: Pre-Tensioning is an important step in the SAM sample testing process, providing uniform loading of the sample and consistent starting point. The pre-tensioning process applies a low tensile load to the specimen (0.5 N) then moves to zero load position. After a short waiting period (10s) any necessary adjustments are made manually to account for relaxation in the specimen. Pre-tensioning process is programmed in advance through the Instron's Bluehill interface software to enable automatic pre-tensioning before starting the main test.
3. Setting up Pressure: This step begins by entering the desired pressure level value which vary at 20, 40, 60 and 80 kPa into the LabVIEW program. This value will be used to control the pressure applied during the test.
4. Setting up Frequency and Actuation mode: Configure the actuation mode and frequency in the pressure box by entering the desired values through the control panel. This step enables selecting the specific mode, either cyclic or static, and frequency at which the actuation will be performed at 0.2, 0.5, and 1 Hz.
5. Main Test Initiation: To initiate the test, the first step is to click on the "start" button within Instron's Bluehill interface software. This triggers the pre-tension process, ensuring that the initial load conditions are set. Once the load reaches the designated 0.5 N, the pre-tension process will stop, indicating that the SAM is at the desired initial test condition, which makes it ready for applying the pressure through activating the pressure box.
6. Data Recording: Throughout the test, data is collected, including time, force and pressure parameters. These data are essential for analysing the performance of SAM during the test.
7. Completion and Data Collection: In the cyclic test, the test ended after completing 10 actuation cycles, while in the static test, the test ended after 60 seconds. Once the test is complete, the test is ended following these steps:

a. Press the same "running" green button in the pressure box to stop the actuation.
b. Stop the test in the Instron program to end sending load data to the control system.
c. Stop the LabVIEW program to end receiving pressure data from the Pressure Sensor.

8. Data Saving and Documentation: In the procedure for conducting the block force test, the synchronized data, including time (in milliseconds), load (in volts), and pressure (in volts), is saved in LabVIEW. After that, the graphical data that generated by the load testing machine is exported just as a reference if needed. Additionally, all relevant information, such as test setup details, test parameters, and the obtained results, is accurately documented.

5.1.3.3 Data Processing

The data processing procedure for the output of the block force test involves a protocol to analyse data. The goal is to obtain valuable results from this data and provide conclusions relevant to the objectives of the study. To improve data analysis, the data processing includes creating clear data visuals like graphs and charts. These visuals are important for presenting and understanding the data well. Figure 5-10 presents a flowchart that outlines the steps for conducting the data processing of the block force test.

The procedure outlining a series of steps, including data collection, calibration, examination, and importation into MATLAB. These steps enable comprehensive analysis and visualization of the data, which comprises 144 tests varying based on differences in the samples and test conditions.

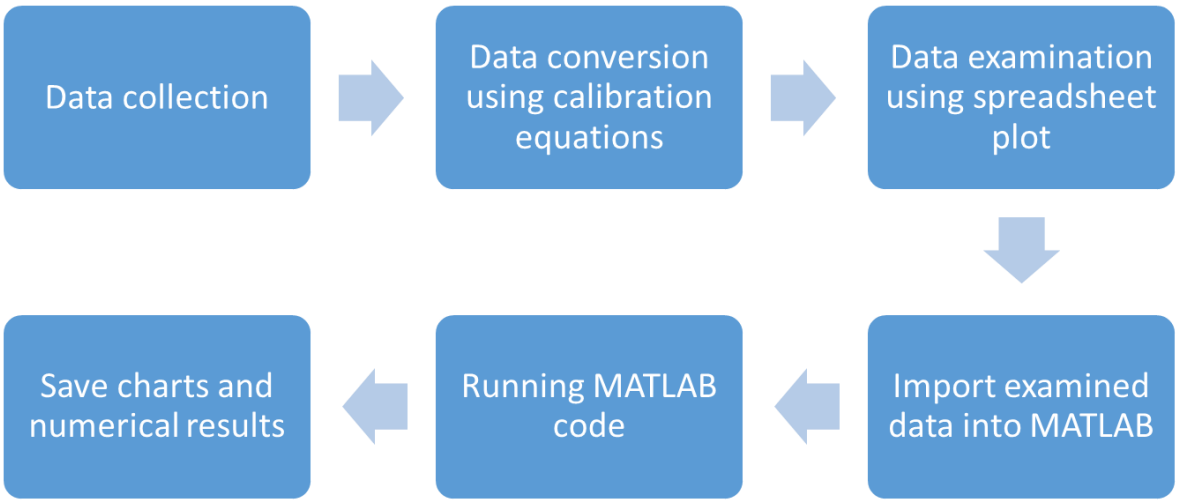

Figure 5-10: Flowchart for the data processing procedure of the block force test.

Procedure:

1. Data Collection: Load tests are conducted on samples under various conditions, including different frequencies and pressure levels. The output row data, including voltage of internal pressure, and load values, are collected.
2. Data Conversion: Pressure and load measurements are converted from volts to kPa and N, respectively, using calculated calibration equations.
3. Data Examination: Converted load and internal pressure data are plotted in a spreadsheet to investigate any issues might arise within the raw data.
4. Data Importing: Examined data is imported into MATLAB and named to identify the sample and the test condition.
5. Running MATLAB codes: The generated results include the following:
    a. Synchronized pressure-force data with highlighting cycle's component.
    b. Time and force values at peak pressures for each cycle.
    c. Average peak pressures and forces with standard deviations (STD).
    d. Average cycle data for all cycles with standard deviations (STD).
    e. Time intervals for each component of the cycle.
6. Data Saving: Numerical calculated results is exported in spreadsheets format, and charts are saved as JPEG and MATLAB figures. The MATLAB data sheet is also saved for potential future editing.

The four MATLAB codes include the following:

Previously, data processing was done using Microsoft Excel due to its familiarity. However, MATLAB has been adopted because it allows for automated processing through coding for the large amount of data while Excel often requires a lot of manual entry. The data analysis involves several MATLAB codes created for various purposes. These codes are summarized and categorized into three types based on their specific objectives. The output of these codes will be the resultant charts that will be presented in the results section. The MATLAB code is detailed in Appendix 8.

Code-1

Code-1 concentrates on producing synchronized pressure and displacement cycles over time. Figure 5-11 presents flowchart of the Code-1 for data processing and resultant charts. This code generates three charts: the first chart illustrates synchronized pressure and displacement cycles and highlights the cycle components.

In the displacement cycle, five important events can be captured:

1- Trigger of internal pressure: When the pressure is first detected.
2- Trigger of actuation: When the actuation is first detected.
3- Peak displacement point: Typically occurring at the end of the actuation phase.
4- End of the de-actuation effect: When the effect of the de-actuation is finished.
5- End of the idle phase: The start of a new cycle.

Based on these events, the cycle can be divided into four time intervals (displacement cycle components), as follows:

1- Pre-conditioning: This interval starts from the triggering of the pressure and continues until the triggering of the actuation (first detection of a displacement). It is calculated as: Pre-conditioning = Actuation Trigger - Pressure Trigger.
2- Actuation: This interval starts from the initiation of contraction to the peak contraction point. It is calculated as: Actuation = Peak - Actuation Trigger.
3- De-actuation: This interval starts from the pressure release to the end of the de-actuation effect, showing a quick and sharp drop below the average bottom in response to the pressure release. It is calculated as: De-actuation = End of De-actuation - Peak.

4- Idle: This interval starts from the end of the de-actuation stage to the next pressure trigger, representing a steady state where the pressure source remains inactive. It is calculated as: Idle = End of De-actuation - Start of new cycle.

The second chart overlays seven sequential displacement cycles, enabling an assessment of cycle variations and repeatability. The third chart displays average and STD calculations from the data in the second chart, with the STD visually depicted by a shadow area over the average line. Additionally, the code is generating data in a spreadsheet table presenting key outcomes, such as the maximum displacement of each cycle, delay between pressure and displacement cycles, and detailed time intervals for cycle components.

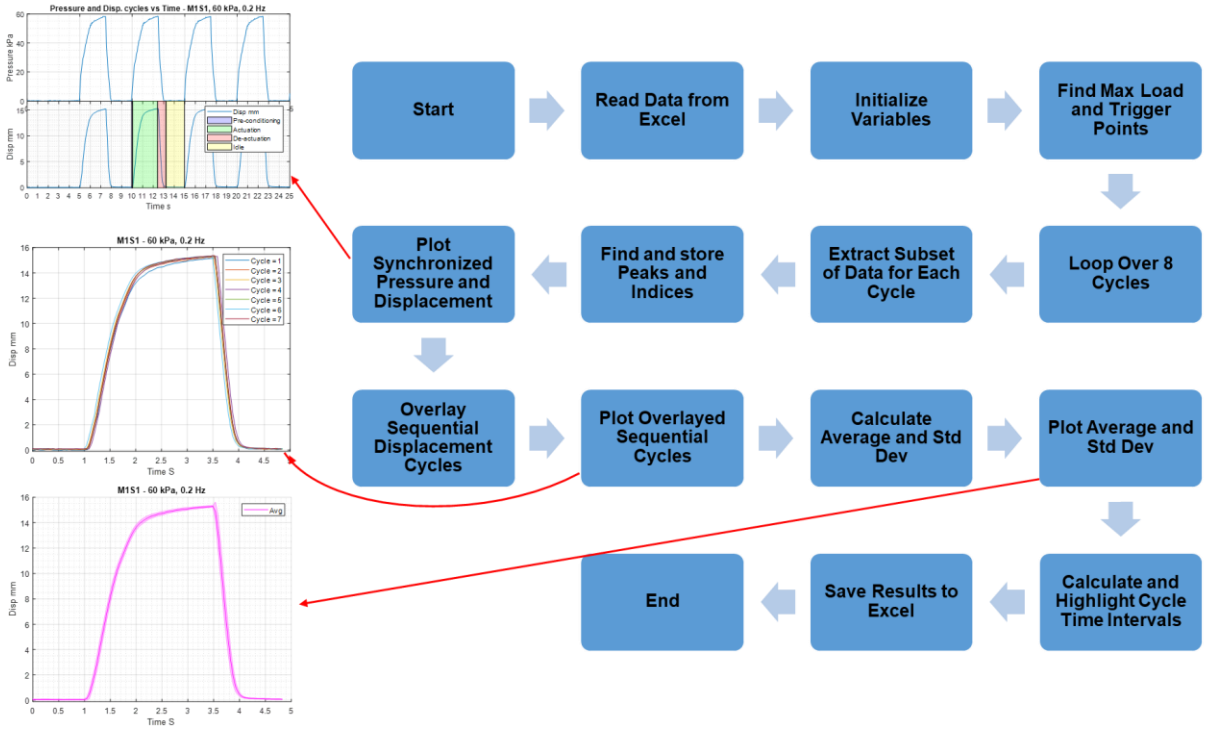

Figure 5-11: Flowchart of the Code-1 for data processing and resultant charts.

Code-2

After obtaining the main results by using the first code, three comprehensive comparison methods will be presented in the results sections to facilitate the analysis and comparison of the performance of the three models of SAM. The methods include assessing the pressure effect, frequency effect, and analysing the time intervals.

Code-2 is utilized to analyse the data obtained from the first code and create figures and numerical outputs. Figure 5-12 presents flowchart of the Code-2 for data processing and resultant charts. This code is employed to generate a plot containing four line graphs depicting displacement. This plot demonstrates the impact of varying input pressure levels (applied at 20, 40, 60, and 80 kPa) while maintaining a consistent frequency of 0.2 Hz. Then, the same code is applied in a different scenario to demonstrate the effect of actuation frequency changes at 1, 0.5, and 0.2 Hz while keeping pressure constant at 60 kPa. Each line graph in these plots should represent average and STD calculations from seven consecutive cycles.

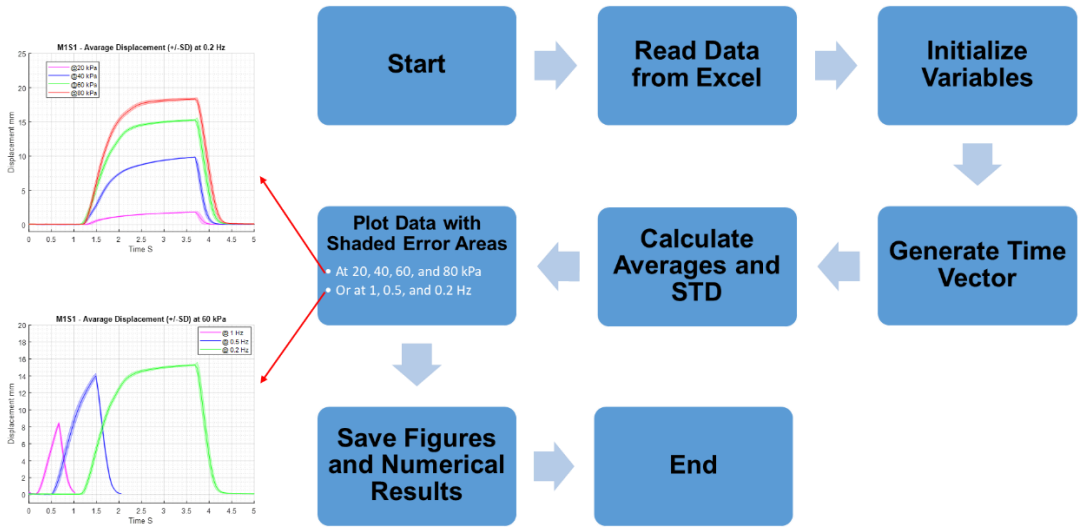

Figure 5-12: Flowchart of the Code-2 for data processing and resultant charts.

Code-3

Code-3 generates bar graphs displaying the average peak values of specific parameters. These graphs are used in all three comprehensive comparison methods: assessing the pressure effect, frequency effect, and analysing the time intervals. Figure 5-13 presents flowchart of the third code for data processing with generating charts of time intervals as an example. They provide a straightforward visual analysis of the measured parameters and are applied in various scenarios, such as evaluating the range of contraction of different SAM models under different input pressure and frequency conditions. These bar graphs also include STD bars to illustrate data variability.

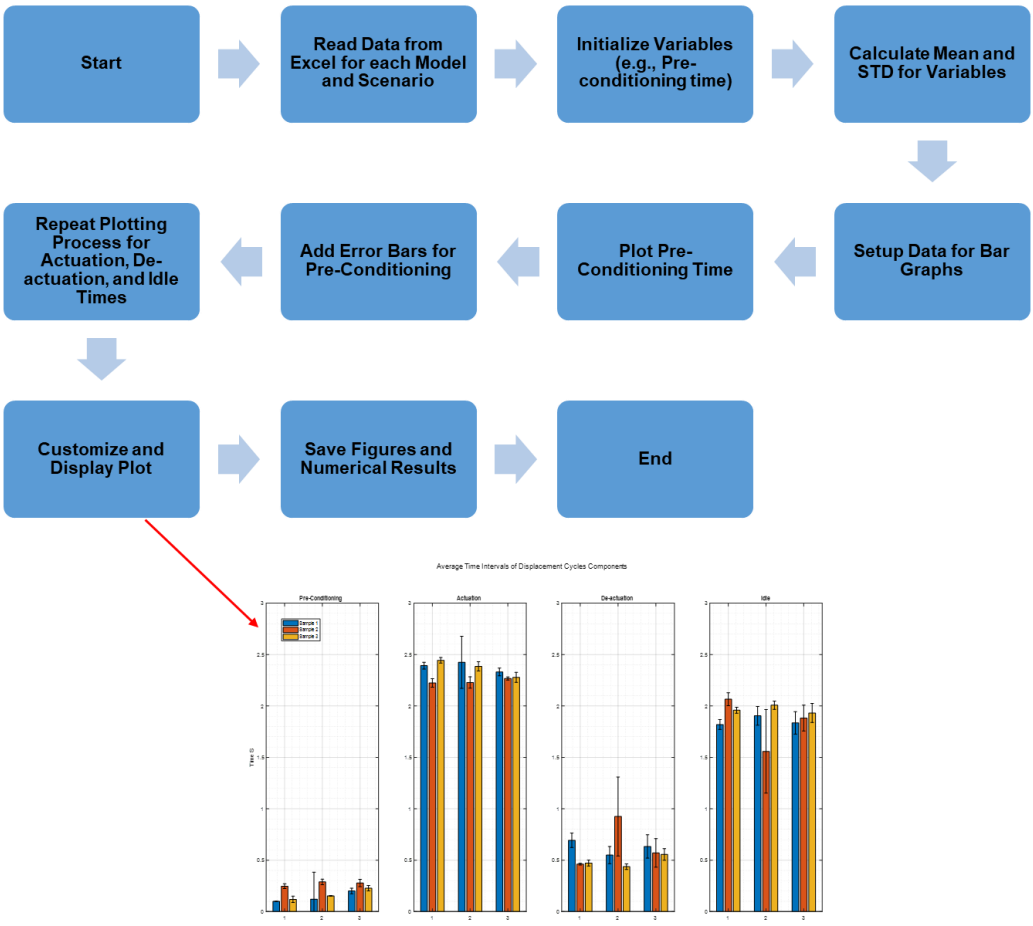

Figure 5-13: Flowchart of the Code-3 for data processing (with using the time interval analysis as an example).

5.1.4 Results

5.1.4.1 Cyclic Tests

In the results section of the block force test, the data output type chosen for analysis primarily includes charts. The charts present a detailed visual representation of the cyclic and static test data. Cyclic tests involve subjecting SAM to repeated pressurizing and air releasing cycles.

Main Charts (5-14 and 5-15)*:*

For each test, three charts were generated to comprehensively capture the data. The first chart (5-14) offers a synchronized display of pressure and load cycles. The second chart (5-15a), derived from the first chart, overlays seven sequential cycles,

facilitating an assessment of cycle variations and repeatability. The third chart (5-15b), derived from the second chart, presents an average and standard deviation calculations of the overlays seven sequential cycles.

In this study, three different SAM designs (Model-1, Model-2, and Model-3 shown in Figure 5-1) were examined. Each design was tested under varying conditions, including four three frequencies and four pressure levels, resulting in a total of 144 test conditions. According to the outcomes across different samples and three figures per each test (First, Second, and Third charts), a total of 432 figures were generated for this initial analysis (main charts), making the analysis thorough and extensive.

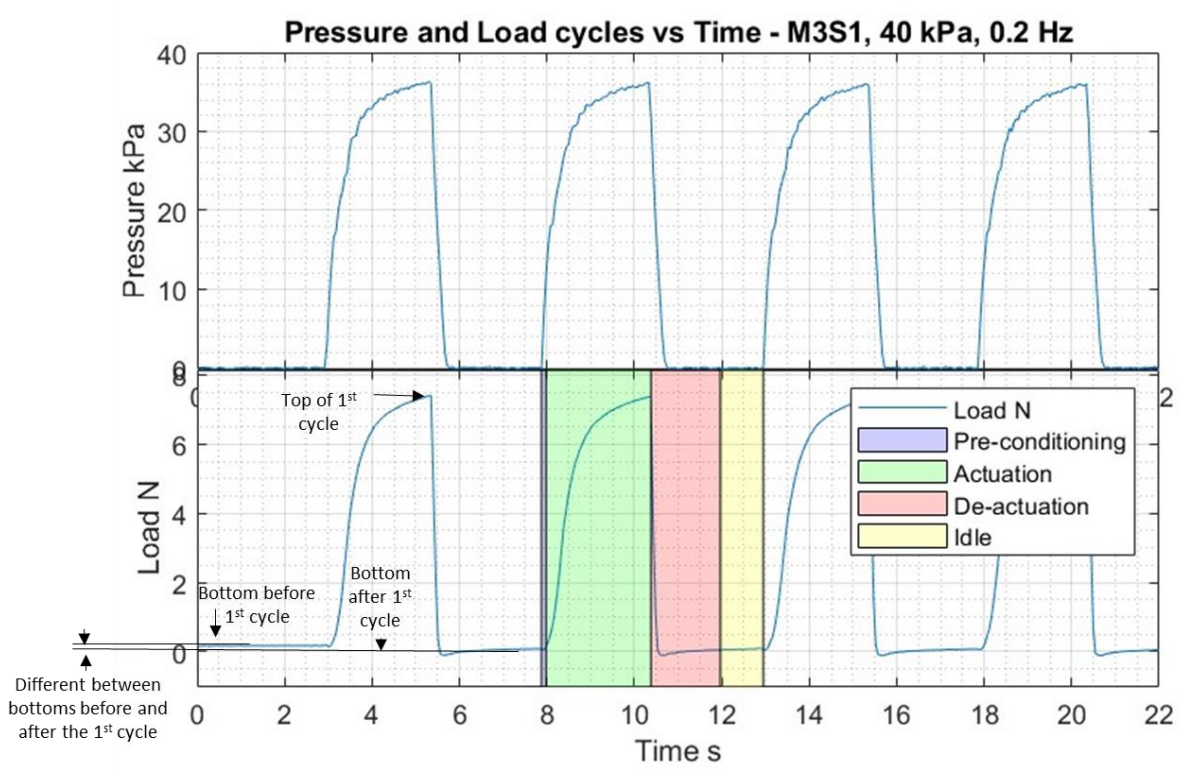

Figure 5-14: Synchronized display of pressure and load cycles, featuring color highlights that distinguish cycle components, including pre-conditioning, actuation, de-actuation, and idle phases.

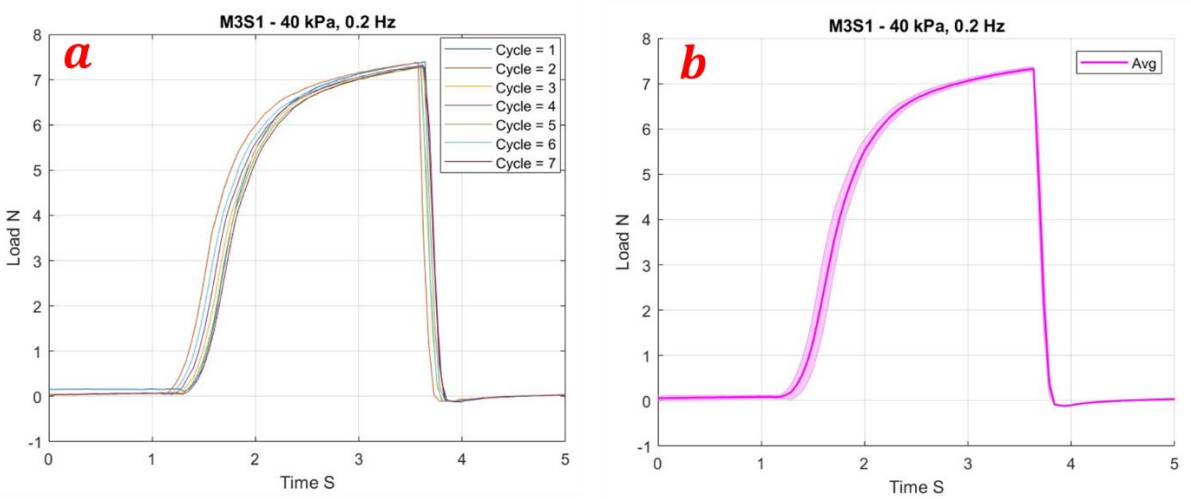

Figure 5-15: a) derived from 5-14, overlays seven sequential cycles, facilitating an assessment of cycle variations and repeatability and b) derived from (a), presents an average and standard deviation calculations.

Main Charts (5-14 and 5-15) - ***Observations****:*

The pre-conditioning state begins when the pressure is activated spend short duration, where it is ranging between 0.052 s to 0.4 s at 0.2 Hz. A slight decrease in load is seen to occur immediately after pressure activation, indicating an initial expansion in SAM before the start of the contraction movement. This initial expansion is sudden, generating a minor negative force directed toward the load cell. This pattern repeats consistently throughout all load cycles. In the actuation period, there is minimal or no delay between pressure and load peaks. The de-actuation period shows a quick and sharp drop below the average bottom, responding to pressure release. The idle period represents a steady state, with the pressure source remains inactive, and the effect of the de-actuation response has ended.

Figure 5-14 shows consistent results across all samples through all cycle components (pre-conditioning, actuation, de-actuation, idle). Additionally, Figure 5-15a shows high repeatability between the load cycles, as evidenced by the tight overlay of the seven sequential cycles. The consistency in the load patterns across different cycles indicates minimal variation, suggesting reliable performance under the test conditions. In Figure 5-15b, derived from Figure 5-15a, presents the average load cycle with the STD represented by the shaded area, showing clearer confirms for the high repeatability.

5.1.4.1.1 Pressure Effect

The first comprehensive comparison of the block force test results involved a fixed frequency of 0.2 Hz, with pressure variations at 20, 40, 60, and 80 kPa. The analysis considered all the samples for the three SAMs' models. The resultant data is presented into line graph and bar graph charts. The line graphs for all the samples, comprehensively showed in Figure 5-16, presents the average load cycles with STD. To facilitate the comparison, the y-axis of all charts is unified. This approach, together with the schematic drawing for the models within charts, summarizes and illustrates an extensive data set in a visual form.

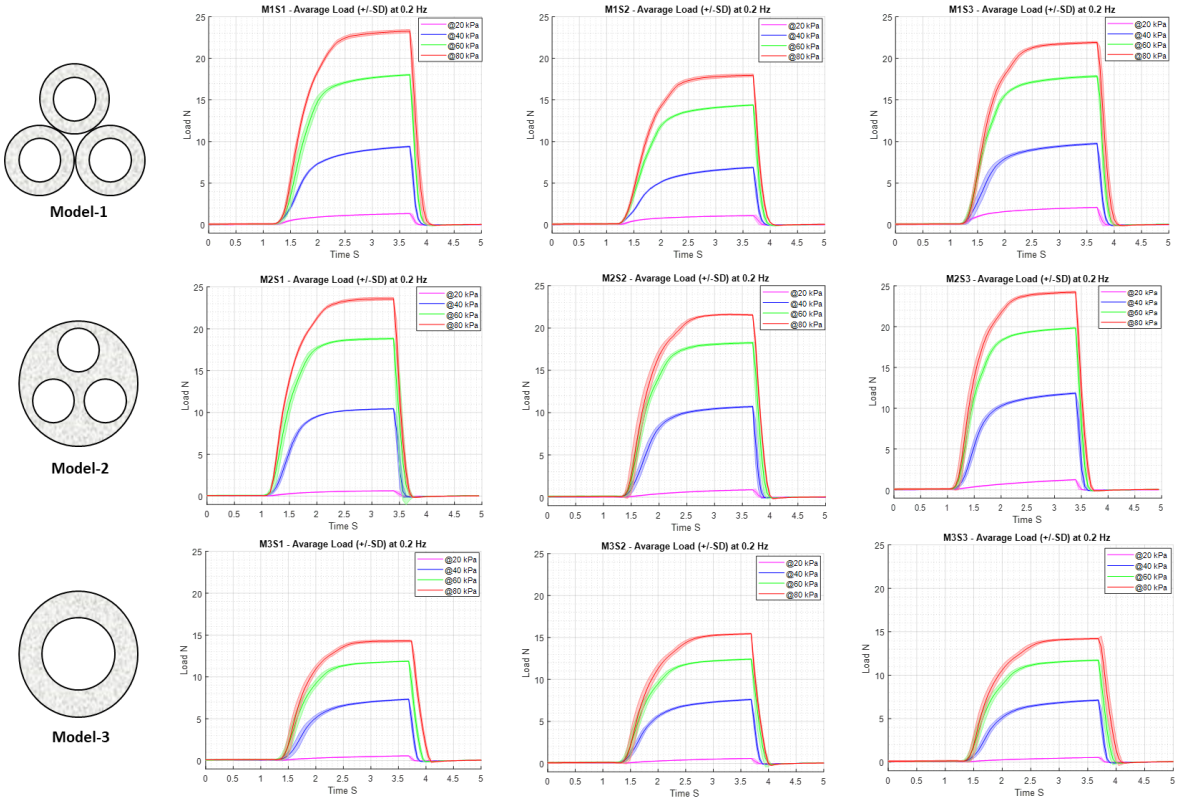

Figure 5-16: Comprehensive comparison of the block force test results involved a fixed frequency of 0.2 Hz, with pressure variations at 20, 40, 60, and 80 kPa.

*<u>Dynamic</u> load of SAM's Models Across Pressure Levels - **observations**:*

Several key observations can be achieved from the analysis of Figure 5-16. Firstly, there is a significant correlation between the pressure level and the amount of

generated force. As the pressure increases, the force also increases, highlighting a positive relationship between these two variables.

Additionally, the generated force in Sample-2 of Model-1 is noticeably lower compared to Sample-1 and Sample-3. This discrepancy may be occurred due to defects in the fabrication process. As Model-1 is a more complex design, it is more likely to contain fabrication variation affecting its repeatable performance. Conversely, the simpler design of Model-3 makes it more likely to exhibit repeatable behaviour among the samples.

The three models can be ranked in the following order, from highest to lowest generated force, Model-2 > Model-1 > Model-3. Furthermore, it can be noted that the variance in generated force between Model-1 and Model-2 is more pronounced at a pressure of 60 kPa compared to 40 kPa. This happened because SAMs often exhibit more responsiveness at higher pressure levels.

The SAM's contraction force also changes at various rates depending on the pressure level. For instance, the charts clearly show a sharp increase in force as the pressure rises from 20 kPa to 40 kPa and similarly from 40 kPa to 60 kPa. However, the rate of force increases when pressure is raised from 60 kPa to 80 kPa is relatively minor.

Lastly, STD between the load cycles, represented by the shadow area in the charts, is minimal for all samples. However, this STD tends to increase as the pressure levels increase, indicating the impact of pressure on the consistency of load cycles. These observations provide valuable understanding about the performance of SAMs in response to varying pressure conditions.

Peak load of SAM’s Models Across Pressure Levels:

Bar charts in Figure 5-17 show the average maximum generated force for the pressure of 20, 40, 60, and 80 kPa, all at a frequency of 0.2 Hz. Each chart within the figure displays load values for three model samples under specific pressures. The difference between Figure 5-16 and Figure 5-17 lies in their focus, where Figure 5-16 illustrates overall data of average load cycles, while Figure 5-17 focus on providing a comparison of peak values among samples of each model under various pressures. The y-axis for the four charts is unified to clarify the comparison between the samples' performances under various pressure.

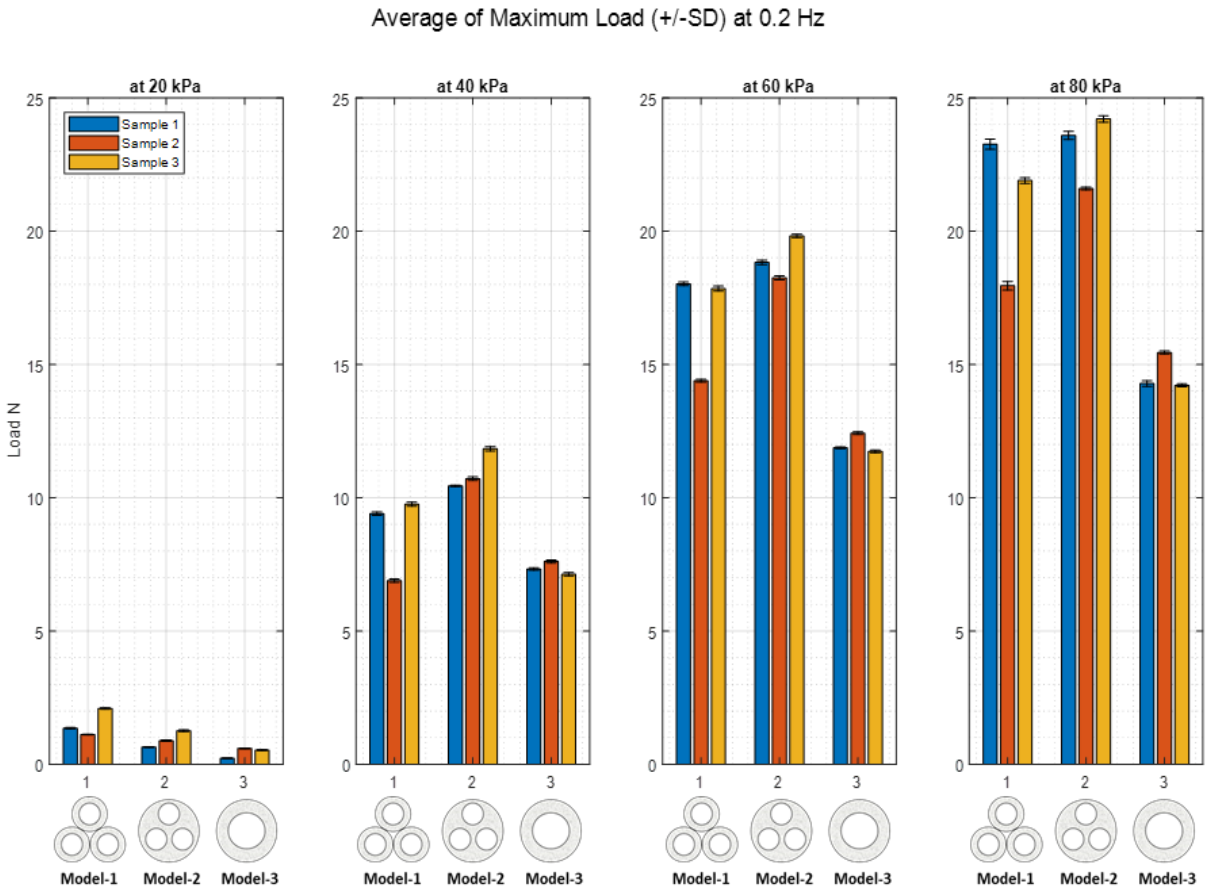

Figure 5-17: Four separate bar charts of the peak resultant force, with each chart corresponding to input pressure levels at 20, 40, 60, and 80 kPa.

*<u>Peak</u> load of SAM's Models Across Pressure Levels - **Observations**:*

Figure 5-17 shows several important insights into the performance of the SAMs' models. It is observable that the pressure significantly affects the amount of the generated force since when the pressure increases, the force increases. Model-3 demonstrates minimal variation in the generated force, mainly due to its simple design, which results in the smallest deviation between samples during fabrication and testing.

Model-2 generally exhibits good repeatability, with minor variation between its samples. However, as the pressure increases, the variation between samples also increases, indicating the sensitivity of Model-2 to higher pressure levels.

At 20 kPa, the models exhibit the following ranking in terms of decreasing generated force: Model-1 > Model-2 > Model-3. However, at pressures higher than 20 kPa, the order is reversed to Model-2 > Model-1 > Model-3. These observations highlight the

importance of understanding each actuation condition to be able to predict SAM behaviour under varying pressure scenarios.

The STD of repeated cycles for all samples at 20 kPa is the lowest, signifying greater stability and repeatability at lower pressures. In contrast, STD is the highest at 80 kPa, indicating more variability and inconsistency in performance. However, the variation in STD between the samples at 40 and 60 kPa is not relatively high, suggesting a relatively stable performance within that pressure range.

All samples from the three models were tested across various conditions. Initial test results indicate that Model-2 (with three cavities in a cylindrical soft body) and Model-1 (featuring three soft filaments in a tube shape) generally generate higher forces compared to Model-3 (consisting of a single larger soft tube with a single cavity). These findings at that stage led to further investigation into the reasons behind the significant difference in force generation between the first two models and Model-3.

One aspect explored was the internal surface area of the cavities within each model. Calculations of the internal surface area show that Model-1 and Model-2 have a larger internal surface area compared to Model-3. This observation suggests that the internal surface area might directly influences the generated force. It appears that as the internal surface area increases, the generated force also increases. Further insight into this phenomenon will be provided in the detailed analysis in the upcoming results section of this chapter that allow deeper understanding.

5.1.4.1.2 Frequency Effect

In the second comprehensive comparison of block force test results, the analysis is conducted under consistent conditions of 60 kPa pressure while varying the actuation frequency between 1, 0.5, and 0.2 Hz. This analysis includes the same outcomes of the cyclic tests, with three samples tested for each model. Additionally, the output data is presented in the same form of charts, providing a deep understanding of the SAM's behaviour under different frequency scenarios. The analysis is structured into two layouts. The first layout (Figure 5-18) comprises nine separate charts, each featuring four-line graphs that show the whole actuation and de-actuation behaviour of the SAM under different frequencies. The second layout (Figure 5-19) presents four separate bar charts, with each bar chart representing only the maximum load at the specified actuation frequencies.

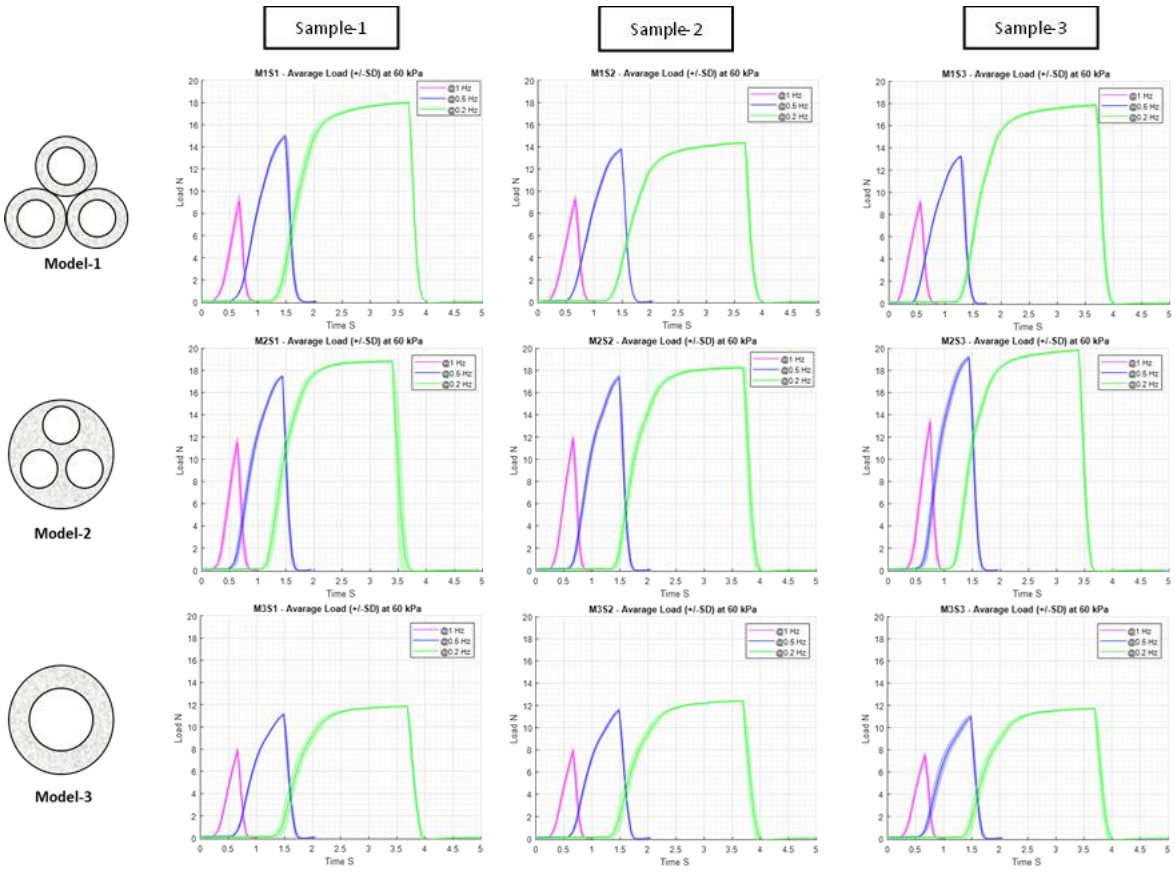

Figure 5-18: Comprehensive comparison of block force test results, the analysis is conducted under consistent conditions of 60 kPa pressure while varying the actuation frequency at 1, 0.5, and 0.2 Hz.

*<u>Dynamic</u> load of SAM's Models Across Frequency Levels - **Observation**:*

The observations drawn from the comprehensive line graph figure highlight several key findings. Firstly, it is clear that actuation frequency significantly influences the generated force; with a decrease in frequency resulting in a longer time to reach peak actuation. At 1 Hz, it is notable that the time is insufficient for all samples to reach their maximum actuation capability, indicating a frequency-related effect on actuation. Additionally, when the actuation run at low frequency like 0.2 Hz, Sample-2 of Model-1 exhibits lower generated force than Samples 1 and 3. However, at 0.5 Hz, the generated force for Sample-2 is more comparable to that at Samples 1 and 3, suggesting a potential deviation with Sample-2's actuation performance when fast actuation.

The curves at 1 Hz appear relatively symmetric around the peak point, resulting in similar actuation and de-actuation times. Conversely, curves at 0.5 and 0.2 Hz are less symmetric, leading to a longer actuation time compared to de-actuation. At lower frequencies (0.5 and 0.2 Hz), SAM has more time to respond to the applied pressure during actuation, allowing for more gradual inflation. In contrast, de-actuation (the return to its original state) often occurs more quickly as it is aided by the release of pressure, which accelerate the process. At higher frequencies (1 Hz), the SAM has less time to fully respond, causing more symmetry in the actuation and de-actuation phases as both happen relatively quickly due to the rapid cycling of pressure. Furthermore, the design of Models 1 and 2 could provide them with larger internal areas for the soft component cavities, enhancing their force-generating capability. This is notable at both low and high frequencies.

Finally, standard deviation (STD) between the load cycles, represented by the shadow area, is generally minor for all samples, indicating consistent performance and repeatability with frequency variation. Model-3's samples exhibit greater repeatability among the samples, likely due to its simpler design.

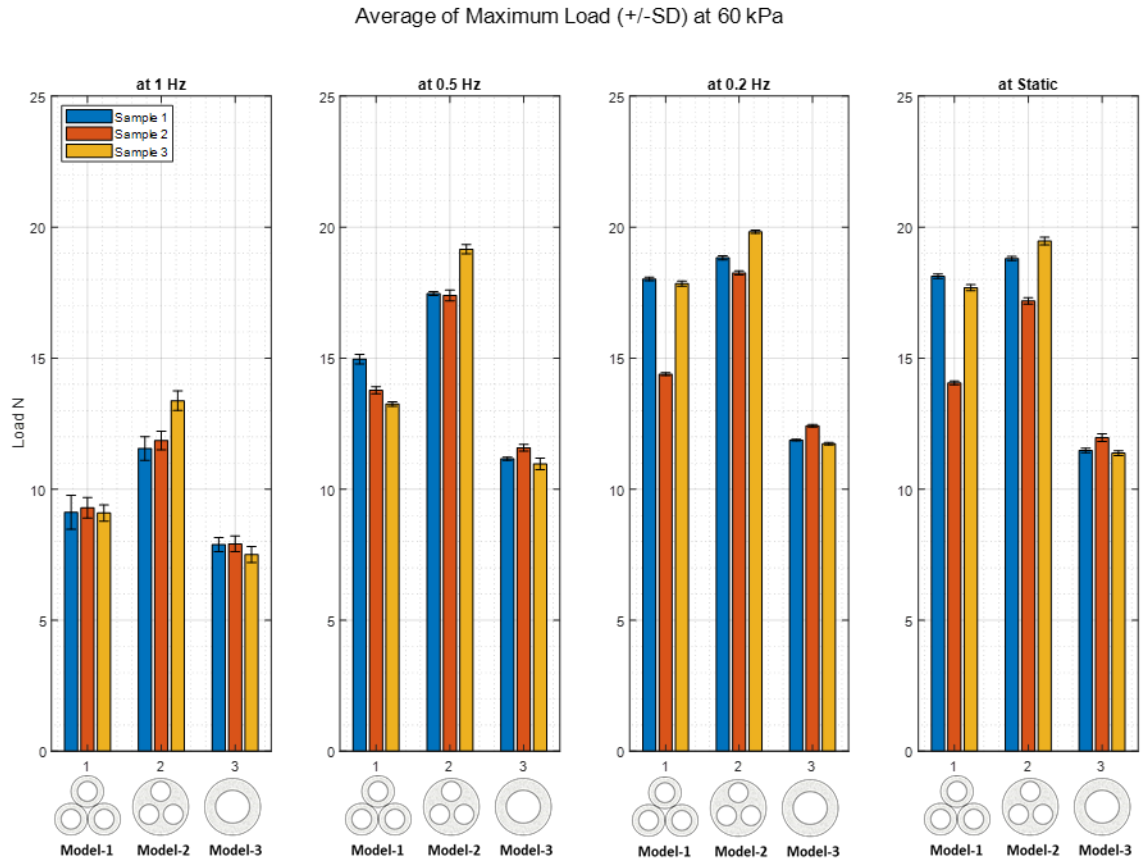

Figure 5-19: Four separate bar charts of the peak resultant force, with each chart corresponding to the actuation frequency at 1, 0.5, and 0.2 Hz.

<u>Peak</u> load of SAM's Models Across Frequency Levels - Observation:

The observations obtained from Figure 5-19 provide a clear understanding for the effects of varying frequencies on the generated force. For instance, the repeatable output between samples at various frequency show the consistency and reliability of the data, indicating it can be relied upon for further analysis and conclusions.

The maximum generated force (Peak) between frequencies of 0.5 Hz and 0.2 Hz appears quite similar, with a higher range at 0.2 Hz due to the extended time periods of actuation. However, the data for Model-1, shows a noticeable deviation in the maximum generated force between frequencies of 0.5 Hz and 0.2 Hz. This suggests that Model-1 requires a longer duration to reach its peak capability. In contrast, Model-2 and Model-3 exhibit consistent increase between frequencies of 0.5 Hz and 0.2 Hz.

At a frequency of 1 Hz, Model-1 and Model-3 display high repeatability. However, as the frequency decreases, Model-1's repeatability reduce, while Model-3 consistently maintains a high level of repeatability. This suggests that despite Model-3 generating

the lowest force, its simple design makes it more likely to achieve consistent performance across both comparisons (pressure effect comparison and frequency effect comparison).

Comparing the average of the maximum generated force among the models across all frequencies, Model-2 consistently surpasses Model-1 and Model-3. The rank order remains Model-2 > Model-1 > Model-3 under all frequency conditions, emphasising the impact of SAM's configuration variations on force generation.

STD observations over the bar graphs indicate that STD increases with higher frequencies. For instance, at 1 Hz, the STD is noticeably larger than at 0.2 Hz for all models. This difference reflects the impact of faster oscillations, as seen in the 1 Hz case, on the repeatability of the results.

5.1.4.1.3 Time Interval

In this third comprehensive comparison of the results of cyclic block force tests (shown in Figure 5-20), a detailed examination of time intervals is conducted. The analysis focuses on a specific testing condition which is actuation at a frequency of 0.2 Hz and pressurization at 60 kPa, considering all the samples. This layout consists of four bar charts that provide the time intervals of the various components within a load cycle, including pre-conditioning, actuation, de-actuation, and idle phases. Each bar represents the interval of the average of seven load cycles. These bar graphs facilitate an overall comparison for the SAM's models and assessing their time characteristics.

*Comparative Analysis of Load Cycle Time Intervals - **Observations**:*

In the observations obtained from the time intervals layout graph, several key findings are identified. First, when comparing the average time intervals of the load cycles among the samples, it becomes clear that Model-1 exhibits the shortest duration during the pre-conditioning state. This signifies that Model-1 initiates actuation more rapidly than the other models. This behaviour appears due to the configuration of the soft component in Model-1, which features three soft filaments with a larger overall diameter, resulting in a tighter braided sleeve over the soft component.

Moving to the actuation state, all models produce similar results, although Model-1 shows slightly longer time. Notably, the variation between samples and the STD bars (STD bars represents the variation between the cycles) are minimal during the pre-

conditioning and actuation phases. This is explained by the gradual actuation process when the SAM is pressurized, leading to increased stability and repetitiveness among samples and cycles. In contrast, the de-actuation phase experiences a sudden pressure drop, causing a sharp data decrease and lower data consistency.

Another thing to notice is how the pre-conditioning and actuation stages are connected. When the pre-conditioning time increase, the actuation time decrease, and vice versa. The same relationship applies to the de-actuation and Idle states, where longer de-actuation durations lead to shorter idle durations, and vice versa. The preference is for a shorter de-actuation duration and a longer idle state, indicating a faster settling of the SAM after the de-actuation phase. Analysing the bar graph shows that Model-1 achieves this transition to the idle state more rapidly compared to Model-2 and Model-3.

The delay between the internal pressure and the load cycle is considered by measuring the time between their peaks. One important observation is the minimal to no delay between the peak of pressure and load, indicating a high coincidence between the two cycles.

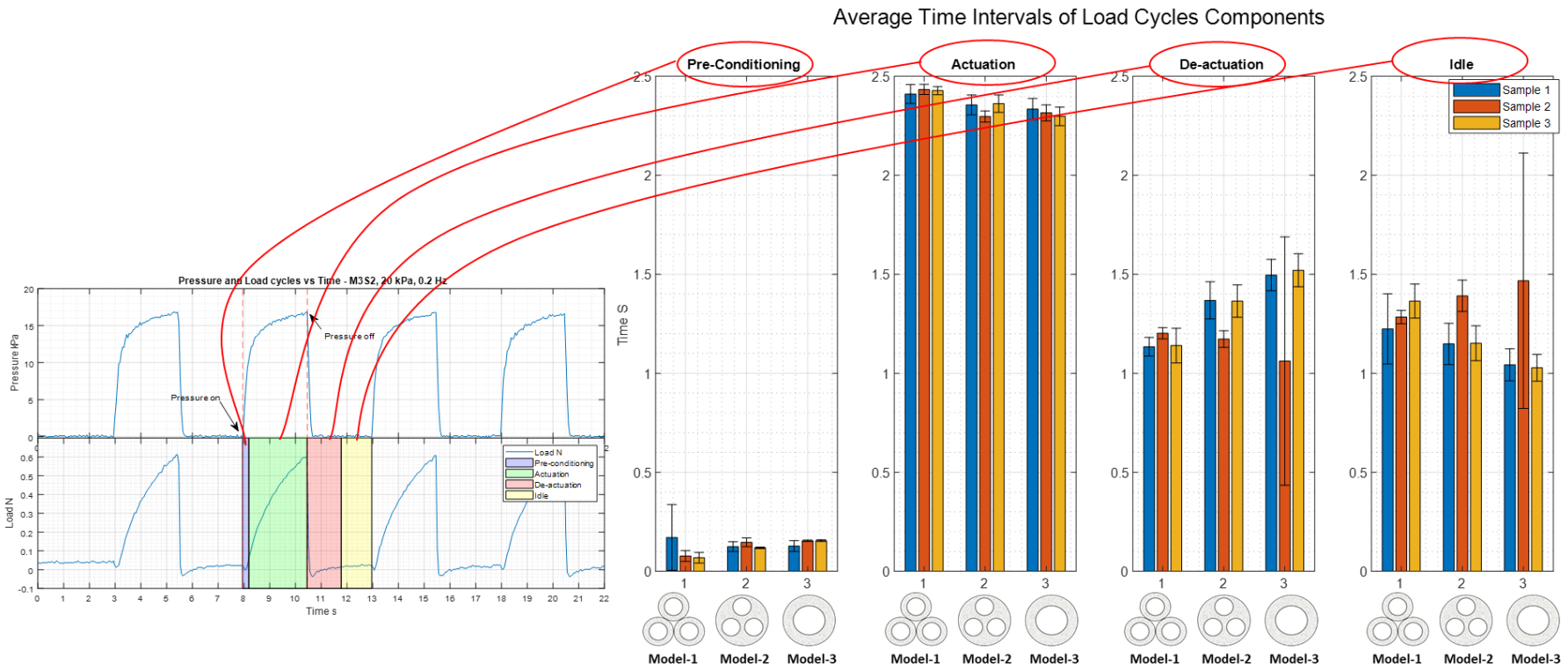

Figure 5-20: Comprehensive comparison of the time intervals results for the cycles of the block force tests at a frequency of 0.2 Hz and pressurization at 60 kPa.

5.1.4.2 Static Tests

The analysis in this section is focused on static actuation under a constant pressure of 60 kPa. The figures included in this analysis provide a detailed insight into the performance of SAMs' models during static actuation. Figure 5-21 comprises nine charts that synchronize line graphs, representing internal pressure and load static actuation. These charts use colour highlights to distinguish different cycle components, such as pre-conditioning, actuation, peak, and de-actuation phases. This figure allows for a comprehensive understanding of SAM's models behaviour under static actuation conditions.

Figure 5-22 shows six separate bar charts, each representing different data points: peak, maximum, last peak, average peak, standard deviation of peak, minimum point, and average idle. Each chart has nine bars, offering a comprehensive evaluation of SAM's performance characteristics during static actuation. Lastly, Figure 5-23 shows a bar graph chart that provides the time intervals of the static loading cycle component, helping to analyse how SAM behaves over time during static actuation.

*Static load of SAM's Models at 60 kPa - **Observation**:*

The internal pressure during the tests nearly reaches 60 kPa, especially because the pressure in the static test is held for a longer duration, allowing enough time to meet the input pressure (Internal pressure: is the measured pressure through the test while Input Pressure: is the pressure that applied from the pressure supplier). The only exceptions are Sample-1 and Sample-2 of Model-2 since they are slightly lower than the input pressure with average pressure of 57.03 kPa for Sample-1 and 56.38 kPa for Sample-2. Despite this, these two samples still generate a high force, even when compared to the generated force by Sample-3 of Model-2. In Sample-3 of Model-2, the Internal Pressure meets the Input Pressure all through the period of the peak actuation.

By looking to both the pressure and load graphs shown in Figure 5-21, we observe consistent behaviour across all the samples of the three models. In the pressure graphs, it takes around 12 seconds for the internal pressure to reach a level that is very close to the maximum input pressure. Once it reaches the maximum pressure, it remains stable until the pressure is stopped, which indicates the stability of the pneumatic system within SAM.

In the load graphs, the components of the load cycles (pre-conditioning, actuation, peak, and de-actuation) show consistent behaviour for all samples. The pre-conditioning interval is very short, and during the Actuation interval, the load gradually increases until it reaches its maximum point. The load is then held steady during the Peak interval until the pressure is stopped. The maximum point of the peak interval usually occurs in the first quarter. However, there might be a slight unobservable decrease in the load in the middle of the peak interval, it quickly returns to stability. In the de-actuation interval, the load undergoes a rapid and steep drop, going below zero, and then it gradually adjusts until it reaches the idle condition.

Conducting the static load experiment offers the advantage of assessing the behaviour of the SAM under constant pressure. The very minor range of load fluctuations across all SAM models reflects the reliability of using them in soft robotics applications that require high stability.

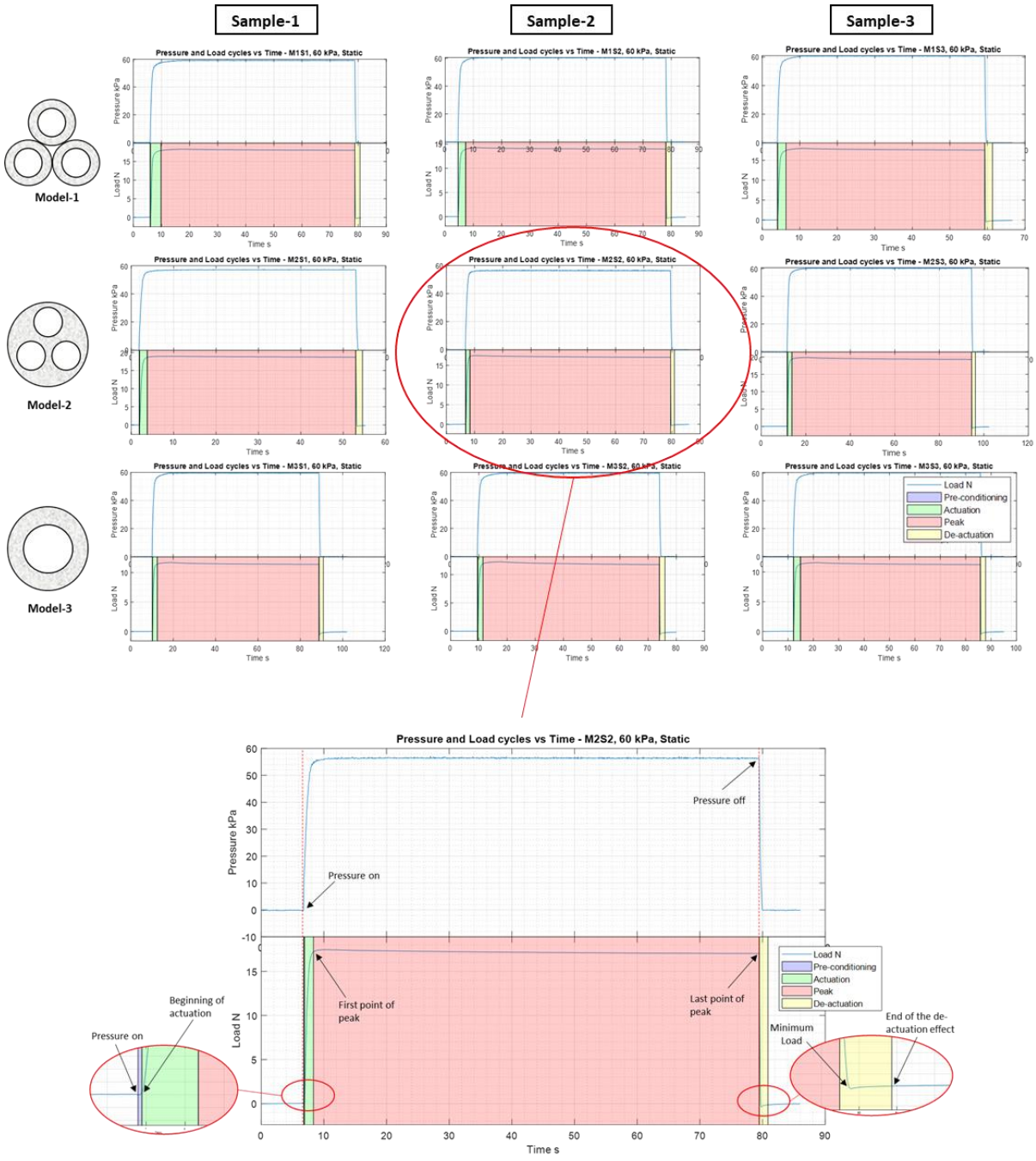

Figure 5-21: Synchronize line graphs representing internal pressure and load static actuation at pressure level of 60 kPa. These charts use color highlights to distinguish different cycle components, such as pre-conditioning, actuation, peak, and de-actuation phase.

Peak Events at Static load of SAM's Models at 60 kPa:

Figure 5-22 comprises six separate bar charts, each focused on different data points: the first point of peak, maximum point, last peak point, average of peak, standard deviation of peak, minimum point over the entire cycle, and average of idle. Wider

insight is presented here for several data points with more focuses on studying SAM's models within the peak region. These bar charts, each featuring nine bars, allow a collective evaluation of SAM's detailed performance characteristics in static actuation scenarios. Only the "Average of peak" has a standard deviation as it represents an average of multiple points, unlike the other data points that show single values.

*Peak Events at Static load of SAM's Models at 60 kPa - **Observation**:*

In Figure 5-22 when the load at 0.2 Hz (cyclic) is compared to static pressure, it is clear that they are very similar, with just a bit more load at 0.2 Hz. This happens because at static pressure, the peak interval is longer, and the maximum value is calculated by averaging several points during this time. Furthermore, the observation shows that the STD is slightly larger at static pressure for the same reason. Among the samples, Model-3 shows the best repeatability among the samples followed by Model-2, and then Model-1.

The bar graphs, covering the entire peak region from start to finish, display very similar values. This shows a convergency from the first peak point to the maximum point and all the way to the last point, highlighting the stability in this region. The notable low STD at the average of peak supports this idea, showing the SAM's consistent performance in the peak region.

Normally, the highest point in the peak region is following the first peak point. This pattern is observed across the SAM's samples. It's also important to mention that the last point in the peak region consistently has lower values than the average.

During static actuation, the minimum load occurs just after the pressure is released at the start of the de-actuation phase. This pattern is consistent across all samples, highlighting a characteristic feature of the SAM's behaviour during this phase. There is no noticeable variation in the measured minimum load among the samples.

In static pressure tests, the load during the idle phase does not return to the starting point (zero) but shows a slight deviation below zero. This is due to hysteresis, a common feature in soft actuators, where the force generated during loading and unloading varies. However, in cyclic tests, only the first cycle consistently shows a minor deviation in the idle phase, while the following cycles are highly repeatable.

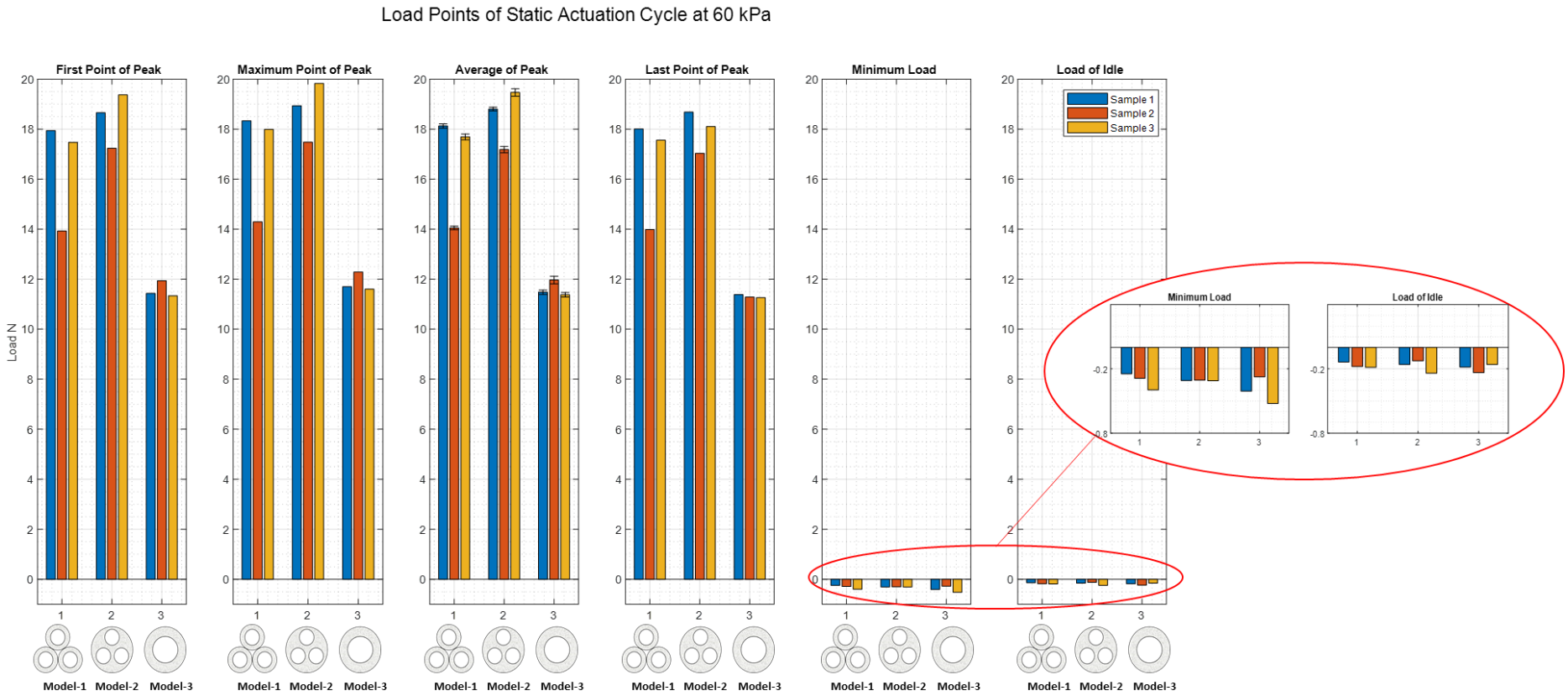

Figure 5-22: Six separate bar charts, each dedicated to specific data points: the first point of peak, maximum point, last peak point, average of peak, standard deviation of peak, minimum point over the entire cycle, and average of idle.

Comparative Analysis of Static Load Time Intervals:

The time intervals for the static loading cycle components are displayed in Figure 5-23 in a bar graph chart. Differences exist between the static pressure experiments and cyclic experiments (frequency). In static pressure experiments, time intervals are measured within a single actuation cycle. In contrast, in cyclic experiments (frequency), measurements are derived from the averages of 7 cycles, excluding the first cycle. Consequently, there are no STDs displayed here on the bar graphs, as STDs within the cyclic experiments reflect variations between load cycles. Furthermore, it is important to note that all time intervals (pre-conditioning, actuation, and de-actuation) show different results when compared to the cyclic experiments.

*Comparative Analysis of Static Load Time Intervals - **Observation**:*

The observations from Figure 5-23, in the pre-conditioning interval, the models show varying durations, with Model-1 requiring the least time for pre-conditioning, followed by Model-2 and Model-3. A shorter pre-conditioning duration enhance a faster actuator response, which is a desirable behaviour in soft robotics applications. Conversely, in the Actuation interval, Model-2 is the fastest, followed by Model-3 and Model-1. Shorter actuation times mean quicker achievement of the actuator's maximum capability.

In the de-actuation interval, Model-2 again is faster, with Model-1 and Model-3 following. Shorter de-actuation durations mean the actuator reaches the idle state more rapidly. These comparisons highlight that Model-2 has higher ability at reaching its maximum force-generating capability and transitioning to idle mode quickly, which is a desirable performance. In contrast, Model-3 takes longer time to achieve these two metrics, proving that using multiple cavities is an effective technique for enhancing soft actuator performance in term of force and speed of response.

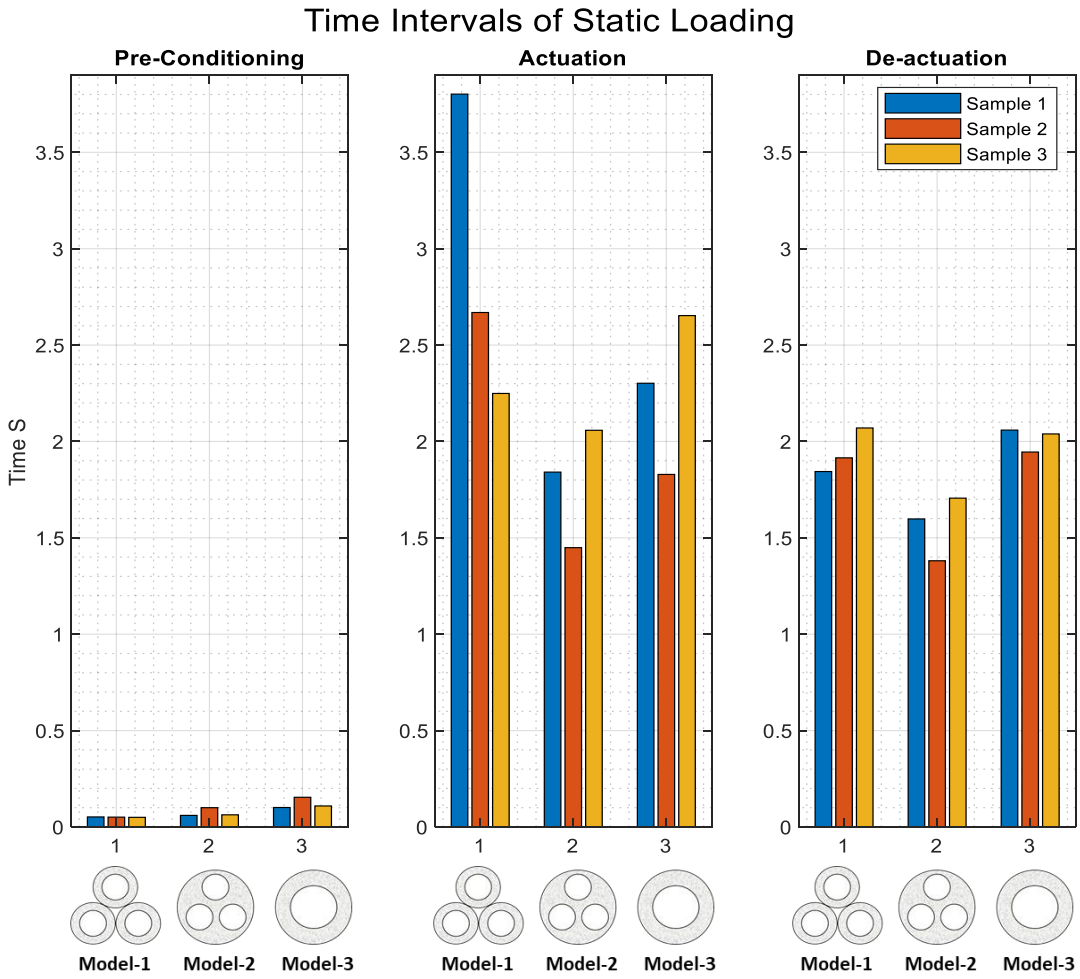

Figure 5-23: The time intervals associated with the static loading cycle components, pre-conditioning, actuation, peak, and de-actuation phases.

5.1.4.3 Summary of Key Observations

Model Performance:

- Model-2: Consistently generated the highest force across most pressure levels and actuation frequencies.
- Model-1: Produced slightly lower force than Model-2 but higher than Model-3. The larger internal surface area in Model-1 and Model-2 compared to Model-3 could be a factor in their higher force generation.
- Model-3: Generated the least force but with least variability due to its simpler single-cavity design.

Pressure Effect on Force Generation:

- Force Increase with Pressure: All models exhibited significant force increases with higher input pressures. For example, Model-2's force increased by approximately 90% when pressure was raised from 20 kPa to 60 kPa.
- Model-1's Tighter Fit: At lower pressures (20 kPa), Model-1's tighter fit within the braided sleeve led to higher force generation compared to Model-2 and Model-3. However, this advantage diminished at higher pressures.
- Consistency: Higher pressures resulted in increased STD, which means more variability in performance.

Frequency Effect on Force Generation:

- Force Consistency: Higher actuation frequencies resulted in greater variability (STD) in generated force, in other word, reduced repeatability at higher frequencies.
- Model Sensitivity: Model-1 showed greater sensitivity to frequency changes, while Model-2 and Model-3 maintained more consistent performance.

Time Intervals Analysis:

- Pre-conditioning and Actuation Times: Model-1 had the shortest pre-conditioning time, while Model-2 and Model-3 had shorter actuation times. This shows different response speeds among the models.
- De-actuation and Idle Times: Model-1 transitioned quickly to the idle state post-de-actuation that highlight its rapid settling after de-actuation.

Force Generation Under Static Conditions:

- Load Comparison Between Static and Cyclic: When the load at 0.2 Hz (cyclic) is compared to static pressure, it is clear that they are very similar, with just a bit more load at 0.2 Hz.
- Internal Pressure Stability: The internal pressure during the static tests remained stable, closely matching the input pressure that means a reliable pneumatic system within the SAMs.
- Peak Load Behaviour: The maximum load was typically reached quickly during the peak actuation phase and remained stable until pressure release.

- De-actuation Phase: Load rapidly decreased post-pressure release, stabilizing to a slightly negative value due to hysteresis effects common in soft actuators.
- Time Interval Analysis: Model-1 required the least time for pre-conditioning, while Model-2 achieved the fastest actuation and de-actuation times, highlighting its efficiency in transitioning between states.

5.1.5 Discussion

The variation in the generated force indicates that the design of the soft component has a direct impact on the amount of the generated force. Model-3, represents the traditional simple model of SAM in soft robotics, generates the least force, which mean that the force performance can be improved through developing the soft component design. However, this research proposes Model-1, made of multiple soft filaments, as a novel SAM that expected to generate the highest force. The common conceptual design between Model-1 and Model-2 is that they both have multiple cavities. Both models generated high force, and they were close to each other. Having multiple cavities might have various effects. First, it can enhance the interaction between the chambers of the soft components which might lead to generate higher force. Second, the larger internal surface area in Model-1 and Model-2 compared to Model-3 could be a factor in their higher force generation. It is important to note that the internal surface area refers to the exposed surface inside the cavities, while the wall thickness refers to the material thickness of the soft component itself. As discussed in Chapter 4, the sectional areas of the cavities and wall thicknesses in all three models are equal, ensuring similar volumes of cavities and soft materials across the models. However, this does not guarantee equal internal surface areas of the cavities because the variation in cavity shapes and configurations in each model impacts the total internal surface area, even when their volumes are equivalent.

Notably, 20 kPa represents a relatively low pressure for SAM actuation, providing a valuable data for evaluating their performance under conditions of low-state actuation. The outer diameter of the soft component in Model-2 and Model-3 is identical, and they both fit inside the same braided sleeve. In contrast, the soft component (three filaments) of Model-1 has a larger outer diameter, causing them to be more tightly packed in the braided sleeve. The outer diameter of the soft component of Model-2 and Model-3 is 10.39 mm, while it is 12.93 mm for Model-1 as shown in Figure 5-1. Consequently, under low pressure conditions like 20 kPa,

Model-2 and Model-3 generate less force because this pressure is not sufficient to cause soft component expansion that can overcome the resistance of the braided sleeve. However, at pressures higher than 20 kPa, the soft component expands sufficiently, causing the braided sleeve to contract significantly. This effect of tightening the soft component inside the braided sleeve, as seen in Model-1, becomes more pronounced at low pressure and diminishes at higher pressure.

Based on the load tests of SAMs found in the literature, the generated forces vary widely, ranging from 12 to 700 N. In contrast, this research found that the force generated by SAMs under a static pressure of 60 kPa ranged from 11 to 19 N. This discrepancy is expected due to the use of different soft materials, braids, components, testing methodologies, input pressures, and other factors in various studies.

From the previous observation, it can be stated that increasing pressure and decreasing frequency both lead to an increase in the generated force. Comparing graphs where pressure and frequency are held constant, it becomes evident that altering the pressure has a more pronounced impact than changing the frequency (within the selected levels of pressure and frequency). For instance, in Model-2, the comparison of 0.2 Hz and 1 Hz frequencies shows a 30% increase in the average maximum generated force, from 12.5 N to 18 N. In contrast, when the pressure is changed from 20 kPa to 60 kPa, the force increases by approximately 90%, rising from 1.8 N to 18 N. This observation emphasizes the significant influence of the level of the input pressure on the generated force by SAM.

Static tests allow us to observe the behaviour over a longer duration. It is noted that the internal pressure generally takes sufficient time to reach the input pressure level. However, some samples, such as Sample-1 and Sample-2 of Model-2, did not reach the input pressure of 60 kPa, showing a minor gap. This indicates possible issues within the SAM sample or the pneumatic connections. Nevertheless, this minor gap between internal and input pressure did not significantly affect the generated force. The actuator and its pneumatic activation system demonstrate resilience by maintaining good performance despite minor pressure inefficiencies.

The comparison of peak load measurements between the cyclic test at 0.2 Hz and the static pressure test shows that the loads are very similar, with the cyclic test showing a slightly higher load. This might occur due to the continuous application and release of pressure, which enhances the material's response. The static pressure test, with its longer peak interval, averages the maximum value over several points, resulting in a slightly lower average peak load and a larger STD.

5.2 Displacement Test

5.2.1 Introduction

This section continues the work done in Section 5.1, specifically in testing new aspect of how much SAMs can contract. The contraction test involves the evaluation of the same three SAM designs of Model-1, Model-2, and Model-3 (Figure 5-24). Each model is tested under different conditions, including four frequencies and four input pressure levels, amounting to a total of 72 test scenarios. Important details about the methodology of the displacement test are discussed widely in this section.

As detailed previously in the literature review chapter, methods in the existing literature do not fully capture the maximum contraction capability of the SAM due to the effect of tension [70]. This tension is generated by the weight usually or tension applied to the end of the SAM, which prevent a pure contraction movement without any load effect. This gap led to the development of a new methodology that provides clear insights into SAM free contraction behavior. It also enables a precise exploration of how various SAM model designs respond to different levels of pressure and frequencies.

The characterization analysis procedures aim to align with the force characterization methods, ensuring a consistent approach for evaluating SAM’s performance. An important outcome of these tests is the examination of actuation time that offers valuable insights into the contraction behaviour from various perspectives. This analysis allows users to choose a SAM model that suits the specific requirements of their application.

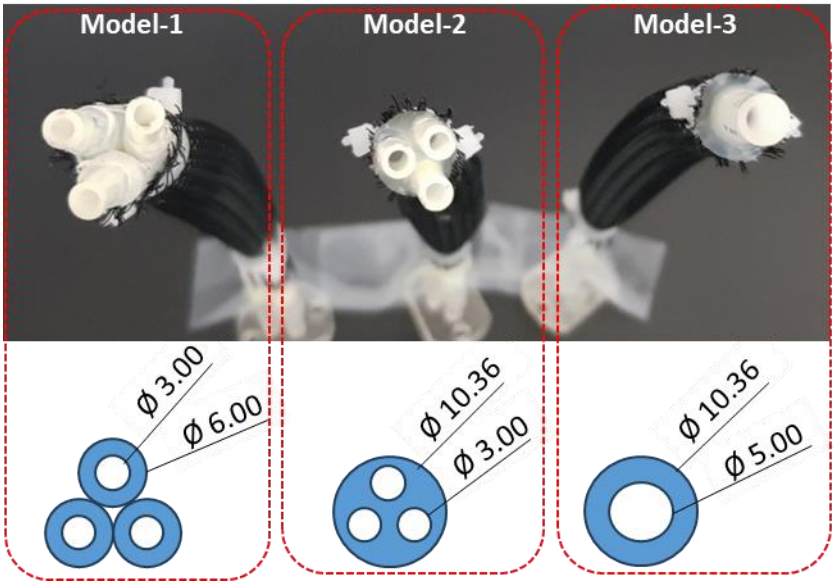

Figure 5-24: The developed SAM Models

5.2.2 Objectives

A set of goals is defined below to direct the displacement experiments. These objectives act as guidelines for exploring the behaviour of SAMs models and for comparing their displacement capabilities.

> **Objective 1**: Develop a testing methodology for determining the range of contraction (displacement) in SAM.
>
> **Objective 2**: Measure SAM capabilities in achieving a specific displacement under particular pressure or actuation conditions.
>
> **Objective 3**: Assess and compare the displacement performance of various SAM models.

By characterising the free response of the SAMs, this section contributes valuable outcomes to the primary goals of this research, enhancing our understanding of SAM models capabilities.

5.2.3 Experimental Setup

5.2.3.1 Development of the Test Setup

The progression from the initial version to the finalized setup involves significant enhancements. The setup evolves from its initial form to achieve an ideal (finalized) configuration, facilitating accurate measurements of SAM contraction. The initial setup took inspiration from previous research and was designed to efficiently conduct the displacement test [69]. A universal load tester (Instron 5943) machine serves as the frame for this test setup, allowing consistency by using the same frame for both the block force test and the displacement test and ensuring a uniform experimental environment.

A key challenge in creating the displacement test setup was identifying a precise method to measure the amount of contraction in SAM models. Figure 5-25 illustrates how the SAM's configuration changes during the activation. This axial contraction is the primary mechanism through which the SAM shortens during activation. However, because the SAM is a deformable body, the pressure inside it creates a radial expansion, leading to an increase in its diameter. This deformable nature can cause non-linear (not in a single degree of freedom) contraction and complicate accurate measurements.

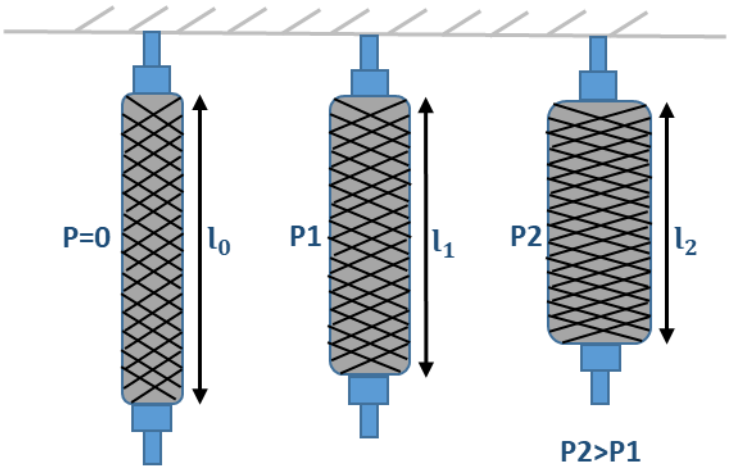

Figure 5-25: The changes in SAM's configuration according to the input pressure.

One approach that was evaluated to measure SAM's contraction is utilizing video analysis software that designed for assessing motion. This involves analysing and quantifying the captured video of SAM's contraction, allowing the observation of its

changes over time. Despite video analysis software provide useful tool for measuring the amount of contraction, it depends on the quality of the video, calibration, and the precision of manual annotations. Experimental models, especially those equipped with advanced sensors, can provide more accurate and precise data.

From the initial phases of developing this test setup, the IL-065 displacement sensor is utilized. A member of Keyence's IL Series, the IL-065 is an analogue laser displacement sensor made for precise distance measurements. Different IL Series models offer varied measurement ranges. Specifically, the IL-065 can accurately detect distances ranging from 55 to 105mm away from its sensor head, making it suitable for measuring the contraction of SAM. The IL-065 sensor is designed with a compact body, facilitating easy mounting in diverse experimental setups.

One of the experimental setups was established by placing the laser sensor on the lower holder of the Instron and hanging the SAM from the top holder (The Crosshead). The SAM was assembled in the Instron frame using the same method as in the block force test, using the same 3D printed adapters. To enable unrestricted contraction, no weight was added to the lower part of the SAM. A white circular acrylic plate was attached to the lower part of the SAM, serving as a target for the laser beam emitted by the laser sensor.

This experiment produced satisfactory outcomes as the laser sensor effectively measured the change in the SAM length. However, due to the lower part of SAM moving freely, the motion observed was not entirely linear. Pure linear motion, which involves movement along a single dimension with only one degree of freedom, is preferred. To achieve this, a customized equipment was utilized in the finalized testing setup. The following section will demonstrate the finalized setup for the displacement test, presenting a detailed methodology for assessing the pure linear contraction of SAM.

5.2.3.2 Test Setup

Figure 5-26 shows the setup of the displacement test for the SAM’s models. The frame of the Instron machine is ideal to assemble the setup of the displacement test and ensure a consistency in the environment test with the force test. The setup of the test comprises five overall 3D printed adaptors noted in Figure 5-26 with Adaptor-1, Adaptor-2, Adaptor-3, Adaptor-4, and Adaptor-5. The addition of these adaptors in the displacement test setup ensures precise alignment and secure attachment of the SAM, enhancing test consistency and reliability. Adaptor-2, specifically designed with outlets to feed pressure into the SAM. Also, the design of

the adaptors simplifies assembly and disassembly, allowing for easy adaptation across different models. More details about the adaptors are shown in the Appendix 5.

Adaptor-3 is connected to Adaptor-4 with screws that creates a connection between the lower part of SAM and the head of a key component in this setup called Cylindrical Piston. Adaptor-4 is designed in a cup shape in order to interlock the head of the Cylindrical Piston inside it (shown in Figure 5-26).

The Cylindrical Piston is a key mechanical component in the displacement test setup, providing frictionless movement along an accurate linear path. The purpose of using this component is to ensure that the movement caused by SAM contraction follows a precise vertical linear path without applying any external load or tension. In free contraction tests (without applying any load or using this technique), SAM may contract with minor lateral deviations, which do not precisely capture its contraction capability. To address this, the Cylindrical Piston prevents side movements, keeping the contraction along the axis of the SAM, ensuring one degree of freedom (1 DoF) motion and repeatability across different samples. Unlike contraction tests that apply tension to keep the SAM straight, this setup avoids the load effect, allowing for pure linear contraction without the influence of external forces or tension that could limit the SAM's full contraction potential.

The Cylindrical Piston is made of acrylic and has a frictionless shaft that can move linearly along the cylinder body. The head of this cylinder is a circular acrylic piece that is connected to Adaptor-4. The lower end of the shaft (from the bottom of the Cylindrical Piston) is adhered to a non-transparent circular acrylic piece used as a target surface for the laser beam. When SAM contract, it pulls the head of the piston linearly upward, which leads to move the circular target upward. The sensor's receiver detects the reflected laser light, which is influenced by the target's distance. An example of four sequential states of SAM's contraction from 0 to maximum level of contraction is illustrated in Figure 5-28.

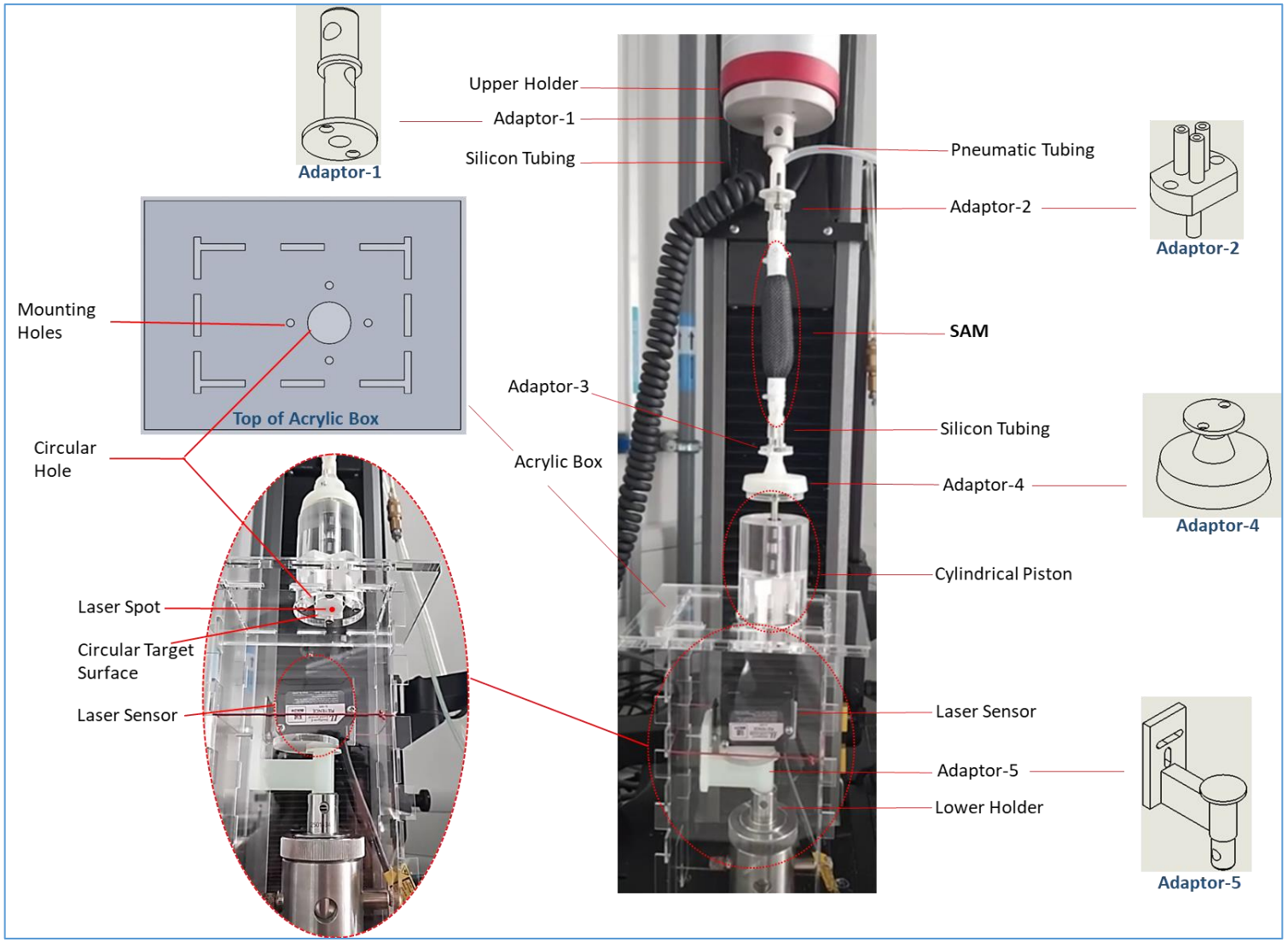

Figure 5-26: The finalized setup for testing the SAM's contraction within the Instron machine frame.

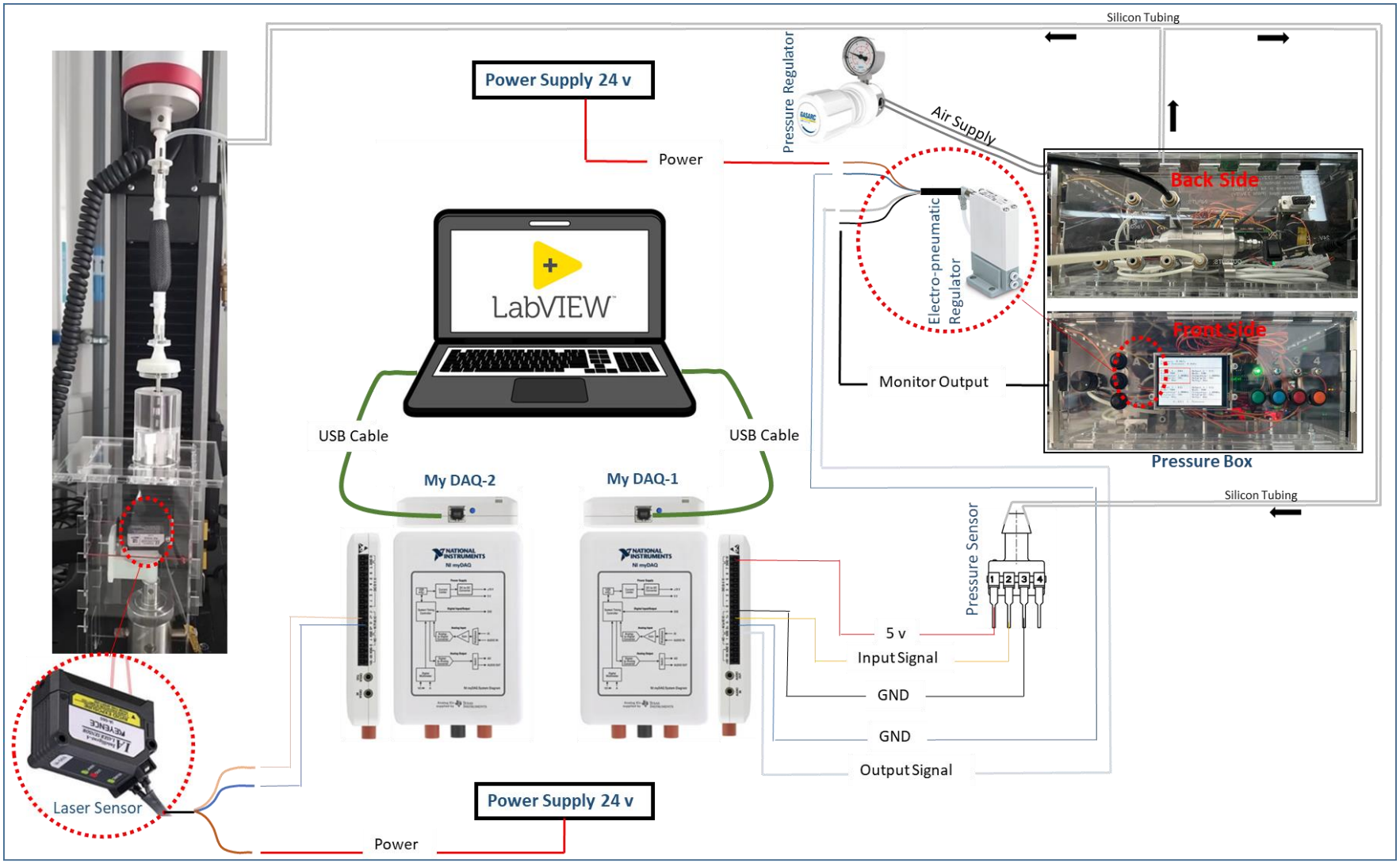

Figure 5-27: Comprehensive illustration of both the electronic and pneumatic circuits used in the optimum displacement test setup.

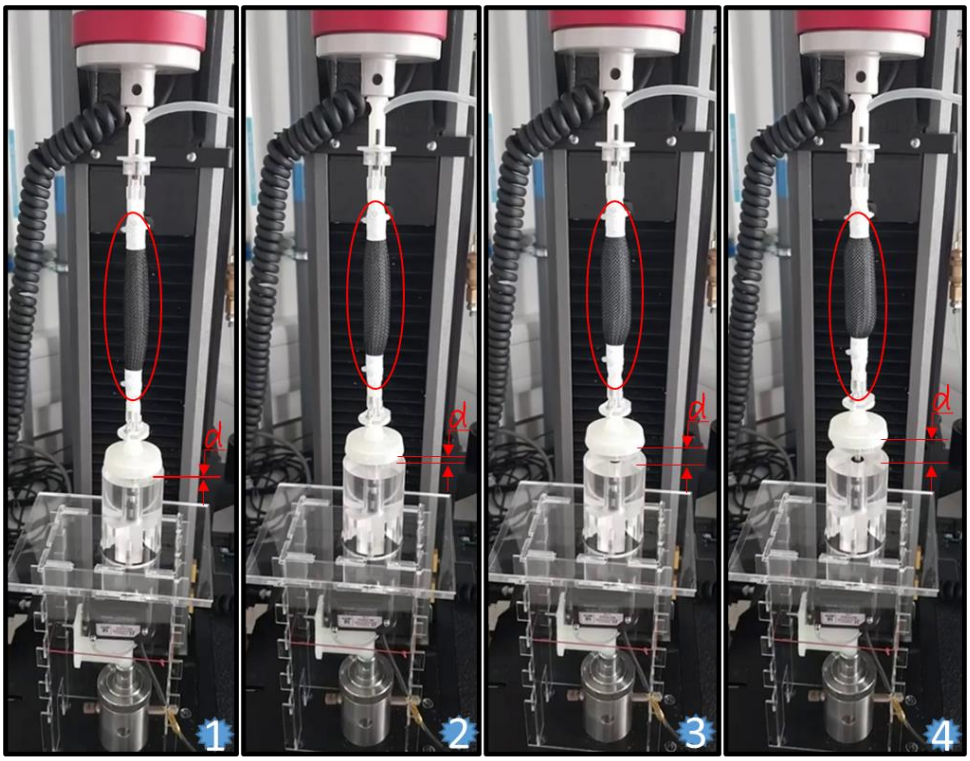

Figure 5-28: Four sequential states of SAM's contraction from zero to maximum level of contraction.

The Cylindrical Piston is placed over an acrylic box that manufactured by laser cutting machine. This acrylic box is created to mount the Cylindrical Piston in the designed position and to protect the laser sensor. By looking again at Figure 5-26, it can be seen that all the components of the setup are connected in a linear vertical line. The top surface of the Acrylic Box (Figure 5-26) used to secure the Cylindrical Piston onto the top of the acrylic box.

Figure 5-27 illustrates the comprehensive diagram of both electrical and pneumatic connections used in the displacement test setup. It's important to note that two DAQ systems are incorporated into the setup. This incorporation is necessary due to the limitation of analogue pins, which are insufficient to accommodate the required interfacing with all system components. Most of the pneumatic and electric connections of the displacement station's testing and control system remain consistent with the same components of the force test. The laser sensor receives a return pulse that is reflected from the target. The laser sensor precisely measures the time that the travel of the emitted laser pulse spends to hit the target and return to the sensor. The sensor calculates the distance to the target using the equation:

$$distance = \frac{(speed_{light} \times time)}{2}$$ Equation 15

The equation is divided by 2 because the laser pulse implements a round trip to the target. The calculated distance is then sent as a conditioned voltage to the DAQ system device. The conditioned signal is sent to the DAQ system through a direct wiring, where it arrives as an analogue signal. This data is then shown on the LabVIEW software, providing a synchronized recording of laser displacement measurements with the time and internal pressure signal.

In the calibration process, SAM is removed from the setup and Adaptor-4 (the cup) is joined with screw directly to Adaptor-1 to move the target upwards and downwards through the Cylindrical Piston. The laser sensor is calibrated by measuring voltage readings at known distances, which are set by adjusting the position of the Instron' Crosshead. Each increment is carefully documented by recording the corresponding voltage readings.

Figure 5-29 provides a line graph of laser sensor voltage readings and their associated measured distances. To ensure accuracy, the data points were collected through 10 repetitions. These data points were then used to create a calibration curve. This calibration curve was created through curve fitting, employing linear fitting in Excel. The goodness-of-fit was evaluated using the R-squared value, which was zero, indicating that the voltage data obtained by the laser sensor was perfectly linear with the proportional increase in distance. This process resulted in the derivation of a mathematical equation that effectively models the data points $y = 20x$.

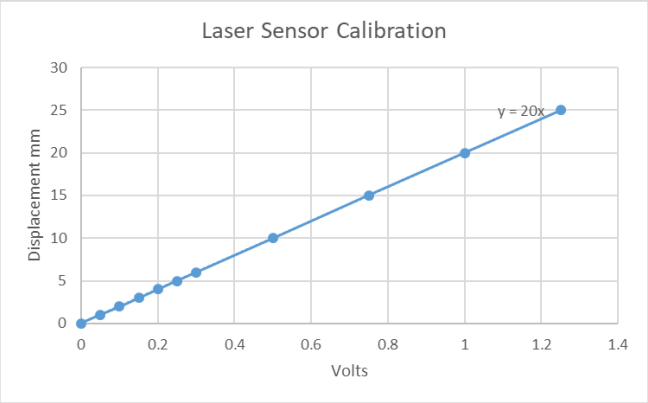

Figure 5-29: Laser sensor voltage readings and their corresponding displacement.

Precise control of the Electro-pneumatic Regulator and the solenoid valve, along with their settings, is crucial for achieving the desired system performance. In these tests, the output mode is configured as Pulse Width Modulation (PWM) mode. The PWM was always set at a 50% duty cycle, indicating that the signal is on for half of the time and off for the other half. This consistent duty cycle ensures precise control of pressure along with the actuation frequency. The actuation frequencies varied with the same values used in the force characterization (Section 5.1). In the results section, there will be a graph of supply pressure vs. time, showing PWM mode and frequency for pressure control.

This configuration establishes a well-organized and controlled testing environment to allow precise control to achieve the desired displacement measurement. It ensures an accurate assessment of a pure linear contraction produced by SAM under different conditions. In addition, it ensures convenient process of assembling and dissembling SAM from the setup that contributing to efficient testing operations through easy replacements for the samples.

5.2.3.3 Displacement Test Procedure

The characterized SAM’s samples previously tested in the block force test are undertaken in this test as well. The characterisation is conducted on the three different SAM designs, Model-1, Model-2, and Model-3 as shown in Figure 5-1. Each sample is tested under various conditions that includes four various pressure levels actuating at 0.2 Hz and four various actuation frequencies pressurized at 60 kPa. This resulted in a total of 8 test conditions for each SAM sample, leading to 72 tests (8 test conditions x 9 samples). The outcomes from different samples and the creation of three figures per test (First, Second, and Third charts), resulting a comprehensive group of 216 figures across the main charts set that provide a thorough analysis.

This testing procedure identifying the steps for performing a displacement test on SAM using the finalized setup. The protocol is important as it creates guidelines for conducting a dependable and replicable displacement test to measure SAM's range of contraction. The test setup and protocol establish a precise and repeatable method for characterizing SAM. While there are existing research works outlining methodologies for SAM contraction, such as *Wereley et al.* [68], this protocol introduces distinctive elements, including the approach to assembling and disassembling the 3D printed adapter for connecting SAM to the testing setup.

Figure 5-30 presents a flowchart that outlines the steps for conducting this displacement test.

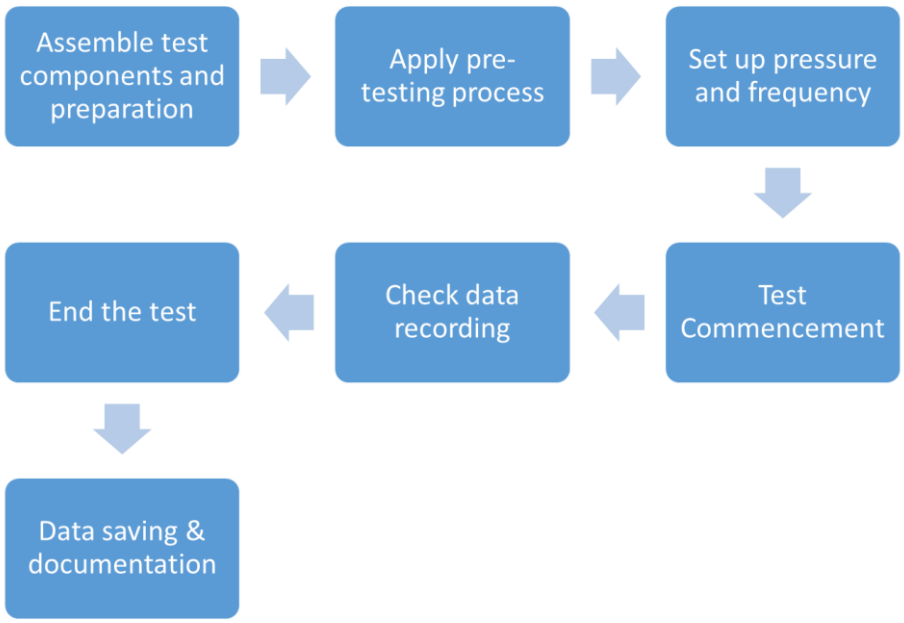

Figure 5-30: Displacement test procedure flowchart.

Procedure:

1. Initial Setup:
   To initiate the testing process, begin by assembling SAM in the Instron machine setup to secure it in place by attaching the adaptors with screws. It is important to interlock the head of the Cylindrical Piston inside Adaptor-4 cautiously to ensure even insertion for proper linear actuation. This interconnection guarantees the correct establishment of a pure linear contraction. Lastly, before starting the pre-testing, thoroughly check all components within the setup to ensure they are functioning correctly and ready to record data.
2. Pre-testing:
   The pre-testing phase is an important step in the SAM's sample testing process. The primary purpose of the pre-testing is to ensure a consistent displacement of the sample before the main test that offers a uniform starting point for each test.
   The pre-testing preparation begins after SAM assembly in the setup. The Instron machine's crosshead is manually moved downward via the Fine Jog until the Cylindrical Piston's head contacts the piston's main body. Due to the

structured distance between the laser sensor and the circular target, the laser sensor records negative distances (ranging from -0.5 to -1.8 mm) when the Cylindrical Piston's head contacts the piston's main body, as it is below the minimum range of 50 mm. Subsequently, the crosshead is adjusted upward until readings from the laser interface software approach zero. A brief waiting period is observed to account for potential relaxation in the SAM's soft components. If any distance readings change due to relaxation, the crosshead is readjusted to achieve displacement balance (zero displacement).

3. Setting up Pressure and Frequency:
   This stage commences by inputting the preferred pressure level into the LabVIEW program. This designated value will regulate the testing activation pressure. The data is transmitted as an electrical signal to myDAQ-1, which then sends the signal to the pressure box to adjust the pressure to the desired level. Concurrently, the desired frequency and actuation mode are set using the pressure box’s control panel.
4. Test Commencement:
   To commence the test, initiate the procedure by selecting the "start" button within the LabVIEW testing program to send the intended input pressure from My DAQ-1 and record the distance and internal pressure. Subsequently, press the "running" green button on the pressure box's control panel to initiate pressure supply from Pin-1.
5. Data Recording:
   Throughout the test, the key parameters are recorded that includes time, displacement, and pressure.
6. Ending the Test:
   All the conducted displacement tests are cyclic actuation, where the test ended after completing 10 actuation cycles. Once the cycles are complete, the test is ended following these steps:
   a. Press the green button in the pressure box (the same button used for activation) to stop the actuation.
   b. Stop the LabVIEW program to end receiving pressure data from the laser and pressure sensor.
7. Data Saving and Documentation:
   After completing the displacement test, synchronized data, including time (in milliseconds), displacement (in volts), and pressure (in volts), is stored as raw data in LabVIEW software. At the same time, all important experimental details, such as test setup details, test parameters, and the output results, are

documented. This guarantees an orderly documentation process to enhance the analysis of the test outcomes.

8. Next Sample Preparation:
   To prepare the next sample for the displacement test, SAM sample is dissembled from the constructed setup. This involves unscrewing the connected adaptors and gently detaching Adaptor-4 from the head of the Cylindrical Piston. Additionally, for the upcoming test, a new sample with a new balancing and pre-testing setup is arranged. These steps ensure a systematic return to the starting point of the previous test and setting the stage for a new test under similar conditions.

5.2.4 Data Processing

The procedure for processing raw data from the displacement test follows a protocol designed to be analysed. The purpose of outlining this data processing protocol is to simplify the process and derive valuable results that provide conclusions relevant to the study's objectives. Enhancing data analysis involves generating clear visual representations, such as graphs and charts.

The process involves a set of steps, including data collection, data calibration, data examination, and importing into MATLAB. These steps allow for a thorough analysis and visualization of the data, including tests that differ based on variations in samples and test conditions. Figure 5-31 presents a flowchart that outlines the steps for conducting the data processing of the displacement test.

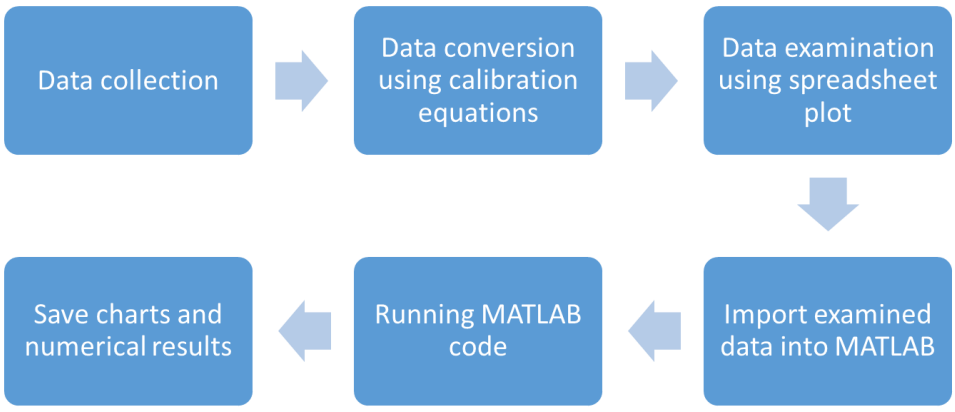

Figure 5-31: Flowchart for the data processing procedure of the displacement test.

Similar to processing data for the block force test (Section), MATLAB software is employed in the data processing of this test to generate analytical results. The analysis involves the same MATLAB codes designed for similar purposes, which were grouped into three types based on their specific goals.

5.2.5 Results

The processed data output type for analysis in the displacement test results section mainly comprises charts that provide a detailed visual representation of the cyclic test data. These charts illustrate the cyclic tests when SAM undergoes repeated cycles of pressurizing and air releasing.

*Main Charts (*Figure 9 and Figure 10)*:*

Collectively capturing the data for each test involved the generation of three charts. Figure 5-32, the first chart, provides a synchronized display of pressure and displacement cycles. Derived from the first chart, Figure 5-33a overlays seven sequential cycles to enable an assessment of cycle variations and repeatability. The third chart, Figure 5-33b, is derived from Figure 5-33a and presents the average and STD of the overlays from the seven sequential cycles.

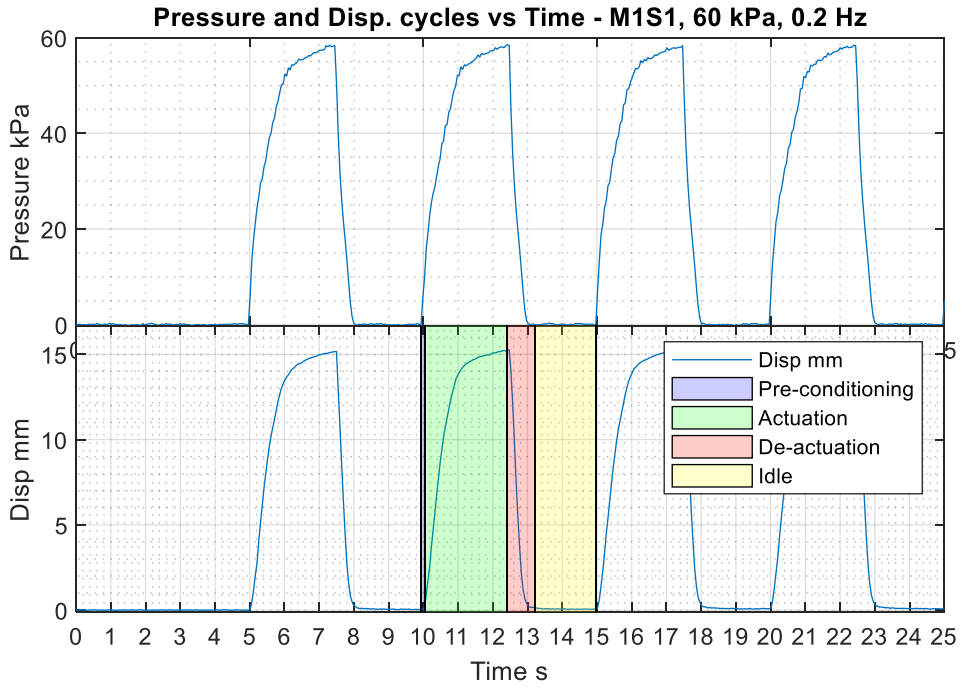

Figure 5-32: Synchronized display of pressure and displacement cycles, featuring colour highlights that distinguish cycle components, including pre-conditioning, actuation, de-actuation, and idle phases.

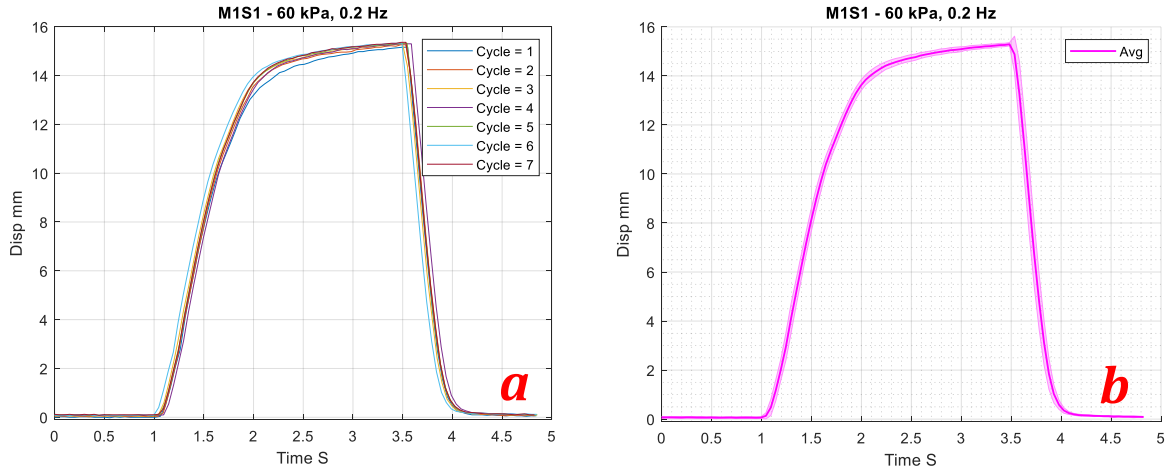

Figure 5-33: a) derived from Figure 5-32, overlays seven sequential displacement cycles and b) derived from (a), presents an average and STD of the seven cycles.

*Main Charts (*Figure 9 and Figure 10) - ***Observations****:*

In examination of the peaks of pressure and displacement, it is clear that there is a very small or no delay between them which is proof their near alignment. The drop from the peak displacement to the bottom is characterized by sharp and rapid decrease. However, unlike the load cycle behaviour, the displacement does not drop below the average of the bottom value in response to the sudden release of pressure.

Additionally, in the displacement cycles, we do not observe any slight decrease in displacement after the pressure is triggered, unlike the load cycles. This indicates that the phenomenon of minor expansion before contraction does not affect the movement of the SAM. It is important to note that there is a difference in how SAM is assembled for the load and displacement tests. In the load test, SAM is blocked from both ends to measure the block force. On the other hand, in the displacement test, SAM is blocked from the inlet end (upper side) and the closed end (lower side) is allowed to move freely in a linear manner.

The range of repeatability between the displacement cycles at one test is clearly evaluated in Figure 5-33a and b. In most of the samples, the curves of the cycles show repetitive patterns across all the cycle components (pre-conditioning, actuation, de-actuation, idle). This repetitive behaviour, along with the very minor STD, represent high stability in the output data of the displacement test.

In general, the displacement cycles are smoother and show fewer fluctuations compared to the load cycles. Moreover, the idle state is more stable and longer in the displacement graphs because the pressure source remains off, and the effect of the de-actuation response has already ended quicker.

5.2.5.1 Pressure Effect

In this first comprehensive comparison of displacement test results, the analysis focused on all the three model designs of SAM, each with three samples. The fixed frequency for this comparison is set at 0.2 Hz, while input pressure variations are applied at 20, 40, 60, and 80 kPa. This resulted in a total of 36 unique cases for examination (3 models x 3 samples x 4 conditions). The resulting data is visually presented through two collective layouts.

In the first layout, Figure 5-16, line graphs provide an overview of the complete actuation and de-actuation behaviour of the three SAM designs across the four input pressure levels. In the second layout, Figure 5-17, represents bar charts to show

only the peak resultant displacement for each SAM design, corresponding to input pressure levels of 20, 40, 60, and 80 kPa. To enable a straightforward comparison, the y-axis is standardized across all charts at 25 mm in both layouts.

*Dynamic Displacement of SAM's Models Across Pressure Levels - **observations**:*

From the analysis of Figure 5-34, several key observations can be made. Firstly, a notable correlation exists between the pressure level and the range of contraction. This indicates a positive relationship between these two variables, with the contraction increasing as the pressure rises.

In Model-1, all the samples show similar behaviour through the actuation cycles. Additionally, the minor STD reflect the high repeatability between the displacement cycles. However, Sample-1 provides slightly higher range of contraction under all the testing pressures.

Among the samples of Model-2, a noticeable similarity is clear. What sets them apart is the behaviour observed when Sample-2 is activated under 40 and 60 kPa, where it shows minor fluctuations occur in the average line graphs before reaching the peak point. These fluctuations indicate a slight degree of variability between cycles, particularly in the phase prior the peak. However, at the minimum pressure of 20 kPa and the maximum pressure of 80 kPa, the average line graph appears smooth. These minor fluctuations are not observed in any other samples, which indicates that the fluctuations may be attributed to issues in either the test setup, such as the connection with the 3D printed connectors, or the pneumatic system, such as the pressure regulator or tubing.

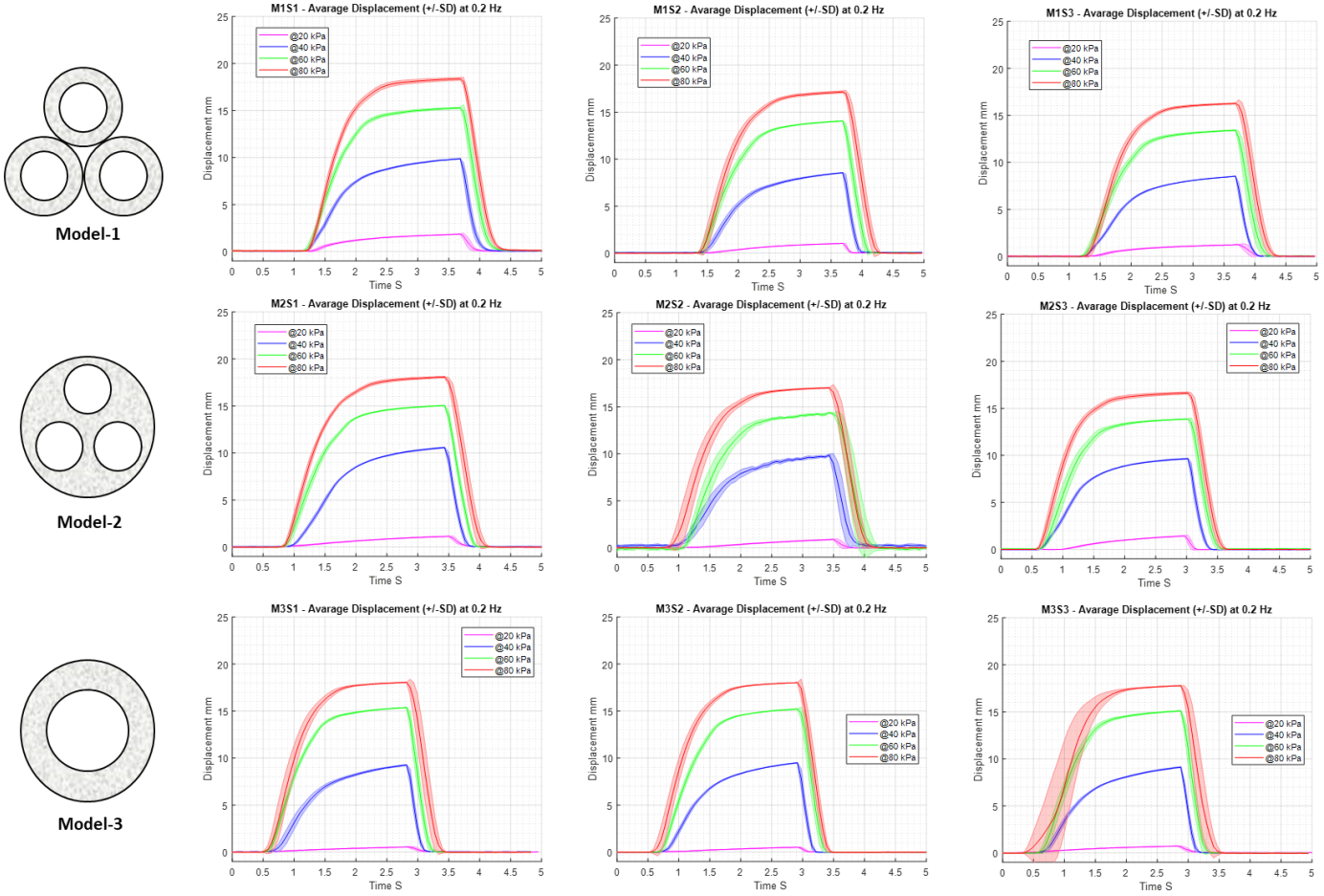

Figure 5-34: Comprehensive comparison of the displacement test results involved a fixed frequency of 0.2 Hz, with pressure variations at 20, 40, 60, and 80 kPa.

In the samples of Model-3, similar to the findings of the block force test, the contraction range of Model-3 samples shows the highest repeatability. However, it is worth noting that in Sample-3, there is a notably high STD in the actuation region. A high STD does not necessarily indicate a significant deviation between cycles, instead, it refers that one of the cycles is occurring before or after the other cycles. An advanced or delayed cycle does not necessarily indicate a deviation in SAM's performance but indicate a timing inconsistency within the pneumatic system. This inconsistency can be led by deviations in the valve or pressure regulator from the given signal wave, causing advance or delay the output pressure cycles.

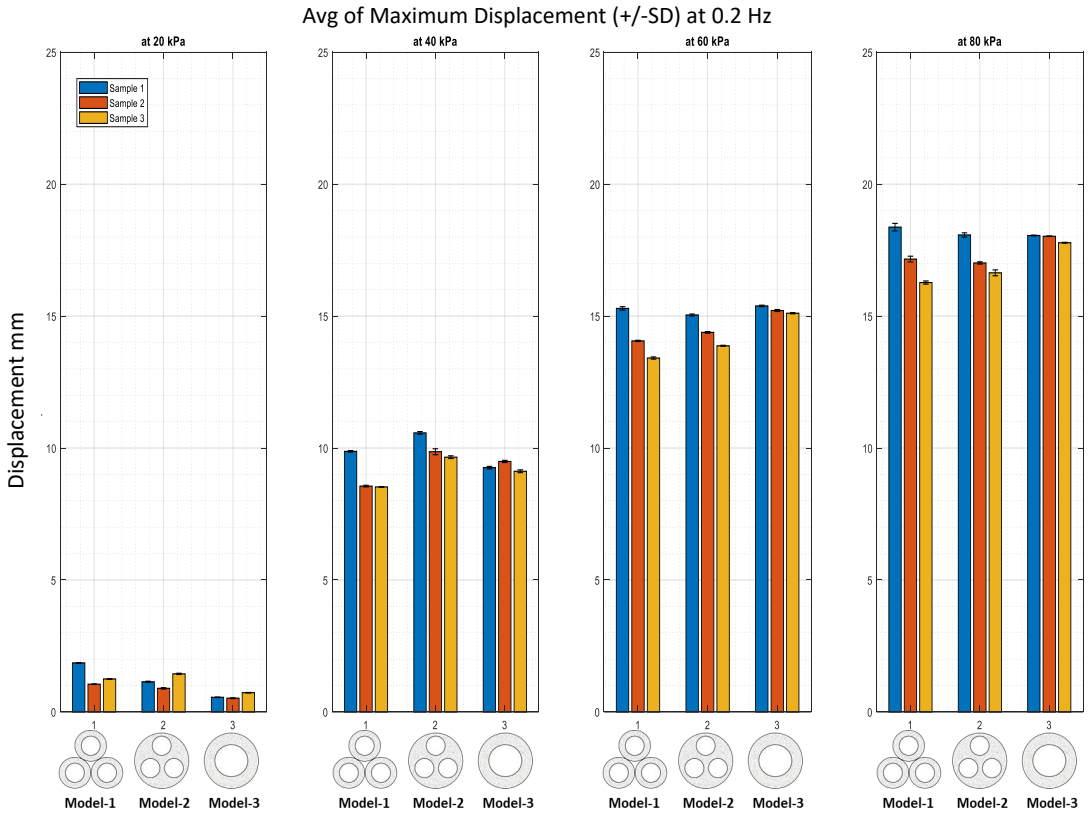

Figure 5-35: Four bar charts of the peak resultant displacement, with each chart corresponding to input pressure levels at 20, 40, 60, and 80 kPa.

*<u>Peak</u> load of SAM's Models Across Pressure Levels - **Observations**:*

In Model-3, as previously explained, there is minimal variation among the samples. This is particularly clear in the bar graph, where a single point (peak) is compared, as opposed to the line graph that involves comparing sets of points. This emphasizes the earlier explanation that Model-3 being the simplest among the

models, results in minimal variation between samples during the fabrication and testing processes.

The samples of Model-1 and Model-2 show good repeatability with minimal variation. Nevertheless, with an increase in pressure, the variation between the samples also rises. Moreover, it is noteworthy that the STDs of the displacement bar graphs are remarkably small for all samples, signifying a common high level of repeatability in the displacement cycles.

Under low pressures (20 and 40 kPa), the comparison of contraction ranges among the three models indicates that Model-1 and Model-2 slightly surpass Model-3. However, at high pressures (60 and 80 kPa), Model-3 slightly surpass Model-1 and Model-2.

Upon analysing both the line and bar layouts that aim to evaluate the effect of input pressure (constant frequency) on SAM's contraction range, it is evident that the results show the limited influence of changing the configuration of the soft component (SAM models) on SAM's contraction range.

5.2.5.2 Frequency Effect

In the second comprehensive comparison of displacement test outcomes, the examination performed under consistent conditions of 60 kPa pressure while altering the actuation frequency at 1, 0.5, 0.2 Hz and static actuation. The analysis is organized into two formats. The initial layout (Figure 5-18) involves nine distinct charts, each presenting four line graphs. The subsequent layout (Figure 5-19) involves four bar charts, each representing only the maximum displacement at specified actuation frequencies. Understanding how varying actuation frequencies impact the SAM’s performance allows to optimize its operation. This optimization is important for achieving the desired outcomes in different applications.

Before proceeding with this analysis, it is important to understand that the input pressure is a periodic signal consists of on and off states. Typically, the signal starts with the off state, and the pulse width of both on and off states is identical. Therefore, at 1 Hz, SAM actuates for 0.5 seconds and remains off for 0.5 seconds. At 0.5 Hz, SAM actuates for 1 seconds and remains off for 1 seconds. At 0.2 Hz, SAM actuates for 2.5 seconds and remains inactive for an equal duration of 2.5 seconds.

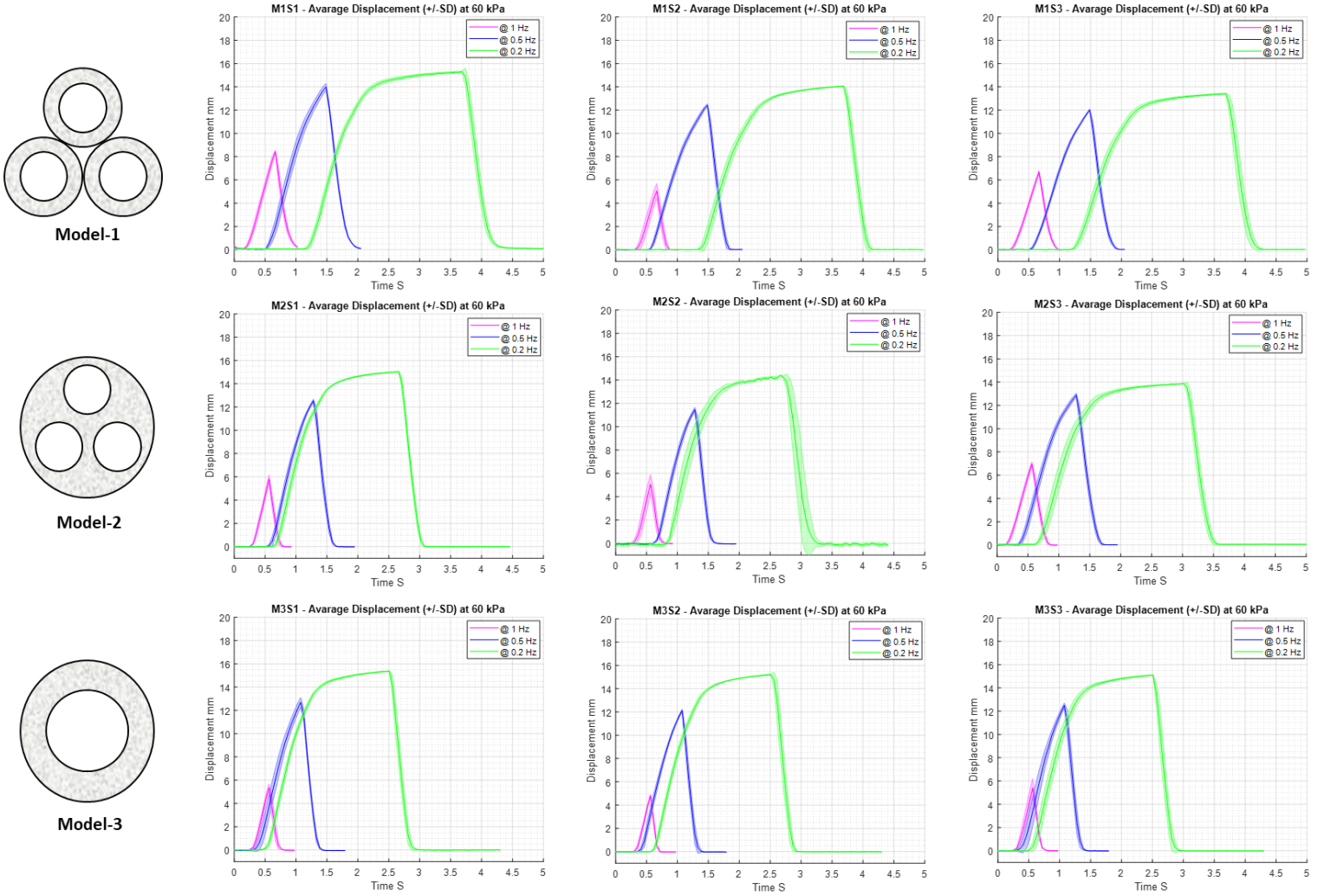

Figure 5-36: Comprehensive comparison of displacement test results, the analysis is conducted under consistent conditions of 60 kPa pressure while varying the actuation frequency at 1, 0.5, and 0.2 Hz.

*Dynamic Displacement of SAM's Models Across Frequency Levels - **Observation**:*

Among the models, Model-3 shows the highest repeatability. Despite the overall minimal STD between displacement cycles for all samples, Sample-2 of Model-2 exhibits a noteworthy high STD at 0.2 Hz, suggesting slight variations between cycles.

The influence of frequency on SAM's range of contraction is clear. As the frequency decreases, SAM has more time to achieve a higher level of contraction. However, at 1 and 0.5 Hz, insufficient time is allocated to reach SAM's maximum capability of contraction. This observation is reflected in the curve's shape, which appears as a symmetric curve around the peak point, where the actuation and de-actuation sides are almost identical. In contrast, at 0.2 Hz, the actuation and de-actuation behaviour is more observable as SAM spends more time in the actuation interval.

Examining the actuation region of the 0.2 Hz curves reveals two distinct phases: a sharp increasing phase and a gradual increasing phase (Figure 5-37). The sharp phase initiates rapidly at the beginning of the actuation condition, lasting approximately 1 second, while the gradual phase represents a slow rise over around 1.5 seconds. In Figure 5-37, the red star placed between the two phases serves as a visual indicator of the transition point, where the rate of increase reduces.

Although the three models exhibit overall similar behaviours, there are slight variations in the ratio between the two actuation phases. Model-2 and Model-3, for example, show a shorter gradual increasing phase with averages of 1.399 and 1.3966 seconds, respectively, while Model-1 has an average gradual increasing phase of 1.500 seconds, indicating a longer time spent in the gradual phase and a smaller rate of displacement. The time intervals of both sharp and gradual increasing phases are presented in Table 5-1. The table presents the starting and ending points for both phases, with the average column providing the mean across three samples within one model. Lastly, the slope column indicates the calculated slope of the line graph within each phase.

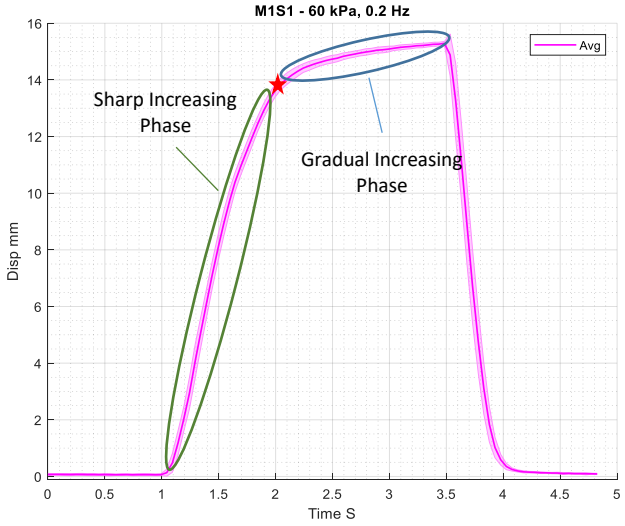

Figure 5-37: The average range of displacement cycles of the SAM when pressurized with 60 kPa at 0.2 Hz for Sample-1 of Model-1 as an example. The actuation region of the curve reveals two distinct phases: a sharp increasing phase and a gradual increasing phase.

Table 5-1: The time intervals of both sharp and gradual increasing phases as shown in Figure 5-37.

	Sharp Inc					Gradual Inc				
	1st point	2nd point	Total	Avg	Slope	1st point	2nd point	Total	Avg	Slope
M1S1	1.044	1.944	0.9		20.8	1.944	3.483	1.539		0.8
M1S2	1.216	2.121	0.905	0.904	17.84	2.121	3.567	1.446	1.500333	0.6
M1S3	1.101	2.008	0.907		17.32	2.008	3.524	1.516		0.816327
M2S1	0.605	1.536	0.931		19.95082	1.536	2.907	1.371		0.634921
M2S2	0.833	1.743	0.91	0.899333	18.44262	1.743	3.105	1.362	1.399333	0.819672
M2S3	0.554	1.411	0.857		18.21569	1.411	2.876	1.465		0.408163
M3S1	0.42	1.374	0.954		17.36364	1.374	2.809	1.435		0.625
M3S2	0.494	1.457	0.963	0.965667	18.86667	1.457	2.829	1.372	1.396667	0.566038
M3S3	0.456	1.436	0.98		19.80357	1.436	2.819	1.383		0.508475

*<u>Peak</u> Displacement of SAM's Models Across Frequency Levels - **Observation**:*

Figure 5-38 and Table 5-2 summarize the data of the bar charts of the peak resultant displacement, with each chart corresponding to the actuation frequency at 1, 0.5, 0.2 Hz, and static actuation. The table include three categories: the mean maximum displacement of seven sequence displacement cycles, the average value across the three samples, and the rate of increasing between the actuation frequencies.

Observing the cycles' STD over the bar graphs shows an increase with higher frequency. For instance, at 1 Hz, the STD of the second sample of Model-1 is 0.638,

whereas it significantly reduces to 0.023 at 0.2 Hz, representing a reduction of %96.39.

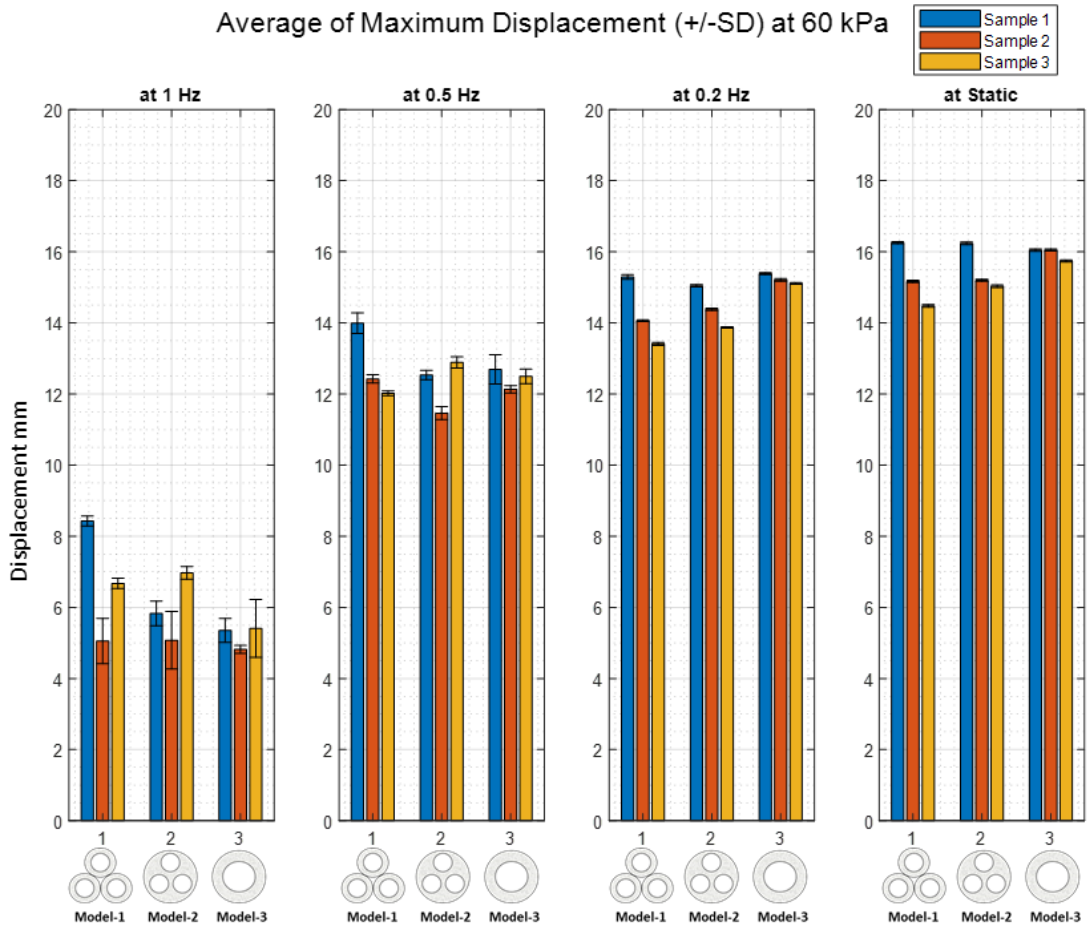

Figure 5-38: Four separate bar charts of the peak resultant displacement, with each chart corresponding to the actuation frequency at 1, 0.5, and 0.2 Hz.

The repeatable displacement among samples within each model demonstrates the reliability and consistency of the obtained data. Notably, as the frequency decreases, the repeatability of the samples increases.

Analysing the average maximum displacement for all models at various frequencies shows that their values are highly similar. At 1 Hz, Model-1 exhibits superiority with an average displacement of 6.719 mm, compared to 5.958 mm for Model-2 and 5.193 mm for Model-3. Similarly, at 0.5 Hz, Model-1 leads with 12.810 mm compared to 12.436 mm for Model-3 and 12.293 mm for Model-2. Subsequently, at 0.2 Hz and static, Model-3 surpasses the others with 15.236 mm and 15.946 mm, respectively.

In all models, the rate of increase in maximum displacement between 1 Hz and 0.5 Hz exceeds the rate between 0.5 Hz and 0.2 Hz. The ranking of the rate of increase from 1 Hz to 0.5 Hz is Model-3 > Model-2 > Model-1, with increases of %58.24, %51.53, and %47.55, respectively. From 0.5 to 0.2 Hz, the order remains the same but with smaller rate increases: %18.37, %14.80, and %10.12 for Model-3, Model-2, and Model-1, respectively. From 0.2 Hz to Static, the rate of increase is almost identical for Model-1 and Model-2 at %6.84, slightly less in Model-3 at %4.45. This comparison suggests that Model-3 can reach its maximum displacement capability faster than Model-1 and Model-2. Further details about time intervals and the response of the three models will be presented in the following section.

Table 5-2: The data of the bar charts of the peak resultant displacement.

	Displacement				Average				Rate of increasing		
	Disp @ 1 Hz	Disp @ 0.5 Hz	Disp @ 0.2 Hz	Disp @ Static	Disp @ 1 Hz	Disp @ 0.5 Hz	Disp @ 0.2 Hz	Disp @ Static	From 1 Hz to 0.5 Hz	From 0.5 to 0.2 Hz	From 0.2Hz to Static
M1S1	8.429	13.99	15.29	16.25	6.719	12.81	14.253333	15.3	47.54879	10.126286	6.8409586
M1S2	5.054	12.42	14.06	15.17							
M1S3	6.674	12.02	13.41	14.48							
M2S1	5.829	12.53	15.04	16.24	5.958	12.293333	14.43	15.49	51.534707	14.807115	6.8431246
M2S2	5.074	11.46	14.38	15.2							
M2S3	6.971	12.89	13.87	15.03							
M3S1	5.351	12.69	15.39	16.05	5.1933333	12.436667	15.236667	15.946667	58.241758	18.376723	4.4523411
M3S2	4.82	12.13	15.21	16.05							
M3S3	5.409	12.49	15.11	15.74							

5.2.5.3 Time Interval

In this third comprehensive comparison of cyclic displacement tests, the examination specifically focusing on time intervals. A single testing condition involving actuation at a frequency of 0.2 Hz and pressurization at 60 kPa is applied. The scope comprises all samples from the three SAM's model. Deeper insight into the resultant timestamps of key events and the corresponding time intervals within the displacement cycle is provided in Appendix 5, showing the analysis outcomes for the first sample of Model-1 subjected to an input pressure of 60 kPa and an actuation frequency of 0.2 Hz. The resulting data is visually presented in Figure 5-39, utilizing a bar graph layout featuring four bar charts. These charts offer a comprehensive breakdown of time intervals within a displacement cycle, covering pre-conditioning, actuation, de-actuation, and idle phases. Through these bar graphs an assessment of SAM models time characteristics is provided.

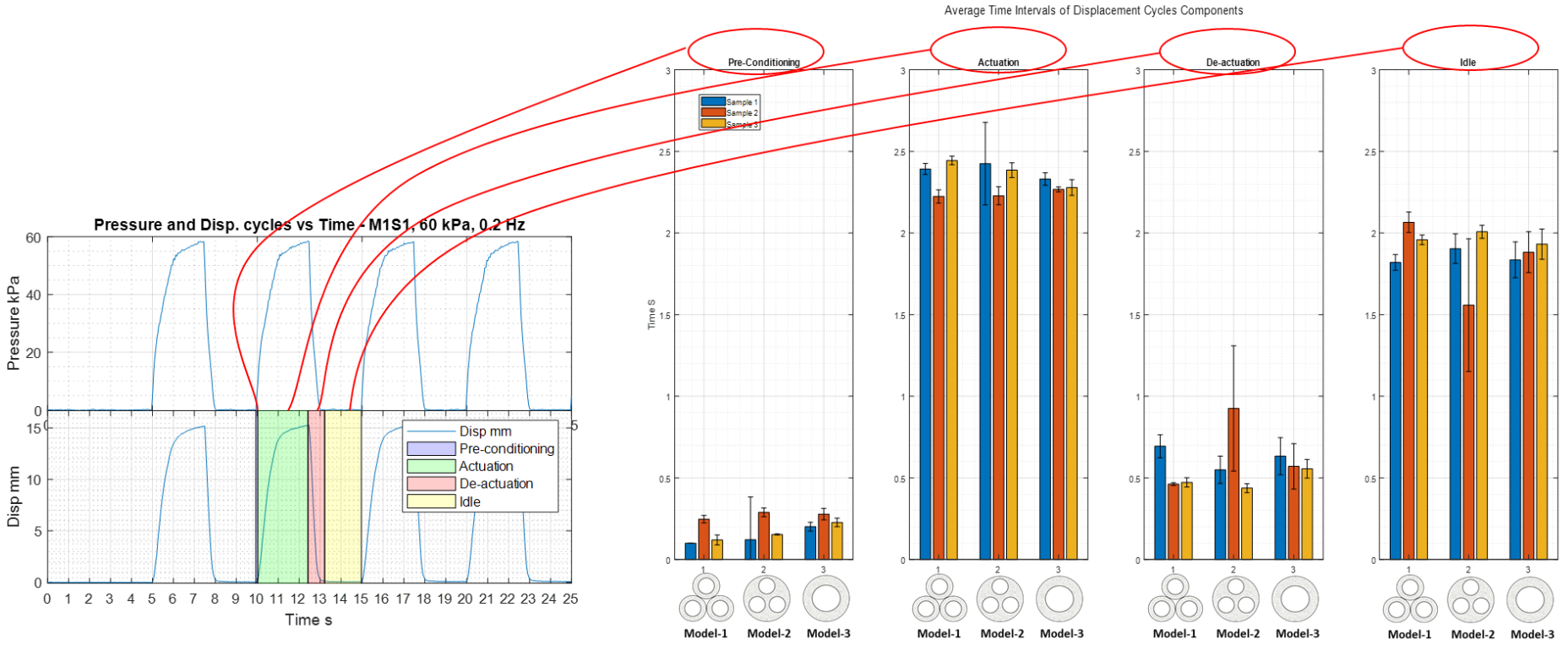

Figure 5-39: Comprehensive comparison of the time intervals results for the cycles of the displacement tests.

*Comparative Analysis of Displacement Cycle Time Intervals - **Observations**:*

When comparing the *Pre-conditioning* interval of displacement cycles among the samples, it's clear that Model-1 exhibits the shortest duration, whereas Model-3 displays the longest duration. This observation aligns with previous findings in load cycles, where Model-1 demonstrated the fastest *Pre-conditioning*, initiating actuation more rapidly than other models. This behaviour is attributed to the SAM's configuration in Model-1, featuring three soft filaments with a larger overall diameter, resulting in a tighter braided sleeve over the soft component.

Among the displacement cycles, the *Pre-conditioning* interval averages 0.155 mm with an STD of 0.080 for Model-1, followed by Model-2 with an average of 0.187 mm and an STD of 0.088, and finally Model-3 with an average of 0.235 mm and an STD of 0.039.

All models exhibit similar results during the *Actuation* state, with average actuation intervals of 2.353 mm for Model-1, 2.346 mm for Model-2, and 2.292 mm for Model-3. Notably, as the *Pre-conditioning* interval increases, the *Actuation* duration decreases, a trend also observed between the *De-actuation* and *Idle* intervals. In the *De-actuation* interval, Model-1 displays the shortest duration with an average of 0.542 mm, while Model-2 exhibits the longest duration with an average of 0.637 mm.

Despite small variations between samples in all intervals and small STDs of displacement cycles, the second sample of Model-2 shows a notably high STD, especially in the *De-actuation* and *Idle* intervals. Additionally, compared to all other samples, it demonstrates a higher *De-actuation* interval and a lower *Idle* interval than the average.

Comparing the displacement cycle to the load cycle, the displacement cycle shows a shorter *De-actuation* interval, resulting in a longer *Idle* period. It's important to note that the actuator setup differed in force test, where it is being blocked from both sides that lead to distinct behaviour within the actuation cycle. Examining the De-actuation interval is interesting as it offers an assessment of the required time to reach the *Idle* state.

The bar graph illustrates that Model-1 slightly has a longer idle state than both Model-2 and Model-3. From a performance standpoint, a shorter *De-actuation* duration and a longer *Idle* state are preferred for applications requiring a fast return to the settled state.

Table 5-3 summarize the outcomes of the time interval analysis, including three categories: the mean time interval of the displacement cycle, the average across the three samples, and the STD across the three samples. Each category presents the

time intervals of the cycle components that includes the *Pre-conditioning, Actuation, De-actuation*, and *Idle* phases.

Table 5-3: The outcomes of the time interval analysis in seconds.

	Displacement				Average of 3 Samples				STD of 3 Samples			
	Pre-conditioning	Actuation	De-actuation	Idle	Pre-conditioning	Actuation	De-actuation	Idle	Pre-conditioning	Actuation	De-actuation	Idle
M1S1	0.099	2.392	0.693	1.819	0.155	2.3533333	0.5423333	1.948	0.08029944	0.1149841	0.1305769	0.12386686
M1S2	0.247	2.224	0.462	2.066								
M1S3	0.119	2.444	0.472	1.959								
M2S1	0.121	2.425	0.549	1.904	0.187333333	2.346	0.637	1.823	0.08863596	0.1041297	0.2556247	0.23520417
M2S2	0.288	2.228	0.925	1.558								
M2S3	0.153	2.385	0.437	2.007								
M3S1	0.2	2.331	0.633	1.836	0.235	2.2923333	0.586	1.88333333	0.039610605	0.0340196	0.0413884	0.04801389
M3S2	0.278	2.267	0.57	1.882								
M3S3	0.227	2.279	0.555	1.932								

5.2.5.4 Summary of Key Observations

Model Performance:

- The synchronization of pressure and displacement cycles shows very minimal delay between peak pressure and peak displacement, indicating effective alignment.
- The displacement drop from the peak is sharp and rapid, but does not drop below the average bottom value, unlike load cycles.
- Displacement cycles do not show a slight decrease after pressure is triggered, indicating that the minor expansion that observed in force test does not lead to minor contraction.
- High repeatability is observed across displacement cycles, with minor STD indicating stable and consistent data.

Pressure Effect on Force Generation:

- A positive correlation exists between pressure levels and the range of contraction.
- Model-1 shows consistent behaviour across samples, while Model-2 exhibits minor fluctuations at 40 and 60 kPa.
- Model-3 demonstrates the highest repeatability, but a notable high STD in the actuation region for one sample indicates timing inconsistencies within the pneumatic system.

Frequency Effect on Force Generation:

- Lower frequencies allow SAM more time to achieve higher contraction levels. At higher frequencies (1 Hz and 0.5 Hz), SAM does not reach its maximum contraction capability.
- As frequency decreases, the repeatability of samples increases, indicating more consistent performance at lower frequencies.
- At 0.2 Hz, two distinct phases are observed in the actuation region: a sharp increasing phase followed by a gradual increasing phase.
- Model-1 spends more time in the gradual phase compared to Model-2 and Model-3, indicating a smaller rate of displacement.
- Model-3 shows the highest peak displacement at 0.2 Hz, while Model-1 leads at 1 Hz and 0.5 Hz.

Time Intervals Analysis:

- Model-1 exhibits the shortest Pre-conditioning interval, indicating faster initiation of actuation, where the same behaviour was observed in force tests.
- Displacement cycles are smoother with fewer fluctuations compared to load cycles, and the idle state is more stable and longer.
- The actuation intervals are similar across all models, while Model-1 shows the shortest De-actuation interval, that is preferred for applications requiring a quick return to a settled state.
- Minor variations in De-actuation and Idle intervals between samples are observed, with Model-2 showing a notably higher De-actuation interval for one sample.

5.2.6 Discussion

5.2.6.1 Test Setup Reliability

The near alignment of pressure and displacement peaks, with minimal delay, supports the effectiveness of the displacement test setup quality in achieving synchronized actuation. This aligns with our findings from the force test from the previous section (Section 5.1 Block Force Test) with smaller delay observed in the displacement test. Another indicator of the test setup quality is the high repeatability observed across displacement cycles, with minor STDs, indicates stable and consistent performance.

The consistent behaviour of Model-1 and Model-3 across samples reflect the effectiveness of their designs. However, Model-2 exhibited minor fluctuations at

certain pressure levels, which is attributed to minor defection or inconsistencies in one of the samples. Aside from these fluctuations, Model-2 also showed consistent behaviour.

5.2.6.2 Models Performance

The analysis of peak displacement across various frequencies shows that Model-1 performs best at higher frequencies (1 Hz and 0.5 Hz), while Model-3 excels at lower frequencies (0.2 Hz) and under static conditions. This indicates that Model-1 could be more suited for rapid actuation applications, while Model-3 performs better in scenarios requiring maximum displacement and higher consistency. In the previous section, the results of the block force test clearly indicate the superiority of Model-2 followed by Model-1 and then Model-3. However, in the displacement test discussed here, there is no significant impact of changing the configuration of SAM's design on the range of contraction.

The time interval analysis revealed that Model-1 has the shortest pre-conditioning interval, indicating faster initiation of actuation. The actuation intervals were similar across all models, while Model-1 showed the shortest de-actuation interval and a longer idle state. Given that Model-1 is a more complex design, comprising three separate soft filaments actuating independently, it was unexpected for it to reach the idle state quicker than the other models. It was expected that the interaction among the three soft filaments within the braid (strain-limiting component) would require a longer time to settle. This unexpected performance suggests that Model-1 is better suited for applications requiring a quick return to the idle state.

5.2.6.3 Comparison with Literature

The SAMs' models studied in this research exhibited a contraction range of 0.90-15.45% at pressures of 20-80 kPa. The testing methodology and this performance was compared to the findings of *Takosoglu et al.* [70] and *Kothera et al.* [68] to evaluate SAMs.

1- *Takosoglu et al.* [70] conducted displacement tests on two types of soft actuators: Festo Fluidic Muscle and Shadow Air Muscle. These actuators, made of materials with higher stiffness and shore-hardness, required higher input pressures of 100-700 kPa and 60-350 kPa, respectively.
The setup used in this research to measure the range of contraction differs from the methodology used by *Takosoglu et al.* [70] The main difference is the

way the actuator is positioned vertically within the test setup. *Takosoglu et al.* [70] used weights to keep the actuator under tension, while we used a frictionless connection to align the actuator in a vertical linear position (as mentioned in Section 5.2.3.1). Our method provides valuable insights by isolating the effect of weight on the SAM's behaviour. In contrast, the method used by *Takosoglu et al.* [70] allows exploration of the correlation between weight scenarios and the range of contraction.
Despite the significant differences in material and required pressure, the range of displacement for SAMs was comparable to those studied by *Takosoglu et al.* [70]. The Festo Fluidic Muscle contracted approximately 2-18% at 100-700 kPa, and the Shadow Air Muscle contracted 1-12% at 60-350 kPa. This shows that SAMs, made from low shore-hardness material (Ecoflex 50), can achieve similar contraction ranges with much lower pressure, demonstrating their efficiency.

2- The test setup in this research is similar to the one used by *Kothera et al.* [68] Both setups used an Instron 8841 servo-hydraulic testing machine to measure load and position, a Jun-Air/Newport air compressor to supply pressure, and LABVIEW software for data collection. Additionally, both approaches monitored pressure using a pressure transducer.
Kothera et al. [68] measured blocked force and free contraction at different pressures, similar to our method. However, our research also varied the actuation frequency, providing a deeper understanding of the actuator's behavior. A limitation in *Kothera et al.'s* [68] procedure was the lack of a clear method to ensure the actuator stayed on a pure linear track during contraction. Our methodology addressed this by ensuring movement occurred in a vertical linear orientation.
Kothera et al. [68] reported results for a McKibben actuator with a soft tube length of about 200 mm, an inner diameter (ID) of 9.5 mm, and an outer diameter (OD) of 15.24 mm. The contraction ranged from 0.75% to 4.25% at pressures between 70 kPa and 415 kPa. In comparison, our Model-3 SAM has a tube length of about 110 mm, an ID of 5 mm, and an OD of 10.36 mm. The SAM's contraction ranged from 0.90% to 15.45% at pressures between 20 kPa and 80 kPa.

These results indicate that the SAM in our research achieves higher contraction even at significant lower pressures. Similar findings were observed when comparing our SAM with the actuators studied by both *Takosoglu et al.* [70] and *Kothera et al.*

[68], with a more significant difference noted in *Kothera et al.*'s [68] results. This enhanced contraction performance can be attributed to the use of softer materials and optimized components in the SAMs.

5.2.7 Summary

This section continued the characterization work by focusing on the contraction capabilities of SAMs. It evaluated three SAM models (Model-1, Model-2, and Model-3) under various conditions, including different frequencies and pressure levels, to determine their range of contraction. The study addressed the limitations in existing methodologies by developing a new approach that isolated the effects of weight and provided precise measurements of free contraction behaviour.

5.2.7.1 The Experimental Setup

The experimental setup evolved significantly from its initial form to ensure accurate measurements of SAM contraction. A key component is the IL-065 displacement sensor, which provides precise distance measurements. The setup includes the use of a universal load tester (Instron 5943) and a frictionless cylindrical piston to maintain a pure linear contraction path. This well-organized and controlled testing environment allows for the accurate assessment of SAMs' linear contraction under different conditions, ensuring reliable and efficient testing operations.

5.2.7.2 Test Procedure and Data Processing

After presenting the finalized experimental setup, the section outlines the detailed procedure and data processing methodology for conducting displacement tests on the three SAM designs (Model-1, Model-2, and Model-3). Each SAM was tested under eight different conditions, varying in pressure levels and actuation frequencies, resulting in a total of 72 tests. Then, data processing follows a structured protocol to derive meaningful results from the raw test data. The procedure includes data collection, calibration, examination, and importing into MATLAB for analysis. Three main codes were created to facilitate a comprehensive analysis and comparison of the performance of the three SAM models.

Chapter 6 Case Study: SAM in Practical Application

Building upon the foundational chapters that detailed the design, fabrication, force testing, and displacement testing of the soft actuator, this chapter takes a practical turn by presenting a comprehensive case study. The objective is to explore the real-world application of the developed soft actuator and analyse its performance in a specific scenario. Different models of SAM will be integrated into a carefully optimized case study frame, allowing for an in-depth analysis of its performance in a practical context. The case study methodology builds upon prior research efforts that aim to provide valuable insights into SAM's practical application while addressing issues related to measurement precision and enhancing the overall experimental setup for a more robust analysis.

6.1 Introduction

In the previous chapters, a detailed evaluation for the technical aspects of SAM development covering its design, fabrication, force generation, and displacement range. Now, in Chapter 7, the focus is shifted to see how SAM performs in the real world through a practical case study. The simplicity and biomimetic properties of SAM have taken increasing attention for their various applications in various real-world scenarios. By exploring the literature on McKibben air muscle applications, researchers have highlighted their contributions to fields such as robotics, medical devices, rehabilitation, and industrial automation [76].

The main goal is to check how SAM works in an actual setup by placing it in a structure that makes SAM mimic muscle movement. SAM is used as muscles to actuate a dynamic system and studying how it behaves under different conditions that diverse according to the pressure, frequency, and attached weight. The same SAM’s samples were used in previous force and displacement experiments are used here to evaluate their performance and to see how they handle a real-world scenario. Important details about the methodology of the case study experiment are discussed widely in this chapter.

Furthermore, new models are designed, fabricated, and tested within the case study framework to assess the conceptual design of SAM on a larger scale. In the augmented version, Model-1 comprises 6 filaments, maintaining the same filament size as the original version. Model-2 features 6 cavities, with the cavity diameter remaining consistent with the original version. Model-3 keeps a simple design with a

single cavity, but with bigger size to equalize the volume of the soft material and cavities of the other Model-1 and 2 within the new version.

To understand SAM's performance, the following metrics are considered: internal pressure within the pneumatic system, SAM’s range of contraction, change in the joint angle of the dynamic system, and the angular velocities within the dynamic system. The data for these metrics are arranged into synchronized plots, providing insights into how SAM and the dynamic system respond under specific conditions: 60 kPa pressure and 0.2 Hz frequency. These tests involve subjecting SAM to repeated pressurizing and air-releasing cycles to mimic the rhythmic movements like the practical scenarios SAM may encounter in.

This chapter will provide visual analyses to assess the movement of SAM and its influence on the dynamic system motion. The visual characterization procedures through comprehensive bar charts aim to align with the previous methods of force and displacement to ensure a consistent approach of analysis. The primary goal is to gain more insights into SAM's behavior and to enhance the experimental approaches for improved results.

6.2 Objectives

To gain a comprehensive understanding of how SAM performs in practical applications and interacts with dynamic systems, a case study is proposed. This section outlines the investigation and seeks to achieve the following objectives:

Objective 1: Design a robust dynamic system that serves as an effective case study for the application of SAM.

Objective 2: Develop a testing methodology to assess SAM's capabilities in real-world applications.

Objective 3: Measure the targeted metrics within SAM and the established dynamic systems.

Objective 4: Assess, analyse, and compare the performance of various SAM models.

6.3 Experimental Setup

6.3.1 Development History of the Case Study

SAM closely mimic the structure and function of natural muscles, which makes it an ideal choice for replicating human-mimetic movements. This biomimetic design ensures that the case study reflects the complex and dynamic nature of human muscle behaviour. The compliance and adaptability of SAM allows for a wide range of motion that resembles the flexibility of human muscles. This characteristic is important for creating a bicep model that can mimic the movements of the human bicep in a simple way. The bicep muscle is visible example for the linear SAM movements, including flexion and extension of the arm, which makes it conducive to experimental setups.

The human bicep consists of multiple muscles which enable the arm to perform complex motion. Replicating this function by incorporating multiple SAMs into a system can enable motion in multiple degrees of freedom. The complexity of controlling multiple degrees of freedom enhances the realism of the system's motion. However, operating SAM in one degree of freedom simplifies the control and design of the system that makes it more straightforward and enables the analytical comparison with the results of the force and displacement tests.

Creating the case study setup involved a significant challenge, primarily in identifying a precise method for imitating the bicep's movement in a simple way. Figure 6-1 visually shows the conceptual design of the dynamic system within the case study that designed to imitate the bicep's movement in a single degree of freedom. The axial contraction, represented in the figure, serves as the primary mechanism by SAM that undergoes shortening and release during activation, resulting in the flexion and extension of the arm.

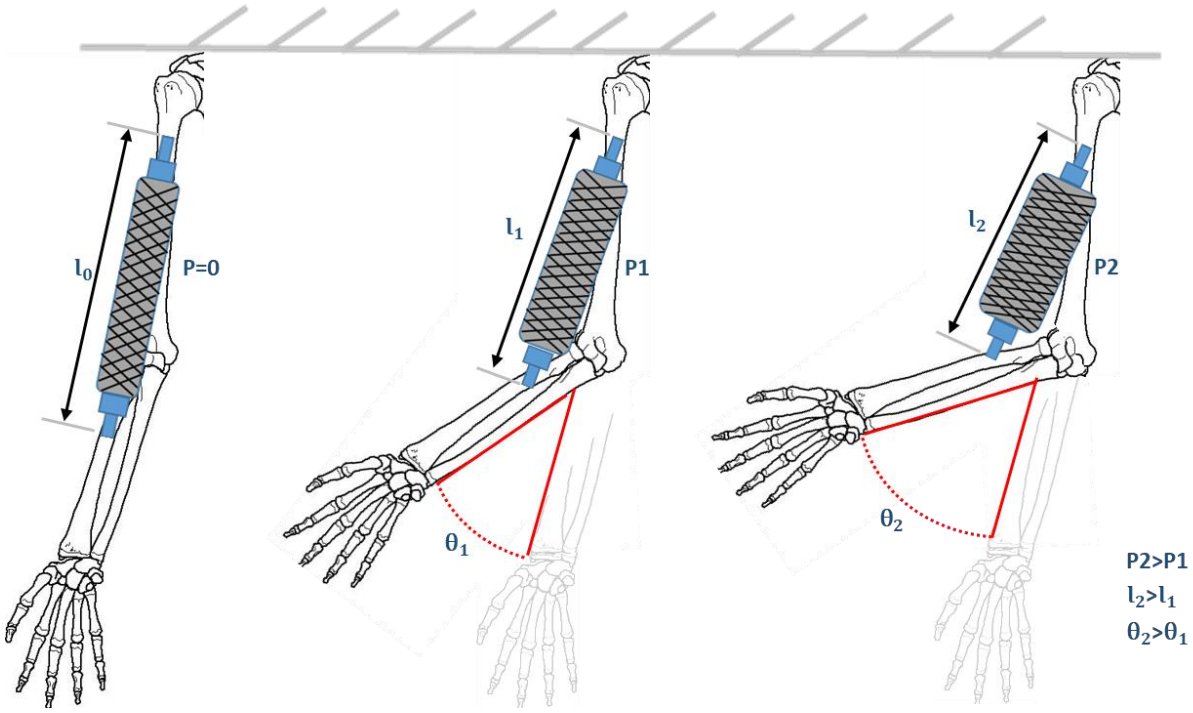

Figure 6-1: The concept of the case study through mimicking the movement of the bicep in a single degree of freedom.

The transition from the initial version to the optimized setup encountered important improvements. The case study setup underwent a transformation from its initial state to a finalized configuration that enables precise measurements of SAM's target metrics. Initially inspired by several research works [74], the setup was made to efficiently construct the dynamic structure for the case study through utilizing materials help to achieve the designed kinematic system. Appendix 6 shows two configurations of the dynamic system to provide examples of the evolutionary history of developments to the case study structure.

6.3.2 Finalized Configuration

The finalized case study's dynamic system involved utilizing a pivot joint connected with aluminium strut profiles. The pivot joint is commonly employed to enable rotational movement of strut profiles around a central axis. This configuration addresses the limitations encountered in earlier setups, providing effective solutions for improved performance and reliability. Specifically, the connection of SAM with the aluminium arms has been developed to enable adaptable movement of SAM within the dynamic system. Additionally, a structure of aluminium struts has been constructed to fix and secure the frame of the arms from the upper end of the upper

arm. Also, a 3D-printed adaptor has been developed and joined with screw to the tip of the lower arm for hanging additional weight.

The finalized case study configuration is visually explained in Figure 6-2, showing how the dynamic system is firmly fixed and secured within fixed frame. The adaptable connection of SAM to the aluminium segments is displayed which emphasize the flexibility achieved in SAM's movement within the setup.

Two essential components, Adaptor-1 (on the upper arm) and Adaptor-2 (on the lower arm), are shown in Appendix 6. Additionally, it includes Adaptor-3, a 3D-printed component designed to support additional weight vertically. Furthermore, it provides details about the revolute joint that connects both ends of the SAM with the arms, allowing rotational movement around a fixed axis.

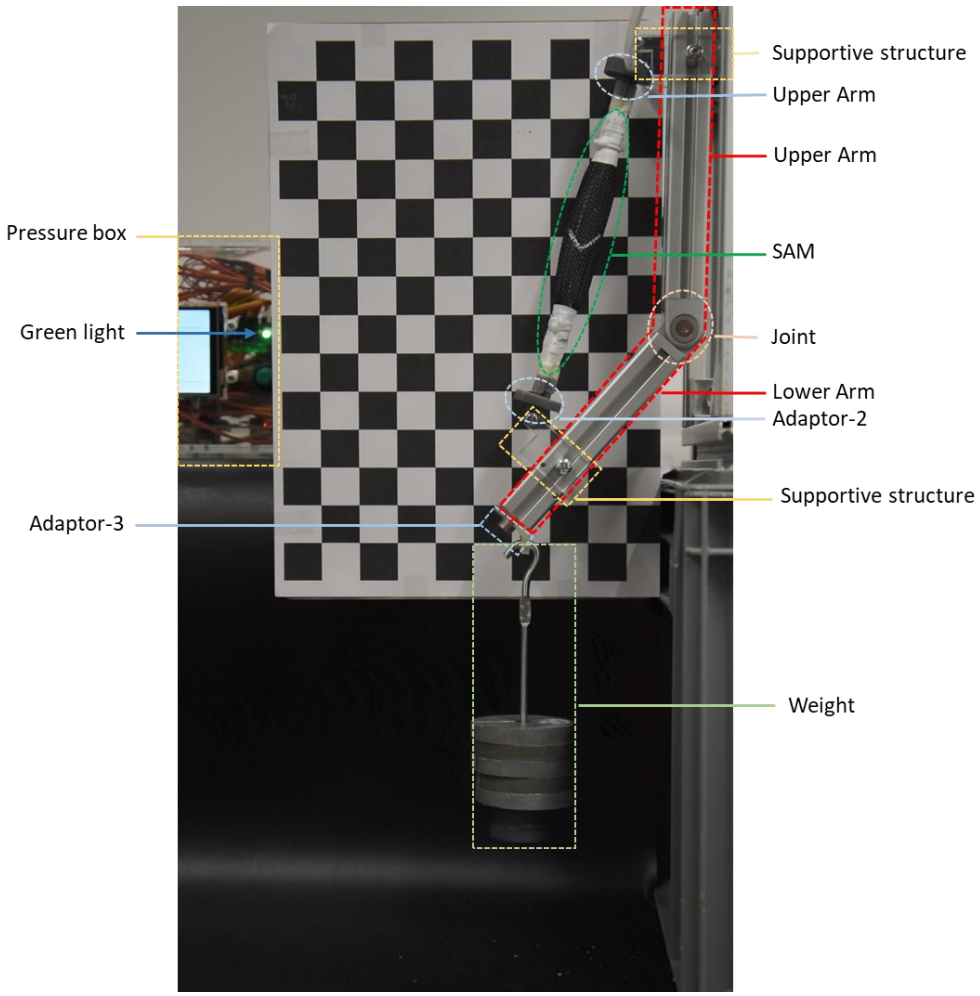

Figure 6-2 the finalized case study configuration.

6.4 Experimental Methodology

6.4.1 Key Metrics

The experiment of the dynamic system involves measuring several key metrics that varies in accordance with the input pressure, actuation frequency, and model of SAM. These metrics provide a comprehensive understanding of the system's behaviour and performance.

1- The internal pressure of the SAM in kPa, serving as an indicator of the pressure inside SAM during activation.
2- The displacement of the soft actuator in mm, showing the range of SAM's contraction and extension throughout the actuation and de-actuation phases.
3- The angle formed between the segments of the arm is measured in degrees. This metric provides a representation of the flexion and extension of the aluminium arm that is key for understanding the dynamic changes in the arm's configuration during the activation of the SAM.
4- The speed at which the lower arm rotates around the joint is measured in mm/s. This metric offer information about the speed at which the arm undergoes flexion and extension.

The key objective is to examine the functionality of three distinct SAM designs, acting as muscle-like components, and to compare their performances under varied experimental conditions. The study utilizes the original tested SAM samples to evaluate their real-world performance of the case study experiment. Moreover, another set of SAM models (Model-1, Model-2, and Model-3) are designed at a larger scale and tested within the case study framework.

To investigate actuation under various conditions, variations in both frequency and pressure during the tests is applied. The input pressure is adjusted between 40, 60, and 80 kPa. These adjustments, coupled with variations in frequency, simplified into four specific pressure-frequency conditions:

- Condition-1: Under 40 kPa and frequency 0.2 Hz.
- Condition-2: Under 60 kPa and frequency 0.2 Hz.
- Condition-3: Under 60 kPa and frequency 0.5 Hz.
- Condition-4: Under 80 kPa and frequency 1 Hz.

In the first three cases, consistent variations between pressure and frequency were selected. Conditions 1 and 2 share the same frequency but different pressures, while Conditions 2 and 3 vary the frequency with constant pressure. In Condition-4, new pressure and frequency are set to explore the system's behaviour at high actuation

frequency. A higher frequency leads to shorter actuation time, thus requiring higher pressure (80 kPa) for effective actuation and performing the desired contraction movement. Under each condition, there are three subplots (bar charts), illustrating the different weight scenarios hung on the end of the lower arm. Within each condition, three weight scenarios hung on the end of the lower arm are considered:

- No weight.
- 300 g.
- 600 g.

6.4.2 Video Analysis Method

The method employed to measure the metrics of the dynamic system involves the use of video analysis software specifically designed for motion assessment. This entails the examination and quantification of captured video of SAM's contraction and arm movements, enabling the observation of its dynamic changes throughout a timeframe. To assess the metrics of the dynamic system, a video capturing its movement is recorded using camera. The camera is precisely positioned, and the camera holder is adjusted to ensure stability and consistency throughout the recording process.

In the background of the dynamic system, a checkerboard pattern is featured, enabling the camera calibration for vision-based analysis. Capturing images of this known pattern enables precise calibration of the camera, providing easily detectable features for accurate tracking of SAM and the desired spots within the aluminium segments.

The input pressure’s electrical signal allows for the correlation between the electrical signal and the other parameters of the system to be visually assessed. The electrical signal is obtained through manual tracking of the green light in the pressure box (shown in Figure 6-2). This tracking involves specifying the time when the "green light" illuminates to indicate the start of activation, and then specifying the time when the light turns off. This process is repeated for all cycles. Subsequently, the electrical signal data is created by manually entering the corresponding time values into a spreadsheet. Specifically, "0" is entered when the "green light" is off, and "1" is entered when the "green light" is on.

6.4.3 Augmented Set of SAM

In this second part of the case study, the same aluminium arm is used with a SAM that is made out of 6 filaments for Model-1, 6 cavities for Model-2, and a single cavity for Model-3 that is equivalent to Model-1 and 2's cavity volume. More details about the conceptual design of the augmented set of SAM were provided in Chapter 4. As per the original case study, the SAM is connected to an aluminium segment to mimic the biceps movement. The aim of this experiment is to have a deeper understanding of multi-filament and multi-cavity actuators by evaluating their functionality as muscle-like components with bigger scale. This will be achieved by comparing the performance of the three different models under various conditions. The weightlifting test of the augmented set of SAMs, which evaluates the models' ability to lift weights by measuring contraction and braiding angle under increasing loads, is detailed in Appendix 6.

6.4.4 Test Procedure

This testing protocol outlines the steps for conducting tests on the dynamic system using the finalized setup. The procedure establishes instructions for performing a reliable test to quantify the desired metrics. While previous research, such as the work of Nabae Na *et al* [74], has outlined methodologies for testing SAM within a case study, this protocol introduces unique elements, notably the method of connecting SAM to the arms. Moreover, the testing procedure guarantees uniform initial testing conditions by utilizing a fixed point to connect SAM to the arms. It is worth noting that while having exactly the same length for SAM's samples should guarantee a uniform initial angle between the upper and lower arms, minor variations are observed due to the manual fabrication and connection of SAMs to the adaptors. Figure 6-3 presents a flowchart that outlines the steps for conducting this displacement test.

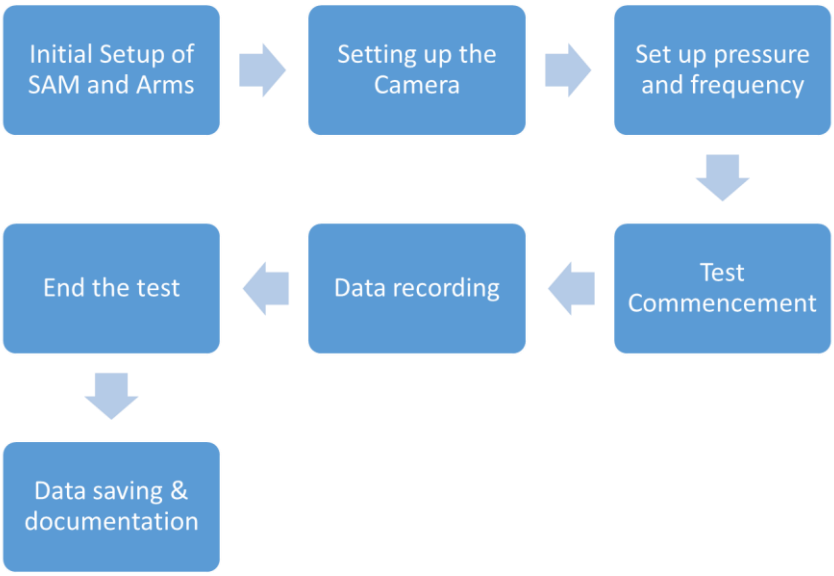

Figure 6-3: Case study's test procedure flowchart.

Procedure:

1. Initial Setup:
    a. Remove the aluminium arms from the holding frame by unscrewing the nuts. This facilitates for precise assembly of SAM on a table.
    b. Connect SAM to Adaptor-1 and Adaptor-2 using silicon tubes for a secure fit. Insert SAM's end and the adaptor port 5 mm into the silicon tube to ensure a tight connection. Figure 6-4 shows the insertion of both parts into the silicon tube.
    c. Attach Adaptor-1 and Adaptor-2 to the acrylic supportive structure on the upper and lower arms to form the revolute joints (see Appendix 6 for more details). Secure the adaptors in the middle of the supportive structures using screws, washers, and nuts.
    d. Lastly, reassemble the dynamic system (aluminium arms incorporated with SAM) to the holding frame with bolts and nuts, ensuring the upper arm is vertical.
2. Setting up the camera:
    In filming the tests of the dynamic system, the camera and its holder are adjusted to ensure optimal recording conditions. The camera is positioned to obtain a clear view of the dynamic system's movements. It is crucial to note that the height and position of the camera holder are fixed for all the tested samples, ensuring a consistent frame for every video. The importance of this

standardized setup lies in the fact that the method used to measure the metrics of the dynamic system relies on video analysis software.

3. Setting up Pressure and Frequency:
   Entering the desired pressure level and actuation frequency follows the same procedure as in load and displacement tests.
4. Test Commencement:
   Initiate the test by clicking the "start" button in the LabVIEW testing program to send the input pressure from MyDAQ-1 while receiving and recording internal pressure. Activate camera recording and ensure the tester's voice captures essential test information like SAM's model, sample, actuation frequency, and pressure level. This voice recording aids in identifying the video later during data processing. Finally, press the "running" green button on the pressure box's control panel to initiate pressure supply from Pin-1.
5. Ending the Test:
   All tests are concluding after 7 cycles. To end the test:
   a. Pressing the green button on the pressure box.
   b. Stopping the LabVIEW program.
   c. Ending the video recording.
6. Data Saving and Documentation:
   Following test completion, raw data in the form of synchronized time (in milliseconds) and pressure (in volts) is stored in LabVIEW software. Subsequently, the video is saved in a manner that ensures an organized documentation process to enhance the analysis of the test outcomes.

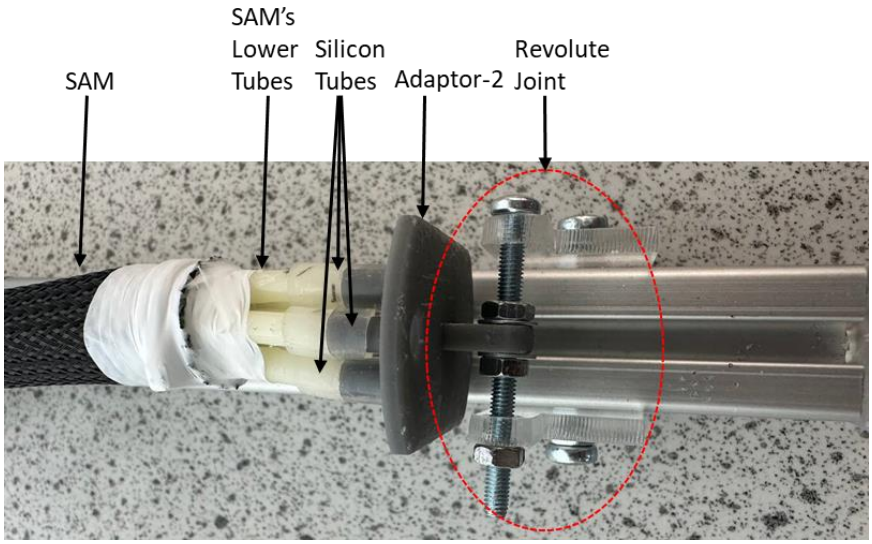

Figure 6-4: Silicone tubes are employed to connect and secure the SAM ends with the Adaptor-1 and Adaptor-2's port.

6.4.5 Data Processing

The procedure for processing the recorded videos from the test follows a protocol designed to analyse data gathered under different test conditions. The purpose of outlining this data processing protocol is to simplify the process and derive valuable results that provide conclusions relevant to the case study's objectives. Enhancing data analysis involves generating clear visual representations, such as graphs and charts. These visuals play an important role in effectively presenting the data.

The measurement of the linear displacement of the SAM and the angular movement of the arm using Kinovea software involves a systematic approach. In the recorded videos, a set of points is defined to enable measurements (shown in Figure 6-6). The identified points are marked using the software tools, with Point-1, Point-2, and Point-4 serving as fixed points, while Point-3 and Point-5 are set for tracking the movement of the lower arm and SAM, respectively. The software's tracking tools follow the linear displacement of the SAM's lower end and the angular movement of the lower arm. The fixed points, consistent over time, serve as references for calculating desired metrics through vector calculations. The angular speed of the lower arm can then be calculated by identifying the angular displacement over time. The sequential figures in Figure 6-5 illustrate the trajectories for measuring SAM’s range of displacement and the change in the arms' angle.

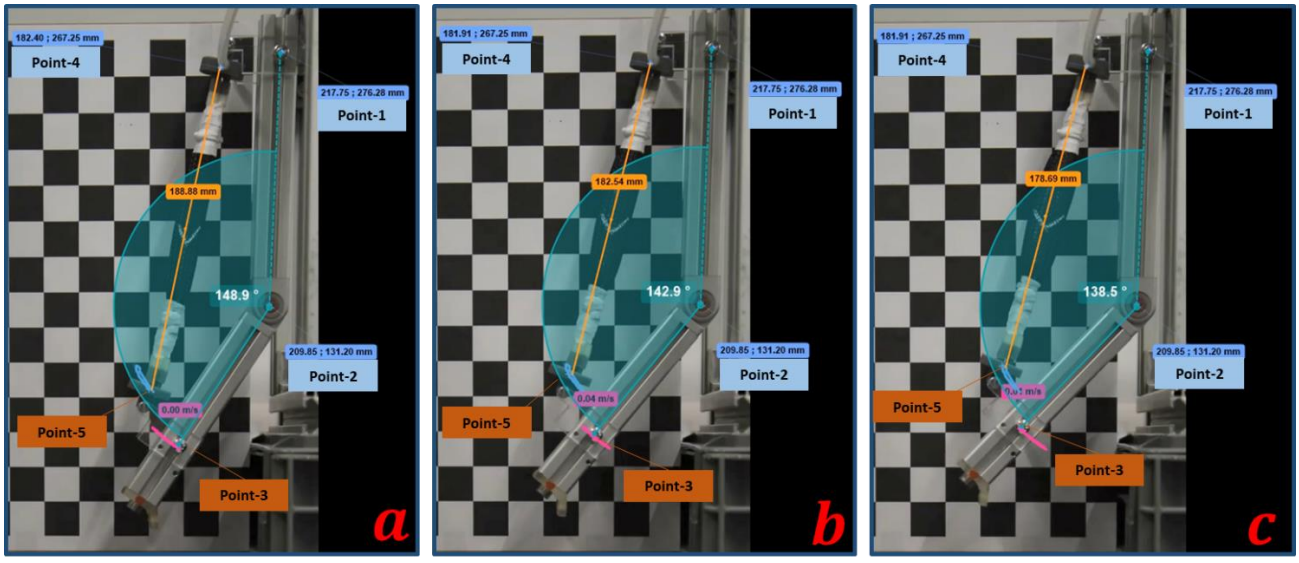

Figure 6-5: The analyzed sequence of the motion of the dynamic system

Linear Displacement Calculation:

The linear displacement of SAM is calculated by determining the distance between Point-5 and Point-4 using the formula:

$$\left|\vec{l}\right| = \sqrt{(x_5 - x_4)^2 + (y_5 - y_4)^2} \quad \text{Equation 16}$$

$$\delta l = l_n - l_0 \quad \text{Equation 17}$$

Here, $\left|\vec{l}\right|$ is the length of the vector, and δl, l_n, and l_0 represent the amount of contraction, the length, and the original length, respectively.

Angle Calculation Between the Arms:

The angle between the two vectors of the arms is determined using the dot product. In Figure 6-6, coordinates are represented, where a represents the upper arm, and b represents the lower arm. The following formulas are used to calculate the components and magnitudes of the vectors:

$$a_x = |x_2 - x_1| \quad \text{Equation 18}$$

$$a_y = |y_2 - y_1| \quad \text{Equation 19}$$

$$b_x = |x_3 - x_2| \quad \text{Equation 20}$$

$$b_y = |y_3 - y_2| \quad \text{Equation 21}$$

$$|a| = \sqrt{{a_x}^2 + {a_y}^2} \quad \text{Equation 22}$$

$$|b| = \sqrt{{b_x}^2 + {b_y}^2} \quad \text{Equation 23}$$

$$\theta = \cos^{-1}\frac{a.b}{|a||b|} \quad \text{Equation 24}$$

$$\delta\theta = \theta_n - \theta_0 \quad \text{Equation 25}$$

Here, the components and are the x- and y-coordinates of the upper arm vector a, and b_x and b_y represent the x- and y-coordinates of the lower arm vector b. The magnitudes of these vectors are denoted by $|a|$ and $|b|$. The angle θ is the angle

formed between the two arms, with representing the change in this angle over time. θ_n refers to the current angle, while θ_0 is the initial angle.

Speed Calculation of the Lower Arm:

The speed of the lower arm is calculated by determining the time derivatives of its position in both the x- and y-directions. The velocity components are expressed as follows:

$$v_x = \frac{dx(t)}{dt} \quad \text{Equation 26}$$

$$v_y = \frac{dy(t)}{dt} \quad \text{Equation 27}$$

$$v = \sqrt{{v_x}^2 + {v_y}^2} \quad \text{Equation 28}$$

Here, In the speed calculation, v_x and v_y represent the velocities in the x- and y-directions, respectively, and v is the resultant speed of the lower arm.

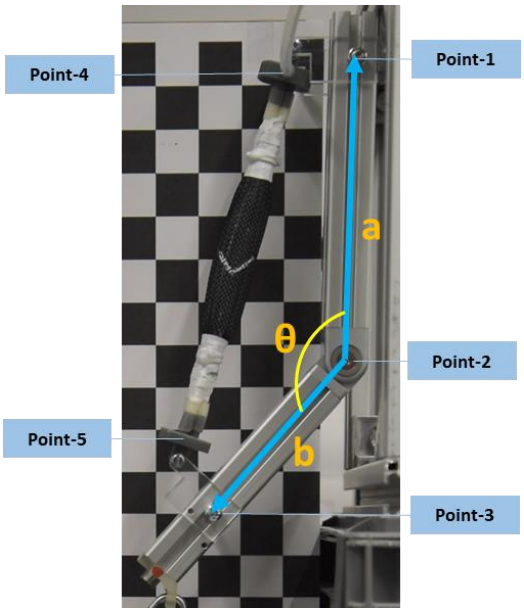

Figure 6-6: The coordinate vectors of the dynamic system

As the points set to be tracked, Kinovea software records the coordinates of these points over time. The data export feature is utilized to save the tracked coordinates

into a spreadsheet format. The produced data include the fixed coordinates of Point-1, Point-2, and Point-4, and the tracked points, Point-3 and Point-5, where three columns are generated for each points include x and y coordinates in mm and time in millisecond.

The second step of the data processing involves importing this data into MATLAB software to analyze and generate charts and statistical tables. The MATLAB processing involves the Code-1 and Code-2 that detailed previously in Chapter 5 with minor editing to adapt the experimental data of the case study.

Code-1 is designed for a thorough analysis of a dynamic system's behaviour. After loading the data, the code processes and cleans it to ensure accuracy in subsequent calculations. Three key metrics: $\delta\theta$ (reflecting the angle change between arm segments), δl (indicating the contraction of the SAM), and v (indicating the angular velocity) are then calculated from the kinematic data. These metrics are synchronized with the internal pressure data that provide a comprehensive view of the dynamic system's performance. Moreover, the code conducts statistical analyses on the outcomes of pressure, contraction, angle change, and angular speed. The outcomes are visually presented in a single figure, which effectively involves the synchronized metrics over time. Additionally, the code generates two tables that stored in an Excel format, containing important statistical numbers and peak values.

Code-2 is employed in the outcomes from the Code-1. This code is designed to generate bar charts illustrating the average peak values of specific parameters. These bar graphs facilitate comprehensive comparison methods that include the assessment of different scenarios of SAM’s Model, pressure, frequency, and weight.

The test results section will present processed data in the form of line charts, bar charts, and statistical tables that offer a comprehensive visual demonstration of the analysed data. These charts illustrate the effect of varying testing conditions on measured metrics. The main plots are synchronizing the measured metrics to provide essential insights into the soft actuator's performance and its effects on arm movement.

The process involves a series of steps, including data collection, pressure data calibration, video processing, exporting data from the video, importing data into MATLAB, and generating analytical results. Figure 6-7 presents a flowchart that outlines the steps for conducting the data processing of the case study.

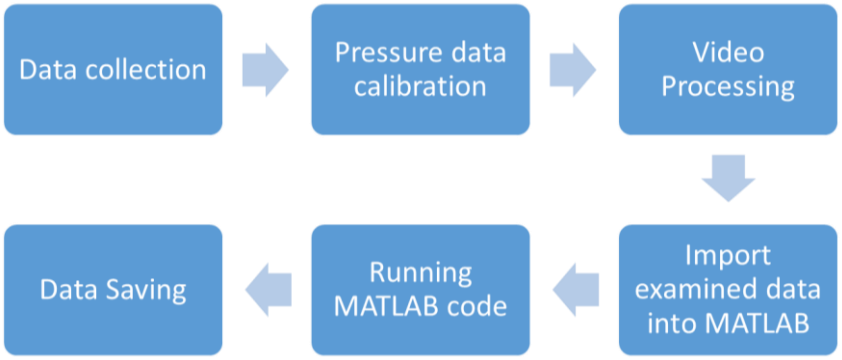

Figure 6-7: Flowchart for the data processing procedure of the case study.

Procedure:

1. Data Collection:
   Conducting tests involves the measurement of pressure and the recording of video, including various samples and test conditions characterized by changes in frequencies and pressure levels. It is important to categorize and label the collected data to ensure each test is distinctly identified along with its corresponding files.
2. Pressure data calibration:
   The transformation of internal pressure measurements from volts to kPa is carried out within a spreadsheet by employing the calibration equations. Subsequently, the converted internal pressure data is graphed within the spreadsheet to allow for the identification of potential issues within the raw data.
3. Video Processing:
   To process the videos using Kinovea software in this test, these steps are followed:
   a. Import the video file slated for analysis.
   b. For accurate measurement of coordinates, calibration is performed using known dimensions in the video. This is typically achieved by defining the length of seven blocks of the checkerboard as 140 mm to inform the software about the real-world measurement.
   c. The movement in the video is tracked by marking key points for tracking and measurement.
4. Data Importing:
   Importing the spreadsheet containing tracking points into MATLAB and then the workspace is labelled to specify both the sample and the test condition.
5. Running MATLAB Code:

The code's compatibility with the imported sample data is confirmed before executing the MATLAB code.

6. Data Saving:
   The computed numerical outcomes are stored in a spreadsheet, and charts are saved in both JPEG and MATLAB figure formats.

6.5 Results

6.5.1 Original Set of SAM

6.5.1.1 Initial Outcomes

The experimental data is displayed as a layout of synchronized multiple plots, all aligned along a common x-axis representing time, in seconds. Figure 6-8 shows a synchronized layout generated from each test that is exemplified by the third sample of Model-1 at 60 kPa and 0.2 Hz, lifting a weight of 300 g. Since each of the 12 testing conditions is applied to 9 samples, there will be a total of 108 figures (12 conditions x 9 samples) similar to Figure 6-8.

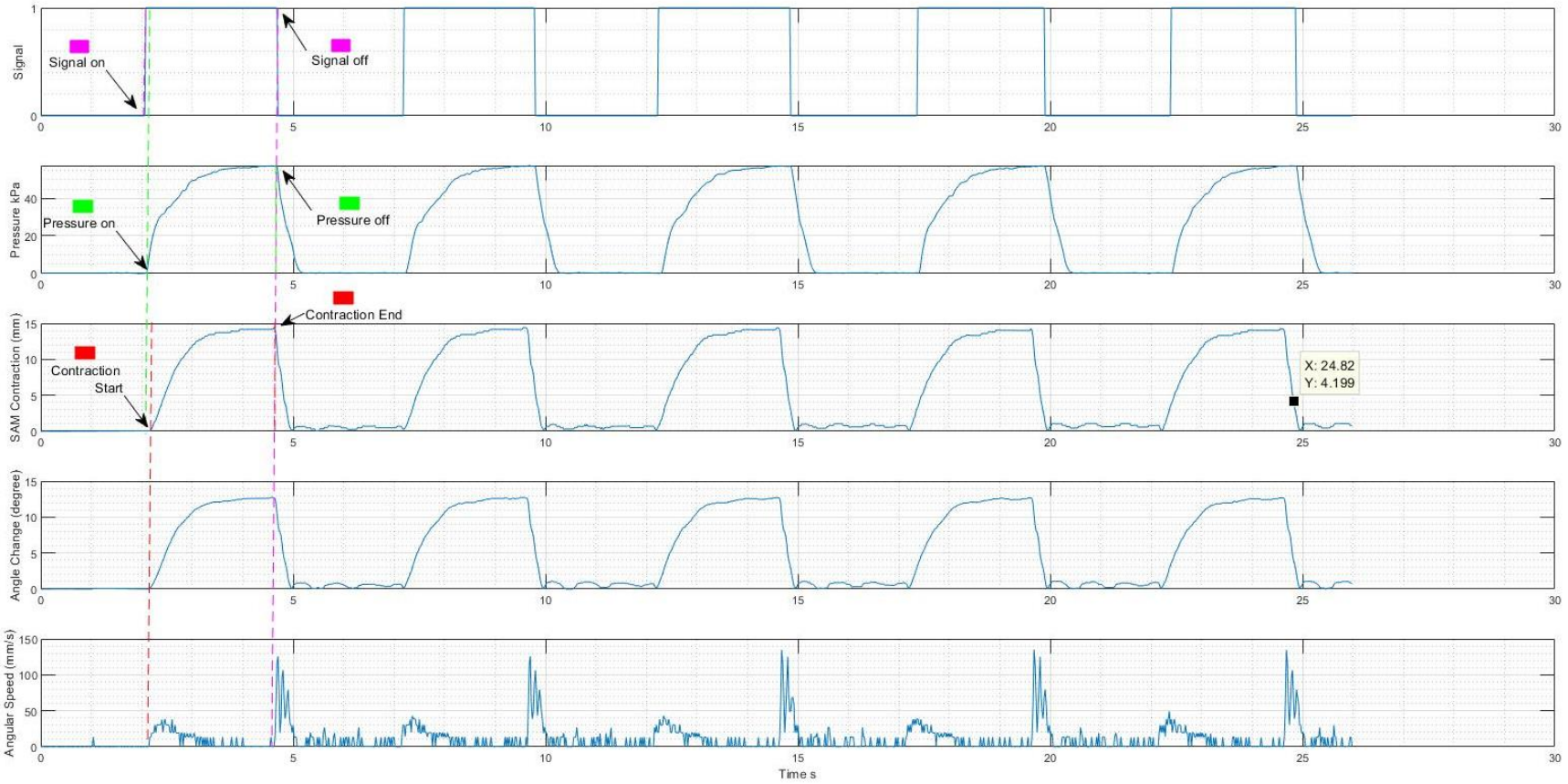

Figure 6-8: Synchronized display of internal pressure of SAM, SAM's Contraction, change in joint angle, and lower arm angular velocity for the third sample of Model-1 at 60 kPa and 0.2 Hz, lifting weight of 300 g.

*Initial Outcomes - **Observation**:*

The behaviour of SAMs' contraction and joint angle waves resembles pressure wave due to the linear relationship between pressure and the other system parameters. However, velocity waves may not exhibit the same visual similarity to pressure because velocity is a derivative of displacement with respect to time.

Coloured dashed lines are placed at the cycle's beginning and end to illustrate the system parameters' response to the input pressure. The input signal's start and end are marked in purple, while the internal pressure and SAM contraction are marked in green and red, respectively. Notably, a slight delay exists between the input signal and internal pressure at the beginning. Similarly, SAM contraction initiates after the start of internal pressure which indicate that pressure is detected before SAM begins contracting. Joint angle and arm velocity commence at the same time with SAM contraction. This indicates that the contraction of SAM is the only factor that impacts the joint angle change within the dynamic system. Further details about this delay are provided upon in a subsequent section.

Examining the contraction graph shows similarities to the behaviour observed in the previous chapter on displacement tests. For instance, the drop from the peak contraction to the bottom is sharp and rapid, while the actuation phase gradually increases until reaching the peak. This indicates that SAM shows the same behaviour in both the case study test and the pure displacement test.

Analysing the entire arm's velocity cycle indicates that the highest velocity occurs during the de-actuation region due to the sudden pressure drop. However, during the actuation region, lower arm angular velocity is highest at the beginning of phase which suggest that SAM can generate the most force during these times.

6.5.1.2 Comparative Analysis:

In this section, bar graphs and tables are provided for a detailed comparison of the key parameters obtained from the case study experiments. These parameters include the internal pressure of SAM, SAM's contraction, joint angle, and lower arm angular velocity. The analysis is focused on the evaluation of these parameters under varied experimental conditions and weight configurations. To simplify the comparison given the experiment's multiple variables, the focus is placed specifically on the maximum value of each parameter, aiming to facilitate the analysis of the extensive output data.

In the comprehensive comparisons, the analysis focused on all the three model designs of SAM, each with three samples. Each key parameter is analysed in a comprehensive layout contains four bar plots, representing the measured parameter under the four frequency-pressure conditions and the three weight scenarios. Figure 6-9 to Figure 6-13 display the internal pressure of SAM, SAM's contraction, joint angle, lower arm angular velocity, and delay between internal pressure and other parameters, respectively. Within each subplot (bar chart), a comparison is made between Model-1, Model-2, and Model-3, with each model consisting of three samples. Therefore, there are a total of nine samples in each subplot.

To facilitate data explanation, each figure is followed by a table to mirror the data presented in the figures. While the bar graphs are utilized to visually compare the peak values of key parameters across different models and conditions, the table offers a more compact and numerical representation of the same data, focusing on the statistical analysis. For example, Table 6-1 presents the average of the cycles' peaks of internal pressure of each sample under four frequency-pressure conditions and 3 weight scenarios. In the table, "M" represents the model and "S" represents the sample. For instance, M1S1 means the first sample of Model-1. The table also provides the average of three samples to reduce the impact of individual variations when we compare the performance between the models. The third part of the table provides the increasing rate between the conditions, where each comparison is provided with different purpose. Comparing Condition-1 with Condition-2 enable assessing the effect of varying the input pressure from 40 to 60 kPa while the frequency remains constant at 0.2 Hz. On the other hand, Comparing Condition-2 with Condition-3 enables assessing the effect of varying the frequency.

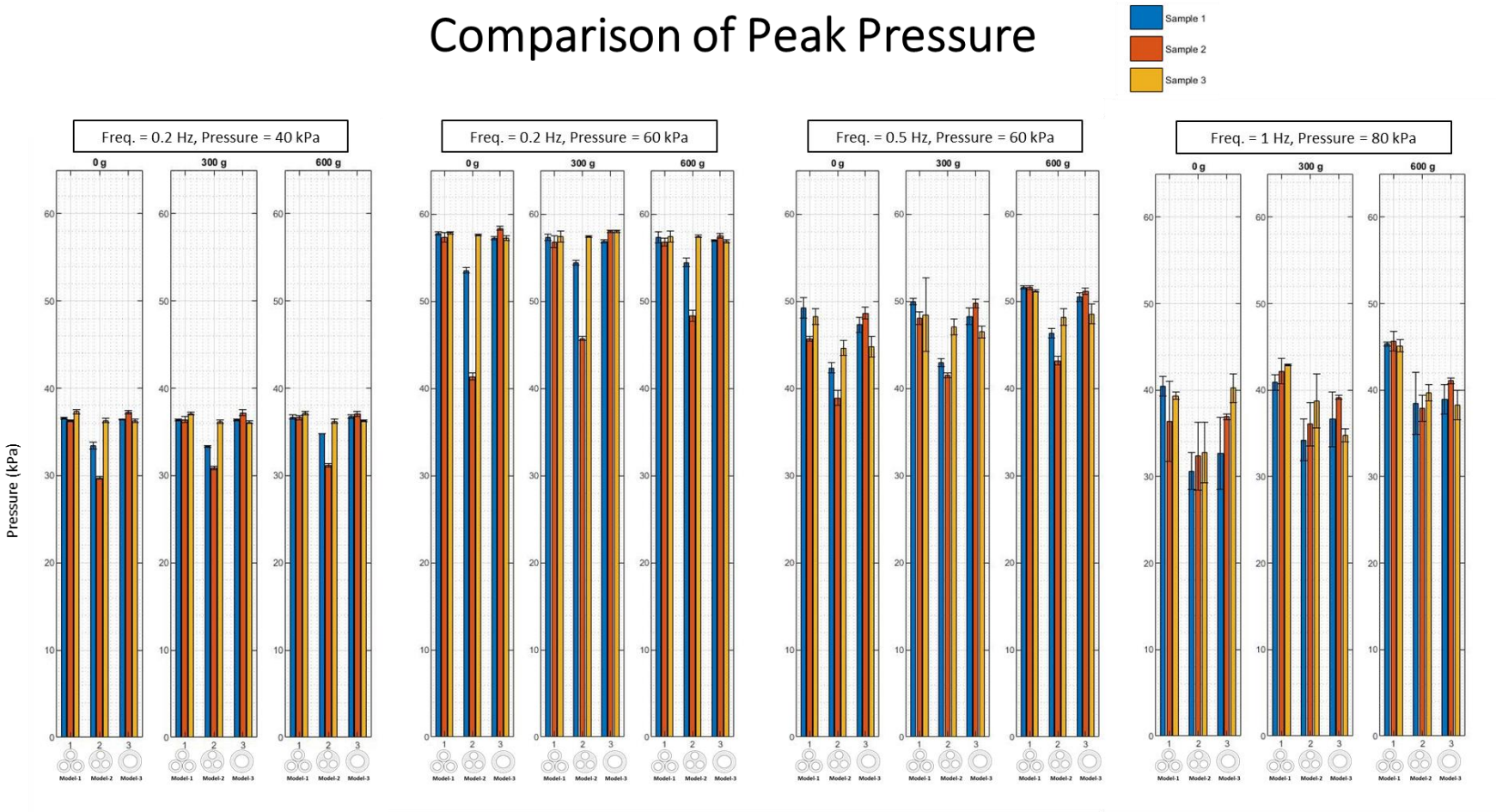

Figure 6-9: Illustrates four testing conditions, displaying the peak resultant internal pressure. Below each condition, there are three corresponding charts depicting weight scenarios at 0 g, 300 g, and 600 g.

Table 6-1: The average of the cycles' peaks of internal pressure of each sample under four frequency-pressure conditions and 3 weight scenarios.

Weight (g)	Model	Max Internal Pressure (kPa)				Average of 3 Samples (kPa)								Inc./Red. Rate (%)	
		Cond-1 0.2Hz-40kPa	Cond-2 0.2Hz-60kPa	Cond-3 0.5Hz-60kPa	Cond-4 1Hz-80kPa	Cond-1		Cond-2		Cond-3		Cond-4		From Cond-1 to Cond-2	From Cond-2 to Cond-3
						Avg	STD	Avg	STD	Avg	STD	Avg	STD		
0	M1S1	36.56	57.76	49.25	40.48	36.72	0.5574944	57.6266667	0.2844878	47.7333333	1.8305282	38.7333333	2.116255	36.28%	-20.73%
	M1S2	36.26	57.3	45.7	36.38										
	M1S3	37.34	57.82	48.25	39.34										
	M2S1	33.43	53.53	42.36	30.62	33.16	3.2933114	50.8233333	8.451564	41.9666667	2.8802141	31.92	1.14346	34.75%	-21.10%
	M2S2	29.74	41.35	38.91	32.37										
	M2S3	36.31	57.59	44.63	32.77										
	M3S1	36.41	57.24	47.28	32.68	36.65	0.5322593	57.6066667	0.6524824	46.8933333	1.9292831	36.61	3.780172	36.38%	-22.85%
	M3S2	37.26	58.36	48.6	36.93										
	M3S3	36.28	57.22	44.8	40.22										
300	M1S1	36.41	57.33	49.99	40.89	36.6366667	0.3839705	57.1766667	0.3464583	48.82	1.0337795	41.9933333	1.026466	35.92%	-17.12%
	M1S2	36.42	56.78	48.03	42.17										
	M1S3	37.08	57.42	48.44	42.92										
	M2S1	33.36	54.42	42.93	34.23	33.4733333	2.6618102	52.5166667	6.0826009	43.82	2.8800521	36.3566667	2.283535	36.26%	-19.85%
	M2S2	30.87	45.71	41.49	36.07										
	M2S3	36.19	57.42	47.04	38.77										
	M3S1	36.41	56.86	48.25	36.64	36.57	0.567186	55.9733333	2.6152693	48.15	1.632299	36.8533333	2.207744	34.67%	-16.25%
	M3S2	37.2	58.03	49.73	39.16										
	M3S3	36.1	53.03	46.47	34.76										
600	M1S1	36.72	57.33	51.6	45.34	36.8366667	0.2650157	57.1766667	0.3464583	51.4433333	0.237557	45.3633333	0.265769	35.57%	-11.14%
	M1S2	36.65	56.78	51.56	45.64										
	M1S3	37.14	57.42	51.17	45.11										
	M2S1	34.78	54.42	46.34	38.47	34.06	2.5765869	53.3866667	4.6469811	45.8933333	2.5198677	38.67	0.896883	36.20%	-16.33%
	M2S2	31.2	48.31	43.18	37.89										
	M2S3	36.2	57.43	48.16	39.65										
	M3S1	36.74	56.92	50.47	38.94	36.69	0.3774917	57.0966667	0.3682843	50.0466667	1.3651496	39.44	1.474992	35.74%	-14.09%
	M3S2	37.04	57.52	51.15	41.1										
	M3S3	36.29	56.85	48.52	38.28										

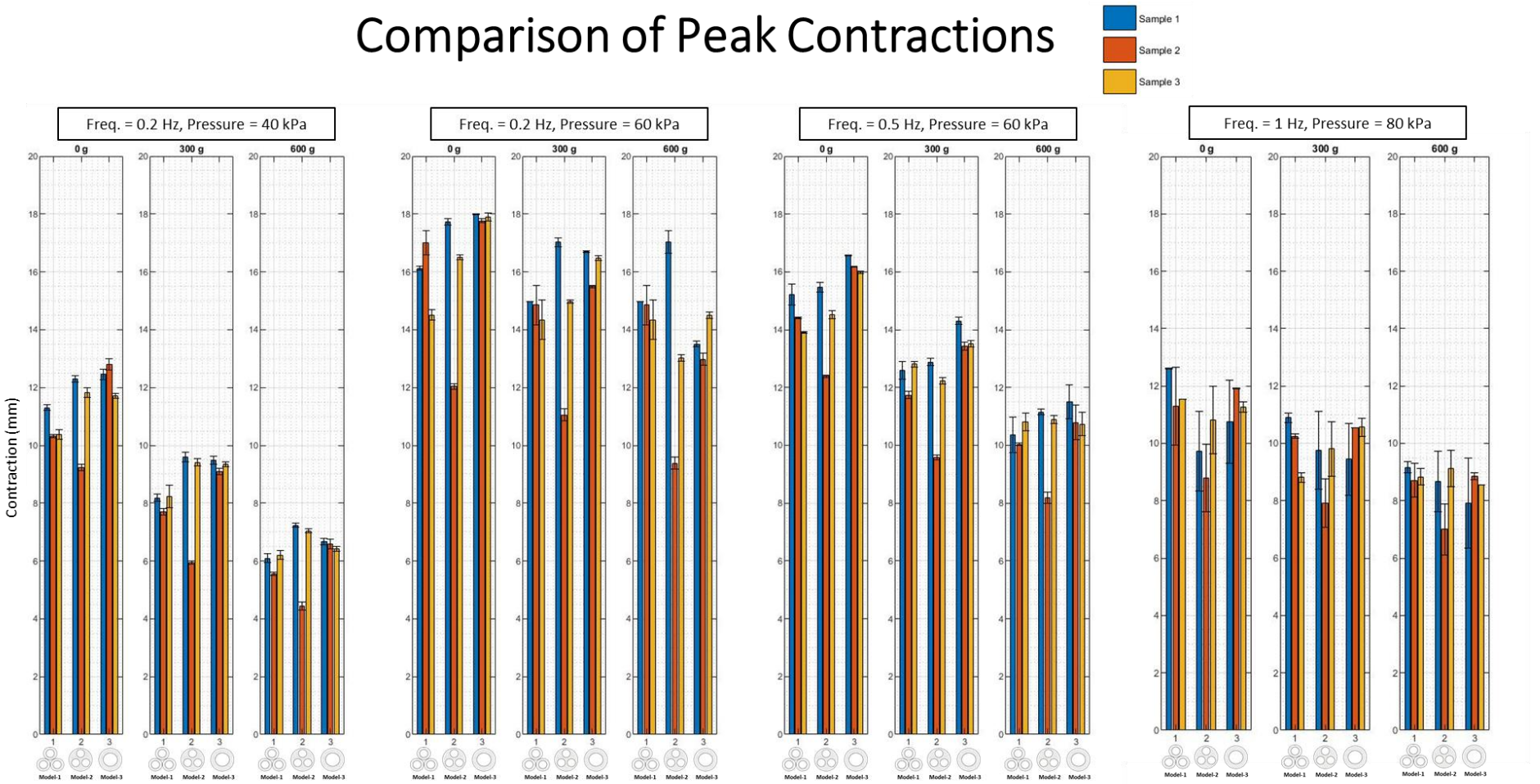

Figure 6-10: Illustrates four testing conditions, displaying the peak resultant SAM's contraction. Below each condition, there are three corresponding charts depicting weight scenarios at 0 g, 300 g, and 600 g.

Table 6-2: The average of the cycles' peaks of SAM's contraction of each sample under four frequency-pressure conditions and 3 weight scenarios.

Weight (g)	Model	Max Contraction (mm)				Average of 3 Samples (mm)								Inc./Red. Rate (%)	
		Cond-1 0.2Hz-40kPa	Cond-2 0.2Hz-60kPa	Cond-3 0.5Hz-60kPa	Cond-4 1Hz-80kPa	Cond-1 0.2Hz-40kPa		Cond-2 0.2Hz-60kPa		Cond-3 0.5Hz-60kPa		Cond-4 1Hz-80kPa		From Cond-1 to Cond-2	From Cond-2 to Cond-3
						Avg	STD	Avg	STD	Avg	STD	Avg	STD		
0	M1S1	11.30	16.12	15.22	12.61	10.67	0.544	15.88	1.273	14.51	0.661	11.81	0.699	32.77%	-9.39%
	M1S2	10.33	17.01	14.41	11.30										
	M1S3	10.39	14.50	13.91	11.53										
	M2S1	12.30	17.72	15.46	9.72	11.12	1.648	15.42	2.992	14.13	1.574	9.78	1.016	27.88%	-9.18%
	M2S2	9.24	12.04	12.39	8.79										
	M2S3	11.83	16.51	14.53	10.82										
	M3S1	12.45	17.99	16.57	10.75	12.30	0.535	17.89	0.111	16.25	0.296	11.31	0.581	31.22%	-10.09%
	M3S2	12.75	17.77	16.18	11.91										
	M3S3	11.71	17.90	15.99	11.26										
300	M1S1	8.18	14.97	12.60	10.89	8.03	0.298	14.72	0.335	12.38	0.567	9.98	1.065	45.43%	-18.87%
	M1S2	7.69	14.85	11.74	10.25										
	M1S3	8.23	14.34	12.81	8.81										
	M2S1	9.59	17.03	12.88	9.76	8.31	2.055	14.35	3.032	11.57	1.742	9.16	1.074	42.10%	-24.09%
	M2S2	5.94	11.06	9.59	7.92										
	M2S3	9.40	14.97	12.23	9.80										
	M3S1	9.48	16.69	14.31	9.44	9.30	0.203	16.22	0.641	13.75	0.484	10.19	0.647	42.66%	-17.94%
	M3S2	9.08	15.49	13.43	10.55										
	M3S3	9.34	16.48	13.52	10.57										
600	M1S1	6.09	14.97	10.37	9.16	5.95	0.342	14.72	0.335	10.41	0.386	8.90	0.233	59.58%	-41.45%
	M1S2	5.56	14.85	10.04	8.71										
	M1S3	6.20	14.34	10.81	8.83										
	M2S1	7.23	17.03	11.16	8.67	6.24	1.559	13.14	3.831	10.08	1.651	8.27	1.119	52.55%	-30.39%
	M2S2	4.44	9.37	8.18	7.00										
	M2S3	7.04	13.03	10.90	9.13										
	M3S1	6.67	13.50	11.51	7.92	6.55	0.128	13.66	0.773	11.01	0.431	8.44	0.477	52.02%	-24.03%
	M3S2	6.57	12.98	10.79	8.85										
	M3S3	6.42	14.50	10.74	8.55										

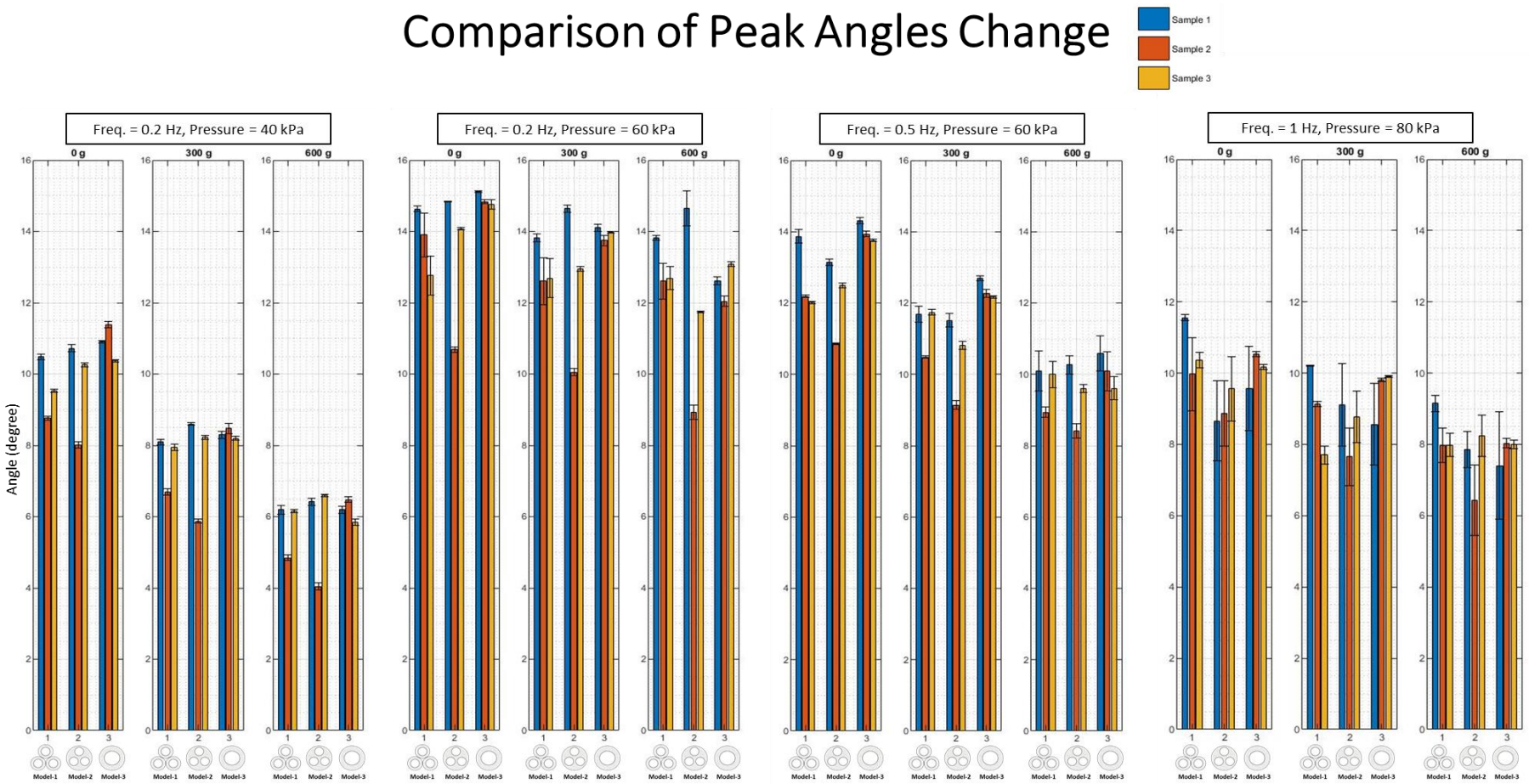

Figure 6-11: Illustrates four testing conditions, displaying the peak resultant joint angle. Below each condition, there are three corresponding charts depicting weight scenarios at 0 g, 300 g, and 600 g.

Table 6-3: The average of the cycles' peaks of change in joint angle of each sample under four frequency-pressure conditions and 3 weight scenarios.

Weight (g)	Model	Max Change in Joint Angle (degree)				Average of 3 Samples (degree)								Inc./Red. Rate (%)	
		Cond-1 0.2Hz-40kPa	Cond-2 0.2Hz-60kPa	Cond-3 0.5Hz-60kPa	Cond-4 1Hz-80kPa	Cond-1 0.2Hz-40kPa		Cond-2 0.2Hz-60kPa		Cond-3 0.5Hz-60kPa		Cond-4 1Hz-80kPa		From Cond-1 to Cond-2	From Cond-2 to Cond-3
						Avg	STD	Avg	STD	Avg	STD	Avg	STD		
0	M1S1	10.48	14.63	13.87	11.56	9.59	0.862	13.76	0.942	12.69	1.026	10.63	0.827	30.35%	-8.46%
	M1S2	8.76	13.90	12.19	9.97										
	M1S3	9.52	12.76	12.01	10.37										
	M2S1	10.72	14.84	13.14	8.65	9.66	1.456	13.20	2.215	12.16	1.180	9.02	0.471	26.82%	-8.55%
	M2S2	8.00	10.68	10.85	8.86										
	M2S3	10.26	14.08	12.49	9.55										
	M3S1	10.91	15.12	14.30	9.56	10.89	0.505	14.90	0.191	14.00	0.276	10.08	0.485	26.95%	-6.48%
	M3S2	11.38	14.83	13.93	10.52										
	M3S3	10.37	14.76	13.76	10.16										
300	M1S1	8.09	13.82	11.69	10.22	7.57	0.769	13.04	0.677	11.31	0.708	9.01	1.263	41.92%	-15.33%
	M1S2	6.69	12.61	10.49	9.12										
	M1S3	7.94	12.69	11.74	7.70										
	M2S1	8.59	14.64	11.51	9.10	7.56	1.483	12.54	2.321	10.48	1.223	8.50	0.758	39.73%	-19.65%
	M2S2	5.86	10.05	9.13	7.65										
	M2S3	8.23	12.94	10.81	8.76										
	M3S1	8.29	14.11	12.70	8.55	8.32	0.137	13.95	0.182	12.38	0.280	9.42	0.755	40.34%	-12.62%
	M3S2	8.47	13.75	12.28	9.81										
	M3S3	8.20	13.98	12.17	9.90										
600	M1S1	6.19	13.82	10.09	9.14	5.73	0.768	13.04	0.677	9.67	0.643	8.36	0.673	56.08%	-34.85%
	M1S2	4.84	12.61	8.93	7.97										
	M1S3	6.15	12.69	9.99	7.98										
	M2S1	6.41	14.64	10.27	7.85	5.68	1.429	11.77	2.860	9.43	0.942	7.51	0.953	51.76%	-24.82%
	M2S2	4.03	8.92	8.41	6.43										
	M2S3	6.59	11.74	9.60	8.24										
	M3S1	6.19	12.61	10.58	7.40	6.17	0.316	12.58	0.521	10.09	0.485	7.81	0.355	50.97%	-24.60%
	M3S2	6.47	12.04	10.09	8.03										
	M3S3	5.84	13.08	9.61	8.00										

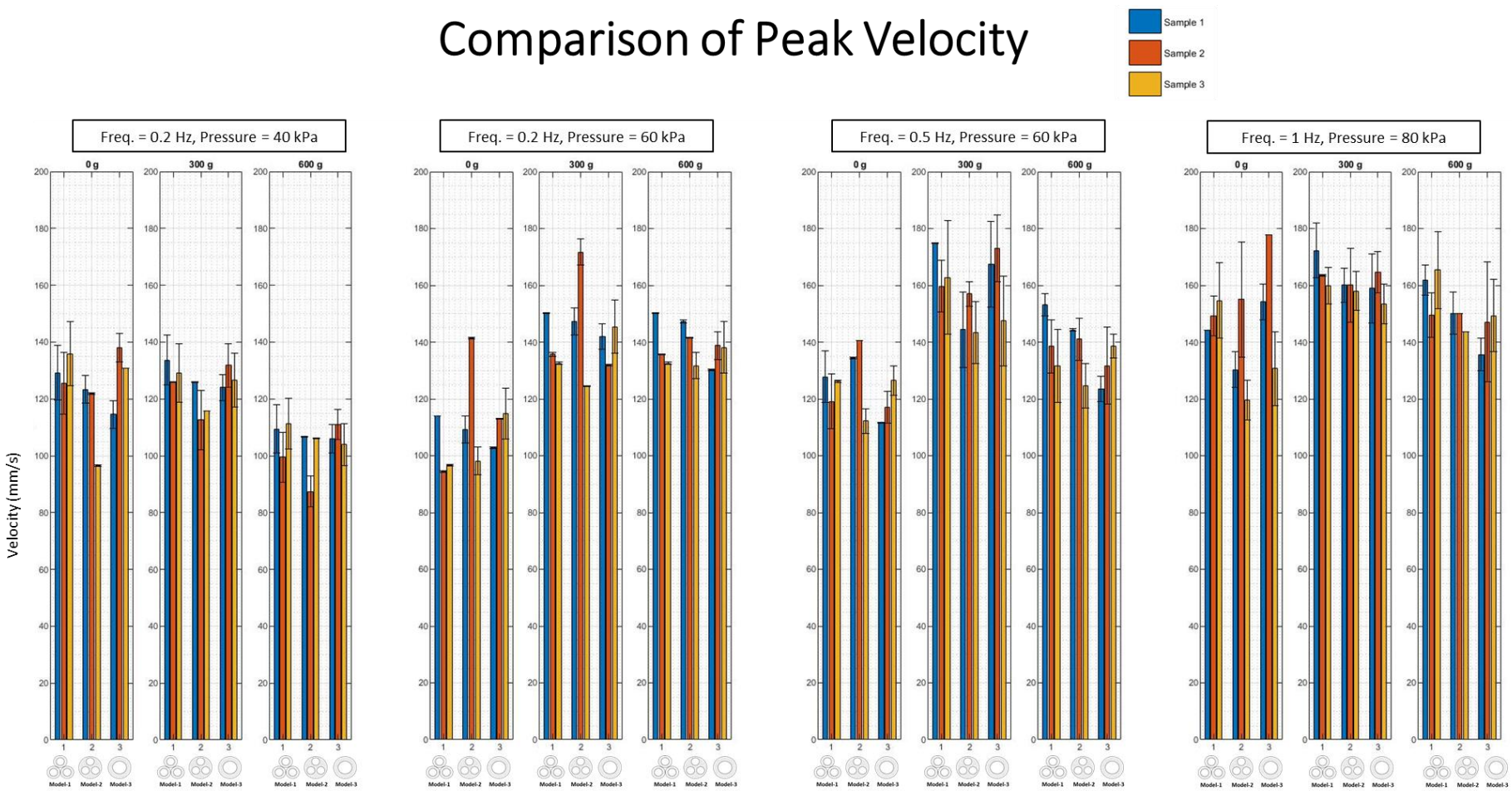

Figure 6-12: Illustrates four testing conditions, displaying the peak resultant arm's velocity. Below each condition, there are three corresponding charts depicting weight scenarios at 0 g, 300 g, and 600 g.

Table 6-4: The average of the cycles' peaks of the arm velocity of each sample under four frequency-pressure conditions and 3 weight scenarios.

Weight (g)	Model	Max Arm Velocity (mm/s)				Average of 3 Samples (mm/s)								Inc./Red. Rate (%)	
		Cond-1 0.2Hz-40kPa	Cond-2 0.2Hz-60kPa	Cond-3 0.5Hz-60kPa	Cond-4 1Hz-80kPa	Cond-1 0.2Hz-40kPa		Cond-2 0.2Hz-60kPa		Cond-3 0.5Hz-60kPa		Cond-4 1Hz-80kPa		From Cond-1 to Cond-2	From Cond-2 to Cond-3
						Avg	STD	Avg	STD	Avg	STD	Avg	STD		
0	M1S1	129.10	113.90	127.70	144.20	130.10	5.272	101.68	10.630	124.33	4.594	149.33	5.201	-27.95%	18.22%
	M1S2	125.40	94.54	119.10	149.20										
	M1S3	135.80	96.61	126.20	154.60										
	M2S1	123.30	109.20	134.40	130.30	113.91	15.074	116.24	22.478	129.13	14.915	134.93	18.198	2.01%	9.98%
	M2S2	121.90	141.40	140.70	155.00										
	M2S3	96.52	98.13	112.30	119.50										
	M3S1	114.60	102.80	111.60	154.10	127.80	11.985	110.23	6.507	118.33	7.490	154.20	23.550	-15.94%	6.85%
	M3S2	138.00	113.00	117.00	177.80										
	M3S3	130.80	114.90	126.40	130.70										
300	M1S1	133.70	150.20	174.80	172.30	129.53	3.968	139.53	9.375	165.77	7.975	165.17	6.435	7.17%	15.83%
	M1S2	125.80	135.80	159.70	163.40										
	M1S3	129.10	132.60	162.80	159.80										
	M2S1	126.00	147.40	144.40	160.00	118.07	7.032	147.87	23.603	148.23	7.522	159.33	1.155	20.15%	0.25%
	M2S2	112.60	171.70	156.90	160.00										
	M2S3	115.60	124.50	143.40	158.00										
	M3S1	124.00	142.00	167.40	159.00	127.43	3.983	139.80	6.966	162.63	13.402	158.97	5.550	8.85%	14.04%
	M3S2	131.80	132.00	173.00	164.50										
	M3S3	126.50	145.40	147.50	153.40										
600	M1S1	109.50	150.20	153.20	161.80	106.76	6.374	139.53	9.375	141.17	10.977	158.87	8.394	23.49%	1.16%
	M1S2	99.47	135.80	138.60	149.40										
	M1S3	111.30	132.60	131.70	165.40										
	M2S1	106.60	147.40	144.30	150.10	100.03	10.949	140.23	7.939	136.60	10.608	147.90	3.811	28.67%	-2.66%
	M2S2	87.39	141.60	141.00	150.10										
	M2S3	106.10	131.70	124.50	143.50										
	M3S1	106.00	130.10	123.50	135.60	106.93	3.592	135.63	4.801	131.23	7.511	144.00	7.357	21.16%	-3.35%
	M3S2	110.90	138.70	131.70	147.10										
	M3S3	103.90	138.10	138.50	149.30										

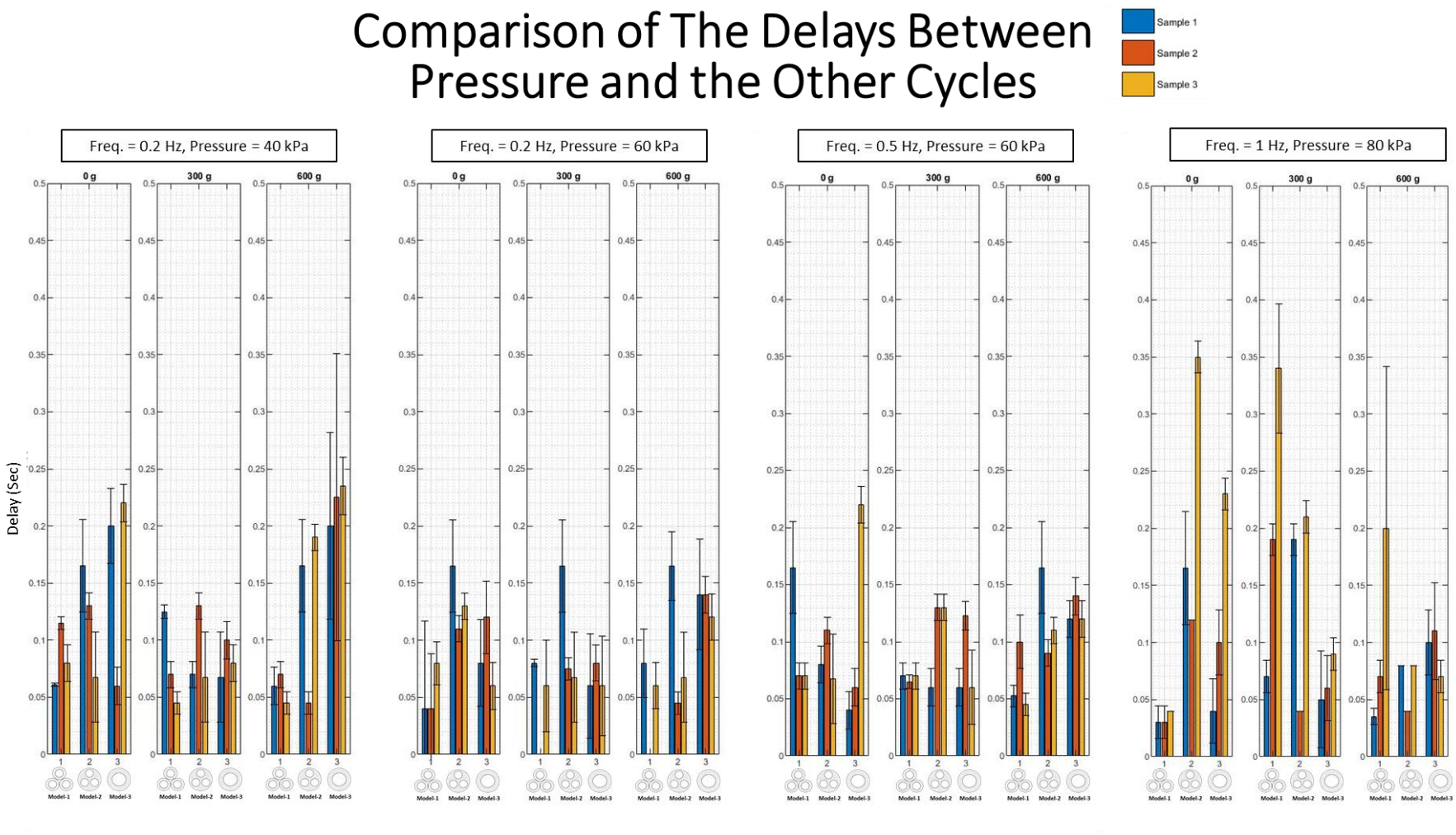

Figure 6-13: Illustrates four testing conditions, displaying the peak resultant delay between the internal pressure and contraction/angle/velocity. Below each condition, there are three corresponding charts depicting weight scenarios at 0 g, 300 g, and 600 g.

*Comparison of Peak **Internal Pressure** - **Observation**:*

By observing the pressure bar graphs (Figure 6-9), we can see that the rank of conditions is as follows: Condition-2 > Condition-3 > Condition-1 > Condition-4. At higher frequencies, there is greater variation between the samples. This is because lower frequencies lead to higher stability in the soft actuator's performance.

At Condition-2 with no weight attached, the rank of internal pressure among the models follows this order: Model-1 > Model-3 (approximately equal to Model-1 in many cases) > Model-2. The second sample of Model-2 consistently exhibits the lowest internal pressure under all conditions. This low internal pressure is one of the reasons behind Model-2's lower overall values. Additionally, Model-2 displays the highest STD due to the second sample’s odd result. In most other conditions, the same rank order among the models is repeated.

The rate of increase in internal pressure varies when comparing different conditions (shown in last column in Table 6-1). To have a reference point for comparison, Condition-1 is selected as it generally shows the lowest output values. For instance, in the first sample of Model-1 with no weight attached, the average internal pressure at Condition-1, Condition-2, Condition-3, and Condition-4 are 36.72, 57.62, 47.73, and 38.73 kPa, respectively. The rate of increase between Condition-1 and Condition-2 is 36.27%, while it is 23.07% between Condition-1 and Condition-3, and 5.19% between Condition-1 and Condition-4. This trend is consistent with all samples, where the highest rate of increase is between Condition-1 and Condition-2, while the lowest is between Condition-1 and Condition-4.

As the frequency increases, the standard deviation (STD) of the pressure cycles also increases. In Condition-1 and Condition-4, the measured internal pressure values are similar. However, it is evident that in Condition-4, the variation between samples and the STD are higher due to the high frequency.

The bar graphs (Figure 6-9) show the attached weight does not significantly affect the measured internal pressure. Only small variation is observable between the samples at 0 g, 300 g, and 600 g weights. This indicates that the weight cases do not impact the measured pressure in the system. For example, the average internal pressure of the first sample of Model-1 at Condition-2 is 57.62 kPa with no weight attached, and it is 57.17 kPa with 300 g attached and 57.17 kPa with 600 g attached.

*Comparison of Peak **SAM's Contraction** - **Observation**:*

In a similar way to the internal pressure data comparison, Figure 6-10 covers the peak contraction test results via four bar graphs. After observing the bar graphs, the effect of the hung weight on the range of contraction is clear. As weight increases, the range of contraction of SAM decreases due to the added weight's resistance. For instance, at condition-1, the average displacement of the first sample of Model-1 is 10.67 mm with no weight attached, and it is 8.03 mm with 300 g attached and 5.95 mm with 600 g attached.

Across most conditions and weight scenarios, Model-3 exhibits the highest range of contraction, followed by Model-1 with a small gap and then Model-2 with bigger gap. However, in some scenarios, Model-1 surpasses the others and shows the highest range of contraction. For example, in Condition-1, Condition-2, and Condition-3 with no weight attached, the superiority is for Model-3, while in Condition-4 the superiority is for Model-1.

We can see how SAM responds to different pressures and frequencies by looking at the various test conditions. The rate of increase between Condition-1 and Condition-2 is greater compared to the increase between Condition-1 and Condition-3. For instance, in the first sample of Model-1, the rate of increase between Condition-1 and Condition-2 is 32.77%, while it is 26.46% between Condition-1 and Condition-3, and 9.65% between Condition-1 and Condition-4.

The displacement bar graphs show this ranking order among conditions: Condition-2 > Condition-3 > Condition-1 and Condition-4, with Condition-1 and Condition-4 showing relatively similar behaviour. Unlike the internal pressure measurements, no significant impact of test conditions on the variation between samples (represented by STD in Table 6-2) is observed in the displacement measurements.

The second sample of Model-2 always shows a lower range of contraction compared to the average of all samples at all conditions. In Model-1 and Model-3, there is minor variation in the range of contraction between the samples. Notably, Model-3 always shows the least variation between its samples due to its simpler design, resulting in minor variations during fabrication and testing. For instance, when looking at the average range of contraction at Condition-1 with no added weight, the STDs for Model-1 and Model-3 are 0.544 and 0.535 respectively, while Model-2 shows a higher STD of 1.648. These findings explain how different models and conditions affect the range of contraction of SAM.

*Comparison of peak **change in joint angle** - **Observation**:*

Figure 6-11 represents the peak of the joint angle using the same methodology as the previous parameters. The relative values here between the samples are similar to the values in the contraction. This indicates that the motion of the arm is correlated to SAM's range of contraction. This suggests that analysing the contraction behaviour of the SAM can effectively predict the behaviour of the arm segment under varying load conditions.

A clear relationship exists between attached weight and joint angle in Model-1: as weight increases, the average peak joint angle decreases. For instance, under Condition-1, the initial sample with no weight exhibits an average peak angle of 9.59°. Adding 300 grams reduces the average angle to 7.57°, and with 600 grams attached, the angle further drops to 5.73°. Notably, the standard deviation values also show consistent patterns across weight scenarios.

*Comparison of peak **velocity - Observation**:*

Figure 6-12 represents the peak lower arm angular velocity, following the same methodology as in the previous layouts. The peak velocity consistently occurs during the de-actuation stage, when the lower arm drops due to the sudden air release of SAM. From comparing the bar graphs, it is not clear whether the changes in the input pressure or the attached weight have an influence the peak velocity. Additionally, when comparing the SAM's models, we do not observe any significant impact on the velocity. However, there is a minor influence shown from the variation in frequency. As the frequency increases, the lower arm segment raises and drops a little more rapidly.

*Comparison of **delay** - **Observation**:*

Figure 6-13 shows the short period of delay between the internal pressure and the other synchronized parameters (range of contraction, joint angle, and angular velocity of the lower arm). This delay represents the extra time taken by the system to respond to the internal pressure changes. The time delay is determined by measuring the offset between the beginning of rise in the internal pressure curve and the corresponding points of the other parameters. When the internal pressure begins to rise, there is usually a slight period before the range of contraction, joint angle, and angular velocity respond to these changes. This delay occurs due to factors such as the length of the tubing connections, the soft actuator's mechanical

response times, or control mechanisms like pressure regulator delay. Using lengthy tubing connections caused the air to take longer to travel through tubes, which can result a delay in the actuator's response time. To resolve this delay the tubing length and diameter might be optimized to minimize this delay and improve the actuator's time performance.

In the delay layout, the detected delay spanned a range of 0 to 0.35 seconds. Notably, only two cases out of a total of 108 cases (3 Models x 3 Samples x 3 Weights Scenarios x 4 Conditions) displayed zero time delay. It is important to know that the absence of time delay in these two cases is due to the sampling rate of the recording system. The sampling rate is set at 0.02 seconds, which makes it unable to detect the very minor time delays in the system. In real use, there should be a delay between the internal pressure and the other outputs.

Another observation from this analysis is that there is no clear influence of the test conditions (input pressure, actuation frequency, or additional weight) on the time delay. This indicates that the time delay is independent of the changes in the test conditions. This time delay is an important factor to consider when designing soft actuator systems for real applications that require precise control.

6.5.2 Augmented Set of SAM

6.5.2.1 Main Tests

In the layout of Figure 6-14, multiple plots are synchronized along the time x-axis. The test involves a single sample of each model being subjected to a cyclic actuation pattern: 2.5 seconds of activation at 0.2 Hz and 60kPa, followed by 2.5 seconds of de-activation. This pattern is reflected in the synchronized plots, which reveal the same key relationships parameters: internal pressure (kPa), SAM's contraction (mm), change in joint angle (degrees), and lower arm angular velocity (mm/s).

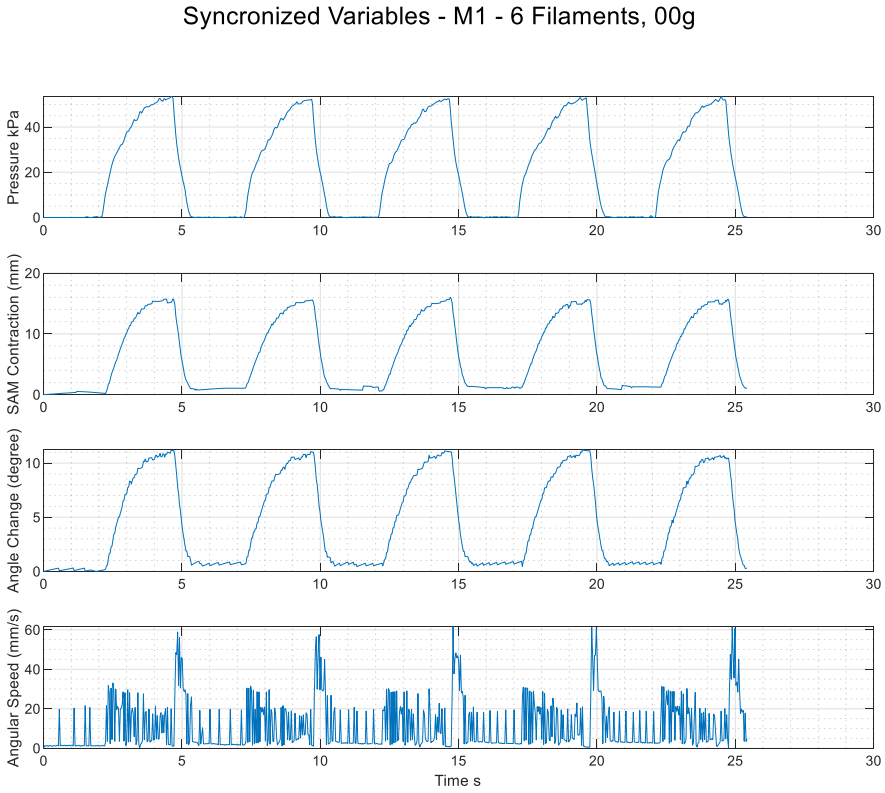

Figure 6-14: Synchronized display of internal pressure of SAM, SAM's Contraction, change in joint angle, and lower arm angular velocity for the augmented set of SAM of Model-1 at 60 kPa and 0.2 Hz, with no attached weight.

Pressure, contraction, and joint angle all exhibit similar cyclical behaviour during both actuation and de-actuation phases. This suggests a strong relationship between the internal pressure of the SAM, its contraction, and the resulting movement of the arm's joint. This behaviour mirrors that of the original set of SAM with 3 cavities/filaments (3C/F), where pressure, contraction, and joint angle cycles showed similar patterns during both actuation and de-actuation phases. Lower arm angular velocity shows fluctuations throughout the cycle, with a significant spike at the transition from actuation to de-actuation. This spike is likely due to the sudden drop in pressure within the SAM, causing a rapid change due to the gravity effect and consequently.

Table 6-5 summarizes the results of the experiments for the three models with three weight case scenarios for each model. Each value in the table represents the peak values observed for various parameters, including internal pressure, contraction, joint angle, and velocity.

Table 6-5: The experimental results for the augmented models of SAM with three weight case scenarios for each model.

Weight (g)	Model	Pressure (kPa)	Contraction (mm)	Joint Angle (degree)	Speed (mm/s)	Delay (s)
0	Model-1	53.1808466	15.7701354	11.0582343	60.76	0.14
	Model-2	54.0806676	15.4657981	10.85905301	63.22	0.1
	Model-3	53.3026529	18.2990737	13.21909359	77.6	0.08
300	Model-1	52.6768924	15.2754588	9.987644765	84.9	0.12
	Model-2	53.8246223	15.3139213	11.31095651	82.27	0.06
	Model-3	56.1699902	18.1263791	13.41897323	92.53	0.66
600	Model-1	51.3256095	13.7507915	10.23349541	82.88	0.06
	Model-2	53.6387996	13.7982848	10.84273133	82.73	0.06
	Model-3	55.3009538	15.5519476	13.31570875	87.3	0.1

The analysis below explains how variations in the SAM model and the attached weight influence SAM's performance metrics such as internal pressure, contraction, joint angle, and velocity:

- **Pressure and Weight**: in Model-1 and Model-2, when the weight increases, the pressure decreases. However, Model 3 did not show a clear relationship between internal pressure and weight. Therefore, no clear correlation can be seen from this experiment between the SAM's internal pressure and weight.
- **Pressure and Models**: without adding weight, the internal pressure readings are similar for all models. In contrast, at 300 and 600 g, the internal pressure is bigger in Model-3 with an observable gap, followed by Model-2 and then Model-1 which show a smaller gap between them.
- **Contraction and weight**: in all models, when the weight increases, the contraction decreases. Notably, the difference in contraction between the scenarios at no weight and 300 g is smaller compared to the difference between the scenarios at 300 g and 600 g weights.
- **Contraction and Models**: Model-3 provides the highest amount of contraction at all weight case scenarios. Model-1 and 2 show very similar results at all weight case scenarios.
- **Joint Angle and weight**: despite an expected correlation between the joint angle and weight because weight has a great effect on SAM’s contraction and the joint angle depends on the SAM’s contraction, we cannot see any effect of adding weight onto the joint angle across all models.
- **Joint Angle and Models**: when comparing the models, Model-3 provides the highest change in the joint angle across all weight case scenarios, followed by Model-2 and then Model-1 with a smaller gap between them.
- **Delay Analysis**: the delay between the internal pressure and the other variables (SAM’s Contraction, joint angle, and velocity) is influenced by various factors such as regulator performance, SAM’s model, the attached

weight. Therefore, we cannot observe a relationship between the period of delay and changing the SAM's model or the amount of the attached weight.

6.5.3 Summary of Key Observations

Internal Pressure Observations:

- Higher frequencies led to greater variations between samples, indicating lower stability at higher frequencies.
- The rank of internal pressure among conditions generally followed Condition-2 > Condition-3 > Condition-1 > Condition-4.
- The weight attached did not significantly impact the measured internal pressure.

SAM Contraction Observations:

- As weight increased, the range of contraction decreased due to the added resistance.
- Model-3 generally exhibited the highest range of contraction across most conditions and weight scenarios.
- The rate of increase in contraction between different conditions showed a greater increase between Condition-1 and Condition-2 compared to other condition pairs.

Joint Angle Observations:

- A clear relationship was observed between the weight attached and the peak joint angle, particularly in Model-1.
- The motion of the arm segment was correlated to SAM's range of contraction, indicating that SAM's contraction directly influenced joint angle changes.

Velocity Observations:

- Peak velocity occurred during the de-actuation stage due to a sudden pressure drop.
- No significant influence of pressure or weight on peak velocity was observed, though minor effects were noted with frequency variations.

Delay Observations:

- The delay between internal pressure and other synchronized parameters (contraction, joint angle, angular velocity) was observed.
- No clear influence of test conditions (input pressure, actuation frequency, or additional weight) on the time delay was found.

Augmented Set of SAM Observations:

- Similar cyclical behaviour in pressure, contraction, and joint angle during both actuation and de-actuation phases was noted.
- Model-3 showed the highest contraction across all weight scenarios, while Model-1 and Model-2 exhibited similar results.
- No clear correlation between the SAM's internal pressure and weight in Model-3 was observed.
- Delay analysis indicated that various factors influenced the period of delay, without a consistent pattern linked to the SAM model or weight.

6.6 Discussion

6.6.1 Performance Analysis of the Key Parameters

The results from Chapter 6's case study experiments are compared to the main characterization results obtained in Chapter 5 (force and displacement). This comparison helps understand how the dynamic system's performance aligns with or diverges from the isolated tests of force and displacement.

In Section 5.1, Model-2 consistently generated the highest force, followed by Model-1 and Model-3. However, in Section 5.2, we could not observe the superiority of Model-2 over the other models because these experiments do not measure force as an independent metric. Instead, the range of contraction is a primary focus in the case study experiments. Referring to the findings of Section 5.2, Model-3 exhibited the highest range of contraction. In Chapter 6, Model-3 also showed significant contraction ranges in the dynamic system. This confirms that the displacement behaviour observed in isolated tests translates well into dynamic applications.

6.6.2 Performance Analysis of SAM

By examining the results of the original and augmented sets of SAMs, it becomes evident that the augmented set shows relative consistency with the original set in terms of internal pressure, contraction, joint angle, and speed. The comparison is based on tests conducted under the condition of 60 kPa and 0.2 Hz.

For internal pressure, both the original and augmented SAMs demonstrated similar performance across different weight scenarios, indicating that lifting more weight does not significantly affect the measured internal pressure in the pneumatic system. However, the range of internal pressure was slightly higher in the original set, varying from 56 to 57 kPa, compared to 52 to 56 kPa for the augmented set. This difference could be due to the larger cavities in the augmented set, which might take longer to reach the maximum pressure (input pressure).

When comparing contraction metrics, both the original and augmented SAMs showed similar performance. In both sets, Model-3 consistently exhibited the highest range of contraction, while Model-1 and Model-2 had a lower range of contraction. However, the augmented set had a slightly higher range of contraction, from 14 to 18 mm, compared to 13 to 16 mm for the original set. This increase could be due to the smaller ratio between the length and diameter of the augmented SAM, allowing for more radial inflation and higher contraction.

In terms of joint angle changes, the results followed the same trend as contraction, with Model-3 consistently exhibiting the highest range of joint angle change. There was no significant difference between the original and augmented SAMs regarding the range of joint angle changes.

Lastly, the angular velocity of the lower arm differed between the original and augmented SAMs. In the original set, Model-2 mostly exhibited the highest range of contraction velocity, while in the augmented set, Model-3 consistently had the highest contraction velocity. The measured velocity represents the peak which occur during the falling motion of the lower arm due to gravity and the attached weight, as there is no component in the dynamic system to extend the arm. This recorded when pressure release, with minor resistance applied by the SAM. The velocity in the original set ranged from around 100 to 145 mm/s, whereas in the augmented set, it ranged from 60 to 90 mm/s. This difference could be due to the higher resistance in the augmented SAM, preventing the lower arm from falling rapidly.

6.6.3 Comparison with Literature

The case study's dynamic system employed a commercially available hinge connected to aluminium strut profiles to enable rotational movement around a central axis. Additionally, SAMs were integrated using a combination of 3D-printed components, acrylic, and steel to create the upper and lower hinges. The testing methodology and performance were compared to the findings of Carvalho *et al.* [76] and Nabae *et al.* [74] to evaluate the performance of this dynamic system.

1- Carvalho *et al.* [76] used lightweight aluminium T-slot sections for the main support structure of their exoskeleton, which included two distinct hinges with an angle sensing arrangement on one hinge. Their design primarily used metallic materials and aimed to support the user's arm for repetitive motion therapy. They used a PAM model with a soft component diameter of 12 mm and a length of 200 mm. Comparing our model to Carvalho *et al.*'s [76] model reveals that, although the diameters of the soft components are similar, Carvalho *et al.*'s [76] PAM is almost twice the length. This longer length likely results in a greater range of contraction. Our results (section 7.5.1) show that the achieved angle between the upper and lower arms of the dynamic system is directly correlated to the range of contraction.
   Another notable difference between the two models is the mechanism used to return the arm to its initial extended position, addressing the antagonistic nature of the muscle actuator. In this research, the exoskeleton is positioned to allow the forearm to fall due to gravity, simplifying the return to the initial position. Carvalho *et al.* [76] used a torsion spring to achieve the same effect during the extension. Our testing showed a driving angle of approximately 13° at 60 kPa, which is minor compared to Carvalho *et al.* [76], who achieved around 0° at 50 kPa, 5° at 100 kPa, and 40° at 400 kPa.
2- Nabae *et al.* [74] utilized 3D-printed links for their two-part link structure, incorporating McKibben muscles. Their method involved coupling parts and end caps, which faced issues related to loose attachment, potentially causing performance inconsistencies due to uncontrolled muscle motion. They used one muscle for extension and two muscles for flexion in their robotic arm, achieving a driving range of approximately 73° at 500 kPa.

The muscle actuators presented by Carvalho *et al.* [76] and Nabae *et al.* [74] demonstrated high contraction capabilities at higher pressures compared to the SAMs used in this research. This difference could be due to the dimensions of the actuators and the design of the dynamic system. Longer muscle actuators lead to more significant contraction and possibly a higher achieved angle

between the arms. Additionally, as discussed in Section 5.2, the materials and components of the SAMs also play a role. Despite the lower contraction capability, SAMs demonstrate a more efficient use of pneumatic actuation at lower pressures, showing more energy-efficient operations. Future improvements could aim to increase the driving angle while maintaining the low-pressure advantage.

Chapter 7 FE Simulation of SAM

7.1 Introduction

This chapter explores into the FE simulation of the SAM, highlighting its importance in understanding how SAM behaves under different loading conditions. FE modelling can play an important role in the development and application of SAM by providing a tool for predicting and validating the parameters of these systems. Relying only on the experimental characterizations to compare the performance of the three SAM's models can be challenging due to the possible inconsistencies in fabrication and testing conditions. By using FE simulations, specific parameters can be precisely controlled, offering a consistent way to replicate and compare behaviours that may be hard to capture through physical testing alone.

The study provides detailed characterizations for three different SAM models and highlights key challenges in FE modelling. These include selecting the appropriate hyperelastic model for the soft component and conducting preliminary FE modeling of the complex braided sleeve. The preliminary FE work on the braided sleeve was necessary due to initial challenges related to excessive stiffness and convergence issues in the simulation. The adjustments made to the material properties helped address these challenges and allowed the simulation to better approximate the real behaviour of the braid. These efforts aim to lay the groundwork for simulating the complete SAM model, integrating both the braid and the soft components.

This chapter discusses these challenges and describes methodologies to overcome them. Furthermore, to validate the models developed, this chapter elaborates on the FE simulations conducted for two specific tests: the displacement test and the block force test. These tests, which replicate the experimental setups described in Chapter 5 respectively, are critical for verifying the predictive accuracy of the FE models against the observed behaviours of the real SAM systems.

7.2 Objectives

This chapter aims to employ FE modelling and simulation techniques to enhance the evaluation of SAM. Accordingly the following objectives are raised:

Objective 1: Develop and simulate a FE model for a soft component without strain limiting component (braid) to analyse its hyperelastic behaviour.

Objective 2: Perform preliminary FE modelling of the braided sleeve to capture its complex geometry and function as the strain-limiting component within SAM.

Objective 3: Conduct FE simulation on the assembled model of SAM to analyse and predict the complex behaviour of the complete SAM actuator.

Objective 4: Validate the reliability of the FE simulations of SAM against experimental findings.

7.3 Modelling of the Braided Sleeve Structure

7.3.1 Real Model of the Braid

The complex motions of braided sleeve, characterized by significant deformation and friction. Considering the complexities of modelling such a system due to its numerous nodes and elements and the inherent nonlinearity, creating an analytical model is complex and time intensive. To address this, a three-dimensional model based on FE analysis has been developed to aid in the design of this braid. The construction of the model proceeded through featuring spirally interlaced fibres (braid segments), as illustrated in Figure 7-1a. To accurately capture the characteristics of the real model of a braided sleeve used in SAM, a piece of the braided sleeve, identical in length to those used in SAM fabrication, was analysed. This piece was 110 mm long, a length chosen to match the length used in the real SAM.

The real braided sleeve was intricately constructed with 56 interlaced fibers, consisting of 28 fibers wound in a clockwise (CW) direction and 28 in a counter-clockwise (CCW) direction. Each of these fibers has a diameter of 0.2 mm. The fibers in the braided sleeve follow a helical path, described as a 3D curve spiralling around a central linear axis. The geometry of this spiral is defined by a pitch of 83.33 mm and a total of 1.5 revolutions around the axis. In developing the 3D FE model of the braided sleeve, these parameters were the guid in creating the FE model.

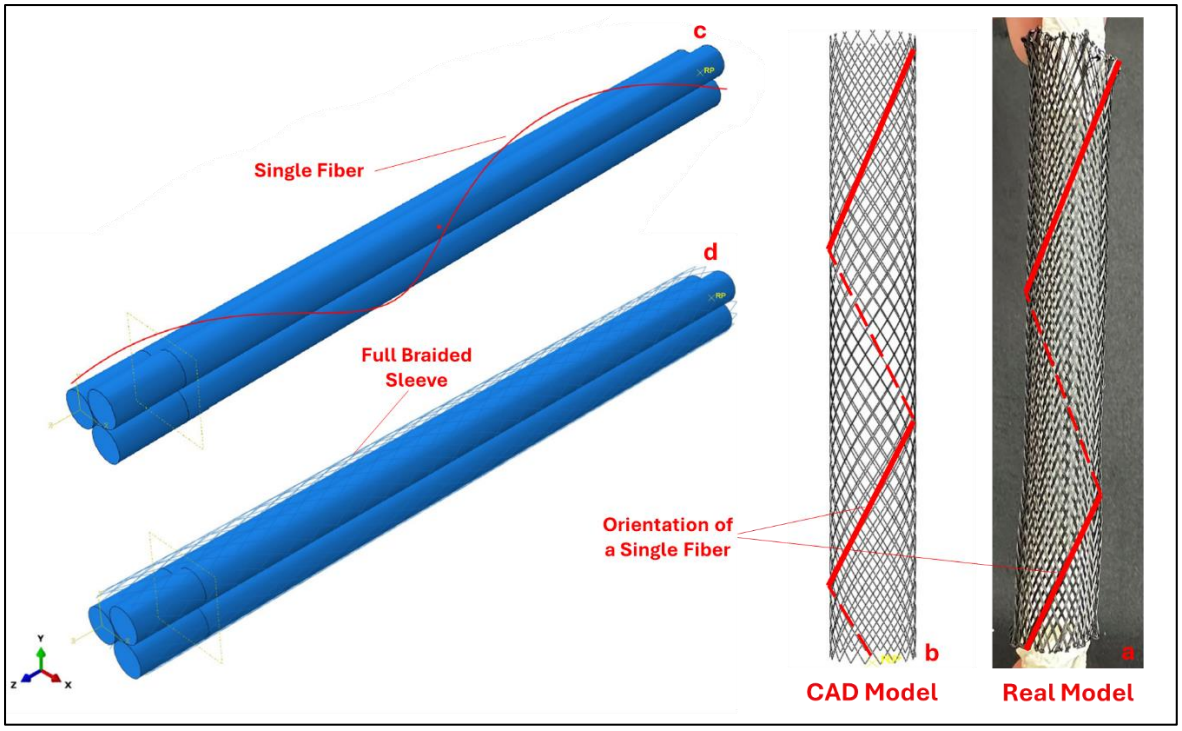

Figure 7-1: (a) Real braided sleeve with highlighted orientation of a single fiber, (b) CAD model of the braided sleeve showing the highlighted fiber orientation, (c) CAD model of a single helical fiber around a soft component, and (d) Full braided sleeve embedded.

7.3.2 FE Model of the Braid

Constructing the 3D geometry of an interlaced braided sleeve can be complex. To address this, the braided sleeve structure was created using "Abaqus PDE," an application accessible within Abaqus/CAE to run Python scripts. The Python script used was adapted from a script provided in a Soft Robotics Toolkit [44] fibers originally designed to create a single helical thread. This thread is typically used to reinforce soft actuators known as "Fiber-Reinforced Actuators." The script was modified to accommodate the features of the braid fiber in the clockwise (CW) direction. Subsequently, another fiber was added in the counterclockwise (CCW) direction. Running the script should create a helical 3D wire structure (shown in Figure 7-1c). Both fiber types were then repeated 20 times to replicate the real contraction motion (shown in Figure 7-1d). CW and CCW components were designed to intersect and having common nodes between them. Regardless of the actual number of fibers in the real braid, the initial modelling progression showed that the quantity of interlaced fibers impacts the behaviour of the contraction.

In creating a fiber in the braid, parametric equations are used to describe a helix in three-dimensional space. The key variables in the equation of a helix include the radius, the angular position, and the pitch. It is important to distinguish between the angular position and the braiding angle. The angular position sets the direction of the fibers, representing the angle that a point on the helix makes with the x-axis (reference direction). The braiding angle is the angle formed where the clockwise and counterclockwise fibers cross each other (shown in the zoom-in in Figure 7-2). Initially, a helical angle of 70° did not allow the SAM to contract much. After testing different angles, we found that 65° was the optimal angle for better performance of the SAM. This modification leads to change the revolutions around the axis from 1.5 to 1.7 (shown in Figure 7-1b).

The real braided sleeve in the SAM is made from PET (Polyethylene Terephthalate). The fibers were modelled using an isotropic elastic material model, with the physical properties of PET sourced from the literature [91]: a density of 1.35E-6 kg/mm^3, a Poisson's ratio of 0.37, and a Young's modulus of 0.7 GPa. However, during the FE simulation, using a Young's modulus of 0.7 GPa led to convergence issues and excessive stiffness, preventing the SAM from achieving the desired contraction. To address this, the Young's modulus was reduced to 0.15 GPa through a series of trials, enabling the FE model to more closely replicate the real model's behaviour and allowing the simulation to converge.

These adjustments on the Young's modulus and braiding angle were considered as preliminary work to facilitate further FE simulations on the full SAM model, which integrates both the braid and soft components. Future work will be required to refine representation of the material properties and improve the accuracy of the model, ensuring a more complete and robust analysis.

These fibers featured a circular cross-section that assigned in Abaqus as a circular beam with a diameter of 0.2 mm. Mesh Control is applied, setting the element type to 'standard linear beam' and defining the approximate global size of the mesh as 0.2. The automatic element meshing is used for the element division to make 68,133 nodes and 23,088 elements. Key details regarding the parameters of the FE model are listed in Table 7-1.

Independent modelling of the braided sleeve before integrating it with the soft component and constructing a full FE model of the SAM helps in early detection of any design defects within the braided sleeve. The lowest nodes of both the CW and CCW fibers are fixed in position by using Encaster boundary condition, while the uppermost nodes are restricted to only allow movement in the Z-direction. A displacement boundary condition of -28 mm is applied to the top nodes of the

braided sleeve. This is the maximum possible displacement in the simulation, as beyond -28 mm, convergence issues arise due to fiber interference. The applied boundary conditions mimic those of the physical model as shown in Figure 7-2. The sequence of coloured sections depicts the sleeve at various stages of contraction, highlighting an increase in diameter and a widening of the braiding angle.

Table 7-1: Key input parameters for FE modelling of the braided sleeve.

Part Module	
Geometry	20 CW and CCW helical fibers
3D Model	Python scripting
Base Feature	3D Wire, circular beam, r=0.2 mm
Dimensions	Fiber angle = 65° Length= 110 mm radius= 5.2 mm

Property Module (SLC)	
material	PET
Density	1.35E-9 tonne/mm3
Young Modulus	150 MPa
Poisson Ratio	0.36

Step Module	
Step type	Static-General
Time Period	1
Increment size	0.05

Load Module	
BC1	ENCASTRE (representing the lower plate)
BC2	Displacement=-28 in z-axis

Mesh module	
Seeding size	0.2
Geometric order	Quadratic

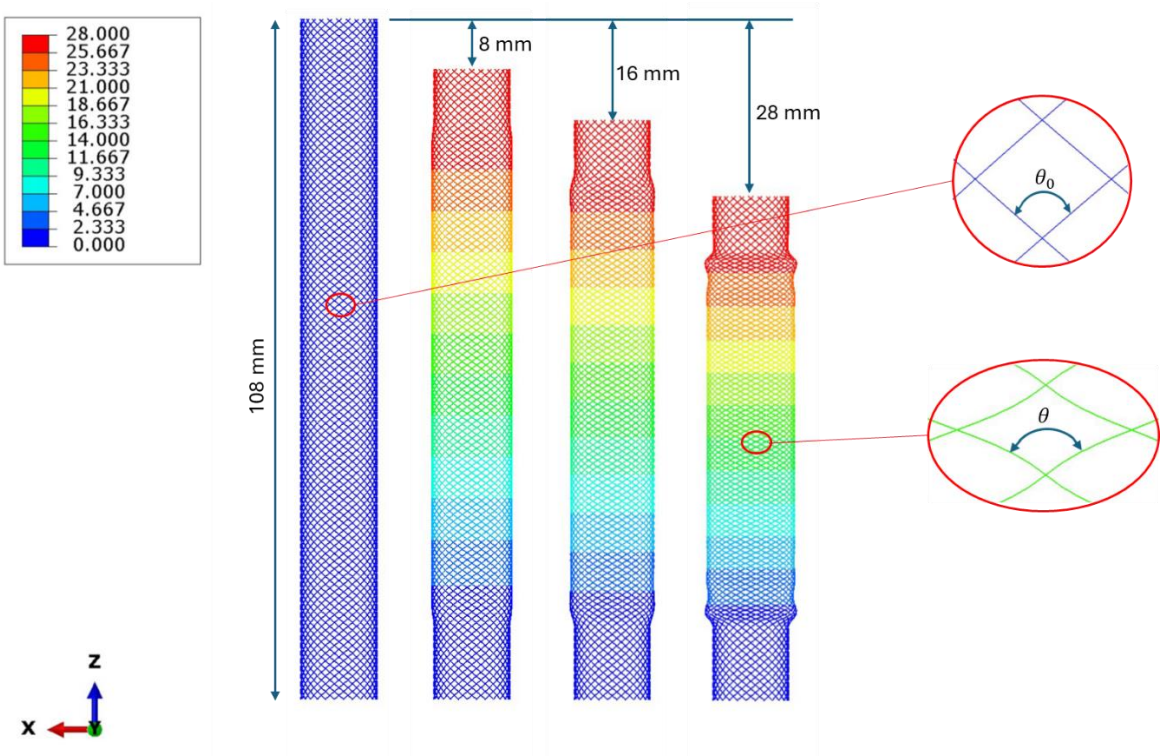

Figure 7-2: The FE model of the braided sleeve, showing its behaviour under a sequence of increasing displacements.

7.4 FE Model of the Soft Component (Without Braid)

7.4.1 FE Modelling Process of the Soft Component

In this section, we explore the FE modelling processes and the resultant outcomes for the soft component of the three models of SAM. This FE modelling is important to explore their behaviour prior to its constraint with the braid. We chose to start with Model-3 due to its simplicity, which facilitates a more straightforward modelling process. Beginning with a CAD model mirroring the geometry fabricated in the laboratory as detailed in Chapter 4, the dimensions were matched to ensure accurate modelling to the real model. The absence of the braid allowed for unrestricted expansion of the soft component, leading to significant linear and radial expansion, as observed experimentally. The behaviour of soft inflatable components without the braided sleeve and its impact on SIC geometry and performance, as investigated through experimental actuation tests, is discussed in Appendix 7.

Various hyperelastic models, such as the Ogden 3rd and Yeoh models by Marechal *et al.* [2] and the three different Yeoh models by Xavier *et al.* [92], were explored to define the material properties of Ecoflex 50 (the chosen material for the real model of

the soft component). However, many of these models failed to accurately represent the behaviour that was observed in the experimental models. Ultimately, one of the hyperelastic model proposed by Xavier *et al.* [92], based on the Yeoh model (see Table **7-2**, hyperelastic model), emerged as the only successful model in replicating the observed inflation behaviour of the soft component. This model was able to capture the complex nonlinear response of the material. Details regarding the modelling parameters are outlined in Table **7-2**, encompassing the parameters for creating of the CAD module, material definition, properties of the step module, applied pressure, boundary conditions, and meshing properties. For the purpose of simplification, the ends of the tube were assigned the same soft material properties. A fixed boundary condition was applied to one of the ends, while the other was left free (as illustrated in Figure 7-3). Then, a uniform pressure ranging from 20 to 80 kPa was applied to the inner surface of the tube. The elements used in this model were hybrid quadratic tetrahedrons, with a seeding size of 1 to generate a mesh comprising 114,412 nodes and 44,936 elements.

In the laboratory setup, in Model-1, the ends of the SIFs were bundled and connected surface to surface using Teflon tape. Replicating this aspect in the FE model required careful definition of constrained end's surfaces. At the lower ends of the SIFs, a single fixed boundary condition was applied to ensure that all three SIFs were bonded from the lower sides. A tie constraint was used to bond the outer surfaces of the upper ends of the three SIFs, as tie constraints are appropriate for defining interactions where no relative motion is allowed between parts.

Table 7-2: Key Input Parameters for FE Modelling of the soft component of Model-3.

Part Module	
Geometry	Long cylinder with single cavity
Base Feature	3D Solid, Extrude
Dimensions	Total Length= 110 mm Cavity Length= 90 mm ID=1.2mm OD=2.8mm

Property Module (soft component)	
Soft material	Ecoflex 00-50
Hyperelastic model	Yeoh, c1=0.019, c2=0.0009, c3=-4.75E-6

Step Module	
Step type	Static-General
Time Period	1
Increment size	0.05

Load Module	
Loads	20, 40, 60, and 80 kPa
BC1	ENCASTRE at lower end

Mesh module	
Element shape	Ted
Meshing technique	Free
Seeding size	1
Geometric order	Quadratic

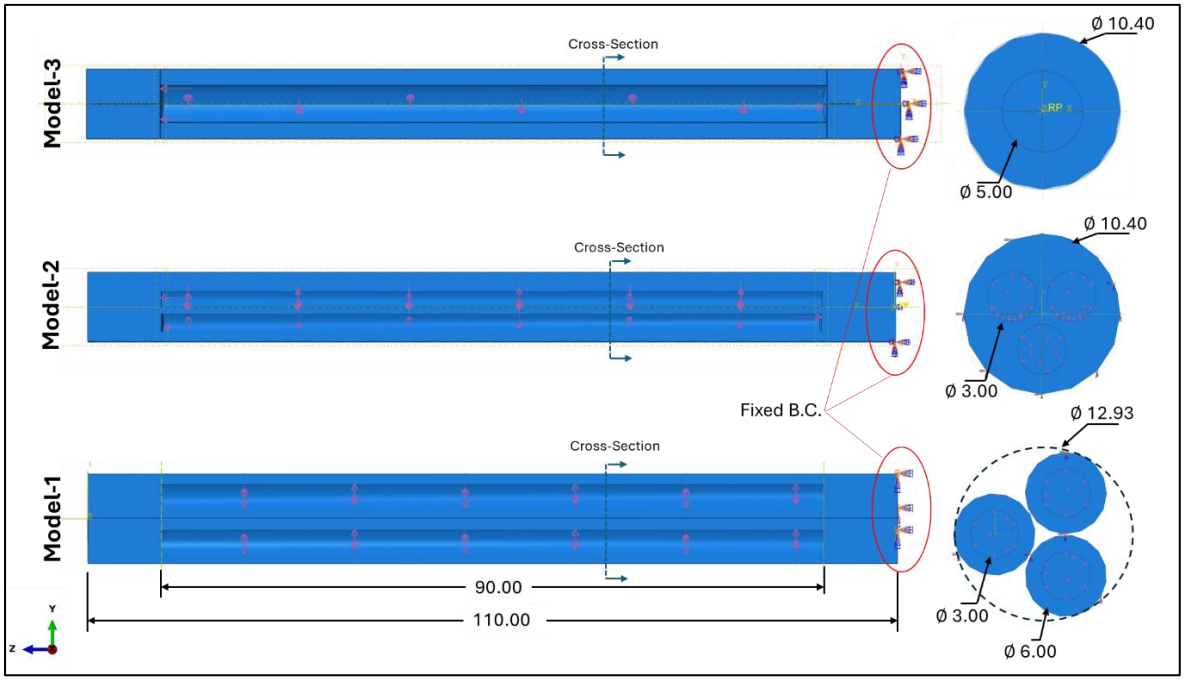

Figure 7-3: Modelling for the soft component of the three models of SAM.

7.4.2 Results of FE Modelling of the soft component

Results of FE Modelling of the soft component - Model-3:

Figure 7-4 shows the progressive inflation states from 0 kPa to 80 kPa from FE modelling results of soft component of Model-3. Displayed are both the longitudinal views and the cross-sectional views at each pressure stage. Notably, as the pressure increases, the wall thickness of the tube become thinner, indicating a direct correlation between pressure and soft material deformation. At 20 kPa, minimal inflation is observed, highlighting the sensitivity of the tube's response to even slight changes in pressure. However, the most significant observation arises between 40 and 60 kPa, where a notable gap in inflation occurs compared to the gradual expansions seen at lower and higher-pressure ranges. This interval appears critical, as it signifies a sharp increase in deformation.

The charts in Figure 7-7 and resultant data in Table 7-3 to show comparison of experimental and FE simulation results for the soft components of Models 1, 2, and 3. Each model's data are presented through two sets of charts, detailing the expansion behaviours in linear and radial direction. For Model-3, there is close alignment at 20 kPa between the real and FE models, with divergence becoming clearer at 40 kPa. However, the agreement improves significantly at 60 and 80 kPa, indicating effective simulation at these higher pressures.

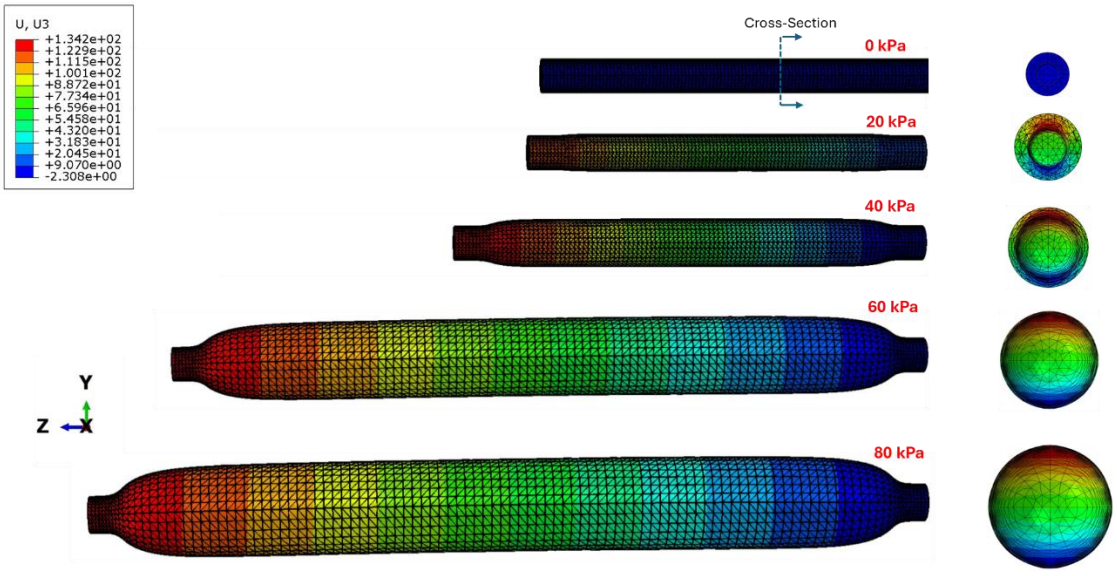

Figure 7-4: The progressive inflation states from 0 kPa to 80 kPa from FE modelling results of soft component of Model-3. Displayed are both the longitudinal views and the cross-sectional views at each pressure stage.

Results of FE Modelling of the Soft Component - Model-2:

The complexity of Model-2 is harder to represent in the FE model (shown in Figure 7-5). The Abaqus warning: "Excessive distortion at a lot of integration points in elements" suggests that the deformation within the elements of the model is becoming too severe, likely due to the complex geometry and the very high deformation of the inner wall of the soft component. This distortion can lead to convergence issues and inaccurate results, causing the job to abort at around 53 kPa. In contrast, Model-3, with its simpler geometry featuring only a single cavity, may experience less severe distortion and thus can withstand higher pressures before encountering convergence problems.

Despite the FE simulation data are available only up to 53 kPa, the trends observed suggest that if the FE simulation could extend beyond 53 kPa, it would likely display close agreement with the real model at higher pressures, similar to Models 3. Similar to the linear expansion, the radial charts are also capped at 53 kPa. The expected pattern of increasing alignment with the real model's data at higher pressures remains consistent with the observations from other models.

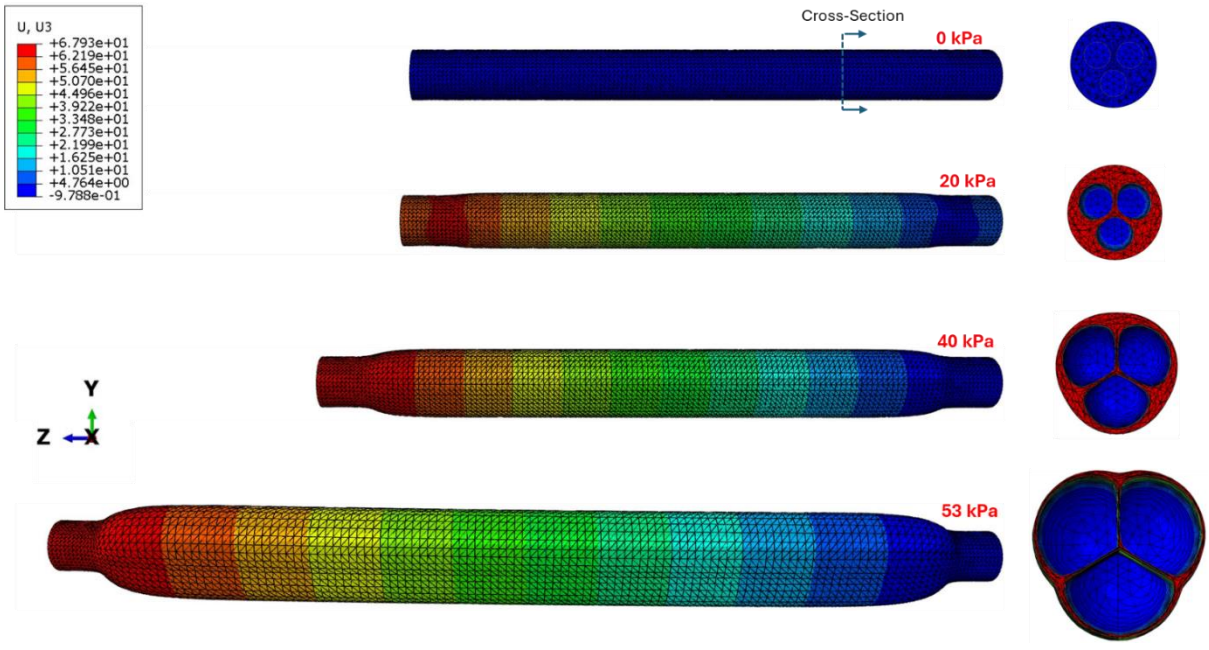

Figure 7-5: The progressive inflation states from 0 kPa to 80 kPa from FE modelling results of soft component of Model-2.

Results of FE Modelling of the Soft Component - Model-1:

Despite the simplicity of the SIFs' geometry, challenges arise when constraining the ends of the SIFs together in the FE simulation. Figure 7-6 shows the progressive inflation states from 0 kPa to 80 kPa from FE modelling results of soft component of Model-1. A warning displayed regarding missing intersection indicates the difficulty of modelling the constraint between two cylindrical objects in the FE simulation.

In Model-1's chart, in Figure 7-7, the linear expansion at both real and FE simulation models shows the lowest agreement at low pressures, with also a notable divergence occurring at 40 kPa. However, this discrepancy reduces, and the models converge closely again at pressures of 60 and 80 kPa. These charts uniquely represent the expansion of a single SIF rather than three. Observations reveal that the behaviour of a SIF in radial expansion closely mirrors the general trends seen in Model-3' soft component that could be due to the similarity of their design.

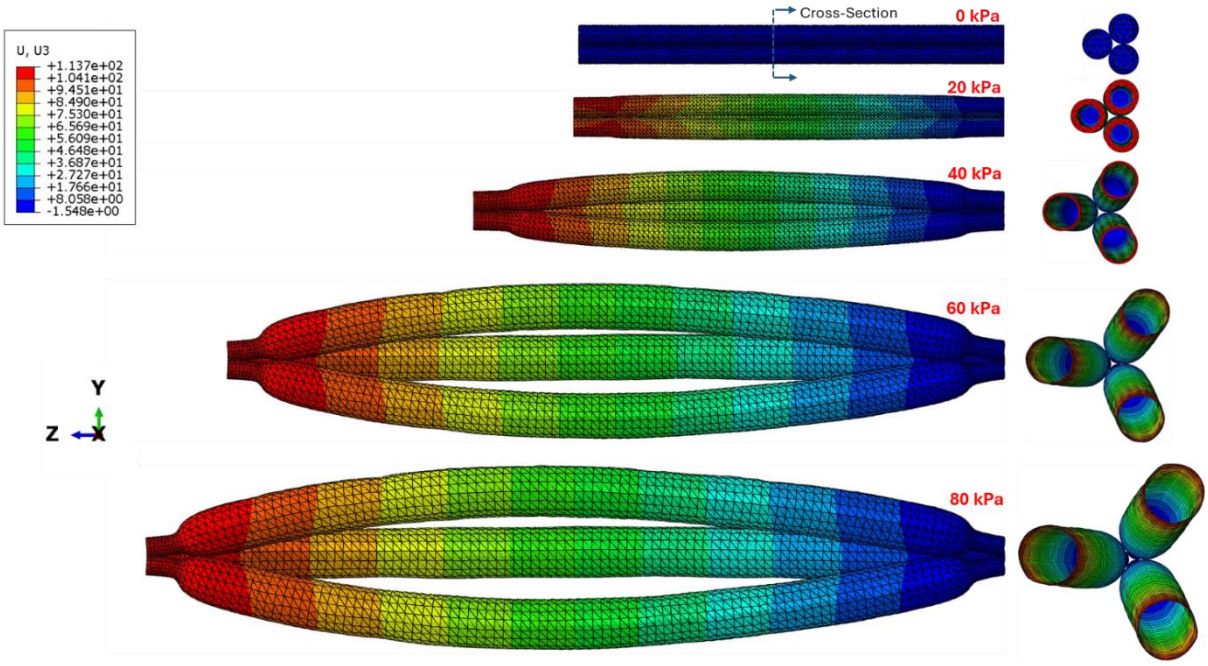

Figure 7-6: The progressive inflation states from 0 kPa to 80 kPa from FE modelling results of soft component of Model-2.

Table 7-3: Comparison of experimental and FE simulation results for linear and radial expansions of the soft components of Model-3, 2 and 1 (mm).

	Pressure	Linear			Radial		
		Real Model	FE Simul.	Error (%)	Real Model	FE Simul.	Error (%)
Model -3	20	20.30	1.57	92.27	10.38	0.68	93.45
	40	69.92	22.85	67.32	15.65	3.79	75.78
	60	97.98	103.62	5.76	18.39	12.19	33.71
	80	127.45	134.20	5.30	18.90	15.06	20.32
Model -2	20	26.38	1.93	92.68	8.04	0.96	88.06
	40	82.77	17.75	78.56	15.25	3.32	78.23
	60	104.09	67.93	34.74	16.06	7.39	53.99
	80	120.75	-	-	18.49	-	-
Model -1	20	6.73	1.47	78.16	5.87	0.42	92.84
	40	68.57	27.74	59.54	8.46	2.47	70.80
	60	97.33	92.35	5.12	9.66	6.27	35.09
	80	110.73	113.70	2.68	10.08	7.56	25.00

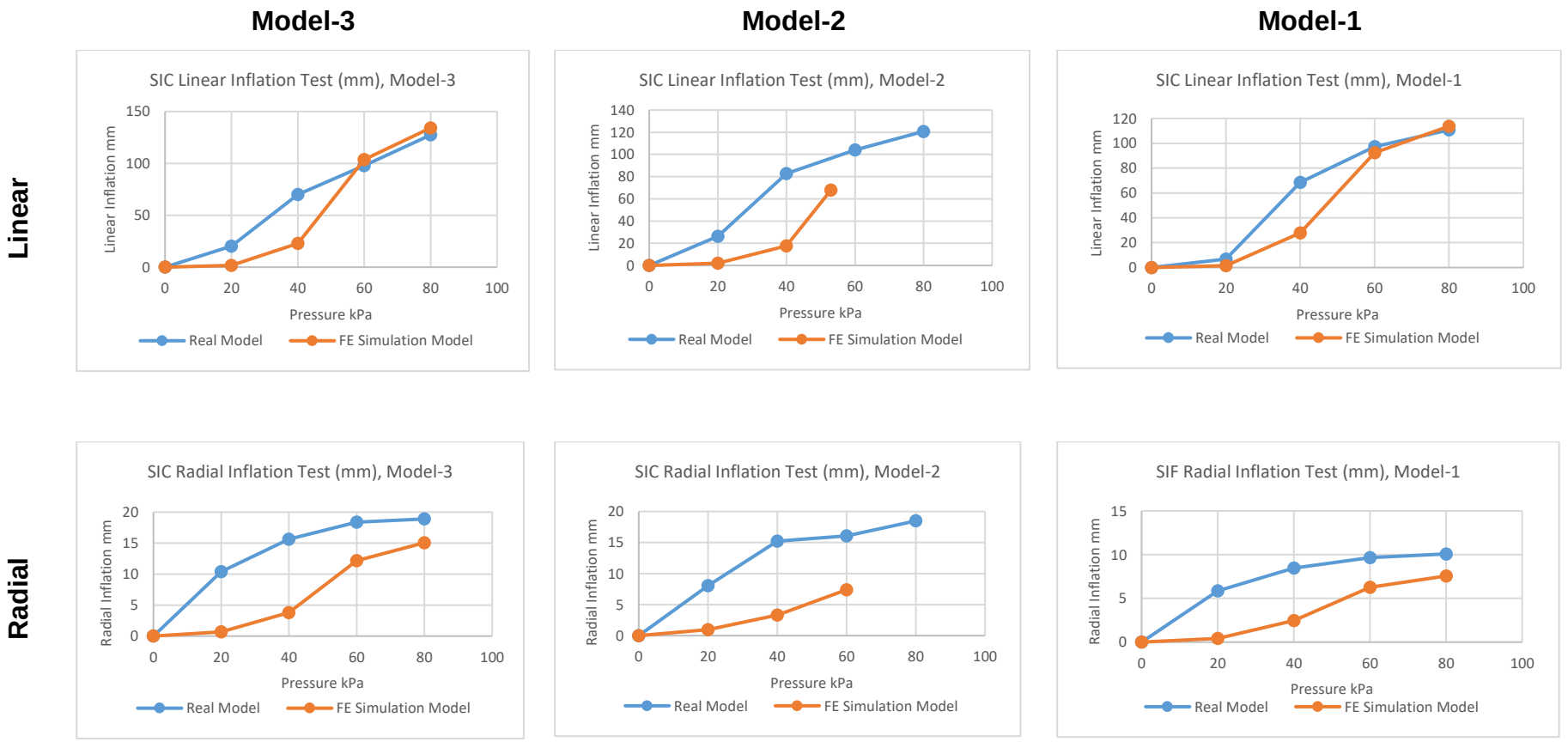

Figure 7-7: Comparison of experimental and FE simulation results for linear and radial expansions of the soft components of Model-3, 2 and 1.

7.5 FE Model of the SAM

The model in this section focuses on analysing the SAM's displacement and force generation under various conditions of input pressure. The nonlinear behaviour observed in the SAM arises from the nonlinear properties of the soft material used for the soft components and significant structural deformation of the braided sleeve. The FE model of the braid structure and soft component, as detailed earlier, facilitated the simulation of the full model of SAM. The same FE models for the soft components of Models 1, 2, and 3 are utilized. However, the braided sleeve is differed only in the diameter, where Model-1 has a larger diameter than Models 2 and 3 (shown in Figure 7-3).

To connect the inflatable component and the braided sleeve effectively, we use a tie constraint. This is necessary because the braided sleeve is modelled in FE modelling as a set of nodes (not a solid surface) so other types of interactions like surface-to-surface are not possible. Trying to make the sleeve bigger than the outer surface of the inflatable part didn't work because the tie constrain type is not effective if the two parts are not fully attached. Therefore, the diameter of the braided sleeve is created equal to the outer diameter of the soft components to ensure a proper constrain application with type tie.

Model-1 requires a longer modelling process because it involves assembling the three SIFs within the braid structure. In its assembly, it is considered that the outer surfaces of the three SIFs are in contact using a surface-to-surface contact, and the braid nodes are in contact with parts of the outer surfaces of the SIFs using a tie constraint (shown in Figure 7-8).

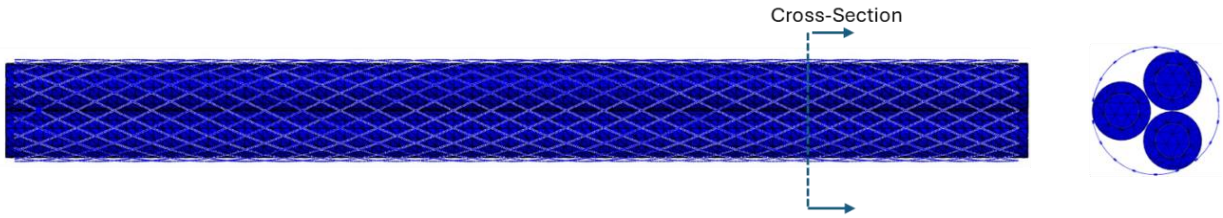

Figure 7-8: Interaction in Model-1 between SIFs and braided sleeve.

7.5.1 FE Model for the Displacement Test

In modelling the displacement test, the bottom end of the SAM is kept in place with a fixed boundary condition, defined through selecting the lowest nodes of the sleeve and a circle of nodes at the bottom edge/s of the soft component. The top end is left without boundary condition to perform the contraction movement freely. The following sections present the key results of the FE modelling for the displacement test for Models-3, Models-2, then Models-1:

Results of the FE Modelling for the Displacement Test - Model-3:

Figure 7-9 provided FE simulation results of the displacement test of Model-3. As the pressure progresses through 0, 20, 40, 60, to 80 kPa, there is a notable contraction and radial expansion of the SAM. The sequence displays both front views and cross-sectional images side-by-side for each state, allowing for examination of the SAM's internal and external structures. Additionally, a zoomed-in view on the contracted state of the SAM's braided sleeve shows that the braiding angle widens as the muscle contracts more. Particularly at 80 kPa, the extended front view alongside the cross-sectional view allows observation of the deformation impacts on both the cavity and the soft component's wall sizes. It is evident from the simulation that as the SAM contracts in length, its diameter correspondingly increases. This behaviour aligns with typical responses observed in real model. Moreover, the model demonstrates even and symmetrical motion, showing uniform behaviour and force distribution.

The chart in Figure 7-12 and Table 7-4 illustrate the contraction range of Model-3 as observed in both experimental and FE simulation models. In the trends observed in the FE simulation model, a more consistent increase in contraction as the pressure increases unlike the real model. At the lower pressure of 20 kPa, a greater contraction is shown by the FE simulation model compared to the experimental model. However, from 40 to 80 kPa, a greater range of contraction is consistently exhibited by the experimental model, exceeding the simulation by about around 40%.

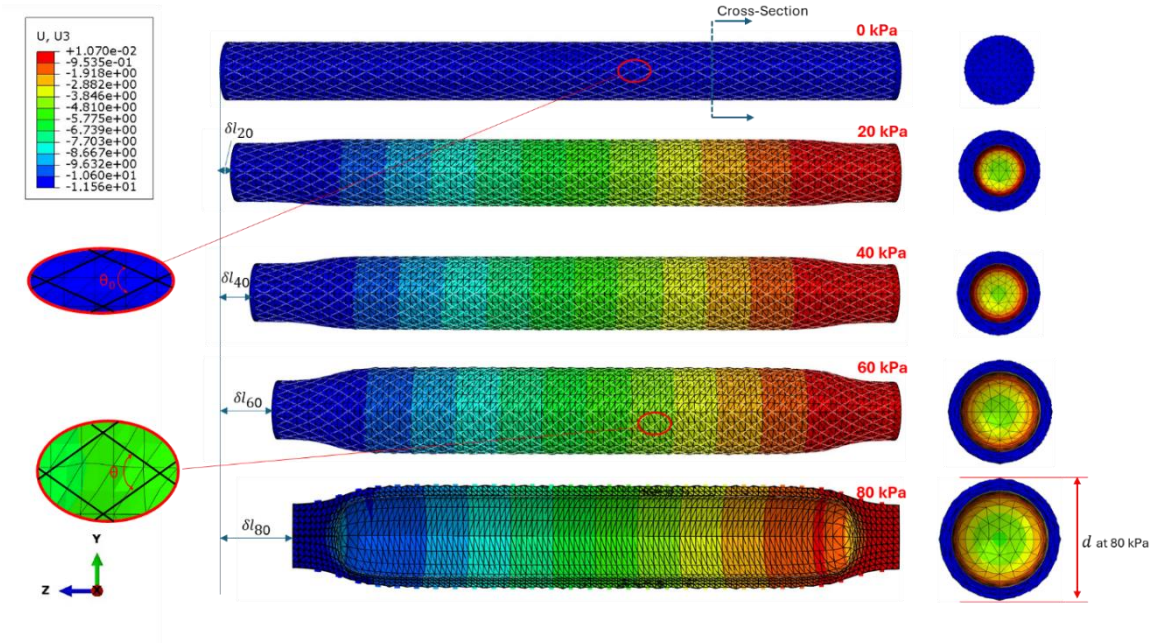

Figure 7-9: The progressive inflation states from 0 kPa to 80 kPa from FE modelling results of SAM of Model-3. This Model replicates the displacement test, displaying both the front and the cross-sectional views at each pressure stage.

Results of the FE Modelling for the Displacement Test - Model-2:

Figure 7-10 illustrates contraction of Model-2 of SAM, which is designed with three equal cavities. The complexity compared to Model-3 highlighted at the simulation state of 80 kPa, where greater distortions within the meshed elements are visible in the front cross sections. Despite these internal distortions, the simulation job was completed successfully up to 80 kPa. In terms of structural behaviour, the asymmetric distribution of the cavities in Model-2 does not impact the behaviour of the outer surface of the soft component or the performance of the braid, which contracts smoothly similar to Model-3.

The comparison of the real and simulation models presented in Figure 7-12 of the contraction range for Model-2 shows similarities to the presentation of Model-3. For Model-2, the experimental model exhibits a significant increase in contraction range when compared to its FE simulation model, particularly in the pressure range from 40 to 80 kPa. Here, the contraction in the experimental model exceeds that of the simulation by approximately 30% that indicates smaller discrepancy than what is observed in Model-3.

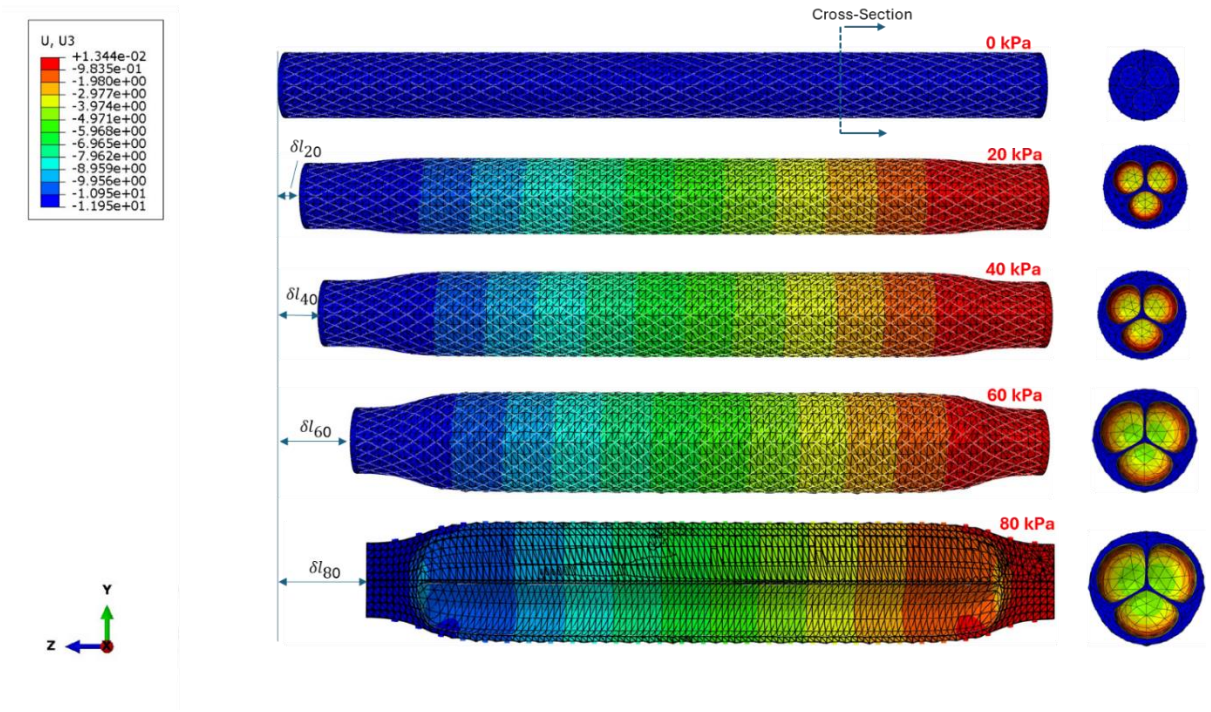

Figure 7-10: The progressive inflation states from 0 kPa to 80 kPa from FE modelling results of SAM of Model-2, replicating the displacement test.

Results of the FE Modelling for the Displacement Test - Model-1:

Figure 7-11 illustrates Model-1, which shows greater complexity than that observed in Model-2 because of incorporating three separate soft inflatable filaments (SIFs). Each SIF interacts with a complex structure of braided sleeve, which poses unique challenges in FE modelling. Notably, cross-sectional views show that the fibers of the braided sleeve intersect the body of the SIFs, highlighting a significant modelling challenge that has observed despite several trials to refine it.

Model-1 employs two distinct types of interactions to manage the relationships between its components: Firstly, a surface-to-surface interaction is utilized between the three SIFs with a set friction coefficient of 1.15 (from literature [93]) to simulate the contact dynamics. Secondly, due to the nature of the braided sleeve being modelled as a 3D wireframe (comprising only nodes and not surfaces), a tie interaction is used to connect the SIFs' surfaces with the braided sleeve's nodes. This approach presents a limitation as it requires the entire surfaces of the SIFs to be in contact with the nodes of the braided sleeve, where any miss-contact causes the nodes not to properly constrain the expansion of the SIFs that lead to potential inaccuracies in simulating the behaviour of the Model-1. Despite these complexities and interaction issues, Model-1 is able to execute a contraction motion, although with a reduced range due to the weak interactions. This outcome, while not entirely

satisfactory in terms of the magnitude of contraction, still demonstrates the feasibility of achieving the desired motion with Model-1 under the current modelling constraints. This highlights the detailed challenges and the potential for further refinement in modelling and simulation techniques in future iterations of SAM with multi-filaments.

The comparison of the contraction range of Model-1 (Figure 7-12) as depicted under pressures up to 80 kPa for the real model and only up to 60 kPa for the simulation model. This limitation in the simulation data is due to the FE analysis being aborted after around 60 kPa. At a lower pressure of 20 kPa, the contraction values of the real model and the simulation model are very close, indicating a good initial agreement between the simulated predictions and actual experimental outcomes. However, as the pressure increases to 40 and 60 kPa, a significant gap emerges, with the real model showing about 70% higher contraction than the simulation. This large discrepancy is attributed to the previously mentioned interaction issues within this model.

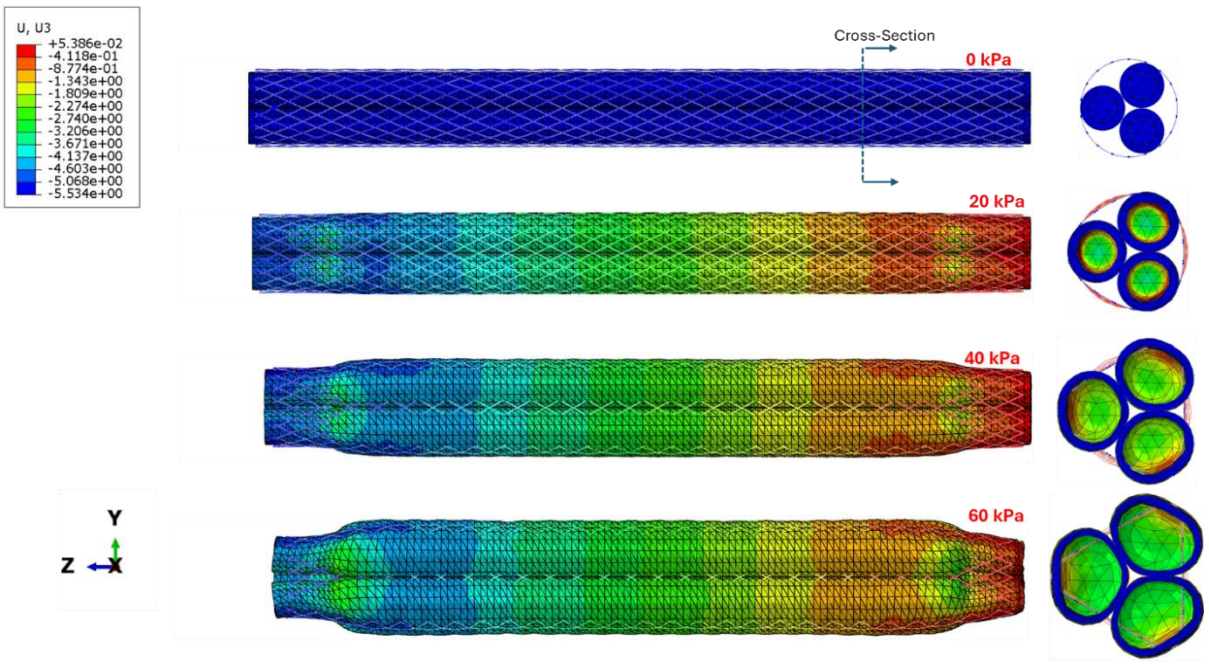

Figure 7-11: The progressive inflation states from 0 kPa to 80 kPa from FE modelling results of SAM of Model-1, replicating the displacement test.

Table 7-4: Comparison of experimental and FE simulation results for range of the SAM's contraction of Model-3, 2 and 1 (mm).

	Pressure	Real Model	FE Simul.	Error (%)
Model -3	20	0.60	2.49	314.34
	40	9.29	4.86	47.68
	60	15.24	9.39	38.37
	80	17.95	11.56	35.61
Model -2	20	1.16	2.90	150.00
	40	10.03	5.41	46.06
	60	14.43	10.46	27.53
	80	17.24	11.95	30.70
Model -1	20	1.16	0.60	48.02
	40	10.03	2.65	73.58
	60	14.43	5.53	61.69
	80	17.24	-	-

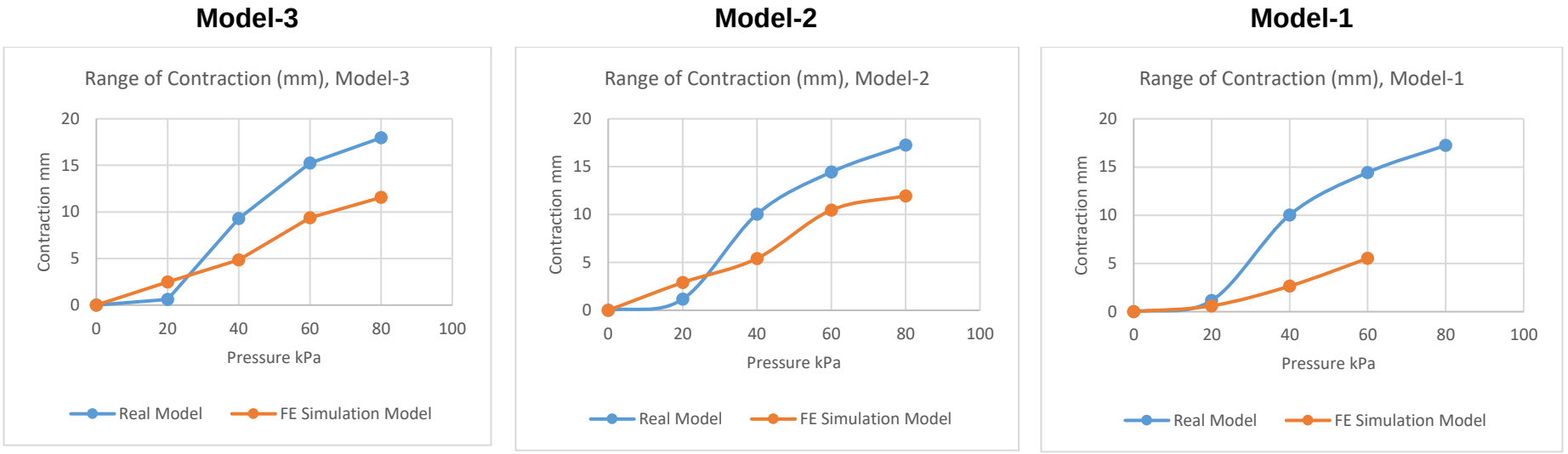

Figure 7-12: Contraction range for SAM models: each chart represents experimental results against FE model.

7.5.2 FE Model for the Block Force Test

The process of FE modelling for measuring the generated force by the models of SAM, as representation for the experimental block force test previously described in Section 5.1, is outlined in this section. The same FE models of SAM for Model-1, 2, and 3 that were earlier illustrated in the displacement tests to conduct the block force test are utilized. For the measurement of block force, both the top and bottom end of the SAM are fixed in space. A pressure load is then incrementally applied from 0 to 80 kPa in a manner consistent with earlier tests. All other FE modelling parameters remain unchanged to ensure the consistency of the simulation across both displacement and block force tests. After complete running the analysis for the FE modelling job, the amount of generated force is calculated. This calculation is performed by summing all the reaction forces on the elements located on the top surface of the SAM's end (as shown in Figure 7-13).

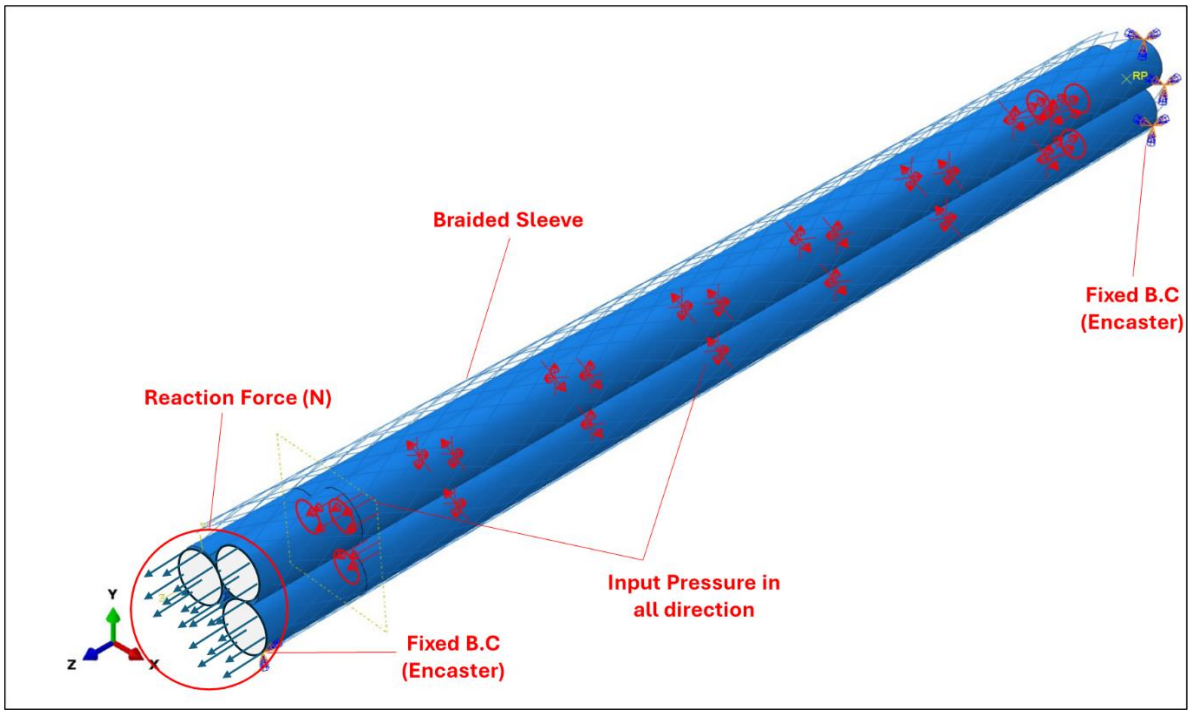

Figure 7-13: Model-1 of SAM with fixed top and bottom ends. The generated force is calculated by summing the reaction forces on the elements at the top surface of the SAM.

Results of the FE Modelling for the Block Force Test - Model-3:

In Figure 7-14, the ends of the Model-3 of SAM are shown to remain fixed in space that ensure the expansion is limited to radial rather than longitudinal displacement.

As the pressure is incrementally increased, an observed increase in the diameter of the SAM is accompanied by a reduction in wall thickness, as evident in the cross-sectional views.

Figure 7-17 compares the generated force between the real model and the FE simulation for all models. In the chart of Model-3, the FE simulation consistently exhibits higher force outputs compared to the real model across all pressure levels. At 20 kPa, the force generated by the FE simulation is approximately 90% higher than that of the real model. This gap narrows at pressures of 40 and 60 kPa, where the FE simulation shows about 30% more force than the real model. At 80 kPa, the gap slightly widens again, with the FE simulation output being about 40% higher than that observed in the real model.

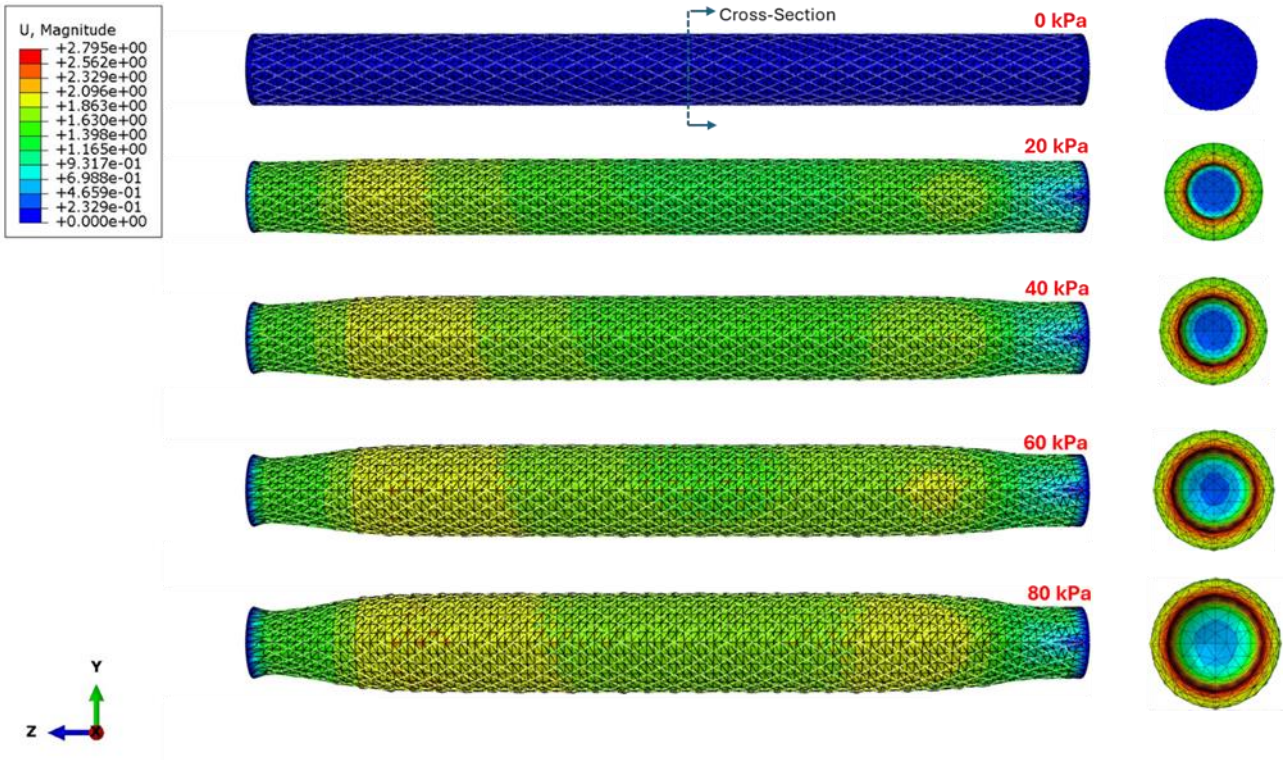

Figure 7-14: The progressive inflation states for the block force test of Model-3.

Results of the FE Modelling for the Block Force Test - Model-2:

The results for the block force test of Model-2 of the SAM are showed in Figure 7-15. As in Model-3, the behaviour of inflation of Model-2 remains consistent. The cross section in Figure 7-15 shows that at the highest-pressure level of 80 kPa, the inner walls are observed to be nearly maximized within the cavities, indicating high stress

across these internal structures. This thinning of the walls under increasing pressures highlights the material's response to the input pressure during the block force test.

The comparison chart in Figure 7-17 shows at 20 kPa, a minor gap in the generated force is noted between the real and FE simulation models, but excellent agreement is observed at all other pressure stages. The close correlation at higher pressures suggests that the FE model effectively captures the mechanical responses of the SAM, particularly in terms of force output under varying operational pressures.

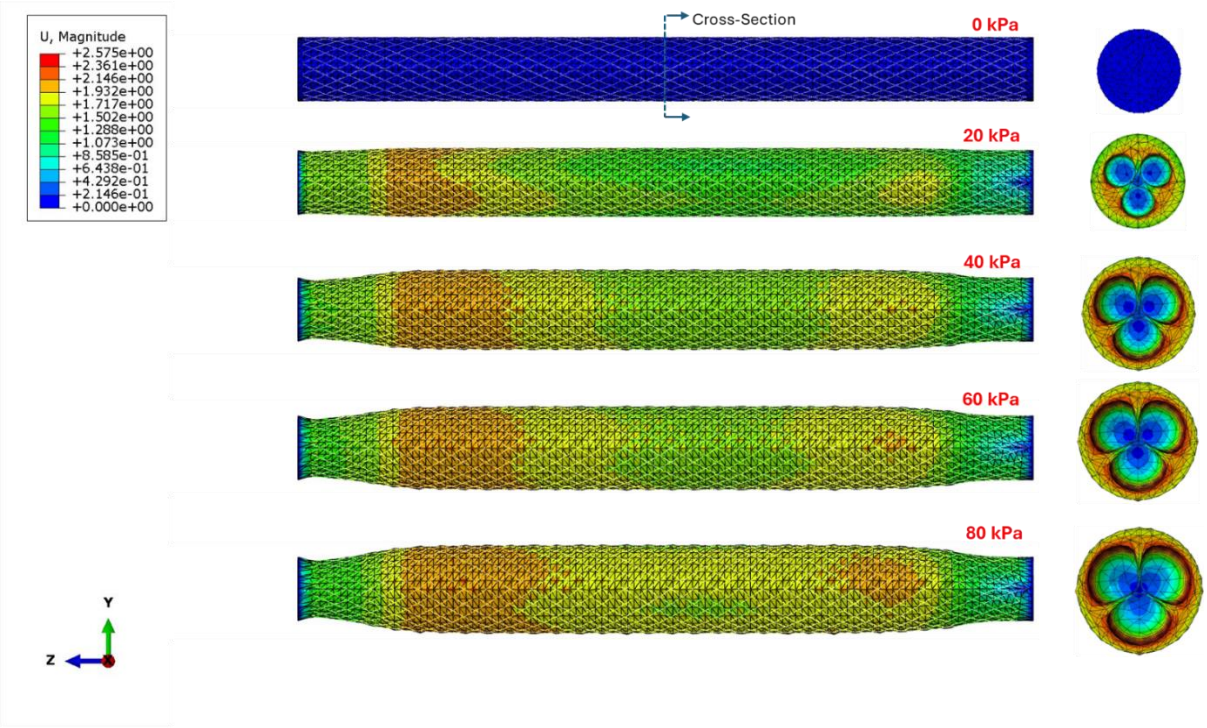

Figure 7-15: The progressive inflation states for the block force test of Model-2.

Results of the FE Modelling for the Block Force Test - Model-1:

Figure 7-16 illustrates the results for Model-1. The test was aborted around 60 kPa due to interaction issues detailed earlier in section 8.5.1, which caused inefficiencies in SAM performance that lead to unreliable force generation results. The cross-sectional views clearly depict the interaction between the braid fibers and the soft filaments within the muscle.

In the chart of Model-1, the simulation showed deviations from the real-world model behaviour. This variation between the FE model and the real model underscoring the

limitations and challenges in accurately simulating the Model-1 behaviour due to interaction complexities.

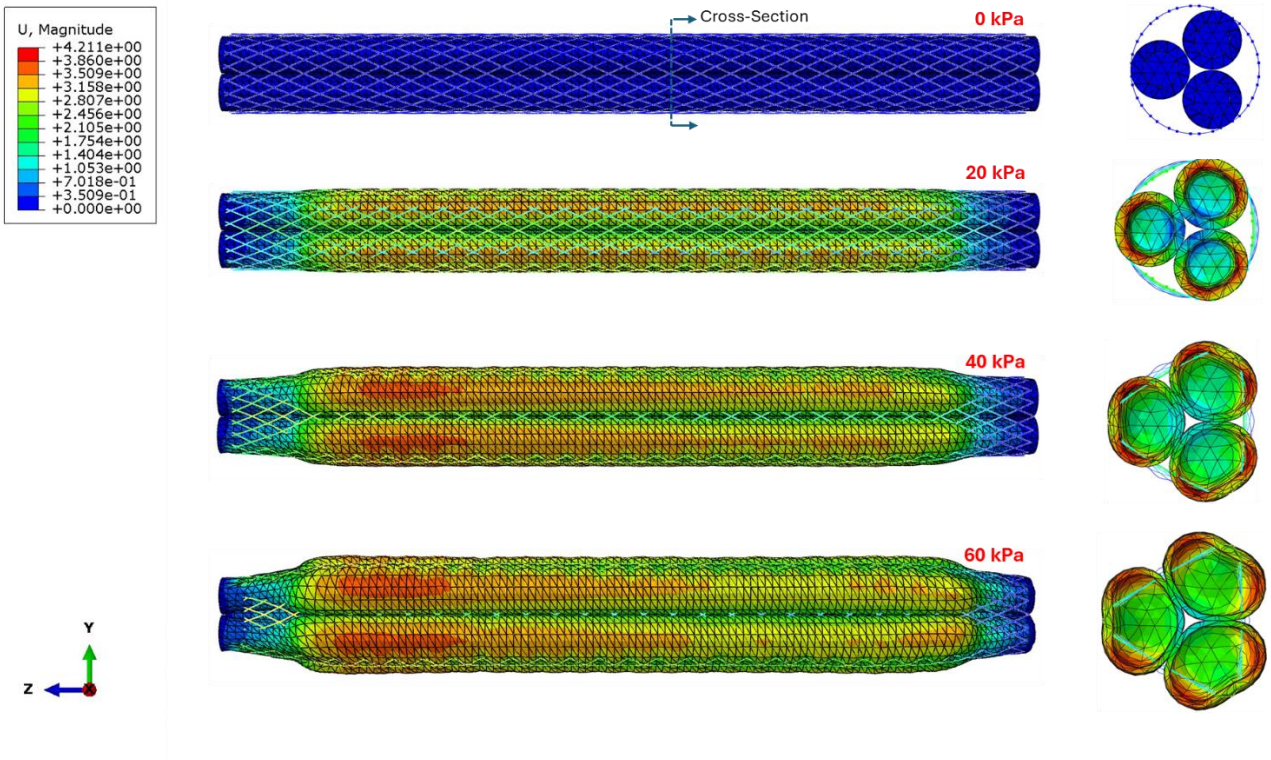

Figure 7-16: The progressive inflation states for the block force test of Model-1.

Table 7-5: Comparison of experimental and FE simulation results for amount of the SAM's force generation of Model-3, 2 and 1 (N).

	Pressure	Real Model	FE Simul.	Error (%)
Model -3	20	0.57	4.54	700.55
	40	7.35	10.23	39.17
	60	12.01	16.41	36.69
	80	14.65	23.08	57.51
Model -2	20	0.93	4.87	424.01
	40	11.00	10.85	1.34
	60	18.97	17.16	9.53
	80	23.13	23.79	2.85
Model -1	20	1.52	0.49	67.87
	40	8.68	1.89	78.23
	60	16.75	4.14	75.27
	80	21.04	-	-

Model-3

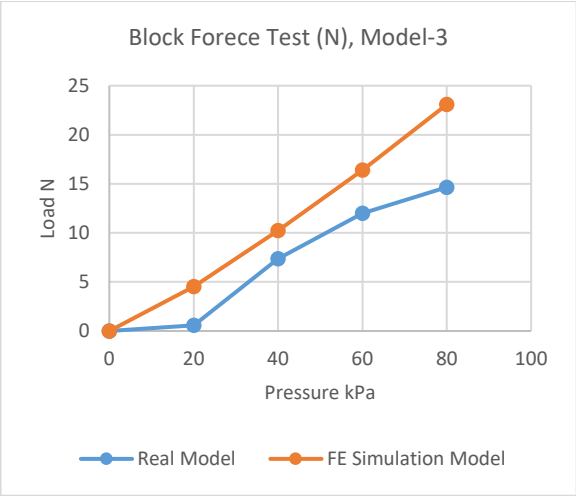

Model-2

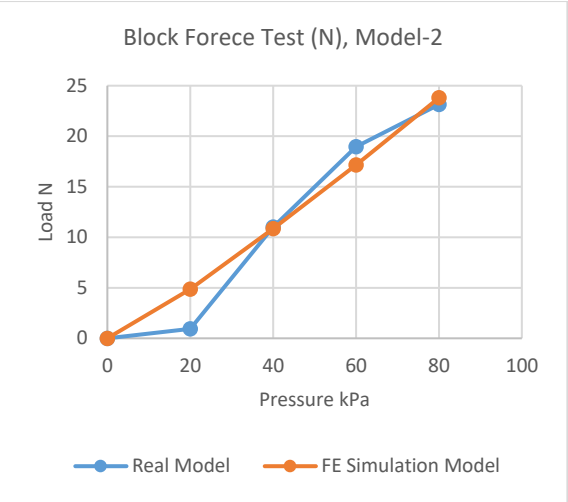

Model-1

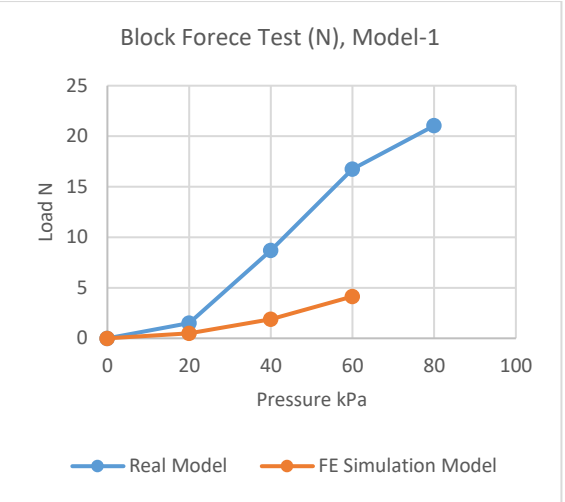

Figure 7-17: Force generation for SAM models: each chart represents experimental results against FE model.

7.6 Discussion

One of the advantages of using FE simulation to evaluate the performance of SAM models is the ability to achieve more controlled and consistent results compared to experiments. In FE simulations, input parameters can be precisely controlled, allowing for a fair comparison between SAM models without the variability introduced by fabrication or testing inconsistencies. While experimental results provide real-world accuracy, they are subject to inconsistencies in manufacturing and testing processes that can affect the results.

As discussed in the literature review (Chapter 2), several researchers have utilized FE simulation for SAMs, including Antonelli *et al.* [71], Tu *et al.* [83], and T. Hassan *et al.* [84]. Each study provided different approaches in modelling the complex geometry of the braid, the materials used for the soft component and braid, and the assumptions to simplify the simulation. While Antonelli *et al.* and Tu *et al.* used simplified approaches, T. Hassan *et al.* [84] developed a comprehensive 3D model of the interlaced braided sleeve using separate software. Our research benefited from these different approaches but is closer to T. Hassan *et al.*'s [84] method, as we also developed a comprehensive 3D model of the braided sleeve using Python scripts in Abaqus PED.

When comparing the agreement between experimental and simulation results in the three papers, all showed a high level of agreement. However, our simulation did not achieve a similar high level of agreement, particularly in the range of contraction, due to the complexity of braid modelling. T. Hassan *et al.* [84] created a single segment using Pyrfomax software, repeated and assembled this segment in CW and CCW in Ansys software, and defined interaction between the fibres through friction coefficient. We attempted a similar approach by defining the friction between the fibres as T. Hassan *et al.* [84] did, but encountered challenges. Specifically, in our model, the braided sleeve structure was created using a 3D wire technique in Python scripts. This approach treats the fibres as a series of discrete nodes rather than a continuous surface. As a result, the contact regions between fibres could not be recognized, making it impossible to accurately define and simulate the frictional interactions between them using the interaction module in Abaqus.

The inability to define these interactions significantly reduced the accuracy of the model in replicating the real physical behaviour of the braided sleeve during contraction and extension. This limitation led to the need for adjustments to the material properties of the braid, specifically reducing Young's modulus, to approximate the braid's behaviour without the defined frictional interactions. While

these adjustments were not ideal, they were essential as a preliminary step to enable the model to converge and facilitate further simulations of the complete SAM.

7.6.1 Soft Component (Without the Braid)

In the FE modelling of soft component (without the braid), several key observations were made. Across all models (Model-1, Model-2, and Model-3), the simulation showed excessive distortion at numerous integration points within the finite elements. A critical pressure range between 40 and 60 kPa was identified, where there is a notable gap in inflation compared to the more gradual expansions seen at lower and higher-pressure ranges. For Model-3 and Model-1, the simulation shows poor agreement with the real model at low pressures of 20 and 40 kPa. However, at higher pressures of 60 and 80 kPa, the discrepancy reduces, and the models converge closely, showing better simulation accuracy. When comparing the agreement between the real model and FE simulation model for linear and radial expansion, Model-3 demonstrated the best overall agreement followed by Model-1. On the other hand, Model-2 faced significant challenges with excessive distortion in the FE model can lead to significant discrepancies between the simulation results and the experimental data across the pressure range.

7.6.2 FE Model of the SAM Displacement Test

For the FE model of the SAM displacement test, several important findings were observed. For Model-3, the trends observed in the FE simulation model show a more consistent increase in contraction as the pressure increases, unlike the real model. This discrepancy is likely due to the interaction between the braid and the soft component, both of which exhibit non-linear behaviour individually. When these two components are combined in SAM, their real interaction introduces further non-linearity. As the soft component expands, the braid restricts this expansion, leading to a complex, non-linear contraction response that depends on both the pressure applied and the interaction between the components. The FE simulation may struggle to fully capture this non-linear behaviour because it simplifies certain parameters.

At a lower pressure of 20 kPa, both Model-2 and Model-3 simulations show greater contraction compared to the experimental models. However, from 40 to 80 kPa, the experimental models consistently exhibit a greater range of contraction. The FE simulation model of Model-2 performs slightly better than Model-3, showing errors of

46.06%, 27.53%, and 30.70% at 40, 60, and 80 kPa, respectively. In comparison, Model-3 shows errors of 47.68%, 38.37%, and 35.61% at the same pressures. On the other hand, the FE simulation model of Model-1 shows decent performance at 20 kPa but performs poorly at higher pressures. This highlights the need for refinement in the FE models to better match the experimental results.

7.6.3 FE Model of the SAM Block Force Test

Several key results were observed from the FE model for the block force test. For Model-3, the FE simulation always shows higher force outputs compared to the real model across all pressure levels. In contrast, Model-2 shows excellent agreement at pressures higher than 20 kPa. The FE simulation model of Model-2 performs better than Model-3, with errors of 1.34%, 9.53%, and 2.85% at 40, 60, and 80 kPa, respectively. In comparison, Model-3 shows errors of 39.17%, 36.69%, and 57.51% at the same pressures. The limitations of Model-1 are also highlighted in the block force test simulation, similar to the simulation of the displacement test, due to the interaction complexities within the model.

Finally, since this research aims to primarily evaluate the performance of SAMs made of multiple filaments (Model-1), the results from this FE simulation show some limitations that need further development and improvement for more reliable results. In future work, addressing the issue of defining the interactions within the braid and between the soft filaments of Model-1 could improve the correlation between experimental and FE simulation models.

7.7 Summary

This chapter focuses on the FE simulation of SAMs' models to understand their behaviour under various pressure conditions and validate the reliability of the FE simulations of SAM against experimental findings. The 3D geometry of the braided sleeve was created using Python scripts in Abaqus PDE, creating a helical 3D wire structure that represents single fiber. The fibers were modelled using an isotropic elastic material model with properties sourced from literature. Key input parameters included the Young's modulus, Poisson's ratio, and density of PET. Some properties of the braided sleeve were modified to adapt the FE modelling requirements and avoid analysis non-convergency. The model then was meshed and adjusted to replicate the real sleeve's contraction motion closely.

The FE modelling of the soft component began with a CAD model, followed by exploring various hyperelastic models to define the material properties of Ecoflex 50. One of the Yeoh model provided in the literature was the only successful in replicating the soft component inflation behaviour. The FE model was created with appropriate geometry, material properties, boundary conditions, and meshing techniques. This modelling for the soft component showed excessive distortion at numerous integration points, especially at higher pressures. The simulations for Models 1, 2, and 3 showed varying degrees of agreement with real models, with Model-3 performing best overall due to its simplicity.

The SAM models' FE simulations focused on analysing contraction and force generation under varying pressures. To conduct this simulation, the soft components and braid are modelled separately then incorporated together to create the full SAM. The SAM’s performance was evaluated through replicating displacement and block force tests, with key findings highlighting the differences between simulated and real model behaviours.

In the displacement test, the FE model of Model-3 showed a consistent increase in contraction with increasing pressure, although the real model exhibited greater contraction at higher pressures. Model-2 faced challenges with excessive distortion but performed better at higher pressures. Model-1 demonstrated interaction issues that led to discrepancies between simulated and real models, particularly at higher pressures.

In the block force test, the FE simulation for Model-3 consistently showed higher force outputs compared to the real model, while Model-2 showed excellent agreement at higher pressures, indicating effective simulation. However, the FE simulation for Model-1 showed significant variation from the real model due to interaction complexities.

Chapter 8 : Discussion and Conclusions

This chapter provides a discussion and conclusion of the research by first presenting an overall discussion of the key findings and their implications for the development and evaluation of SAMs. It then concludes the thesis by summarizing the main contributions and outcomes of the study. Finally, it outlines potential future work, suggesting areas for further research and development to advance the field of soft robotics.

8.1 Overall Discussion

This overall discussion provides a comprehensive analysis of the research findings, focusing on the effectiveness and value of the techniques developed for SAMs. It examines the most effective SAM model and the main limitations of the study. The discussion is structured into subsections that cover a critical analysis of the literature review, soft material characterization, SAM development, SAM characterization, a case study, and FE simulation of SAMs, each offering insights into the study's contributions and areas for further improvement.

8.1.1 Critical Analysis of Literature Review

The literature review identifies several critical research gaps that need addressing to advance the field. The aim of this literature was to present essential aspects of soft robotics with a focus on SAM, and this was successfully addressed through three key objectives. First, the research introduced the field of soft robotics, emphasizing SAM and highlighting the importance of material characterization in developing these actuators. Second, it explored various designs and fabrication methods of SAM, identifying research gaps for future advancements. Third, the study examined the role of FE Analysis in simulating SPAs and SAMs, demonstrating their methodologies and how these simulations enhance the practical application of SAM development.

During the review, it became clear that certain areas, especially the FE analysis, needed more attention than initially planned. By adjusting the focus, the research provided a clearer understanding of how simulations can be conducted for more accurate modelling of SAM. Although summarizing and analysing a large amount of existing research was challenging, this effort provided a foundation for the rest of the study. The literature also highlights the need for innovation in SAM designs,

particularly in the soft components and braids, indicating significant potential for enhancing their performance and efficiency [58].

8.1.2 Soft Material Characterization

This soft material characterization aimed to study the behaviour of various soft materials to understand their mechanical properties for use in SAMs. By defining properties such as tensile strength and stiffness, the characterization process provides an understanding of these materials, aiding in the improvement of actuator design and make informed decisions about material selection.

This characterisation makes several contributions to the field of soft robotics. First, fabricating precise and consistent soft samples was a challenge. Unlike rigid materials, soft samples require careful steps during fabrication, making the process more time-consuming than expected in the research's initial plans. To address this, various techniques were tested and refined, resulting in a robust fabrication protocol.

Second, it establishes a comprehensive, reliable, and repeatable methodology for characterizing soft materials. There is a noticeable absence of comprehensive standardized methodologies for the characterization of soft materials, including all procedures from establishing the characterization methodology and fabricating the soft samples to expressing the results. By addressing the inconsistencies found in previous studies, this research provides a more standardized approach.

Third, the dual focus on both tensile and compression tests sets this research apart. Most existing studies emphasize tensile testing [22][89], while compression tests are often overlooked or only studied in isolation, as seen in the work by Sparks *et al.* [86]. By incorporating both tensile and compression tests, this research offers a more understanding of the mechanical properties of soft materials, which is crucial for applications where the material is subjected to both tension and compression. In our application, the tensile test data was more important since the soft components in SAM are primarily exposed to expansion, making tensile properties such as the ability to withstand tension and the elastic limit more relevant. However, the insights from compression tests, such as compressive strength, contribute to a broader understanding of material behaviour. While this information may be more applicable to other applications involving compressive loads on soft actuators or sensors, like tactile sensors [94], these findings remain valuable for researchers in the field.

The results highlighted significant discrepancies in the tensile and compression properties of materials such as Ecoflex 00-30 when compared to existing literature

[22][86][89]. These differences were attributed to variations in testing conditions, equipment, and specimen preparation. This highlights the importance of standardized testing conditions. By establishing a more consistent methodology, future research can build on these results, leading to more accurate and comparable data across studies. This will facilitate collaboration within the soft robotics community.

8.1.3 SAM Development

In SAM development, the focus was on both design and fabrication processes, inspired by the efficiency of the human muscular system. This chapter successfully addressed its objectives through two key steps. First, conceptual designs for three models of SAMs were created, with Model-1 inspired by muscle cell structure and Models-2 and -3 developed for performance comparison. Second, soft components were fabricated to effectively actuate SAMs. Creating the soft components is a challenge led to several adjustments in the fabrication process. By addressing the fabrication challenges, especially by using 3D-printed moulds and specific techniques, this research offers useful guidance for other researchers. It showcases effective methods for improving the fabrication of soft components. Unlike existing literature that primarily utilized commercial soft tubes such as silicon and rubber tubes, this research focused on fabricating precise soft components designed to meet the requirements of Model-1, Model-2, and Model-3 [62][63].

The fabrication of SAMs is presented through three main phases: mould fabrication, soft component fabrication, and SAM assembly. The detailed fabrication process, from mould creation to final assembly, ensured consistency and reliability in the produced actuators. The resulting produced SAMs facilitated the characterization and evaluation conducted in the subsequent chapters. Each component used in creating SAMs was successfully designed to facilitate testing procedures, including the creation of 3D adapters that easily fit into various testing systems.

8.1.4 SAM Characterisations

The objectives for characterizing SAMs were successfully addressed through experiments and analysis. Chapter 5 focused on developing reliable testing methodologies to evaluate the performance of three SAM models under varying pressure levels and actuation frequencies. Section 5.1 examined the force generation, while Section 5.2 investigated the range of displacement of the SAMs.

Both chapters provided a clear comparative analysis, contributing to an understanding of SAMs' performance.

To enhance the depth of the research, a lot of testing conditions were utilized to make the findings more reliable and applicable to a wider range of real-world scenarios. However, this also introduced challenges, as processing the increased amount of data became more complex and time-consuming. Moreover, presenting this expanded data in a clear manner that facilitated comparison between different SAM models proved to be more difficult.

8.1.4.1 Block Force Test

The study showed that the design of the soft component significantly affects the generated force. Model-3, which represents the traditional simple SAM model, generated the least force. This indicates that force performance can be enhanced through innovative design improvements. Both Model-1 and Model-2, which feature multiple cavities, produced high forces close to each other. The multiple cavities likely enhance the interaction between the chambers of the soft components, contributing to higher force generation. Additionally, the larger internal surface area in Model-1 and Model-2 compared to Model-3 could be a factor in their superior force generation (see 5.1.5 for more details).

According to the load tests of SAMs documented in the literature, the generated forces range widely from 12 to 700 N [56][57][70][71]. In this research, the generated force by SAMs at a static pressure of 60 kPa ranged between 11 and 19 N. This discrepancy is expected due to variations in soft materials, braids, components, testing methodologies, input pressures, and other factors used in different studies. Additionally, traditional SAMs in the literature were often designed for heavy manufacturing applications before the field of soft robotics was established, requiring significant power and high input pressure. In contrast, common applications of soft actuators in soft robotics, such as medical devices, assistive technologies, and bio-inspired robots, involve softer material and lower input pressures.

A key finding from the time interval analysis of load cycles, presented in Section Chapter 55.1.4.1.3, is that Model-1 exhibits the shortest pre-conditioning duration, indicating it initiates actuation more quickly than the other models. This behaviour could be due to the tighter fit of Model-1's soft component (three filaments) within the braid, compared to the identical cylindrical components of Model-2 and Model-3. This suggests that a tighter fit of the soft component inside the braid could enhance the responsiveness of SAM.

8.1.4.2 Displacement Test

Both the block force test and the displacement test shared several key methodological aspects. These included the development of the experimental setup, structured test procedures, and data processing methods. This shared methodology ensured consistent evaluation across both tests.

The analysis of peak displacement across different frequencies showed that Model-1 excels at higher frequencies (1 Hz and 0.5 Hz), while Model-3 performs better at lower frequencies (0.2 Hz and static conditions). This suggests that Model-1 might be more suitable for rapid actuation applications, whereas Model-3 is better for scenarios requiring maximum displacement and higher consistency. In contrast to the block force test results, which indicated the superiority of Model-2, the displacement test showed no significant impact of changing the configuration of SAM's design on the range of contraction.

In the displacement cycles of SAMs, several key events are captured, which divide the cycle into four time intervals: pre-conditioning, actuation, de-actuation, and idle. The time interval analysis indicated that Model-1 has the shortest pre-conditioning interval, indicating faster initiation of actuation. The actuation intervals were similar across all models, with Model-1 showing the shortest de-actuation interval and a longer idle state. This performance was unexpected given Model-1's complex design, suggesting that it is better for applications requiring a quick return to the idle state.

When compared with the findings of Takosoglu *et al.* [70] and Kothera *et al.* [68], it becomes evident that the SAMs in this research achieve similar or higher contraction ranges at significantly lower pressures. Takosoglu *et al.* [70] conducted displacement tests on Festo Fluidic Muscle and Shadow Air Muscle, which required higher input pressures (100-700 kPa and 60-350 kPa, respectively). Despite these higher pressures, the range of displacement for SAMs was comparable, demonstrating the efficiency of the SAMs displacement made from low shore-hardness material (Ecoflex 50) in this study. Similarly, the test setup used in this research was comparable to the one used by Kothera *et al.* [68], who measured blocked force and free contraction at different pressures. Despite some differences in methodology, the SAMs in this study achieved high contraction at lower pressures, highlighting their efficiency.

8.1.5 Case Study

A case study was successfully completed to understand SAM's performance in practical applications and its interaction with dynamic systems. The research designed the dynamic system to develop a comprehensive testing methodology to assess SAM's real-world capabilities. Targeted metrics within both SAM and the dynamic systems were measured, providing an understanding of performance. Furthermore, the study included a thorough assessment, analysis, and comparison of various SAM models, adding another valuable dimension to the characterization process. This was crucial in achieving the research aim by demonstrating how Model-1, inspired by biological muscles, performs compared to Models-2 and Models-3.

The results from the case study show a correlation with the findings from Section 5.2, where Model-3 exhibited slightly the highest range of contraction in both isolated (at lower frequencies) and dynamic tests. This consistency confirms that the displacement behaviour observed in isolated tests translates effectively into dynamic applications. However, unlike the force tests in Chapter 5, the case study focused on measuring the range of contraction (displacement) rather than evaluating the force generated by each model as a performance metric. This is because, in this case study, the measurements rely on video analysis, making it difficult to directly measure the load or force. Instead, the SAM’s capability to lift weight was assessed by adding various weights to the lower arm of the dynamic system and measuring their impact on the performance.

The comparison between the original and augmented sets of SAMs shows that the augmented set demonstrates relative consistency with the original set in terms of internal pressure, contraction, joint angle, and speed. The augmented set exhibited a slightly higher range of contraction, likely due to the smaller ratio between the length and diameter, allowing for more radial inflation. Model-3 consistently exhibited the highest range of contraction in both sets, emphasising its superior performance. This finding of the contraction measurement is not entirely aligned with the research aim, highlighting that while the multi-filament approach (Model-1) was intended to enhance performance by mimicking biological muscles, the traditional single-component design (Model-3) demonstrated superior contraction performance.

Our case study system was compared to similar SAM applications in exoskeleton structures found in the literature. Dynamic system of exoskeleton structures from Carvalho *et al.* [76] and Nabae *et al.* [74] showed high contraction capabilities at higher pressures compared to the SAMs in this research. This discrepancy due to the dimensions of the actuators and the dynamic systems design. Longer SAMs

enhance achieving more significant contraction and a higher driving angle between the arms. Additionally, as discussed earlier (see section 5.2.6.3), the materials and components used in the SAMs also influence their performance.

8.1.6 FE Simulation of SAM

FE simulation of SAMs' models presented to predict and understand their behaviour under various pressure conditions and then validate the reliability of the FE simulations of SAM against experimental findings. It focuses on developing FE model for the soft component of SAMs models without braid, the complex geometry of the braided sleeve, and the complete assembled SAMs models. The use of FE modelling and simulation techniques to enhance the evaluation of SAM was partially achieved, as there was low validity against experimental findings, especially for Model-1. The reliability of these FE simulations was validated against experimental findings, indicating the need for further refinements to improve accuracy and provide a more robust framework for evaluating SAM's performance.

The chapter demonstrates the FE modelling techniques to analyse the complex interactions within the braided structure and soft components. The research builds on previous FE simulations by Antonelli *et al.*, Tu *et al.*, and T. Hassan *et al.* [84] Antonelli *et al.* and Tu *et al.* used simpler methods, while T. Hassan *et al.* created a detailed 3D model of the braided sleeve with specialized software. Our research took advantage of these approaches but aligned more with T. Hassan *et al.*'s [84] method, using Python scripts in Abaqus PED to develop a comprehensive 3D model. Comparing experimental and simulation results, all studies showed good agreement. However, our simulation had less agreement, especially in contraction range due to the complexity of braid modelling. We attempted to define the friction of fibre interaction like T. Hassan *et al.* [84], but the simulation pressure to reach a level proceed as the contact regions were not recognized for our model.

In the FE model of the SAM displacement test, the FE simulation of Model-3 showed a consistent increase in contraction with pressure, unlike the real model, suggesting unaccounted factors in the simulation that might affected the experiments. At 20 kPa, both Model-2 and Model-3 simulations showed greater contraction than experimental models, but from 40 to 80 kPa, the experimental models had a greater contraction range. Model-1 performed decently at 20 kPa but poorly at higher pressures, highlighting the need for refining FE models to better match experimental results. In the FE model of the SAM block force test, the FE simulation of Model-3 consistently showed higher force outputs than the real model across all pressure levels. In contrast, Model-2 had excellent agreement with the real model at pressures above

20 kPa while Model-3 showed larger errors. Model-1's limitations were also evident due to interaction complexities, similar to the displacement test simulation.

Since this research mainly aims to evaluate the performance of SAMs made of multiple filaments (Model-1), the FE simulation results indicate some limitations that require further development and refinement for more reliable outcomes. Future work should focus on better defining the interactions within the braid and between the soft filaments of Model-1 to improve the correlation between experimental and FE simulation models. This will enhance the accuracy and reliability of the simulation results.

8.2 Conclusion

This PhD research assessed the feasibility of the novel multi-filament SAM (Model-1), designed to mimic the behaviour of biological muscles, and compared it with other designs, including Model-2's single body with multiple cavities and Model-3's traditional single cavity design. The findings indicate that incorporating multiple cavities in the design, as seen in Model-1 and Model-2, contributes to an increase in generated force. At 60 kPa and 0.2 Hz, Model-2 outperformed Model-1 by around 8%, and Model-2 generated 35% more force than Model-3. Similar trends were observed at 80 kPa and 0.2 Hz, confirming consistent results across different pressure conditions. However, the displacement tests revealed that changes in the SAM models had no significant effect on displacement performance, as the rankings varied across conditions with only minor differences. For example, at 20 kPa and 0.2 Hz, Model-1 outperformed Model-2 by 15% and Model-3 by 60%, but at 60 kPa and 0.2 Hz, Model-3 showed a 5% superiority over both Model-1 and Model-2. Additionally, in the case study, the performance of the models at high pressures (60 and 80 kPa) mirrored the displacement test results, with Model-3 displaying a minor superiority. At 60 kPa and 0.2 Hz, Model-3 outperformed Model-1 by 12% and Model-2 by 14%. These findings suggest that while mimicking skeletal muscles provided a novel conceptual design for a soft actuator, it did not result in a significant improvement in displacement performance. Nonetheless, studying these models offers valuable insights into how design modifications influence SAM performance, particularly in force generation.

The research's fabrication methods for soft materials were presented in two distinct phases. In the first phase, soft tensile and compression testing specimens were fabricated, which was crucial for understanding the fabrication requirements, techniques, and challenges. The iterative refinement process during this phase

provided valuable insights into achieving precision and consistency in soft material fabrication, which was essential for the subsequent phase involving the fabrication of SAMs' soft components. In the second phase, fabricating the soft components of SAMs presented additional challenges due to the complexity of the design. Despite these difficulties, the soft components were precisely created as planned. The fabrication techniques for the soft inflatable components of SAMs were optimized through iterative refinements, with a focus on precise 3D printed moulds as the ideal method. This approach ensured the production of high-quality soft components, which can also be applied in other applications to fabricate different soft actuators with similar quality.

The techniques and methods used for characterizing SAMs were highly effective in assessing their performance, with the force and displacement metrics providing a comprehensive evaluation. A key innovation was the displacement characterization setup, which restricted movement to a single dimension with one degree of freedom. This approach ensures that measurements accurately reflect the true performance of the SAMs. The contribution is valuable to the field of soft robotics, as it introduces a new technique that allows for more precise evaluations.

FE simulations proved to be a useful tool for comparing the performance of the three SAM models, as they provide a more controlled and consistent way to replicate and analyse their behaviours. This method is particularly beneficial compared to experimental testing, which can be affected by inconsistencies in fabrication and testing. However, some limitations were found in accurately modelling complex interactions, especially in Model-1. Therefore, further improvements in future are needed to increase the accuracy and reliability of these simulations.

The successful design, fabrication, and evaluation of the SAM models in this research, along with the understanding gained about soft component design, provide a strong basis for future improvements in soft robotics. Future research should build on these findings to refine SAM designs and enhance their performance, expanding their potential uses and making them more effective in real-world applications.

8.3 Future Work

Future work addresses the study limitations by enhancing performance of SAM, the measured key metrics, real-world applications, and FE modelling of SAM. The performance of SAMs can be enhanced by improving the design of the soft components. This research evaluated three different configurations, highlighting the need for further studies on aspects such as the internal surface area of the cavity.

Since Model-1 and Model-2 generated higher forces than Model-3, future research should consider modifying the inner diameter of Model-3's internal cavity to assess its impact on performance. Another area for improving the performance involves exploring the effects of different soft materials used in SAMs. For example, the tensile strength of the soft materials could be considered to assess how variations in this property impact SAM performance. This can be achieved by fabricating the soft component using soft materials with varied range of tensile strengths to observe their effects on performance. Further research is needed to understand how the type, material, and size of the braided sleeve affect SAM performance. Lastly, the force test findings showed that a tighter fit of the soft component inside the braid improves SAM's responsiveness, so this should be carefully considered during fabrication to enhance overall performance.

When conducting experimental tests on SAMs, collecting additional data can provide deeper insights into their performance. Force-displacement data is crucial for understanding the relationship between added weight and the resultant contraction output, showing how the SAM contracts under specific loads. Hysteresis loops (which show the difference in force output during pressurization and depressurization cycles) are also important for understanding energy losses and actuation efficiency.

This research demonstrated that SAMs could achieve more efficient pneumatic actuation at lower pressures compared to existing literature, resulting in more energy-efficient operations. This finding suggests that future research should explore potential real-world applications for SAMs, particularly in fields such as robotics, medical devices, and wearable technology, integrating these insights into practical implementations. Each SAM model offers distinct features that can guide future applications: Model-1 demonstrated higher actuation speed, outperforming Model-2 by 25% and Model-3 by 35%, making it suitable for applications requiring rapid responses. Model-2 consistently generated the highest force output, with an 8% higher force than Model-1 and 35% higher force than Model-3, making it ideal for tasks requiring maximum force generation. Model-3, while the simplest design, exhibited superior consistency across samples, which could be advantageous in applications that prioritize reliability and ease of production.

The FE simulation findings underscore the challenges in accurately modelling the complex components of SAMs. Our approach highlights the need for further refinement in FE simulation techniques to achieve better alignment with experimental results. Improving the creation of the braid model and definition of interactions within the braid and between soft filaments is essential for enhancing the accuracy and

reliability of future simulations, particularly for Model-1. This focus will be important for advancing the simulation and overall evaluation of SAM performance.

In the current method, the braided sleeve structure was created using Python scripts to generate the braid geometry. One of the key limitations of this approach is that the interaction between the fibres of the braid, specifically the frictional contact between them, is not defined. In FE simulations, defining interactions is important for accurately replicating the real physical behaviour of the braid. However, in the model created using the 3D wire technique, the fibres are treated as a series of nodes rather than continuous surface. As a result, contact regions between the fibres cannot be recognized, making it impossible to simulate the frictional interaction between the fibres of the braid. This limitation reduces the accuracy of the model in representing the real physical behaviour of the braided sleeve during contraction and extension motion.

To address this limitation, a new method could be employed in future work. The braided sleeve structure can be generated using CAD software, such as SolidWorks, which allows for more detailed geometry creation. The CAD model can then be exported into the FE simulation software, such as Abaqus, where the interaction between fibres can be more accurately modelled by defining contact regions and applying a friction coefficient. This might enable the simulation to better represent the real-world physical interactions within the braid, capturing the way fibres slide and resist each other during SAM contraction and extension. However, this approach will require significantly higher computational time of the simulation.

Developing an accurate model of the braided sleeve and integrating it with the soft component remains a complex challenge that will require expertise from different fields, particularly those with strong backgrounds in FE simulation. The most important step in FE modelling of SAM is to accurately replicate the braid’s geometry, material properties to ensure accurate prediction of its contraction and extension behaviour.

References

[1] F. Ilievski, A. D. Mazzeo, R. F. Shepherd, X. Chen, and G. M. Whitesides, “Soft Robotics for Chemists,” *Angew. Chemie*, vol. 123, no. 8, pp. 1930–1935, 2011, doi: 10.1002/ange.201006464.

[2] M. Cianchetti, C. Laschi, A. Menciassi, and P. Dario, “Biomedical applications of soft robotics,” *Nat. Rev. Mater.*, vol. 3, no. 6, pp. 143–153, 2018, doi: 10.1038/s41578-018-0022-y.

[3] R. J. Full, “Biological Inspiration: Lessons from Many-Legged Locomotors,” *Robot. Res.*, pp. 337–341, 2000, doi: 10.1007/978-1-4471-0765-1_41.

[4] K. Jung, J. C. Koo, J. Do Nam, Y. K. Lee, and H. R. Choi, “Artificial annelid robot driven by soft actuators,” *Bioinspiration and Biomimetics*, vol. 2, no. 2, 2007, doi: 10.1088/1748-3182/2/2/S05.

[5] A. D. Marchese, C. D. Onal, and D. Rus, “Autonomous Soft Robotic Fish Capable of Escape Maneuvers Using Fluidic Elastomer Actuators,” *Soft Robot.*, vol. 1, no. 1, pp. 75–87, 2014, doi: 10.1089/soro.2013.0009.

[6] J. Frame, N. Lopez, O. Curet, and E. D. Engeberg, “Thrust force characterization of free-swimming soft robotic jellyfish,” *Bioinspiration and Biomimetics*, vol. 13, no. 6, 2018, doi: 10.1088/1748-3190/aadcb3.

[7] M. Cianchetti *et al.*, “Soft Robotics Technologies to Address Shortcomings in Today’s Minimally Invasive Surgery: The STIFF-FLOP Approach,” *Soft Robot.*, vol. 1, no. 2, pp. 122–131, 2014, doi: 10.1089/soro.2014.0001.

[8] S. Kim, C. Laschi, and B. Trimmer, “Soft robotics: A bioinspired evolution in robotics,” *Trends Biotechnol.*, vol. 31, no. 5, pp. 287–294, 2013, doi: 10.1016/j.tibtech.2013.03.002.

[9] M. Li, A. Pal, A. Aghakhani, A. Pena-Francesch, and M. Sitti, “Soft actuators for real-world applications,” *Nat. Rev. Mater.*, vol. 7, no. 3, pp. 235–249, 2022, doi: 10.1038/s41578-021-00389-7.

[10] G. Bao *et al.*, “Soft robotics: Academic insights and perspectives through bibliometric analysis,” *Soft Robot.*, vol. 5, no. 3, pp. 229–241, 2018, doi: 10.1089/soro.2017.0135.

[11] G. M. Whitesides, “Soft Robotics,” *Angew. Chemie - Int. Ed.*, vol. 57, no. 16, pp. 4258–4273, 2018, doi: 10.1002/anie.201800907.

[12] N. R. Sinatra, C. B. Teeple, D. M. Vogt, K. K. Parker, D. F. Gruber, and R. J. Wood, “Ultragentle manipulation of delicate structures using a soft robotic gripper,” *Sci. Robot.*, vol. 4, no. 33, pp. 1–11, 2019, doi: 10.1126/SCIROBOTICS.AAX5425.

[13] E. W. Hawkes, L. H. Blumenschein, J. D. Greer, and A. M. Okamura, “A soft robot that navigates its environment through growth,” *Sci. Robot.*, vol. 2, no. 8, pp. 1–7, 2017, doi: 10.1126/scirobotics.aan3028.

[14] S. Aracri *et al.*, “Soft Robots for Ocean Exploration and Offshore Operations: A

Perspective,” *Soft Robot.*, vol. 8, no. 6, pp. 625–639, 2021, doi: 10.1089/soro.2020.0011.

[15] L. Wang, S. G. Nurzaman, and F. Iida, “Soft-Material Robotics,” *Found. Trends Robot.*, vol. 5, no. 3, pp. 191–259, 2017, doi: 10.1561/2300000055.

[16] Y. Sun, Y. S. Song, and J. Paik, “Characterization of silicone rubber based soft pneumatic actuators,” *IEEE Int. Conf. Intell. Robot. Syst.*, pp. 4446–4453, 2013, doi: 10.1109/IROS.2013.6696995.

[17] P. Moseley, J. M. Florez, H. A. Sonar, G. Agarwal, W. Curtin, and J. Paik, “Modeling, Design, and Development of Soft Pneumatic Actuators with Finite Element Method,” *Adv. Eng. Mater.*, vol. 18, no. 6, pp. 978–988, 2016, doi: 10.1002/adem.201500503.

[18] D. Rus and M. T. Tolley, “Design, fabrication and control of soft robots,” *Nature*, vol. 521, no. 7553, pp. 467–475, 2015, doi: 10.1038/nature14543.

[19] Smooth-On Company, “Materials for Soft Robotics Applications.” Accessed: Nov. 29, 2019. [Online]. Available: https://www.smooth-on.com/

[20] Wacker Chemie AG, “ELASTOSIL® M 4601.” Accessed: Mar. 25, 2024. [Online]. Available: https://www.wacker.com/h/en-us/silicone-rubber/room-temperature-curing-silicone-rubber-rtv-2/elastosil-m-4601-ab/p/000018458

[21] M. Mooney, “A theory of large elastic deformation,” *J. Appl. Phys.*, vol. 11, no. 9, pp. 582–592, 1940, doi: 10.1063/1.1712836.

[22] J. C. Case, E. L. White, and R. K. Kramer, “Soft material characterization for robotic applications,” *Soft Robot.*, vol. 2, no. 2, pp. 80–87, 2015, doi: 10.1089/soro.2015.0002.

[23] G. Udupa, P. Sreedharan, P. S. Dinesh, and D. Kim, “Asymmetric bellow flexible pneumatic actuator for miniature robotic soft gripper,” *J. Robot.*, vol. 2014, 2014, doi: 10.1155/2014/902625.

[24] I. 37: 2017 2017, “BS ISO 37 : 2017 BSI Standards Publication Rubber , vulcanized or thermoplastic — Determination of tensile stress-strain properties,” 2017.

[25] B. Standards, “BS ISO 7743 : 2011 BSI Standards Publication Rubber , vulcanized or thermoplastic — Determination of compression stress-strain properties,” 2011.

[26] A. Ali, M. Hosseini, and B. B. Sahari, “A review and comparison on some rubber elasticity models,” *J. Sci. Ind. Res. (India).*, vol. 69, no. 7, pp. 495–500, 2010.

[27] M. Rackl, “Article + Errata Curve Fitting for Ogden, Yeoh and Polynomial Models,” *Ostbayerishce Tech. Hochschule Regensbg.*, no. September, 2017.

[28] Y. Elsayed *et al.*, “Finite Element Analysis and Design Optimization of a Pneumatically Actuating Silicone Module for Robotic Surgery Applications,” *Soft Robot.*, vol. 1, no. 4, pp. 255–262, 2014, doi: 10.1089/soro.2014.0016.

[29] R. W. Ogden, G. Saccomandi, and I. Sgura, “Fitting hyperelastic models to experimental data,” *Comput. Mech.*, vol. 34, no. 6, pp. 484–502, 2004, doi: 10.1007/s00466-004-0593-y.

[30] N. Mavrodontis, “Modelling hyperelastic behavior using test data in abaqus,” Simuleon FEA Blog. Accessed: Apr. 05, 2024. [Online]. Available: https://simulation-blog.technia.com/simulation/modelling-hyperelastic-behavior-using-test-data-in-abaqus

[31] B. McGinty, “Hydrostatic & Deviatoric Stresses.” [Online]. Available: https://www.continuummechanics.org/hydrodeviatoricstress.html

[32] C. Schumacher, E. Knoop, and M. Bacher, “Simulation-Ready Characterization of Soft Robotic Materials,” *IEEE Robot. Autom. Lett.*, vol. 5, no. 3, pp. 3780–3787, 2020, doi: 10.1109/LRA.2020.2982058.

[33] B. Mosadegh *et al.*, “Pneumatic networks for soft robotics that actuate rapidly,” *Adv. Funct. Mater.*, vol. 24, no. 15, pp. 2163–2170, 2014, doi: 10.1002/adfm.201303288.

[34] M. A. Robertson, H. Sadeghi, J. M. Florez, and J. Paik, “Soft Pneumatic Actuator Fascicles for High Force and Reliability,” *Soft Robot.*, vol. 4, no. 1, pp. 23–32, 2017, doi: 10.1089/soro.2016.0029.

[35] K. C. Galloway, P. Polygerinos, C. J. Walsh, and R. J. Wood, “Mechanically programmable bend radius for fiber-reinforced soft actuators,” *2013 16th Int. Conf. Adv. Robot. ICAR 2013*, pp. 1–6, 2013, doi: 10.1109/ICAR.2013.6766586.

[36] K. C. Galloway *et al.*, “Soft Robotic Grippers for Biological Sampling on Deep Reefs,” *Soft Robot.*, vol. 3, no. 1, pp. 23–33, 2016, doi: 10.1089/soro.2015.0019.

[37] N. El-Atab *et al.*, “Soft Actuators for Soft Robotic Applications: A Review,” *Adv. Intell. Syst.*, vol. 2, no. 10, 2020, doi: 10.1002/aisy.202000128.

[38] Y. She, J. Chen, H. Shi, and H.-J. Su, “Modeling and validation of a novel bending actuator for soft robotics applications,” *Soft Robot.*, vol. 3, no. 2, pp. 71–81, 2016.

[39] I. De Falco, M. Cianchetti, and A. Menciassi, “STIFF-FLOP surgical manipulator: design and preliminary motion evaluation,” in *Proc. 4th Workshop Computer/Robot Assisted Surgery (CRAS)*, 2014, pp. 131–134.

[40] B. Tondu and P. Lopez, “Artificial Muscle Ro bot Act u ato r s,” *Control Syst.*, vol. 20, no. 2, pp. 15–38, 2000.

[41] S. Kurumaya, H. Nabae, G. Endo, and K. Suzumori, “Design of thin McKibben muscle and multifilament structure,” *Sensors Actuators, A Phys.*, vol. 261, pp. 66–74, 2017, doi: 10.1016/j.sna.2017.04.047.

[42] B. Gorissen, D. Reynaerts, S. Konishi, K. Yoshida, J. W. Kim, and M. De Volder, “Elastic Inflatable Actuators for Soft Robotic Applications,” *Adv. Mater.*, vol. 29, no. 43, pp. 1–14, 2017, doi: 10.1002/adma.201604977.

[43] M. A. Abd *et al.*, “Impacts of Soft Robotic Actuator Geometry on End Effector Force and Displacement,” *Florida Conf. Recent Adv. Robot.*, vol. 30, no. May, pp. 94–99, 2017, [Online]. Available: http://public.eng.fau.edu/design/fcrar2017/papers/fcrar2017_proceedings.pdf

[44] Soft Robotics Toolkit, “Variation of Motion of Soft Robotics.” Accessed: Nov. 29, 2019. [Online]. Available: https://softroboticstoolkit.com/book/fr-variation-

motion

[45] I. De Falco, M. Cianchetti, and A. Menciassi, “A soft multi-module manipulator with variable stiffness for minimally invasive surgery,” *Bioinspiration and Biomimetics*, vol. 12, no. 5, 2017, doi: 10.1088/1748-3190/aa7ccd.

[46] R. V. Martinez *et al.*, “Robotic tentacles with three-dimensional mobility based on flexible elastomers,” *Adv. Mater.*, vol. 25, no. 2, pp. 205–212, 2013, doi: 10.1002/adma.201203002.

[47] L. Manfredi, L. Yue, and A. Cuschieri, “A 3 DOFs mini variable stiffness soft pneumatic actuator,” *ACTUATOR 2018 - 16th Int. Conf. Exhib. New Actuators Drive Syst. Conf. Proc.*, no. June, pp. 169–172, 2018.

[48] P. Polygerinos, Z. Wang, K. C. Galloway, R. J. Wood, and C. J. Walsh, “Soft robotic glove for combined assistance and at-home rehabilitation,” *Rob. Auton. Syst.*, vol. 73, pp. 135–143, 2015, doi: 10.1016/j.robot.2014.08.014.

[49] R. K. Katzschmann *et al.*, “Dynamically closed-loop controlled soft robotic arm using a reduced order finite element model with state observer,” *RoboSoft 2019 - 2019 IEEE Int. Conf. Soft Robot.*, pp. 717–724, 2019, doi: 10.1109/ROBOSOFT.2019.8722804.

[50] L. Jamone, L. Natale, G. Metta, and G. Sandini, “Highly sensitive soft tactile sensors for an anthropomorphic robotic hand,” *IEEE Sens. J.*, vol. 15, no. 8, pp. 4226–4233, 2015, doi: 10.1109/JSEN.2015.2417759.

[51] T. J. Wallin, J. Pikul, and R. F. Shepherd, “3D printing of soft robotic systems,” *Nat. Rev. Mater.*, vol. 3, no. 6, pp. 84–100, 2018, doi: 10.1038/s41578-018-0002-2.

[52] H. K. Yap, H. Y. Ng, and C. H. Yeow, “High-Force Soft Printable Pneumatics for Soft Robotic Applications,” *Soft Robot.*, vol. 3, no. 3, pp. 144–158, 2016, doi: 10.1089/soro.2016.0030.

[53] E. Sachyani Keneth, A. Kamyshny, M. Totaro, L. Beccai, and S. Magdassi, “3D Printing Materials for Soft Robotics,” *Adv. Mater.*, vol. 33, no. 19, pp. 1–17, 2021, doi: 10.1002/adma.202003387.

[54] A. Zolfagharian, A. Z. Kouzani, S. Y. Khoo, A. A. A. Moghadam, I. Gibson, and A. Kaynak, “Evolution of 3D printed soft actuators,” *Sensors Actuators, A Phys.*, vol. 250, pp. 258–272, 2016, doi: 10.1016/j.sna.2016.09.028.

[55] K. J. Cho, J. S. Koh, S. Kim, W. S. Chu, Y. Hong, and S. H. Ahn, “Review of manufacturing processes for soft biomimetic robots,” *Int. J. Precis. Eng. Manuf.*, vol. 10, no. 3, pp. 171–181, 2009, doi: 10.1007/s12541-009-0064-6.

[56] C. P. Chou and B. Hannaford, “Measurement and modeling of McKibben pneumatic artificial muscles,” *IEEE Trans. Robot. Autom.*, vol. 12, no. 1, pp. 90–102, 1996, doi: 10.1109/70.481753.

[57] M. Doumit, A. Fahim, and M. Munro, “Analytical modeling and experimental validation of the braided pneumatic muscle,” *IEEE Trans. Robot.*, vol. 25, no. 6, pp. 1282–1291, Dec. 2009, doi: 10.1109/TRO.2009.2032959.

[58] B. Tondu, “Modelling of the McKibben artificial muscle: A review,” *J. Intell. Mater. Syst. Struct.*, vol. 23, no. 3, pp. 225–253, 2012, doi: 10.1177/1045389X11435435.

[59] J. G. Nancy A. Curtin, Robert E., Warren F., “Muscle Anatomy.” Accessed: Apr. 08, 2024. [Online]. Available: https://www.britannica.com/science/muscle/Muscle-in-soft-animals

[60] S. Kurumaya, K. Suzumori, H. Nabae, and S. Wakimoto, “Musculoskeletal lower-limb robot driven by multifilament muscles,” *ROBOMECH J.*, vol. 3, no. 1, pp. 1–15, 2016, doi: 10.1186/s40648-016-0061-3.

[61] A. Garriga-Casanovas, A. A. M. Faudzi, T. Hiramitsu, F. Rodriguez Y Baena, and K. Suzumori, “Multifilament pneumatic artificial muscles to mimic the human neck,” *2017 IEEE Int. Conf. Robot. Biomimetics, ROBIO 2017*, vol. 2018-Janua, pp. 809–816, 2017, doi: 10.1109/ROBIO.2017.8324517.

[62] D. Sangian, “‘From Traditional Braiding Methods to Additive Manufacturing for Fabricating Mckibben Artificial Muscles,’” *Biomed. J. Sci. Tech. Res.*, vol. 38, no. 5, 2021, doi: 10.26717/bjstr.2021.38.006211.

[63] G. Andrikopoulos, G. Nikolakopoulos, and S. Manesis, “A Survey on applications of Pneumatic Artificial Muscles,” *2011 19th Mediterr. Conf. Control Autom. MED 2011*, pp. 1439–1446, 2011, doi: 10.1109/MED.2011.5982983.

[64] S. C. Obiajulu, E. T. Roche, F. A. Pigula, and C. J. Walsh, “SOFT PNEUMATIC ARTIFICIAL MUSCLES WITH LOW THRESHOLD PRESSURES FOR A CARDIAC COMPRESSION DEVICE,” 2013. [Online]. Available: http://asmedigitalcollection.asme.org/IDETC-CIE/proceedings-pdf/IDETC-CIE2013/55935/V06AT07A009/4254493/v06at07a009-detc2013-13004.pdf

[65] E. T. Roche *et al.*, “A bioinspired soft actuated material,” *Adv. Mater.*, vol. 26, no. 8, pp. 1200–1206, 2014, doi: 10.1002/adma.201304018.

[66] S. C. Obiajulu and E. T. Roche, “Soft Pneumatic Artificial Muscles With Low Threshold Pressures,” *ASME Int. Des. Eng. Tech. Conf. Comput. Inf. Eng. Conf.*, no. 1, pp. 1–8, 2015.

[67] A. Manuello Bertetto and M. Ruggiu, “Characterization and modeling of air muscles,” *Mech. Res. Commun.*, vol. 31, no. 2, pp. 185–194, 2004, doi: 10.1016/S0093-6413(03)00088-0.

[68] C. S. Kothera, M. Jangid, J. Sirohi, and N. M. Wereley, “Experimental characterization and static modeling of McKibben actuators,” *J. Mech. Des.*, vol. 131, no. 9, pp. 0910101–09101010, 2009, doi: 10.1115/1.3158982.

[69] N. C. Goulbourne and S. Son, “Numerical and experimental analysis of McKibben actuators and dielectric elastomer sensors,” *ASME Int. Mech. Eng. Congr. Expo. Proc.*, vol. 10 PART A, pp. 175–186, 2008, doi: 10.1115/IMECE2007-42495.

[70] J. E. Takosoglu, P. A. Laski, S. Blasiak, G. Bracha, and D. Pietrala, “Determining the Static Characteristics of Pneumatic Muscles,” *Meas. Control (United Kingdom)*, vol. 49, no. 2, pp. 62–71, Mar. 2016, doi: 10.1177/0020294016629176.

[71] M. G. Antonelli, P. Beomonte Zobel, F. Durante, and T. Raparelli, “Numerical modelling and experimental validation of a McKibben pneumatic muscle actuator,” *J. Intell. Mater. Syst. Struct.*, vol. 28, no. 19, pp. 2737–2748, 2017, doi: 10.1177/1045389X17698245.

[72] B. S. Kang, C. S. Kothera, B. K. S. Woods, and N. M. Wereley, “Dynamic modeling of mckibben pneumatic artificial muscles for antagonistic actuation,” *Proc. - IEEE Int. Conf. Robot. Autom.*, pp. 182–187, 2009, doi: 10.1109/ROBOT.2009.5152280.

[73] B. Salahuddin, H. Warren, and G. M. Spinks, “A comprehensive test method for measuring actuation performance of McKibben artificial muscles,” *Smart Mater. Struct.*, vol. 30, no. 4, 2021, doi: 10.1088/1361-665X/abea01.

[74] G. Na, H. Nabae, and K. Suzumori, “Braided thin mckibben muscles for musculoskeletal robots,” *Sensors Actuators A Phys.*, vol. 357, no. April, p. 114381, 2023, doi: 10.1016/j.sna.2023.114381.

[75] K. Kawamura *et al.*, “ISAC : Foundations in Human – Humanoid Interaction”.

[76] A. D. D. R. Carvalho, N. Karanth P, and V. Desai, “Characterization of pneumatic muscle actuators and their implementation on an elbow exoskeleton with a novel hinge design,” *Sensors and Actuators Reports*, vol. 4, no. April, p. 100109, 2022, doi: 10.1016/j.snr.2022.100109.

[77] R. Niiyama, A. Nagakubo, and Y. Kuniyoshi, “Mowgli: A bipedal jumping and landing robot with an artificial musculoskeletal system,” *Proc. - IEEE Int. Conf. Robot. Autom.*, no. April 2007, pp. 2546–2551, 2007, doi: 10.1109/ROBOT.2007.363848.

[78] J. He *et al.*, “Design of a robotic upper extremity repetitive therapy device,” *Proc. 2005 IEEE 9th Int. Conf. Rehabil. Robot.*, vol. 2005, pp. 95–98, 2005, doi: 10.1109/ICORR.2005.1501060.

[79] M. A. Khan, S. Shaik, M. H. Tariq, and T. Kamal, “McKibben Pneumatic Artificial Muscle Robot Actuators - A Review,” *2023 Int. Conf. Robot. Autom. Ind. ICRAI 2023*, pp. 1–6, 2023, doi: 10.1109/ICRAI57502.2023.10089581.

[80] I. Ichim, “Pneumatic Applied To Logistic Systems,” *Ann. Oradea Univ. Fascicle Manag. Technol. Eng.*, vol. 6, no. 16, pp. 2282–2289, 2007, [Online]. Available: http://imtuoradea.ro/auo.fmte/files-2007/MIE_files/ICHIM_Izabella_1.pdf

[81] P. Polygerinos *et al.*, “Modeling of Soft Fiber-Reinforced Bending Actuators,” *IEEE Trans. Robot.*, vol. 31, no. 3, pp. 778–789, 2015, doi: 10.1109/TRO.2015.2428504.

[82] P. Polygerinos *et al.*, “Towards a soft pneumatic glove for hand rehabilitation,” *IEEE Int. Conf. Intell. Robot. Syst.*, pp. 1512–1517, 2013, doi: 10.1109/IROS.2013.6696549.

[83] Q. Tu, Y. Wang, D. Yue, and F. A. Dwomoh, “Analysis on the Impact Factors for the Pulling Force of the McKibben Pneumatic Artificial Muscle by a FEM Model,” *J. Robot.*, vol. 2020, 2020, doi: 10.1155/2020/4681796.

[84] T. Hassan, M. Cianchetti, M. Moatamedi, B. Mazzolai, C. Laschi, and P. Dario, “Finite-element modeling and design of a pneumatic braided muscle actuator with multifunctional capabilities,” *IEEE/ASME Trans. Mechatronics*, vol. 24, no. 1, pp. 109–119, 2019, doi: 10.1109/TMECH.2018.2877125.

[85] C. Schumacher, E. Knoop, and M. Bacher, “Simulation-Ready Characterization of Soft Robotic Materials,” *IEEE Robot. Autom. Lett.*, vol. 5,

no. 3, pp. 3780–3787, Jul. 2020, doi: 10.1109/LRA.2020.2982058.

[86] J. L. Sparks *et al.*, “Use of Silicone Materials to Simulate Tissue Biomechanics as Related to Deep Tissue Injury,” 2015.

[87] J. C. Case, E. L. White, and R. K. Kramer, “Soft material characterization for robotic applications,” *Soft Robot.*, vol. 2, no. 2, pp. 80–87, Jun. 2015, doi: 10.1089/soro.2015.0002.

[88] J. L. Sparks *et al.*, “Use of silicone materials to simulate tissue biomechanics as related to deep tissue injury,” *Adv. Ski. Wound Care*, vol. 28, no. 2, pp. 59–68, 2015, doi: 10.1097/01.ASW.0000460127.47415.6e.

[89] L. Marechal, P. Balland, L. Lindenroth, F. Petrou, C. Kontovounisios, and F. Bello, “Toward a Common Framework and Database of Materials for Soft Robotics,” *Soft Robot.*, vol. 8, no. 3, pp. 284–297, 2021, doi: 10.1089/soro.2019.0115.

[90] R. L. Graham, B. D. Lubachevsky A’, K. J. Nurmela B’l, and P. R. J. Ostergglrd, “DISCRETE MATHEMATICS ELSEVIER Discrete Dense packings of congruent circles in a circle,” 1998.

[91] T. Nozaki and T. Noritsugu, “Motion analysis of McKibben type pneumatic rubber artificial muscle with finite element method,” *Int. J. Autom. Technol.*, vol. 8, no. 2, pp. 147–158, 2014, doi: 10.20965/ijat.2014.p0147.

[92] M. S. Xavier, A. J. Fleming, and Y. K. Yong, “Finite Element Modeling of Soft Fluidic Actuators: Overview and Recent Developments,” *Adv. Intell. Syst.*, vol. 3, no. 2, 2021, doi: 10.1002/aisy.202000187.

[93] S. J. Lee and C. L. Kim, “Influence of surface structure on friction and wear characteristics of silicone rubber for hydraulic rod seals,” *RSC Adv.*, vol. 13, no. 48, pp. 33595–33602, 2023, doi: 10.1039/d3ra06485a.

[94] H. Wang *et al.*, “A Low-cost Soft Tactile Sensing Array Using 3D Hall Sensors,” *Procedia Eng.*, vol. 168, pp. 650–653, 2016, doi: 10.1016/j.proeng.2016.11.237.

Appendix 1: Gantt Chart

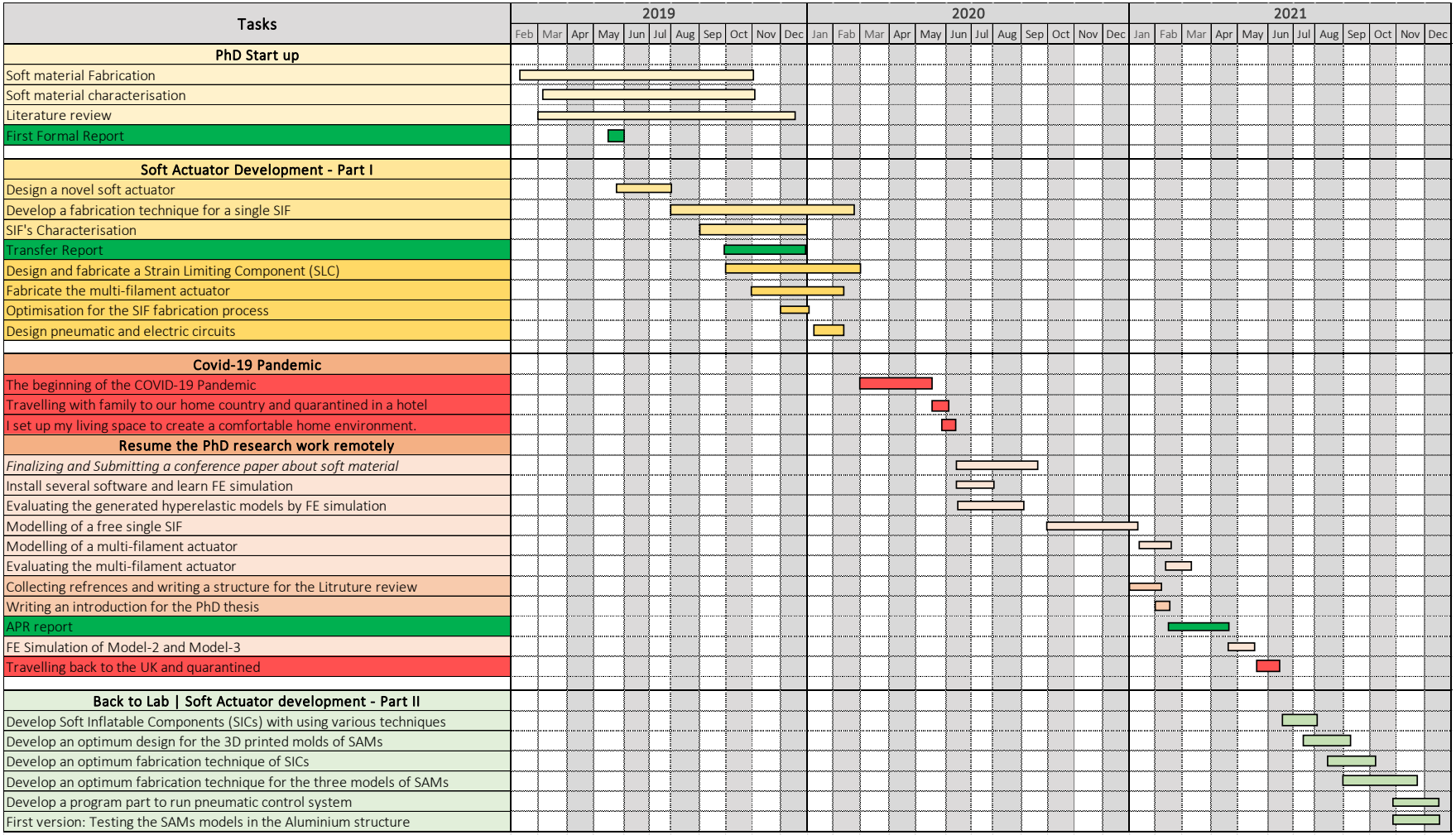

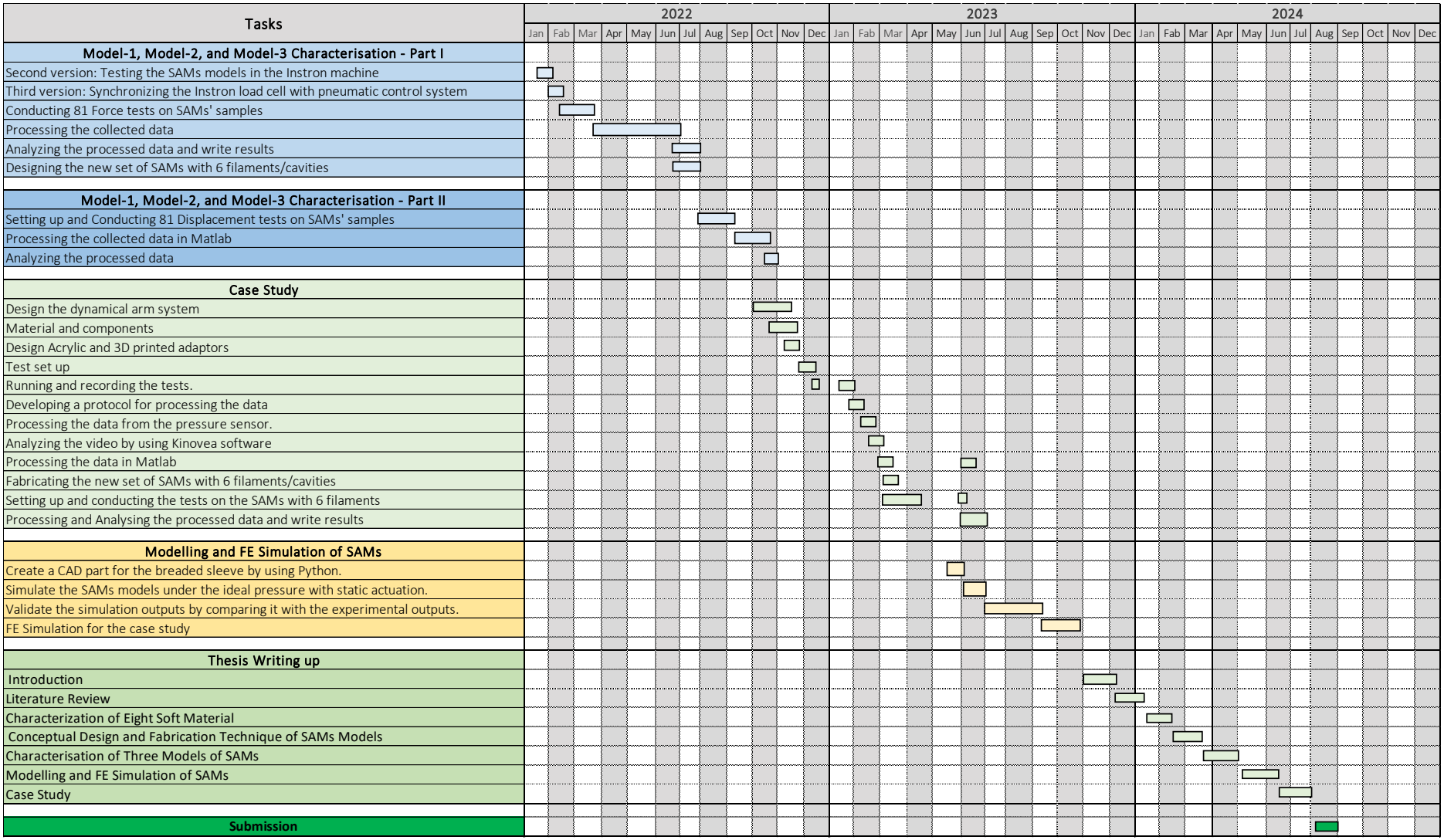
Tasks
2022
2023
2024
Jan Fab Mar Apr May Jun Jul Aug Sep Oct Nov Dec
Model-1, Model-2, and Model-3 Characterisation - Part I
Second version: Testing the SAMs models in the Instron machine
Third version: Synchronizing the Instron load cell with pneumatic control system
Conducting 81 Force tests on SAMs' samples
Processing the collected data
Analyzing the processed data and write results
Designing the new set of SAMs with 6 filaments/cavities
Model-1, Model-2, and Model-3 Characterisation - Part II
Setting up and Conducting 81 Displacement tests on SAMs' samples
Processing the collected data in Matlab
Analyzing the processed data
Case Study
Design the dynamical arm system
Material and components
Design Acrylic and 3D printed adaptors
Test set up
Running and recording the tests.
Developing a protocol for processing the data
Processing the data from the pressure sensor.
Analyzing the video by using Kinovea software
Processing the data in Matlab
Fabricating the new set of SAMs with 6 filaments/cavities
Setting up and conducting the tests on the SAMs with 6 filaments
Processing and Analysing the processed data and write results
Modelling and FE Simulation of SAMs
Create a CAD part for the breaded sleeve by using Python.
Simulate the SAMs models under the ideal pressure with static actuation.
Validate the simulation outputs by comparing it with the experimental outputs.
FE Simulation for the case study
Thesis Writing up
Introduction
Literature Review
Characterization of Eight Soft Material
Conceptual Design and Fabrication Technique of SAMs Models
Characterisation of Three Models of SAMs
Modelling and FE Simulation of SAMs
Case Study
Submission

Appendix 2: Soft Material Characterisation

Appendix 2.1: Evolution of the Tensile Specimen Mould

Optimal fabrication processes and mould designs were achieved after several trials, each incorporating slight modifications. Fig.App 1 illustrates key developments in moulds and fabrication processes:

First Trial*:* The mould was designed to fabricate five specimens at once, with a single injection port at the base connected by narrow runners for even silicone distribution. A metal needle was inserted, and the injection port was sealed with hot glue to prevent leaks and air bubbles. The EFD Precision Fluid Dispenser was used for silicone dispersion. However, issues included air bubbles in the silicone and leaks from the injection port and mould sides.

Second Trial: The mould was adjusted to produce four specimens, maintaining similar runner designs and injection positioning. However, leaks and air bubble formation still exist.

Third Trial*:* Modifications included extending the specimen ends for better grip during testing, applying silicone grease between mould sheets to seal against leaks, and deepening vent ports for improved air release. Leaks were reduced but not solved completely, and air bubbles still formed.

Fourth Trial*:* Additional degassing of the material in the syringe barrel was implemented, and the injection direction was reversed from bottom-up to top-down. The injection was also applied manually instead of using the Fluid Dispenser. Leaks were further reduced, but air bubbles still formed, indicating that the injection direction did not affect bubble formation.

Fifth Trial*:* A 2 mm diameter needle was wrapped in blue tack and placed into the mould's injection port, providing a tighter seal and more stability during injection. However, material leakage and air bubbles formation occurred.

A major challenge encountered was the formation of air bubbles in the specimens during the injection process, attributed to three main factors:

1- Injection port seal: the seal at the injection port was not airtight, allowing air to enter the mold with the silicone liquid. Initially, blue tack was used but failed to provide an airtight seal. The injection port was then moved from the side to

the front of the mold, creating a small hole that perfectly fit an injecting syringe without a metal needle. A circular groove was laser-cut around the port to secure the syringe, successfully sealing the injection port and preventing air bubbles. Fig.App 1 shows the hole and groove that fit the injection syringe are zoomed in (in the sixth trial) for detailed viewing.

2- Injection method: the Fluid Dispenser was initially used to pneumatically inject the material, but the pressurized air trapped air inside the injection syringe. This issue was resolved by manually pressing the piston with a screwdriver, allowing trapped air to escape through slots in the piston (Fig.App 2b).

3- Mixing and degassing: Degassing the soft material mixture with a centrifugal machine is not sufficient to eliminate micro-air bubbles. The most effective technique involved vacuuming the air out during mixing using a centrifugal mixer (THINKY ARE-310, Japan). This device combines vacuum pressure reduction with a rotation and revolution mixing process, effectively removing air bubbles by reducing surface tension and allowing degassing.

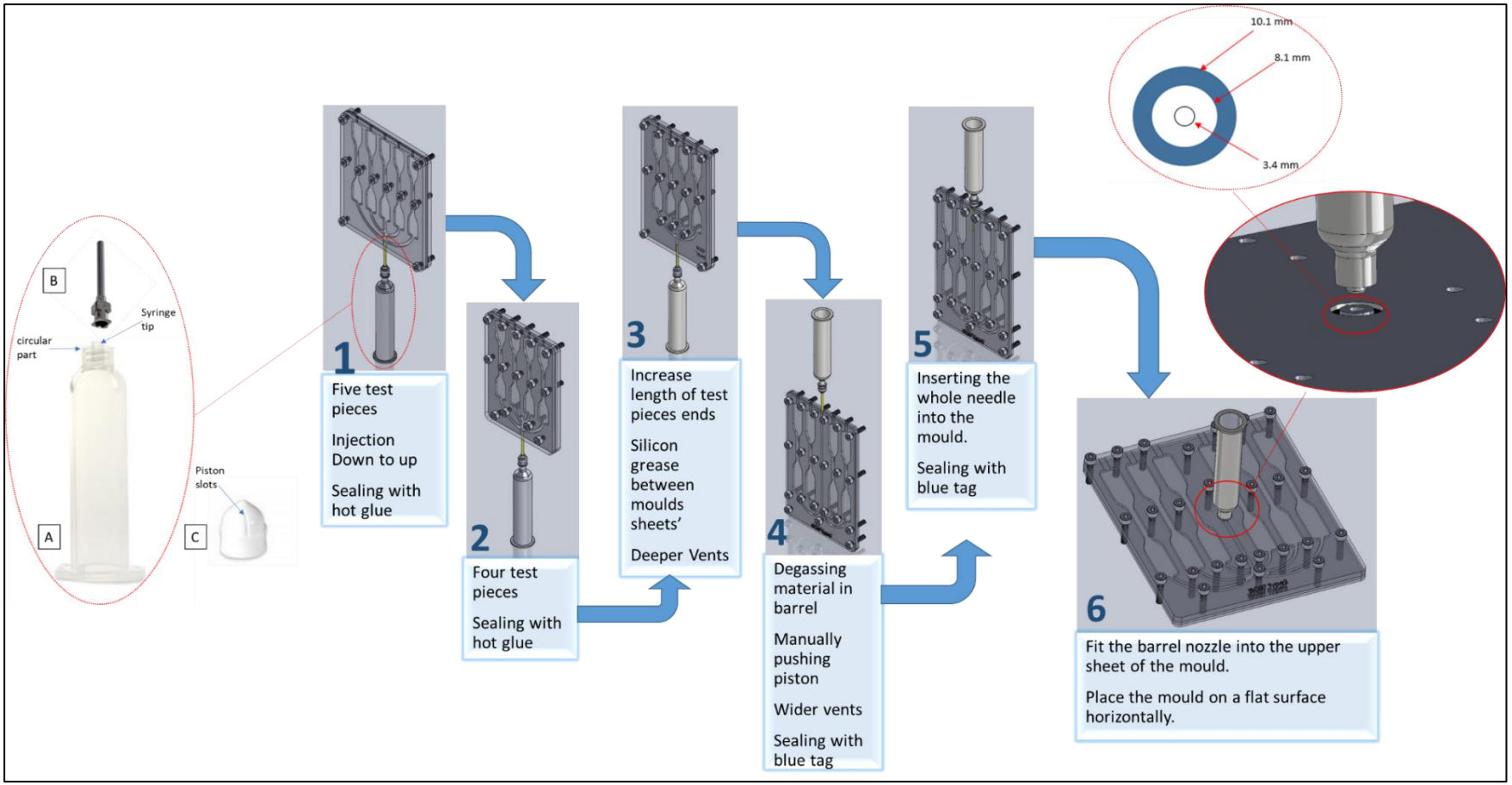

Fig.App 1: history of improvements in tensile mould design from the first trial to the finalized version. The first trial includes a zoom-in on the injection syringe to show its components: (A) injecting syringe, (B) metal luer lock dispensing needle tip, and (C) syringe piston. In the finalized trial (sixth iteration), the hole and groove that fit the injection syringe are also zoomed in for detailed viewing.

Appendix 2.2: Evolution of the Compression Specimen Mould

The ideal fabrication processes and mould designs were achieved after several trials, each incorporating minor adjustments. Fig.App 2 shows some of the important developments in mould designs and fabrication processes.

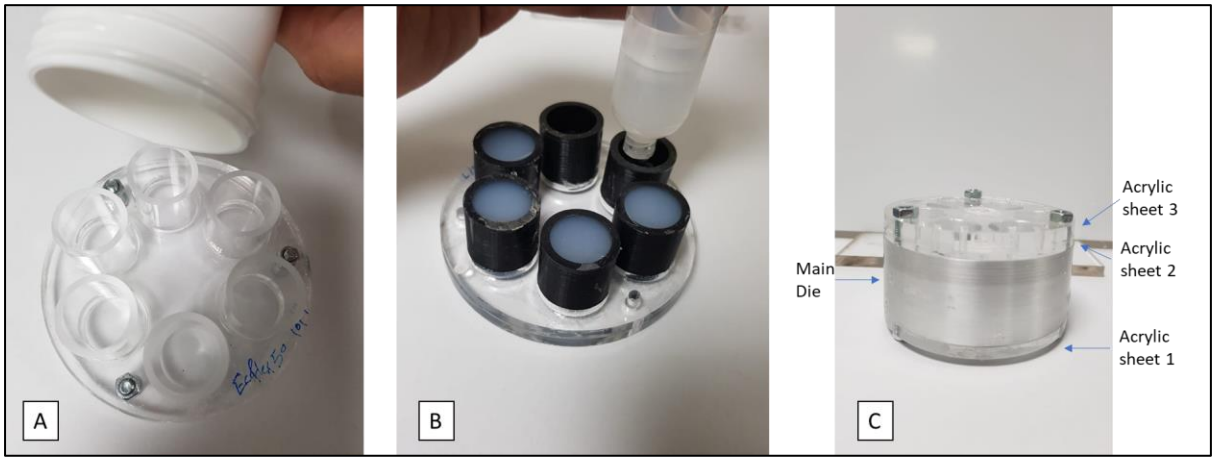

Fig.App 2: History of improvement for the compression specimens Moulds'. A) first trail, B) second trail, and C) third trail (optimum).

First Trial*:* The initial trial used a mould design from a previous researcher, consisting of two acrylic sheets joined by screws (Fig.App 2a). The top sheet had six holes for acrylic tubes, with inner diameters matching the desired specimen's diameter. These tubes, cut to a height of 25 ± 0.5 mm, were filled with pre-silicone poured directly from the mixing jar. This trial faced three main issues: the lack of commercial acrylic tubes with the precise inner diameter of 17.8 ± 0.25 mm, air bubbles in the silicone, and uneven upper surfaces due to manual levelling.

Second Trial*:* For more precise dimensions, the cylindrical parts were 3D printed (Fig.App 2b). The dual acrylic sheet setup was retained, but silicone grease was used instead of screws to enhance sealing and prevent leaks. This trial encountered three problems: imperfect surface finish inside the 3D-printed cylinders, air bubble formation in the silicone, and uneven top surfaces due to the mould not being sealed at the top.

Appendix 2.3: Ejection of Compression Specimen

Here is the detailed method for the ejection of the compression specimens from the aluminium die through a sequence of steps. The challenge of demoulding is notable even after the application of a release agent. Numerous trials to find an efficient method for ejecting the specimens revealed that conventional approaches were insufficient, often requiring excessive time and force that risked effecting the specimens.

The most effective technique identified involves the use of a metal-working vice, a C-clamp vice, and an auxiliary empty aluminium die mould. This method, illustrated in Fig.App 3, is meticulously described through a sequence of steps designed to ensure the gentle and safe ejection of the specimen from the mould:

Step 1: The original die mould is securely clamped in a metal-working vice. This setup stabilizes the mould for the demoulding process. An empty die is then attached to the back of the original die using a C-clamp vice. The jaws of the C-clamp must be carefully positioned to hold the empty die from the back, allowing for the specimen to be transferred from the original die to one of the holes within the empty die. The swivel bottom of the C-clamp vice is precisely positioned over the specimen within the original die. This alignment is crucial for the subsequent ejection process.

Step 2: Turning the handle of the C-clamp vice clockwise initiates the ejection of the specimen, gradually transferring it into the empty die. This controlled movement ensures the specimen is pushed out without damage.

Step 3: Once the specimen is halfway ejected, the handle is turned counterclockwise to release the C-clamp vice, and the empty die is removed. At this point, the specimen can be manually extracted with ease.

These steps are repeated for each specimen. This method showcases the thoughtful engineering and problem-solving efforts undertaken to overcome the challenges of demoulding, particularly for specimens made from elastomers with high Shore hardness.

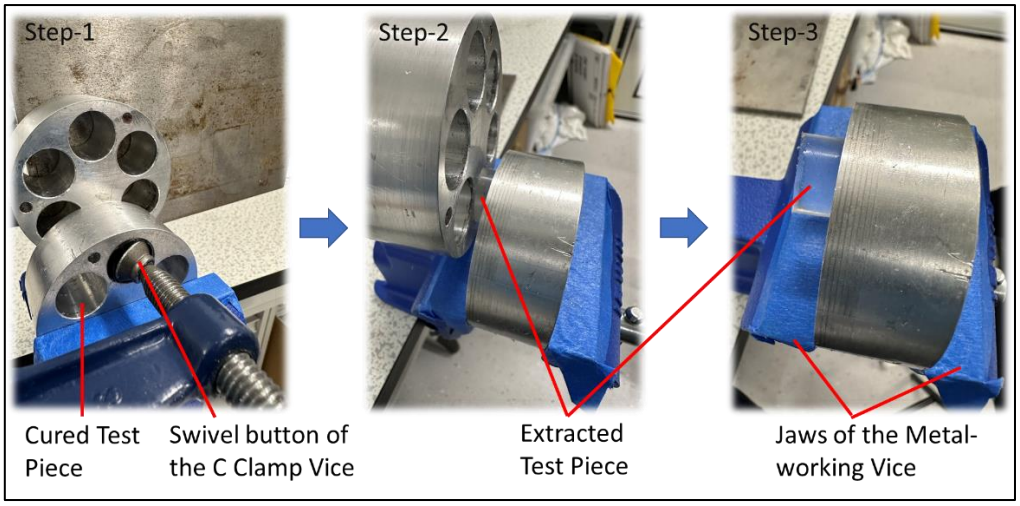

Fig.App 3: sequence of steps designed to ensure the safe ejection of the specimen from the aluminium die.

Appendix 2.4: Tensile Testing Protocol

The following processes are provided to ensure the tensile testing is conducted effectively:

1. Preparation and Setup: Begin by inspecting the connections of all electronic devices and the pneumatic tubes associated with the Instron 5943. Ensuring these connections are secure and functional is crucial before powering on the testing machine. This preliminary step helps prevent any disruptions or inaccuracies during the testing process.
2. Collect Specimens: Select five specimens from the batch of the material intended for testing. It is vital to test multiple specimens to account for variability and ensure the results are statistically reliable.
3. Mark Starting Lines: To guarantee that each specimen is aligned correctly in the testing machine, place each one into a mould to mark the starting line for both ends. This process, as illustrated in Figure 7b, facilitates accurate placement of the specimen within the grippers, ensuring that the tensile force is applied uniformly.
4. Apply Marker Stickers: Affix two circular marker stickers, each with a diameter of approximately 2 mm, on every specimen. These stickers, cut using a laser cutting machine for precision, serve to delineate the change in the gauge length during testing. The placement of these markers is more about their exact distance apart and about their position within the gauge region and along the vertical symmetric line of the specimen.

The choice of circular marker stickers colour is tailored to each material type to ensure that the video extensometer accurately detects the markers during testing. For instance, with Elastosil samples, irregular black marks are used instead of regular white circles, as the video extensometer struggles to detect the regular white circles.

5. Label Specimens: Mark each specimen with a sample number at one end. This identification is crucial for tracking and correlating each specimen with its test results, facilitating clear differentiation in the test report.
6. Select Suitable Load Cell and Lens: It's crucial to select a load cell that matches the anticipated force range and a lens for the video extensometer that can accurately track markers across the wide strain range of the elastomer. For these tests, a 1 kN load cell was utilized. Using the video extensometer is essential to accommodate the high strain properties of elastomers, which differ significantly from those of more rigid materials.
7. Calibrate with Calibration Plates: Perform calibration of the video extensometer using two different calibration plates. This step ensures the accuracy of strain measurements by aligning the extensometer's detection capabilities with the actual dimensions and movements of the specimens.
8. Test Setup in Bluehill Universal: Utilize the Bluehill Universal software to create a new testing method, adjusting parameters across several the software’s windows such as General, Sample, Specimen, Measurements, Calculations, Test Control, Console, Workspace, and Export. This setup allows for precise control over the test conditions, data capture, and result analysis, adapting the process to specific material characteristics and testing objectives.
9. Adjust Grip Pressure: The pneumatic grip on the Instron machine, a critical component for tensile testing, securely fastens specimens in place using air pressure. To avoid slippage without inflicting damage, it is essential to identify and set the appropriate grip pressure. Begin at a lower pressure, incrementally adjusting upwards to discover the ideal level that ensures consistent hold throughout the test. The optimal pressure range to securely maintain the specimen has been determined to be between 20 kPa and 45 kPa. It has been observed that the required pressure increases in correlation with the Shore hardness of the material, indicating a direct relationship between material hardness and the necessary grip pressure for secure testing.

10. Specimen Mounting: Place the specimen into the machine's grips, ensuring it is correctly aligned and securely held in accordance with the marks that introduced in step 3 (Mark starting line).
11. Pre-strain Adjustment: Before testing, manually pre-strain the specimen using the control board of the Instron machine to establish a consistent starting condition for each test. Initiate pre-straining at a level where the force displayed on the Instron interface screen is negative. Carefully move the Instron machine's crosshead upwards until the load cell registers a force, indicating that the specimen has begun to experience tension. Once the machine starts detecting force, halt the pre-straining and adjust the machine settings to balance both force and displacement readings to zero. This process ensures that each test commences from a uniform condition.
12. Commence Test: Begin the test, keeping a hand near the Emergency Stop button as a precaution to quickly halt the machine if necessary to protect the test setup and specimen. The specimen is stretched until failure occurs. Subsequently, the Instron machine's crosshead is programmed to automatically revert to its initial position. The detection of specimen failure, typically indicated by a sharp decrease in force, is facilitated through the adjustment of test parameters of end conditions within the Instron's software interface (Bluehill Universal).
13. Data Collection and Analysis: At the conclusion of the test, export the data to a CSV file for detailed analysis. Review the results, including Force at Break, Maximum Force, Elongation at Break, Modulus, and more, to assess the material's performance under tensile stress.
14. Test Completion: After exporting the results, conclude the test and prepare the machine for the next sample, repeating the process to gather comprehensive data across multiple specimens.

Appendix 2.3: Compression Testing Protocol

The following presents compression tests protocol:

1- Method Configuration in Bluehill Universal Software: A new method is created within the Bluehill Universal Software, selecting the Compression Method from the available applications. While most settings remain at their default parameters, several key adjustments are necessary for our specific testing needs such as Specimen Information, Measurements Selection, and Test Control Parameters. Within 'Test Control,' adjust various parameters across sections such as Start Test, Strain, Pre-Test, Test, and End of Test. Notably,

in the 'Test' section, choose cyclic test mode with a speed of 10 mm/min for 4 cycles. In the Sensitivity field, input 6.25 mm, reflecting the calculation based on the specimen's height of 25 mm and the target of achieving a standard strain of 25%. This is derived from the equation for strain, where represents the change in length and the original length of the specimen.

2- Specimen Collection: Gather five specimens of the elastomer under examination. Mark each specimen with a sample number at one end for clarity in the test report.
3- Fixture Assembly: Prepare the testing apparatus by assembling the two metal plates with the required fixtures.
4- Specimen Placement: According to ISO 7743:2017(E), position the specimen centrally on the lower metal plate without the need for lubricant.
5- Force Balancing: Manually adjust the control board of the Instron machine, moving the Instron machine's crosshead downwards until the load cell registers a force change. Balance force and displacement to initiate the test from a neutral point.
6- Commence Test: Activate the test through the Instron's software interface (Bluehill Universal) by selecting the start option. The test is pre-set to conduct four compression cycles before automatically reverting to its initial position.
7- Data Collection and Test Completion: Upon completing the test, export the results to a CSV file and prepare for the subsequent sample.

Appendix 3: Fabrication of SAM

Appendix 3.1: Fabrication Method Using Commercial Silicon Tubes

The development of the methods described here has mainly focused on the techniques that used moulding processes. Other fabrication methods, such as using commercial silicon tubes, were explored but not extensively detailed due to their limitations in advancing the development process. For example, attempts to make soft filaments from commercial silicon tubes faced challenges related to the high Shore-hardness of the tubes. It was found that stretching those commercial silicon tubes was necessary to reduce stiffness and improve extensibility (as shown in Fig.App 4). The stretching process was carefully measured and monitored using an Instron machine under specific elongation and strain rates, ensuring precision and consistency in the manufacturing process. The soft filaments produced through this technique demonstrated optimal performance, achieving significant expansion upon inflation and reverting to their original size upon deflation. However, as the conceptual designs for Model-2 and Model-3 were proposed, using the same material from commercial silicon tubes (as used in Model-1) became a crucial requirement. Therefore, the fabrication technique involving commercial silicon tubes was not further developed. The main obstacle was the unavailability of resins with the same soft material composition needed for manufacturing in the laboratory setting. Moreover, even if the resin was acquired, the challenging task of manufacturing Model-2 and Model-3 under the same conditions as the factory manufacturing Model-1 presented significant challenges, contributing to the decision to focus on moulding techniques for the refinement of soft filaments in the subsequent stages of development.

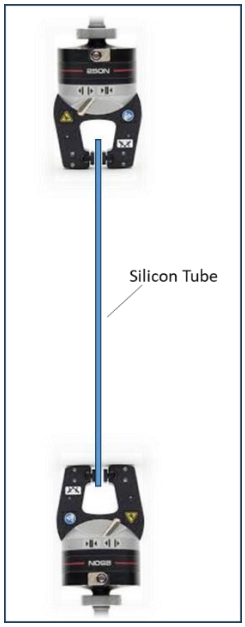

Fig.App 4: Cyclic stretching for pieces of the silicon rubber tube to produce soft filaments under consistent conditions.

Appendix 3.2: Fabrication of Multiple Soft Filament by Moulding in Steel Tubes

In this technique, the same approach and conceptual design as fabrication a single soft filament by moulding in steel tubes were employed but with the objective of producing ten soft filaments simultaneously instead of a single unit. Additionally, efforts were made to address the issue of the internal cavity in the previous trial by replacing S-Steel tube-2 with a nylon line (fishing line) having a diameter of 0.6 mm.

A complex closed mould, consisting of stainless-steel tubes of gauge-8, Nylon lines, acrylic sheets, and steel shafts, was utilized. The stainless-steel tubes were arranged vertically and secured between two groups of laser-cut acrylic sheets. The top group of acrylic plates, having a diameter of 100 mm, employed a conceptual design similar to the mould used for single soft filament fabrication.

This design comprised three acrylic plates bonded together with bolts and nuts, featuring a centrally located injection port in the upper plate. Narrow, curvy runners on the middle acrylic sheet facilitated the flow of the silicon liquid into the S-Steel tubes. Nylon lines were strategically inserted through small holes in the acrylic plates, passing precisely through the centre of the S-Steel tubes. Nylon lines were carefully threaded through aligned holes in the top and bottom acrylic plates, ensuring they ran exactly through the centre of the stainless-steel tubes, providing an accurate alignment for the formation of the internal cavity. Fig.App 5 shows the assembled mould that designed to produce a ten soft filament.

The injection of the pre-silicon, a mixture of Ecoflex 00-50 and a thinning additive, was followed by the curing process at room temperature (Fig.App 6A). Despite achieving mass production with a smooth outer surface (Fig.App 6B), several areas for improvement have been identified.

The complexity of the mould design, incorporating steel tubes, Nylon lines, acrylic sheets, and steel shafts, raises concerns about efficiency and ease of fabrication. Simplifying the mould design could streamline the process and potentially improve overall efficiency. The current complexity of the method may present challenges in scaling up the fabrication process, especially when fabricating more complex soft filaments. Additionally, while the technique successfully yielded good quality soft filaments without observable defects, an issue arose during the inflation phase. When the produced soft filament is inflated, it exhibited a spiral movement (as shown Fig.App 6C). This suggests that the internal cavity may require higher precision to avoid undesired ballooning during expansion.

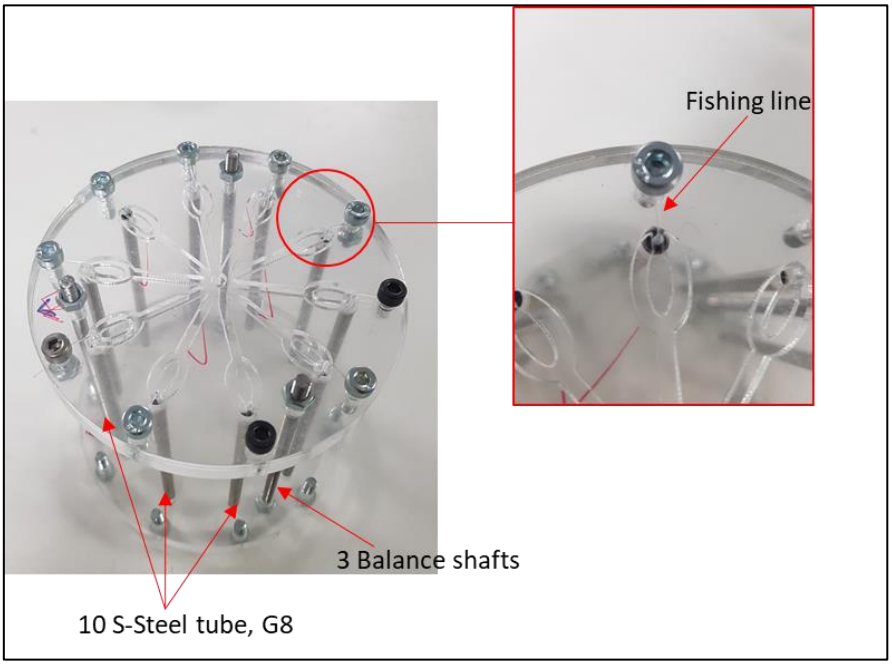

Fig.App 5: The assembled mould that designed to produce ten soft filaments.

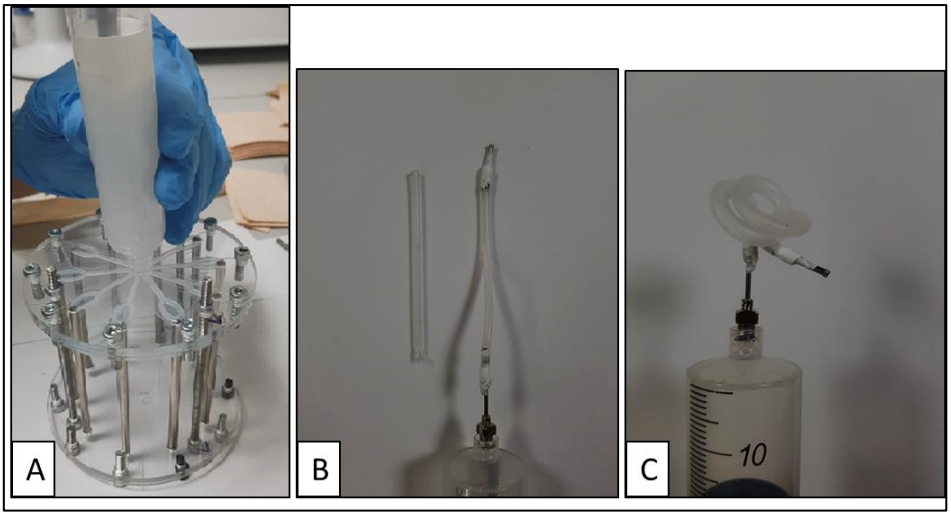

Fig.App 6: A) the injection of the pre-silicon, B) sample of the produced soft filament, C) the produced soft filament exhibited a spiral movement.

Appendix 3.3: Soft Material Waste During Fabrication

These are the processes where the material is being wasted:

1. Discharging Pre-Silicon: Wasting material while transferring pre-silicon from the jar into the injection syringe.
2. Filling the Mould: Pre-silicon needs to overfill the mould to ensure complete filling and release trapped air bubbles, leading to material waste.
3. Post-Filling Waste: Waste occurs after the mould is filled.
4. Injection Syringe Handling: It is recommended not to empty the entire syringe to ease the cleaning process.
5. Cleaning Process: Clean the injection syringe and jars after the pre-silicon fully cures. In its cured state, the material is easier to remove without leaving remnants.

Appendix 3.4: Securing the Braid to the Soft Component

In the context of securing the braided sleeve to the soft component and ensuring the Polyethylene tube's secure placement, some researchers have explored alternative methods such as the consideration of dipping or coating the entire McKibben artificial muscle, a type of SAM, with an elastomer. The purpose of this coating is to uniformly bond the braided sleeve with the soft component and facilitate for faster deflation. This approach, however, introduces a significant limitation to the functionality of the SAM.

The soft material coating, while enhancing the uniformity of the bond and security, restricts the free movement of the braided sleeve. The geometry of the braided sleeve's mesh is designed to function like a scissor linkage, where changes in the angle of the linkage result in linear contraction of the SAM, translating to its actuation. The flexibility and the ability of the braided sleeve to change its geometry are crucial for the effective performance of the SAM, as higher changes in the linkage angle led to greater linear contraction. Therefore, while the elastomer coating provides certain structural benefits, it compromises the essential dynamic characteristics of the SAM, highlighting the importance of balancing security and functionality in the fabrication process. This consideration is vital for ensuring that the SAM can perform its intended movements and operations without being obstructed by the materials used in its construction.

Appendix 4: Block Force Test

Appendix 4.1: Experimental Setup Components

The development history of the block force experiments is presented in Section 5.1. Below are details about the components utilized in each version:

First Version:

On the electrical side, the setup included a circuit comprising the load cell, amplifier, myDAQ device, and a computer equipped with LabVIEW. When SAM is pressurized with air, the load cell generated electronic signals proportional to the applied load.

These signals can be very weak, making them subjected to noise and interference. An amplifier enhances the load cell's signal, making it more robust and easier to process. The amplifier then sends the amplified signal to myDAQ system in order to be collected and analysed through the computer equipped with LabVIEW. myDAQ system is a data acquisition system that connected to the computer via a USB cable. Moreover, LabVIEW is a software was utilized to develop a graphical program responsible for data acquisition and system control.

Second Version:

The Air Reservoir stores and regulates high-pressure air, ensuring a stable supply to the Electro-pneumatic Regulator. The Electro-pneumatic Regulator is important in maintaining the desired air pressure level within the Pressure Box. It regulates air pressure based on electrical input signals from My DAQ-1, ensuring the pneumatic circuit operates at the specified pressure.

The solenoid valve controls air flow from the regulator by opening and closing the air passage in response to electrical input. This control allows for adjusting actuation frequency, output mode, and cycle duty. In tests, output modes are set as static or Pulse Width Modulation (PWM), with PWM mode modulating the pulse width to vary pressure waveforms and enable cyclic actuation.

The myDAQ device is connected the computer that equipped with LabVIEW. This program specified various parameters such as defining input channels, sampling rates, and voltage settings. To obtain meaningful pressure values in kilopascals (kPa), post-data processing was performed using software tools like Excel and MATLAB.

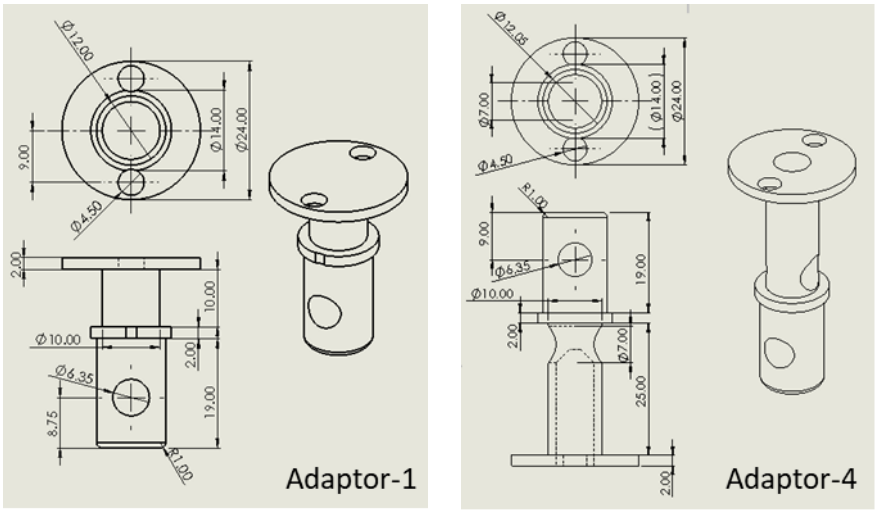

Fig.App 7: Detailed Mechanical Drawing of Adaptor-1 and Adaptor-4.

A bridge circuit within the load cell measures very small changes in resistance. When the load cell deforms under the applied force, it causes an imbalance in the bridge circuit resulting a small signal that is proportional to the applied force. This signal is in the form of a voltage change. The small voltage signal is then amplified within the electronic circuits within the load cell of the Instron. This makes the signal more suitable for the direct measurement.

The upper connector is composed of Adaptor-1 and Adaptor-2, where Adaptor-1 is designed with a cylindrical end that fits into the upper Instron holder and has a hole to insert the key holder, while Adaptor-2, which is also part of SAM, has two ends. The upper side of Adaptor-2 is joined with screws while the lower side is linked to SAM's inlet. Although it's possible to design these two adapters as a single part, they are created as two separate pieces to simplify the process of attaching and detaching SAM from the test setup.

Furthermore, the lower pneumatic connector is composed of Adaptor-3 and Adaptor-4 that joined with screws. Adaptor-4 is hollowed out to accommodate the insertion of a silicone tube. A detailed mechanical drawing of Adaptor-1 and Adaptor-4 is shown in Fig.App 7. Short silicone tubes, each with a length of 10 mm, are used to establish connections between SAM's upper end and the upper pneumatic adapter of SAM, as well as between SAM's upper and lower ends to the Adaptor-2 and Adaptor-3. This approach simplifies the connections between different components of SAM for efficient testing operation.

The Cylindrical Piston is placed over an acrylic box that manufactured by laser cutting machine. This acrylic box is created to mount the Cylindrical Piston in the designed position and to protect the laser sensor. By looking again at Fig.App 10, it can be seen that all the components of the setup are connected in a linear vertical line. The top surface of the Acrylic Box (Fig.App 10) is designed with a 12 mm circular hole, allowing for the detection of target movement. Surrounding the 12 mm hole are four small holes with a 5 mm diameter for 4M screws, used to secure the Cylindrical Piston onto the top of the acrylic box.

During the test, the two grips remain fixed to allow performing the block force test. SAM actuate by applying a controlled input pressure, leading to generate force that load cell records it. A bridge circuit within the load cell measures very small changes in resistance. When the load cell deforms under the applied force, it causes an imbalance in the bridge circuit resulting a small signal that is proportional to the applied force. This signal is in the form of a voltage change. The small voltage signal is then amplified within the electronic circuits within the load cell of the Instron. This makes the signal more suitable for the direct measurement.

Pressure Box:

The Pressure Box receives high-pressure air via an input inlet using a thick Polyethylene tube (OD = 6 mm and ID = 4 mm) and delivers the output pressure using a thin Polyethylene tube (OD = 4 mm and ID = 2 mm). The control unit facilitates the adjustment of the desired frequency through the control panel and screen on the front side of the Pressure Box (Figure 5-27).

The Pressure Box has four pressure outlet pins, with only the first pin utilized for actuation in this test. The Polyethylene tube in the first pin connects to a pneumatic T-connector, feeding the SAM in the setup, while the other branch connects to the pressure sensor for recording internal pressure.

This setup ensures an organized and controlled test environment, offering precise control for achieving the desired metric measurement. It provides accurate evaluation for the force generated by SAM under varying conditions. Additionally, it ensures efficient testing operations by simplifying the attachment and detachment of SAM from the setup.

Appendix 4.2: Block Force Test Procedure

There are several relevant research works that present methodology for the block force test. However, this test protocol provides some unique aspects of the approach such as the approach of using the 3D printed adaptor to connect SAM's samples to the testing setup.

Materials and Equipment:

- Soft Artificial Muscle (SAM)
- Instron machine.
- Tubes and connectors.
- 3D printed adaptors.
- Computer equipped with LabVIEW software.
- Pressure box.
- Pressure sensor.
- DAQ (Data Acquisition) system.
- Safety equipment: goggles.

The amount of the pre-tension is 0.5 N, which is consistently applied to all the samples. The control of pre-tensioning is achieved through the movement of the Instron's crosshead, which is adjusted both manually using the Fine Jog thumbwheel on the control unit and automatically by setting the desired pre-tension via the Instron interface software, Bluehill. The Fine Jog is a thumbwheel used to gently adjust the crosshead's position. This control allows to establish an exact starting point with zero load.

The pre-tensioning preparation process starts after SAM assembly in the setup. It begins by moving downward the Instron machine's crosshead manually via the Fine Jog until load readings become slightly negative. After that, the crosshead is adjusted upward until readings from the Instron interface software approach zero. A short waiting period is needed to account for possible relaxation in the SAM, which contains soft components that may relax. Then, the crosshead is adjusted again if needed to achieve load balance (zero load). At this balance point, force and displacement parameters are set at balance (zero).

Once the load reaches the designated 0.5 N, the pre-tension process will stop, indicating that the SAM is at the desired initial test condition, which makes it ready for applying the pressure. To begin the process of sending the desired input

pressure from My DAQ-1, as well as recording the internal pressure, the "start" button within the LabVIEW testing program is clicked. Then, press the "running" green button located on the control panel of the pressure box to begin the pressure supplying from Pin-1. These sequential steps of starting the test process ensure that the test procedure proceeds consistently for all the samples and facilitate accurate data collection.

Next Sample Preparation: For the next sample preparation in the block force test, SAM is safely disassembled from the test setup within the Instron machine by unscrewing the connected adaptors. Furthermore, in preparation for the next test, the previous sample is deleted from the Instron testing interface program to start new sample with new balancing and pre-tensioning setup. These steps ensure the systematic return to the origin of the previous test to initiate a new one with similar condition.

Appendix 5: Displacement Test

Appendix 5.1: Experimental Setup Components

The setup of the test comprises five overall 3D printed adaptors noted in Fig.App 8 and Fig.App 9 with Adaptor-1, Adaptor-2, Adaptor-3, Adaptor-4, and Adaptor-5. As the figure shown, SAM is connected from the top with Adapter-2 that enables the pressure feeding connection. Adaptor-1 and Adaptor-2 are connected together with screws. Fig.App 8 shows the design of Adaptor-1 that is hollowed from the bottom to allow extending the feeding tube through and inserting Adaptor-2 in. The top side of Adaptor-1 is designed to fit into the Instron upper holder's hole. Adaptor-2 has dual ends, with the first connected to the silicone tube and inserted inside Adaptor-1, while the second end links to SAM's inlet/s. The outlets of Adaptor-2 vary based on the model being tested. For Model-1 and Model-2, three outlets are designed, while a bigger single outlet is configured for Model-3. Although Adaptor-1 and Adaptor-2 could be a single part, they are intentionally kept separate for ease of assembly and SAM removal. Short silicone tubes (10 mm) connect SAM's upper end with Adaptor-2, and the SAM's lower end is linked to Adaptor-3 using similar silicon tubes.

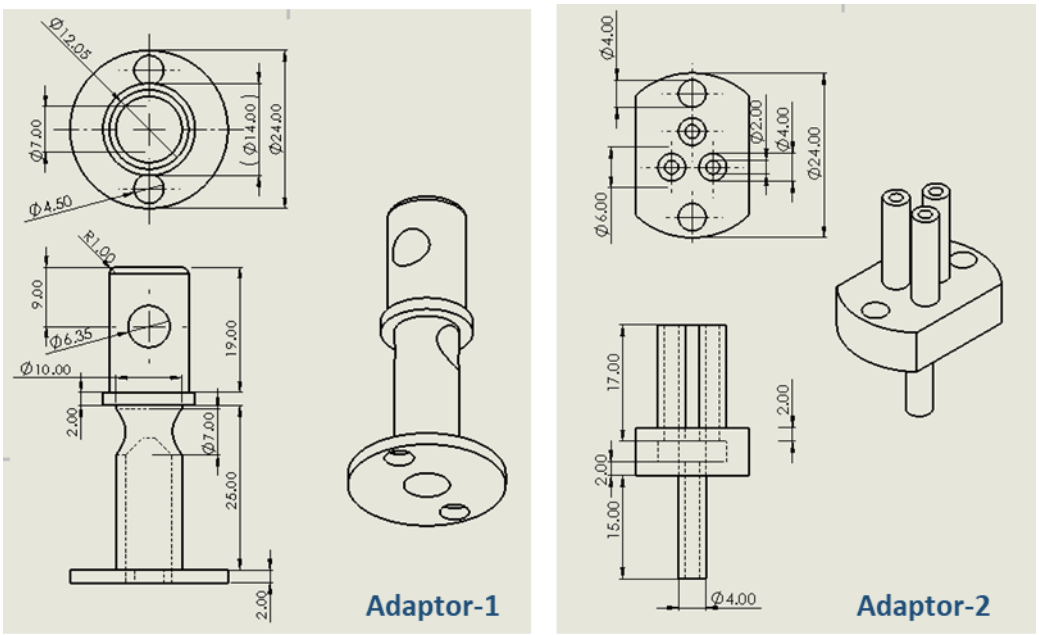

Fig.App 8: Detailed Mechanical Drawing of Adaptor-1 and Adaptor-2.

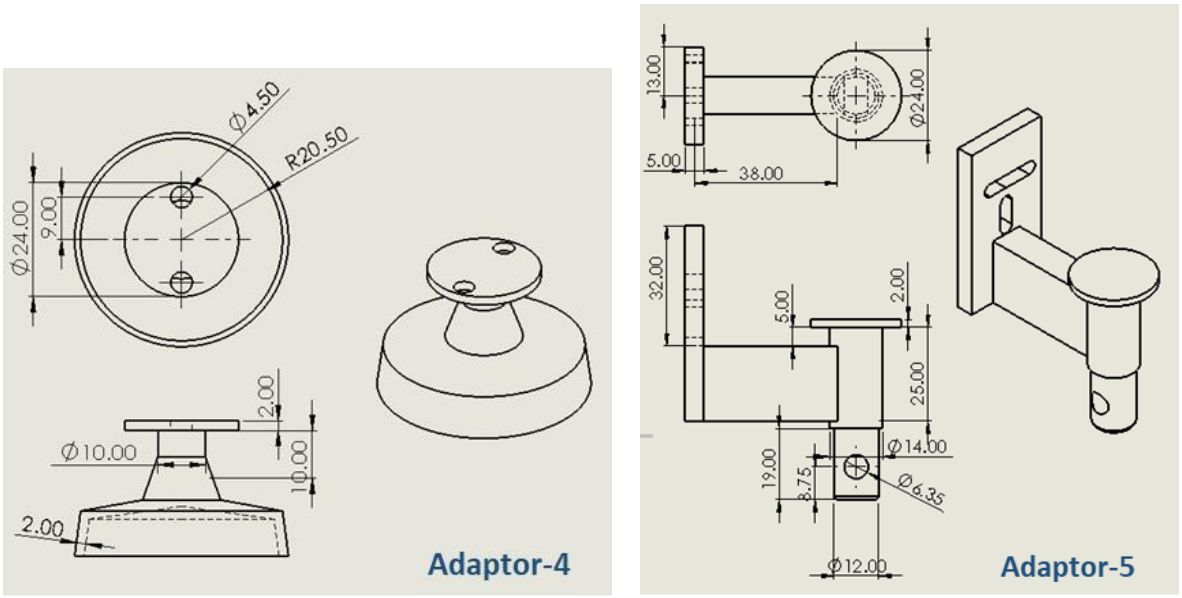

Fig.App 9: Detailed Mechanical Drawing of Adaptor-4 and Adaptor-5.

The Cylindrical Piston is positioned on an acrylic box that was produced using a laser machine. The acrylic box is designed to securely hold the Cylindrical Piston in its intended position and to safeguard the laser sensor. As shown in Fig.App 10, all the components of the setup are aligned in a straight vertical line. The top surface of the Acrylic Box (Fig.App 10a) features a 12 mm circular hole, enabling the detection of target movement. Surrounding the 12 mm hole are four small holes with a 5 mm diameter for 4M screws, used to secure the Cylindrical Piston onto the top of the acrylic box. To accommodate the connection of Laser Sensor wires, rectangular cuts are made on the sides of the acrylic box.

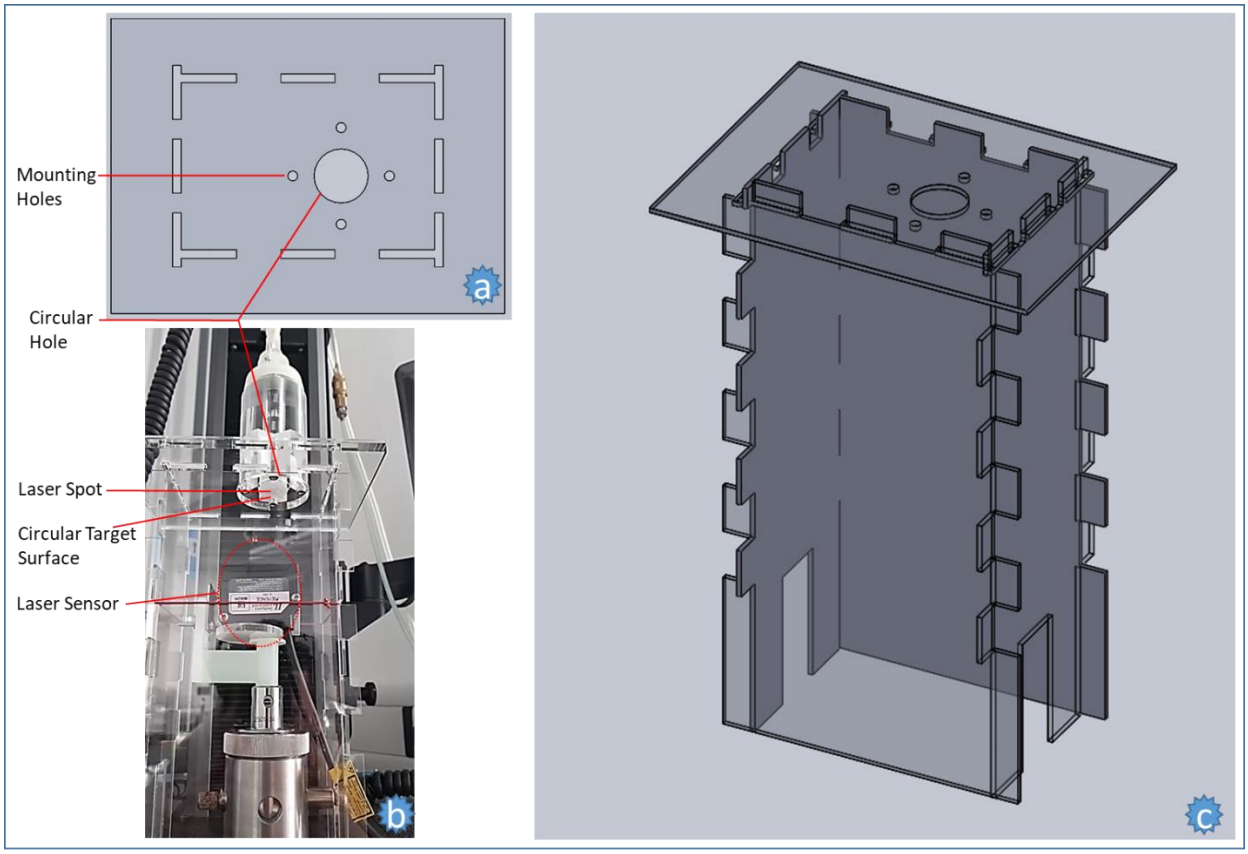

Fig.App 10: Illustrates the measurement mechanism of the displacement test setup. It features a Cylindrical Piston embedded with a frictionless shaft that moves linearly along the acrylic cylinder body. In part (a), the top acrylic plate is positioned over the acrylic structure to mount the Cylindrical Piston. Part (b) provides a real photo of the Cylindrical Piston, showing the circular target surface with the laser beam spot on it. Part (c) shows the acrylic box structure, serving to carry the components and shield the laser sensor.

Appendix 5.2: Results of Timestamps of Key Events

Tab.App 1 displays the timestamps of key events and the corresponding time intervals within the displacement cycle. The provided data serves as an illustration, showcasing the analysis outcomes for the first sample of Model-1 subjected to an input pressure of 60 kPa and an actuation frequency of 0.2 Hz. The table includes two main categories of time-related analysis results. Firstly, the "time of events" category captures five important events in the displacement cycle, namely the trigger of internal pressure, the actuation trigger, the peak displacement point typically occurring at the end of the actuation phase, the end of the de-actuation effect, and the end of the idle phase which is the start of a new cycle. Second, “the time interval category. As detailed in a prior section that illustrating the displacement cycle components, the corresponding time intervals are identified as:

$$Pre - conditioning = Actuation\ Trigger - Pressure\ Trigger$$

$$Actuation\ = Peak - Actuation\ Trigger$$

$$De - actuation\ = End\ of\ De - actuation - Peak$$

$$Idle\ = End\ of\ De - actuation$$

Tab.App 1: displays the timestamps of key events and the corresponding time intervals within the displacement cycle for Sample-1 of Model-1 at input pressure of 60 kPa and actuation frequency of 0.2 Hz.

Cycle	Time of Events					Time Interval					
	Pressure Trigger	Actuation Trigger	Peak	End of De-actuation	End of Idle	Delay	Pre-conditioning	Actuation	De-actuation	Idle	Total_time
Cycle-1	9.934	10.033	12.422	13.221	14.967	0	0.099	2.389	0.799	1.746	5.033
Cycle-2	14.967	15.066	17.465	18.163	19.958	0	0.099	2.399	0.698	1.795	4.991
Cycle-3	19.958	20.057	22.398	23.149	24.956	0	0.099	2.341	0.751	1.807	4.998
Cycle-4	24.956	25.056	27.443	28.102	29.947	0.049	0.1	2.387	0.659	1.845	4.991
Cycle-5	29.947	30.047	32.493	33.104	34.941	0.05	0.1	2.446	0.611	1.837	4.994
Cycle-6	34.941	35.04	37.43	38.074	39.961	0.196	0.099	2.39	0.644	1.887	5.02

Appendix 6: Case Study

The development history of the case study's dynamic system is detailed in Chapter 6. Below are the system configurations for each version:

Appendix 6.1: First Configuration – Universal Engineer Dial Indicator (UEDI)

One of the initial trials conducted to establish a dynamic structure for operating SAM in accordance with the designed configuration involved the use of a Universal Engineer Dial Indicator (UEDI). The UEDI is a precision measurement tool designed for various applications in metrology and quality control. The employed UEDI is equipped with a locking knob located at the joint between the two arms. Turning the locking knob clockwise tightens the locking mechanism and securing the position of the dial and preventing any further movement. In this case study, the knob was unlocked to permit the implementation of a movement resembling that of the bicep.

SAM is attached to the UEDI structure with tape, ensuring that the tape only makes contact with the non-inflatable parts of SAM. Despite this configuration achieving the desired motion, there were some limitations addressed within its dynamic system. The first limitation was the unreliable attachment of SAM to the UEDI arms. Attaching SAM with non-precise fixtures can result in instability and unintended movements, potentially compromising the accuracy of the UEDI arm. Moreover, aligning SAM in a non-repeatable manner with the UEDI arms caused variations in system performance.

Secondly, during testing the model, stiffness issues arisen due to backlash between the components of the joint. This occurred because the UEDI joint is not designed for dynamic motion but rather to enhance the dexterity of the indicator tip in a fixed position. Thirdly, the upper joint of the upper arm was rotatable during actuation, leading to erratic movements while the dynamic system configuration aimed to perform a simple angular motion in a 1 Degree of Freedom (1 DoF).

Lastly, determining the initial position of the system was a challenging aspect of setting up the UEDI arms system for an experiment. The approach used to overcome this challenge involved using a manual protractor to measure a unified initial angle between the two arms with all the SAM samples (Fig.App 11a). However, this approach was insufficient to provide a precise method for creating a repeatable initial position, as it relied on numerous manual adjustments.

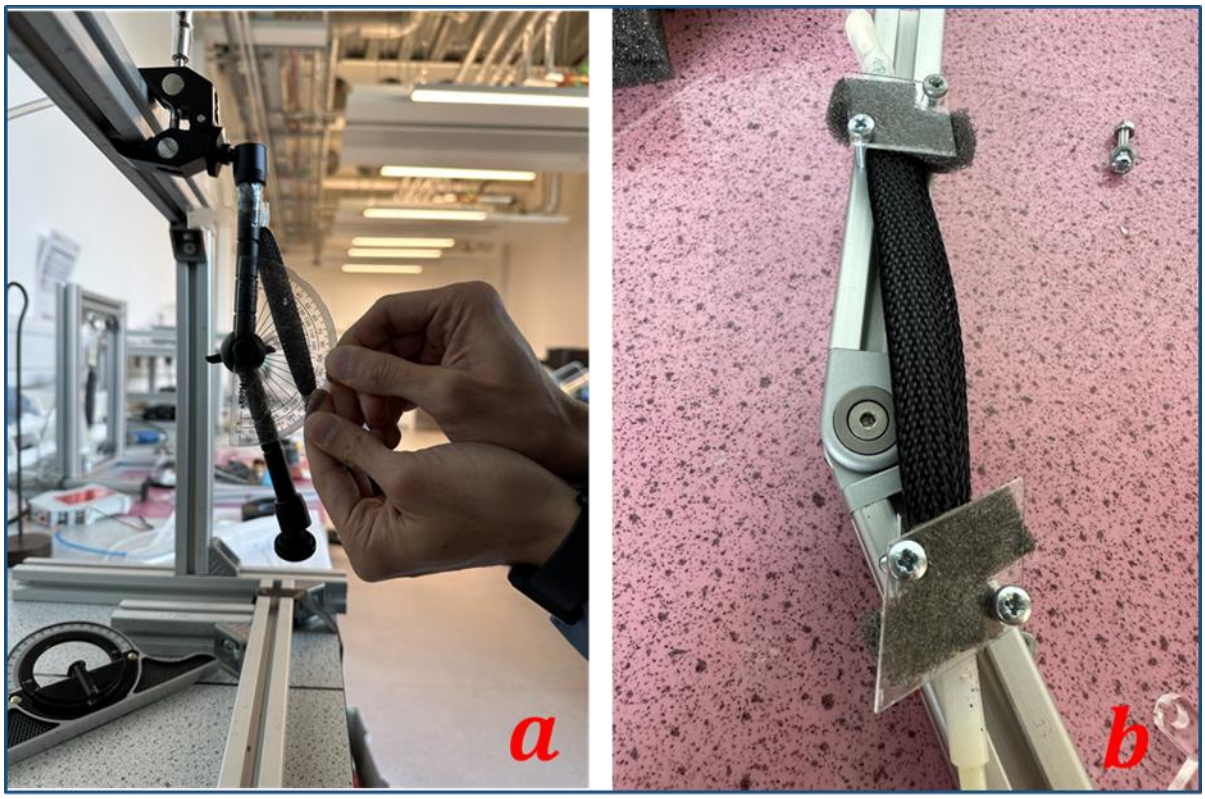

Fig.App 11: Earlier attempts to achieve the desired dynamic configuration. a) shows the initial configuration utilizing UEDI and b) illustrates the second configuration employing an aluminium strut structure.

Appendix 6.2: Second Configuration – Aluminium Strut Structure

The second enhancement to the case study's dynamic system involved utilizing a pivot joint connected with aluminium strut profiles. The pivot joint is commonly employed to enable rotational movement of strut profiles around a central axis.

It has been found that creating a jointed structure resembling an arm in a dynamic system is a suitable solution, enabling angular motion. The maximum angular limit of the utilized pivot joint is 180° which is qualify this range as the desired motion range for the designed dynamic system. The aluminium strut profiles offer a versatile framework for constructing the arm, allowing the design of profiles with suitable lengths and dimensions. Furthermore, they are compatible with fasteners such as bolts and nuts to create a secure structure.

The method of attaching the SAM to the aluminium strut profiles involved designing connectors made of thin acrylic plates. The acrylic connectors were designed using 2D CAD software and then cut with a laser cutting machine. These connectors were designed in a parallelogram shape with the aim of aligning SAM in a repeatable

initial position by positioning it in a specific slot within the connector. As shown in Fig.App 11b, the acrylic connectors are affixed with screws to specific holes that drilled in the upper and lower arms (strut profiles). To ensure a secure attachment, a 1 cm thick sponge, cut to the same shape as the acrylic connectors, was inserted between the SAM and the connectors. This sponge aids in distributing the load evenly over the connectors when tightening the screws due to its deformable nature.

This second configuration offers effective solutions to some of the issues that addressed in the first configuration. This is achieved by employing a more suitable joint for this application, providing a smooth angular motion with no backlash. Additionally, it allows for a simple angular motion in a single Degree of Freedom (DoF) that help to eliminate the erratic movements observed in the previous configuration.

Despite the second configuration overcoming some of the limitations present in the first configuration (UEDI model), it also addressed certain limitations in its dynamic system. For instance, the attachment approach of SAM to the strut profiles was not reliable. After operating this model, we realized that fastening the end part of SAM is not a sufficient method. To ensure that SAM efficiently actuates the dynamic system, its ends need to be connected to the strut profile in a way that allows adaptability of SAM in response to the movement of the dynamic system.

To achieve adaptable movement of SAM within the dynamic system, custom connectors were developed and employed in the optimal system configuration. The following section will demonstrate the optimal setup of the case study system and provide a detailed methodology for assessing the desired metrics of the system.

Appendix 6.3: Finalized Setup Components

Two essential components, Adaptor-1 (on the upper arm) and Adaptor-2 (on the lower arm). Adaptor-1 exhibits three functional sides. Firstly, multiple outlet ports are connected to SAM to supply it with pressurized air. Secondly, a single air inlet port is linked to the pressure supplier. In the centre of Adaptor-1, a small chamber connects the multiple outlet ports to the inlet port, facilitating the air-supply process. Thirdly, an extended part with a hole ensures the proper connection of SAM to the hinges, enabling rotational movement. The tubing used to supply SAM with air pressure involves the utilization of silicone tubes to establish a connection between Adaptor-1’s inlet port and the polyethylene tube extending from the pressure box.

On the other hand, Adaptor-2 has two functional sides. Firstly, multiple solid ports are connected to the lower end of SAM to block the air inside. Secondly, a part

similar to the extended part in Adaptor-1 is designed for the same purpose. Flexible silicone tubes with a length of 10 mm and an internal diameter of 4 mm are employed to connect and secure the SAM ends with the Adaptor-1 and Adaptor-2.

Additionally, Adaptor-3, a 3D-printed component designed to hang additional weight in a vertical manner. The design of Adaptor-3 is detailed in Fig.App 13, showing its two faces with an angle of 120° between them. The first face, featuring a hole in the middle that allows the adaptor to be joined to the tip of the lower arm with screw. The second face is intentionally angled to ensure it faces the vertical direction, facilitating the hanging of weight. This face also includes a hole with a larger size than the weight hanger to allow clearance for the weight hanger to rotate when the lower arm is actuated.

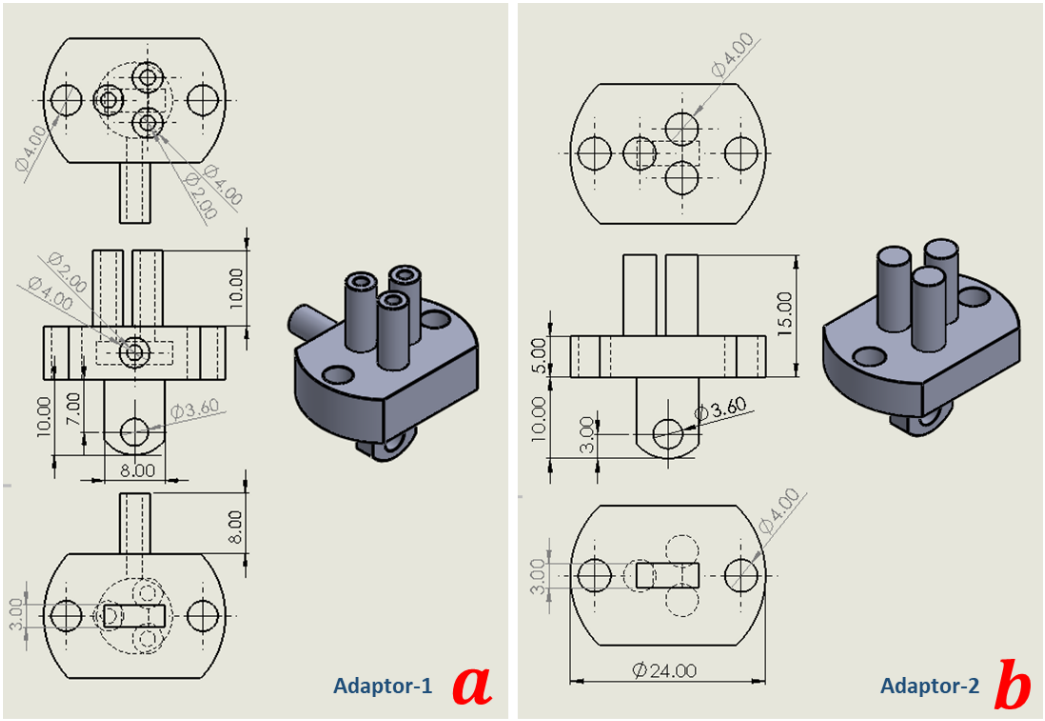

Fig.App 12: a) Detailed drawing of Adaptor-1 located in the upper arm, and b) Detailed drawing of Adaptor-2 located in the lower arm.

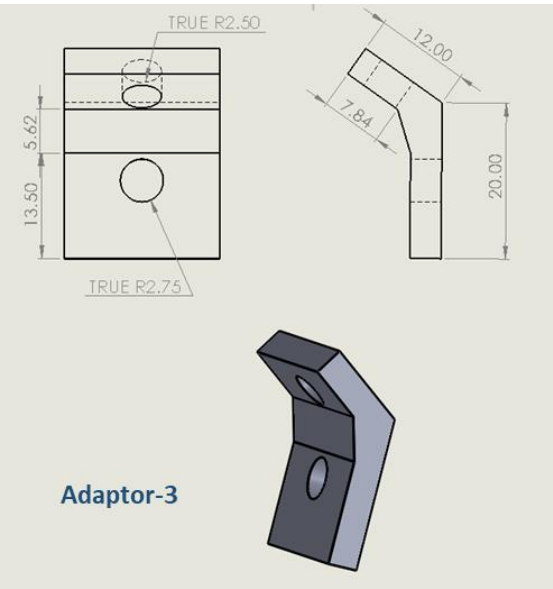

Fig.App 13: The design of Adaptor-3 which is a 3D-printed component designed to hang additional weight in a vertical manner.

Hinge Connector:

The adaptable connection of SAM to the aluminum segments is facilitated through a developed mechanical joint comprising two acrylic pieces, 3D-printed adaptors (Adaptor-1 with the upper arm and Adaptor-2 with lower arm), screws, nuts, and washers. This connection forms a revolute joint that connect both ends of SAM with arms to allow rotational movement around a fixed axis. The acrylic pieces serve as a supportive structure that fixed at specific points over the upper and lower arms, creating a hinge for the shaft. The screw functions as the shaft, establishing an axis that allow rotational movement of the 3D-printed adaptors. Fig.App 14 shows the connection of the revolute joint components.

The securing of components, the shaft and adaptors, in place is achieved by using nuts, while washers act as spacers. Nuts function in stabilizing the entire revolute joint by ensuring that the various components remain securely fastened. Washers function in reducing friction between the nuts and the surface of the other components that contribute to the smooth functioning of the revolute joint.

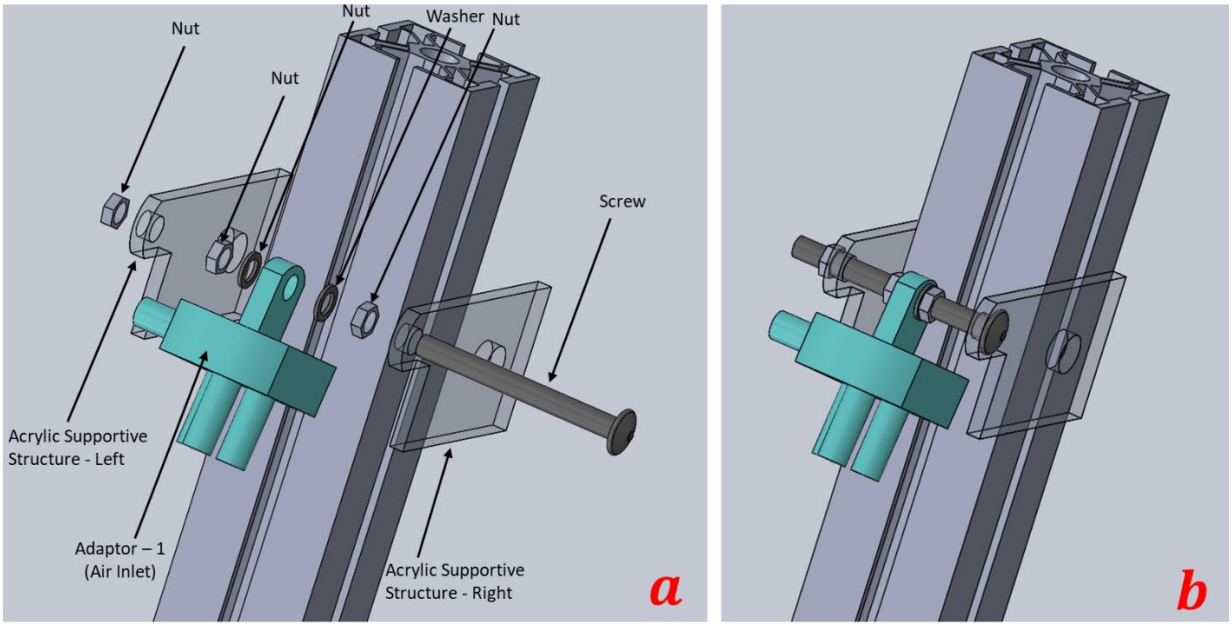

Fig.App 14: Illustrates the connection of the revolute joint components. Subfigure a) displays an exploded view of the components, while subfigure b) presents the combined components.

Assembling Adaptor-1 and Adaptor-2 on the acrylic supportive structure that placed at specific points over the upper and lower arms to establish the revolute joints. Both adaptors are assembled using the same procedures. Firstly, the screw (the shaft) inserted from into the supportive structure half way. Secondly, nut and then washer inserted into the screw half way. Thirdly, the adaptor inserted, then another washer and nut are tighten on the adaptor. Fourthly, the screw is inserted into the other supportive structure. Fifthly, the screw is secured with the supportive structure using a nut. It is important to ensure that the adaptors are placed in the middle between the two acrylic supportive structures. Fig.App 14 shows the connection of the components of the revolute joint.

Appendix 6.4: Weightlifting Test of the Augmented Set of SAMs

This experiment involves testing the three augmented models of SAM. The objective of this experiment is to evaluate the ability of the SAMs Models to lift weights and compare their performance through measuring the amount of contraction and braiding angle. The experiment starts with no weight. After that, the weight is added and increased every two actuation cycles. The experiment follows this increasing weight: 700 g, 1000 g, 1300 g, and 1600 g. After adding each weight, its contraction and braiding angle are measured in both the released and contracted states.

Fig.App 15, showing Model-2 as an example, illustrates the progression through various stages in this experiment. The weight is incrementally increased in sequential figures, ranging from 0 g to 1000 g. The figure presents changes in the two metrics, the range of contraction and the change in braiding angle, for both the Released and Contracted states. Similar figures exist for Model-1 and Model-3.

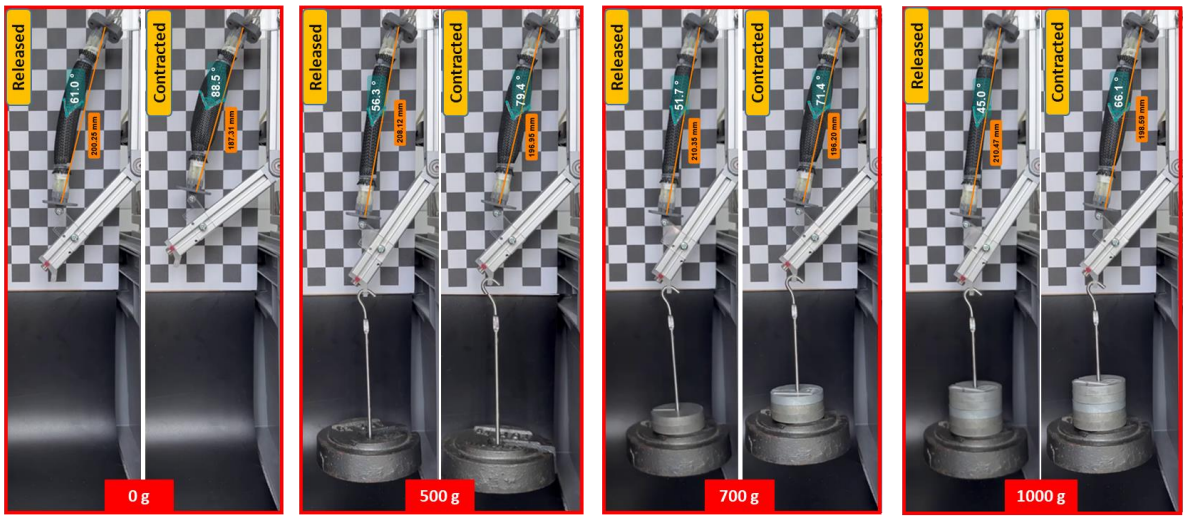

Fig.App 15: Progression of stages in weightlifting test of the augmented models of SAM. The weight is increased at the sequence figures, ranging from 0 g to 1000 g, where each stage comprises two states: Released and Contracted.

The data of the weightlifting experiment is presented in **Error! Reference source not found.**, which shows how different models (Model-1, Model-2, and Model-3) respond to increasing weight by evaluating the change in SAM's length and change in braiding angle through the fully released and fully contracted state.

Notably, when the weight added to the system at the released position, the SAM extends because the weight applies tension the SAM. However, there is a limit to this extension depending on the ultimate extension capacity of the braided sleeve. For instance, in Model-1, at the released position with a 0 g scenario, the SAM length is approximately 197 mm, extending to 206 mm after adding 500 g. Notably, there is no observable change after adding an additional 500 g.

As weight is added in increments (from 0 g to 1600 g), SAM performs smaller contractions and braiding angles. This indicates the weight's influence on the performance of SAM. The decrease in contraction length and braiding angle can be

attributed to the increased load, which resists SAM’s contraction and the braiding angle.

Model Comparison (graphs):

Fig.App 16 presents a comparison of three SAM augmented models through four charts. The charts in the first row show the change in SAM's length at the released and contracted positions, when being loaded with weights increasing from 0 g to 1600 g. The charts in the second row show the corresponding changes in the braiding angle at the released and contracted positions, respectively, under the same load.

The comparison between the models becomes clear when we look at the four key charts in Fig.App 16. These charts show the behaviour of SAM's lengths and braiding angles as the weight increase progressively.

1. Length Change in Released Position: In the first chart, we see how the SAM's length changes when it is in the "released" position. All models behave similarly, especially when the first 500 grams of weight are added, where the length changes sharply. However, Model-3 shows slightly higher extensibility after 700 g.
2. Length Change in Contracted Position: The second chart shows the change in SAM's length when it's in the "contracted" position. This graph demonstrates the weightlifting capability, where the model that shows less influence from the weight increasing, it has a higher capacity to resist the weight. Model-1 and Model-3 have similar behaviour, with Model-2 showing slightly higher ability to withstand the weight.
3. Braiding Angle Change in Released Position: In the third chart, it is observed that as weight is added, the braiding angle reduces. Once again, Model-1 and Model-3 exhibit less change compared to Model-2, indicating that Model-2 interacts more with the added weight.
4. Braiding Angle Change in Contracted Position: The fourth chart demonstrates how the braiding angle changes when SAM is in the "contracted" position with increasing weight. Model-1 shows a sharp reduction from 0 g to 500 g, while Model-2 and Model-3 show a more gradual change. Model-3 is notably less affected by the added weight throughout all weight increments.

These graphs provide a clear insight into how the different SAM models perform when subjected to different weight levels. Model-2 generally shows more favourable characteristics in terms of resistance to weight changes.

Tab.App 2: presents how different models (Model-1, Model-2, and Model-3) respond to increasing weight by evaluating the change in SAM's length and change in braiding angle through the fully released and fully contracted state.

Weight (g)	Model-1				Model-2				Model-3			
	Length		Angle		Length		Angle		Length		Angle	
	Released	Contracted	Released	Contracted	Released	Contracted	Released	Contracted	Released	Contracted	Released	Contracted
0	197.81	183.04	55.7	91.3	200.25	187.31	61	88.5	204.2	191.72	48.2	71.5
500	206.61	193.46	51.7	74.9	208.12	196.95	56.3	79.4	210.74	201.95	42.7	65.8
700	206.4	196.72	48.1	72.4	210.35	196.2	51.7	71.4	216.12	204.96	40	63.7
1000	206.55	199.52	45.1	69.6	210.47	198.59	45	66.1	216.62	208.53	39.8	61.5
1300	211.22	200.64	43.8	69.1	212.24	202.3	40.6	63.4	218.68	211.82	39	58.7
1600	210.39	202.87	43.3	68.6	212.54	202.78	38.4	59.6	219.68	213.3	39.6	58.2

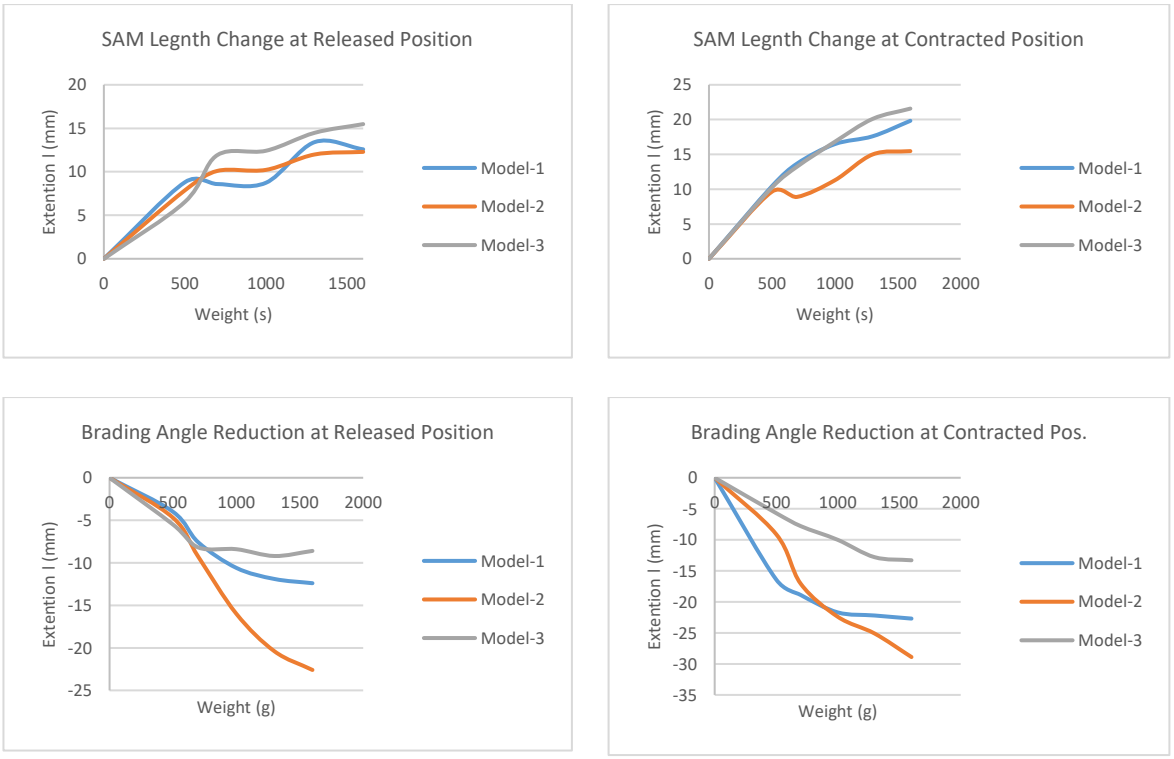

Fig.App 16: comparison of three SAM augmented models through four charts. The charts in the first row show the change in SAM's length at the released and contracted positions, respectively, under varying lifted weights (ranging from 0 g to 1600 g). The charts in the second row show the corresponding changes in the braiding angle at the released and contracted positions, respectively, under varying lifted weights (ranging from 0 g to 1600 g).

Appendix 7: Soft Component Experiments

Appendix 7.1: Actuation Process of Soft Components

In this experiment, an investigation for the behaviour of soft inflatable components is provided without using braid. The braid in SAM is responsible for constraining the inflation of the SIC. Therefore, it mandates its shape and enabling specific motions, such as contraction in the case of SAM. The main objectives of these tests are:

1. To explore the behaviour of SICs in the absence of the braided sleeve. This test seeks to understand how SICs geometry and shape characteristics change when it is actuated.
2. To compare the performance of SICs from different SAM models. While all models share the same braided sleeve geometry and pneumatic connections, their SIC designs are different. Notably, the soft material volume and cavity volume are the same for all three models. Therefore, this comparison emphasizes the impact of SIC design on performance.

Fig.App 17, using Model-1 as an example to present the progression of inflation during the actuation and de-actuation of the SIC. Each point on the chart corresponds to a specific pressure value along the internal pressure curve. The tests are conducted under specific conditions, a frequency of 0.2 Hz and an input pressure of 60 kPa. At this frequency, one full cycle (consists of actuation and de-actuation) spans 5 seconds, with 2.5 seconds for actuation and another 2.5 seconds for de-actuation. The sequence images are captured every 0.5 seconds to follow the inflation and deflation progression.

On the figure, the left side shows the steps of inflation. It begins at 0 seconds and keeps inflation until it reaches its maximum size in this test (it has the ability to expand its size more if the inflation continues for longer than 2.5 seconds).

On the right side, the steps for deflation during de-actuation can be seen, where the SIC shrinks back to its original size at the end of the cycle. The length and width of the SIC are noted with yellow lines in the sequence images during both inflation and deflation. The length measurement is taken from the flat surface of the pneumatic adapter connector on the inlet side to the flat surface of the end closer on the other side. Meanwhile, the width measurement is made at the midpoint of the SIC. This helps in measuring the amount that SIC extends in the linear direction and the amount it expands in the radial direction.

The data of the SIC inflation experiment is presented in **Error! Reference source not found.**, which show how different models (Model-1, Model-2, and Model-3). This

table provides the linear and radial expansion over a full cycle with 0.5 seconds intervals between the measurements.

By looking at the table, a slight variation can be observed in the original lengths (at 0 second) among the models. These variations can be caused by factors like manual assembly of SAMs, variations in pneumatic connectors, and the calibration process that is used in video processing with Kinovea software.

To facilitate the models' performance comparison, the data in the table is shown in line graphs for the changes in linear and radial expansion among the different models. Fig.App 18 comprises two charts that explain the linear extension and radial expansion of the SIC over a duration of 5 seconds and under a pressure of 60 kPa. When evaluating the linear extension chart, a high similarity becomes clear among all three SIC models. However, Model-1 shows notable fluctuations, unlike Models 2 and 3. These fluctuations occur because Model-1 is composed of three filaments that inflate separately which leads to less smooth linear extension.

In the second chart showing radial expansion, Model-2 exhibits symmetry around the peak point, indicating similarity between the inflation and deflation behaviours. In contrast, Model-1 and Model-3 do not exhibit the same symmetry. Model-1 shows the highest radial expansion with the highest fluctuations in the line graph due to the behaviour of the three filaments. Model-3 reaches its maximum radial expansion earlier than Model-2, indicating that the single cavity in Model-3 results in faster radial expansion compared to Model-2. These observations demonstrate how each SIC model behaves during inflation and deflation to understand the performance characteristics.

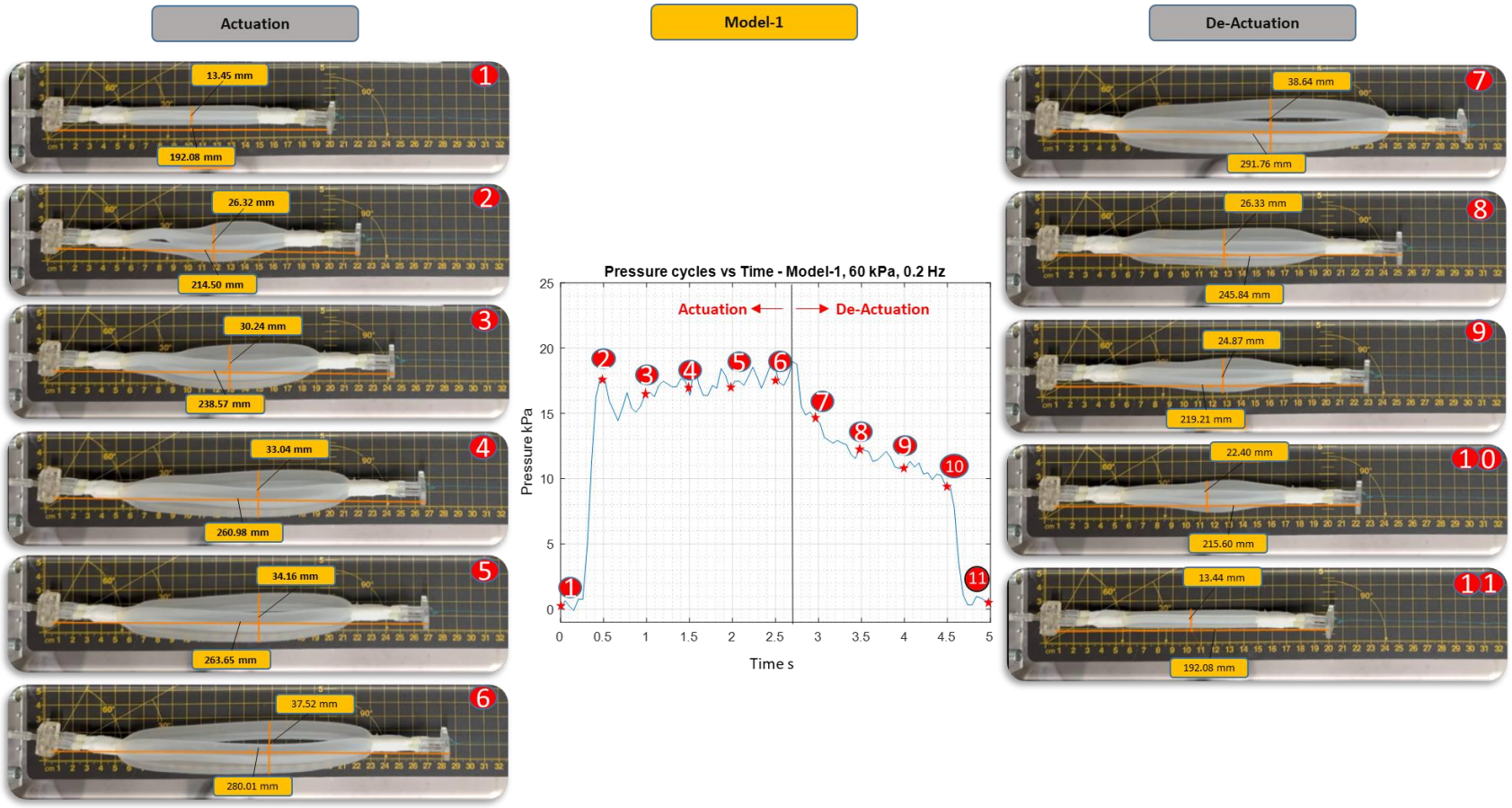

Fig.App 17: Progression of inflation during the actuation and de-actuation of the SIC using Model-1 as an example.

Tab.App 3: Data from the SIC inflation experiment, illustrating the performance of different models (Model-1, Model-2, and Model-3).

Time s	Model-1		Model-2		Model-3	
	Linear	Radial	Linear	Radial	Linear	Radial
0	192.08	13.45	188.36	10.79	195.95	10.53
0.5	214.5	26.32	214.07	18.17	215.43	17
1	238.57	30.24	241.89	21.01	236.24	25.42
1.5	260.98	33.04	261.78	24.56	257.7	27.04
2	263.65	34.16	278.81	26.59	276.73	27.28
2.5	280.01	37.52	288.45	27.27	294.14	27.28
3	291.76	38.65	270.44	23.85	283.04	25.66
3.5	245.84	26.33	250	21.01	266.04	24.45
4	219.21	24.87	224.24	18.17	244.58	22.98
4.5	215.6	22.4	205.7	14.83	222.31	15.6
5	192.08	13.44	192.25	10.8	196	10.53

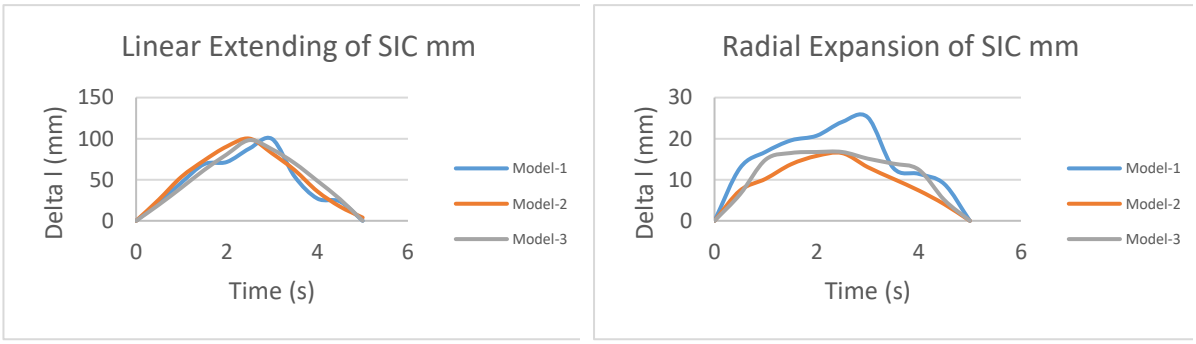

Fig.App 18: Illustrating the linear extension and radial expansion of the SIC over a duration of 5 seconds under a pressure of 60 kPa, displaying the linear extension, while the second chart shows the corresponding radial expansion.

Appendix 7.2: Min Required Pressure to Inflate the Soft Components

The video that recorded to measure the minimum needed pressure was take a perpendicular shooting angle to measure the linear and radial SIC inflation in a 2D projection. The videos recorded the inflation process till the inflation reached its maximum (no more inflation). From conducting several tests, we found that 80 seconds is sufficient time to observe the entire inflation process. As shown in Fig.App 19 and Tab.App 4, a capture was taken each 20 seconds with recording the amount of the linear and radial inflation at each stage. The linear inflation was determined by measuring the displacement between the inlet and end closer

connectors. The radial inflation was determined by measuring the change in SIC's diameter at the middle point.

From the sequence figures of the inflation process, it can be observed that the deformation in Model-1 and Model-2 starts from the middle while in Model-3 starts from the part that is near to the air inlet. The second stage, at t= 20 s, shows SIC's behaviour of the beginning of the inflation. By comparing the speed of Model-2 speeds at the minimum pressure and 60 kPa, we can see a massive difference in SIC inflation linear speed. The speed at the minimum pressure is around %97 slower than the pressure at 60 kPa.

Tab.App 4: Data presenting the linear extension and radial expansion of the SIC, with measurements taken every 20 seconds, recording the amount of inflation at each stage of the process.

Model	Model -1		Model -2		Model -3	
Pressure	18.31 kPa		14.32 kPa		15.64 kPa	
Time (s)	Linear extension (mm)	Radial expansion (mm)	Linear extension (mm)	Radial expansion (mm)	Linear extension (mm)	Radial expansion (mm)
0	187.98	13.48	186.31	10.46	195.6	10.26
20	193.93	19.51	217.61	24.15	196.77	14.29
40	240.07	32.37	250.21	26.06	259.96	27.92
60	268.12	39.18	257.67	25.16	300.78	28.58
80	271.9	40.07	266.67	25.16	313.23	28.57

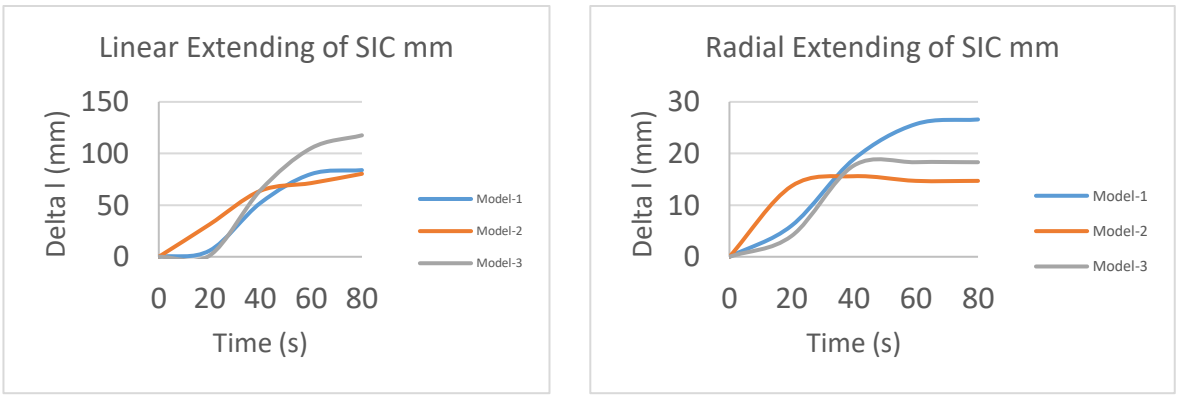

Fig.App 19: illustrating the linear extension and radial expansion of the SIC, taken every 20 seconds. The first chart presents the linear extension, while the second chart depicts the corresponding radial expansion.

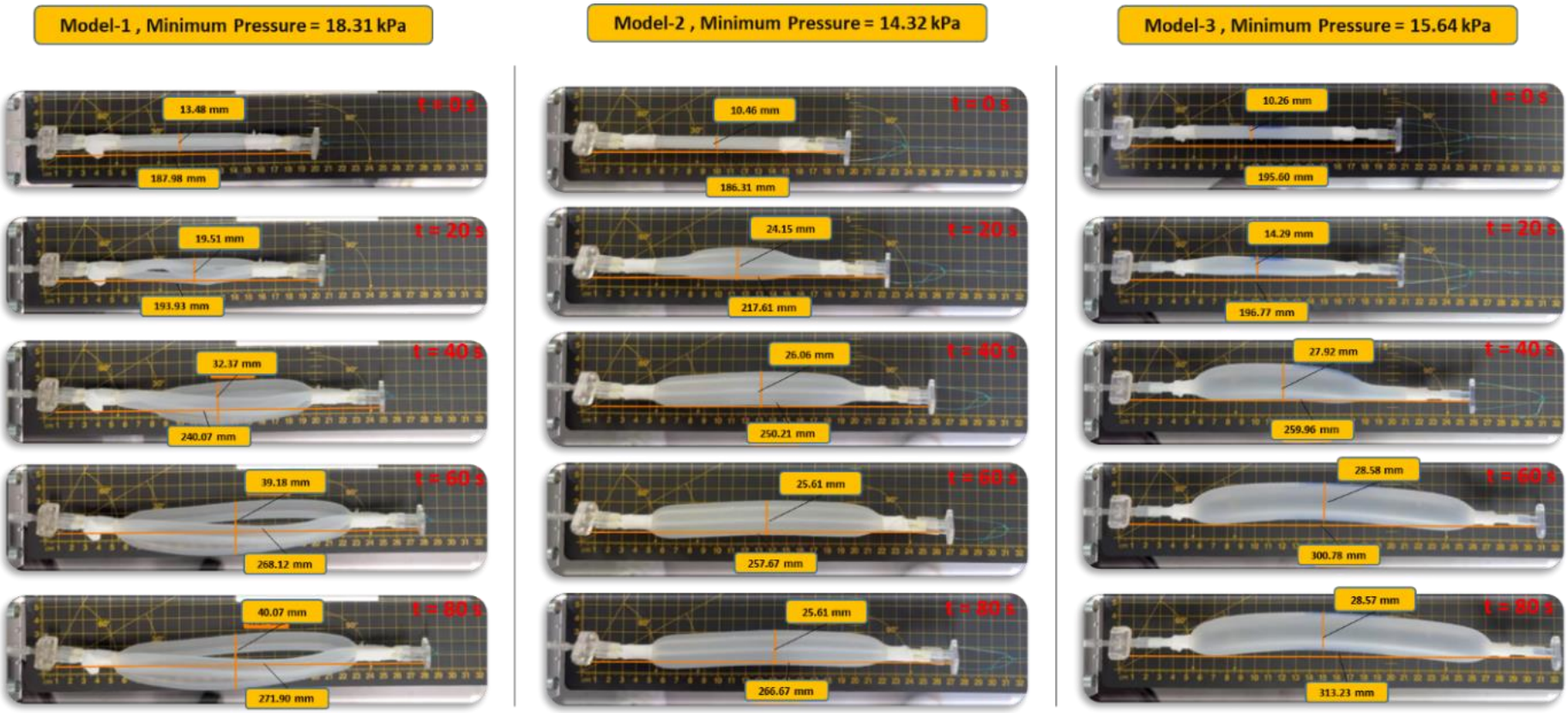

Fig.App 20: Sequential captures taken every 20 seconds, recording the amount of linear and radial inflation at each stage of the process.

Appendix 8: MATLAB Codes

Appendix 8.1: Code-1 for Processing Data from Cyclic Tests

The data analysis utilizes multiple MATLAB codes, each developed for specific purposes. These codes are grouped into four categories according to their distinct objectives. The resulting charts generated by these codes will be presented in the results section.

The first type of code focuses on generating synchronized pressure and load cycles over time. This code produces three figures: the first one shows a synchronized pressure and load cycles, highlighting different cycle components, including pre-conditioning, actuation, de-actuation, and idle phases. The second figure overlays seven sequential cycles, facilitating an assessment of cycle variations and repeatability. The third figure presents average and standard deviation calculations derived from the data in the second chart, with the standard deviation visually represented by a shadow area over the average line. Additionally, it generates data in a spreadsheet table that presents important outcomes, such as the maximum load of each cycle, delay between pressure and load cycle, and time intervals for cycle components.

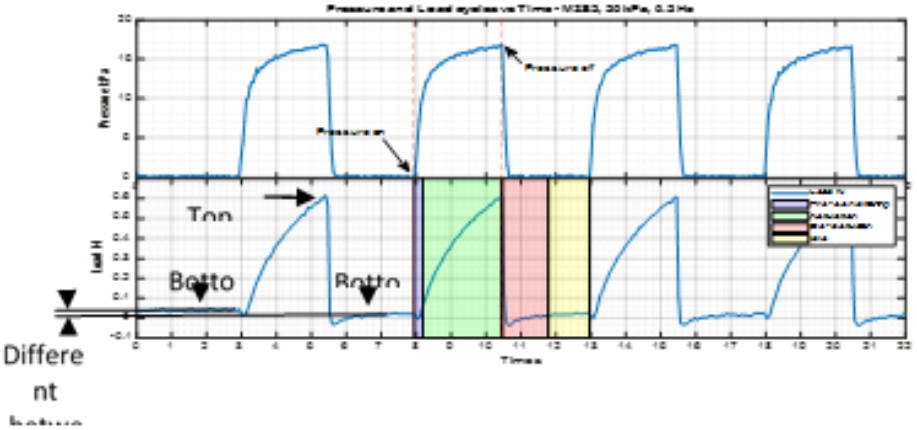

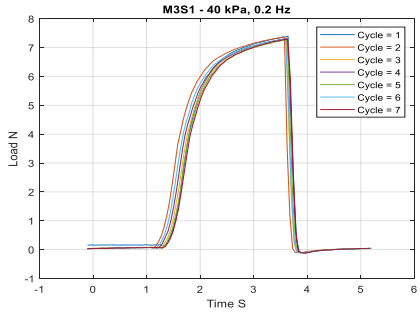

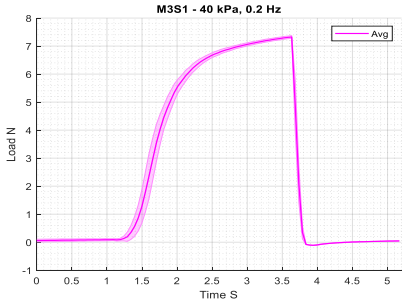

```
clc
clear all

T_selected = readtable('M1V1_Processed.xlsx','Sheet','80-
02h','Range','A2:F912');
T_selected.Properties.VariableNames =
{'time','B','C','D','pressure','load'};

t = T_selected.time;          %%%time
l = T_selected.load;          %%%load
p = T_selected.pressure;      %%%pressure

a=l(1:120);
[lm,lm_id]=max(a);        %lm=l maximum ---- tm=t maximum
ts_id=lm_id-57;           % ts_id=time starting point index(triggerpoint)

length = 100;                                          % Legnth of data, as
sample rate=20>> at 0.2 Hz the number of the cells will be 100 for each
cycle
%%% to find peaks over ther the entire graph %%
peaks_value = [];   peaks_value_p = [];                                  %
just to define Peaks value
peaks_id = [];      peaks_id_p = [];                                  % just
to define Peaks id
o=[]; k=[];
for i = 1:8
    sub_t = t(ts_id:ts_id + length)-t(ts_id);       % sub_t represent time
of one cycle at each iteration
    sub_l = l(ts_id:ts_id + length);       % sub_l represent load of one
cycle at each iteration
    sub_p = p(ts_id:ts_id + length);       % sub_l represent load of one
cycle at each iteration
     o=[o,sub_l];
     k=[k,sub_t];   %time

    %%% to find keaks load and corroskonding time and its cell (id) over
the entire grakh %%
    [max_value, max_index] = max(sub_l);            % find max of sub_l and
its location (cell number)
    peaks_value(i) = max_value;                     % put max values of
load each cycle into array
    peaks_id(i) = max_index + ts_id-1;              % put the location of
max values of each cycle into array. Notice that max_index refere to max at
sub_l. Therfore we need to add start_l_id to refere to l array
    peaks_value_t=t(peaks_id);                      % put max values of
time of each cycle into array

    [max_value_p, max_index_p] = max(sub_p);        % find max of sub_p and
its location (cell number)
    peaks_value_p(i) = max_value_p;                     % put max values of
load each cycle into array
    peaks_id_p(i) = max_index_p + ts_id-1;              % put the location
of max values of each cycle into array. Notice that max_index refere to max
at sub_l. Therfore we need to add start_l_id to refere to l array


   ts_id = ts_id + length;
```

```
grid on
end

figure(1)
x=peaks_id-70;                  %x rekresent the assumed starting point for
the actuation of each cycle according to the known load peak point
n=[]; pp=[]; avg=[];  stdev=[];
for j = 1:7

    tt = t(x(j)-2:x(j+1)+4)-t(x(j));                              % at 1 Hz
    ll = l(x(j)-2:x(j+1)+4);       % sub_l represent load of one cycle at
each iteration
     rr=ll(1:101);
     ss=tt(1:101);  %time

     n=[n,rr];
     pp=[pp,ss];   %time

      [lb, lb_index] =min(rr); tb=ss(lb_index);               %to find
bottom peak value and idex
     lb_avg = mean(rr(lb_index+3 : end-2));                   %to find avg
of the load at the bottom of the cycle

          avg=mean(n,2)-lb_avg;
     stdev=std(n,0,2);

     ll1=ll-lb_avg; g=ll1(1:100);

     txt = ['Cycle = ',num2str(j)];
        plot(ss, rr-lb_avg,'DisplayName',txt)
        hold on
        legend show
        title('M1S1 - 80 kPa, 0.2 Hz');
        grid on
        xlabel('Time S'); ylabel('Load N')
end

Peak_avg=max(avg);

figure(2)
     shadedErrorBar(ss,avg,stdev,'lineprops',{'-m','LineWidth',
1.2},'transparent',true,'patchSaturation',0.2) %M1V3
     hold on
     hold off
     grid on; grid minor;
    legend('Avg','STD')
    xlim([0 5.2]);
    title('M1S1 - 80 kPa, 0.2 Hz');
    xlabel('Time S'); ylabel('Load N')

    figure(3)
x1=subplot(2,1,1);
plot(t(1:600),p(1:600))
ylabel('Pressure kPa')
title('Pressure and Load cycles vs Time - M1S1, 80 kPa, 0.2 Hz');
hold on
% xticks(0:1:22)
xlim([0 22]);
grid on; grid minor;
```

```
l_shifted=l-lb_avg;
Peaks_l=[l_shifted(peaks_id(1));l_shifted(peaks_id(2));l_shifted(peaks_id(3
));l_shifted(peaks_id(4));l_shifted(peaks_id(5));l_shifted(peaks_id(6));l_s
hifted(peaks_id(7));l_shifted(peaks_id(8))];  %%Peaks of load shifted
x2=subplot(2,1,2);
plot(t(1:600),l_shifted(1:600))
p1 = get(x1, 'Position');
p2 = get(x2, 'Position');
p1(2) = p2(2)+p2(4);
set(x1, 'pos', p1);
ylabel('Load N')
xlabel('Time s')
xticks(0:1:22)
xlim([0 22]);
hold on
grid on; grid minor;
hold on

%%%Responsing time
p_peak_1=peaks_value_p(1);
l_peak_1=Peaks_l(1);
ttt=[]; tttt=[]; tt_tr_2=[]; tt_act=[]; tt_dact=[]; tt_p=[]; tt_tr_3=[];
ttm=[]; ttm_id=[];
for q=2:7
t2=t(peaks_id(q));              %%time at 2nd peak
t3=t(peaks_id(q+1));            %%time at 3rd peak
 ttt=[ttt,t2];
 tttt=[tttt,t3];

ptr_id_cycle2 = find(0.5<p & p<p_peak_1 & t>t2-3 & t<t2);   %%find index of
the trigger point of 2nd cycle
ptr_id_cycle3 = find(0.5<p & p<p_peak_1 & t>t3-3 & t<t3);   %%find index of
the trigger point of the next cycle
ptr_id_2=ptr_id_cycle2(1)-1; %%%ptr=pressure trigger point index
ptr_id_3=ptr_id_cycle3(1)-1;
  t_tr_2=t(ptr_id_2);           %% t_tr_2 =time trigger point of 2nd cycle
  t_p=t(peaks_id(q));           %% t_p  =time peak point
  t_tr_3=t(ptr_id_3);           %% t_tr_3 =time trigger point of 3rd cycle


tt_p=[tt_p,t_p];              %%same as t_p, just to show the entire data
tt_tr_2=[tt_tr_2,t_tr_2];
tt_tr_3=[tt_tr_3,t_tr_3];
%%%actuation Mode
ltr_2=l_shifted(ptr_id_2);           %%%ltr_2=load at trigger point
 lact_id_cycle2 = find(1.5*ltr_2<l_shifted & 10*ltr_2>l_shifted & t>t_tr_2
& t<t2);  %%find index of the actuation point of 2nd cycle
 lact_id_2=lact_id_cycle2(1);         %% lact_id_2 =index of actuation
point of 2nd cycle
  t_act=t(lact_id_2);                  %% t_act =time actuation point

  tt_act=[tt_act,t_act];

%%%Deactuation to Idle Mode
tm=t(peaks_id+25);
ttm=[ttm,tm];

tm_id=find(t==ttm(q));
```

```
l_tm=l_shifted(tm_id);
l_dact_id_cycle2 = find(0.8*l_tm<l_shifted & 1.2*l_tm>l_shifted & t>t2+0.45
& t<t_tr_3-0.4);

l_tr_3=l_shifted(ptr_id_3);          %%%l_tr_3=load at trigger point
%  l_dact_id_cycle2 = find(0.6*l_tr_3<l_shifted & l_shifted<l_tr_3*2 &
t>t2+0.45 & t<t_tr_3-0.4);  %%find index of the trigger point of 2nd cycle
 l_dact_id_2=l_dact_id_cycle2(1);
  t_dact=t(l_dact_id_2);

  tt_dact=[tt_dact,t_dact];

Delay(q)=t(peaks_id(q))-t(peaks_id_p(q));
Pre_time(q)=t_act-t_tr_2;
Act_time(q)=t_p-t_act;
Deact_time(q)=t_dact-t_p;
Idle_time(q)= t_tr_3-t_dact;
Total_time(q)=Pre_time(q)+Act_time(q)+Deact_time(q)+Idle_time(q);
end
%Transpose from row to column
Delay= Delay.';
Pre_time=Pre_time.';
Act_time=Act_time.';
Deact_time=Deact_time.';
Idle_time= Idle_time.';
tt_tr_2=tt_tr_2.';
tt_act=tt_act.';
tt_p=tt_p.';
tt_dact=tt_dact.';
tt_tr_3=tt_tr_3.';
peaks_id=peaks_id.';
Peak_avg=Peak_avg.';
peaks_value_p=peaks_value_p.';
Total_time=Total_time.';

%%%filling each periods with different colour
y1 = [l_peak_1/-7 l_peak_1/-7 l_peak_1*1.15 l_peak_1*1.15];

x1 = [tt_tr_2(1) tt_act(1) tt_act(1) tt_tr_2(1)];    %%%filling the
Pre_time
fill(x1,y1,'b')
alpha(0.2)

x2 = [tt_act(1) tt_p(1) tt_p(1) tt_act(1)];          %%%filling the
Act_time
fill(x2,y1,'g')
alpha(0.2)

x3 = [tt_p(1) tt_dact(1) tt_dact(1) tt_p(1)];        %%%filling the
Deact_time
fill(x3,y1,'r')
alpha(0.2)

x4 = [tt_dact(1) tt_tr_3(1) tt_tr_3(1) tt_dact(1)];  %%%filling the
Idle_time
fill(x4,y1,'y')
alpha(0.2)

ylim([l_peak_1/-7.2 l_peak_1*1.1]);
```

```
legend('Load N','Pre-conditioning','Actuation','De-actuation','Idle')
hold off

T1 = table(Delay,Pre_time,Act_time,Deact_time,Idle_time,Total_time);
T2 = table(tt_tr_2,tt_act,tt_p,tt_dact,tt_tr_3);
T3 = table(peaks_id,peaks_value_t,peaks_value_p);
T4 = table(Peaks_l);
T5 = table(Peak_avg);
T6 = table(avg,stdev);
filename = 'M1S1_80_02h.xlsx';
writetable(T1,filename,'Sheet',1,'Range','B1');
writetable(T2,filename,'Sheet',1,'Range','I2');
writetable(T3,filename,'Sheet',1,'Range','O1');
writetable(T4,filename,'Sheet',1,'Range','R1');
writetable(T5,filename,'Sheet',1,'Range','S1');
writetable(T6,filename,'Sheet',1,'Range','T1');
```

Appendix 8.2: Code-2 for Plotting Line Graphs to Observe Metric Effect

The second type of code is used to create a plot featuring four line graphs of load. It illustrates the effect of input pressure levels (applied at 20, 40, 60, and 80 kPa while maintaining a constant frequency of 0.2 Hz). Also, the concept is applied in different scenario to illustrate the effect of actuation frequency variations (at 1, 0.5, and 0.2 Hz while keeping pressure constant at 60 kPa). Each line graph in those plots should represents average and standard deviation calculations from seven sequential cycles. For example, the figure below shows four line graphs of load, illustrating the effect of input pressure levels.

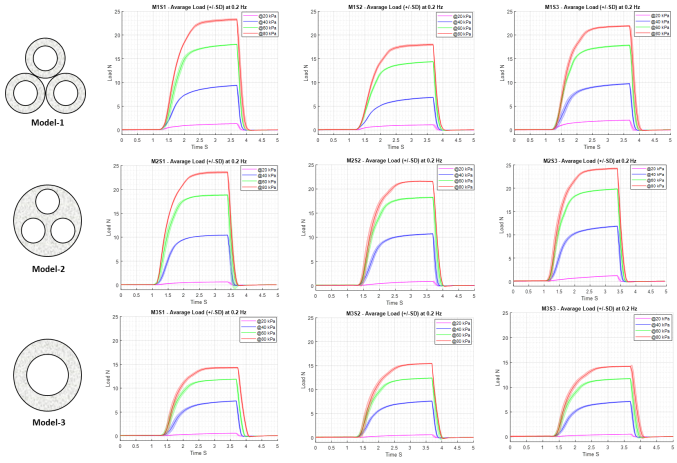


```
clc
clear all

      T1_20 =
readtable('M1S1_20_02h.xlsx','Sheet','Sheet1','Range','T1:U103');
      T1_40 =
readtable('M1S1_40_02h.xlsx','Sheet','Sheet1','Range','T1:U103');
```

```
      T1_60 =
readtable('M1S1_60_02h.xlsx','Sheet','Sheet1','Range','T1:U103');
      T1_80 =
readtable('M1S1_80_02h.xlsx','Sheet','Sheet1','Range','T1:U103');

%       T1_20.Properties.VariableNames = {'avg','stdev'};

      t = (0:0.0512:5.1712)';          %%%time
avg_20 = T1_20.avg;  avg_40 = T1_40.avg;   avg_60 = T1_60.avg;  avg_80 =
T1_80.avg;
stdev_20 = T1_20.stdev;  stdev_40 = T1_40.stdev;   stdev_60 = T1_60.stdev;
stdev_80 = T1_80.stdev;

      figure(1)
     shadedErrorBar(t,avg_20,stdev_20,'lineprops',{'-m','LineWidth',
1.2},'transparent',true,'patchSaturation',0.2)
     shadedErrorBar(t,avg_40,stdev_40,'lineprops',{'-b','LineWidth',
1.2},'transparent',true,'patchSaturation',0.2)
     shadedErrorBar(t,avg_60,stdev_60,'lineprops',{'-g','LineWidth',
1.2},'transparent',true,'patchSaturation',0.2)
     shadedErrorBar(t,avg_80,stdev_80,'lineprops',{'-r','LineWidth',
1.2},'transparent',true,'patchSaturation',0.2)
     hold on
     grid on; grid minor;
    legend('@20 kPa','@40 kPa','@60 kPa','@80 kPa','Location','East')
    xlim([0 5]);
    ylim([-1 25]);
    title('M1S1 - Avarage Load (+/-SD) at 0.2 Hz');
    xlabel('Time S'); ylabel('Load N')
```

Appendix 8.3: Code-3 for Plotting Bar Graphs for the Peak Load to Observe Metric Effect

The third type of code generates bar graphs presenting the average of peak values of specific parameters. These graphs provide a straightforward visual collective comparison among the measured parameters. They are applied in various cases, such as assessing the load performance of different SAM models under varying input pressure and frequency conditions. These bar graphs also include standard deviation bars to indicate data variability. For example, the figure below shows the average of peak values under varying input pressure.

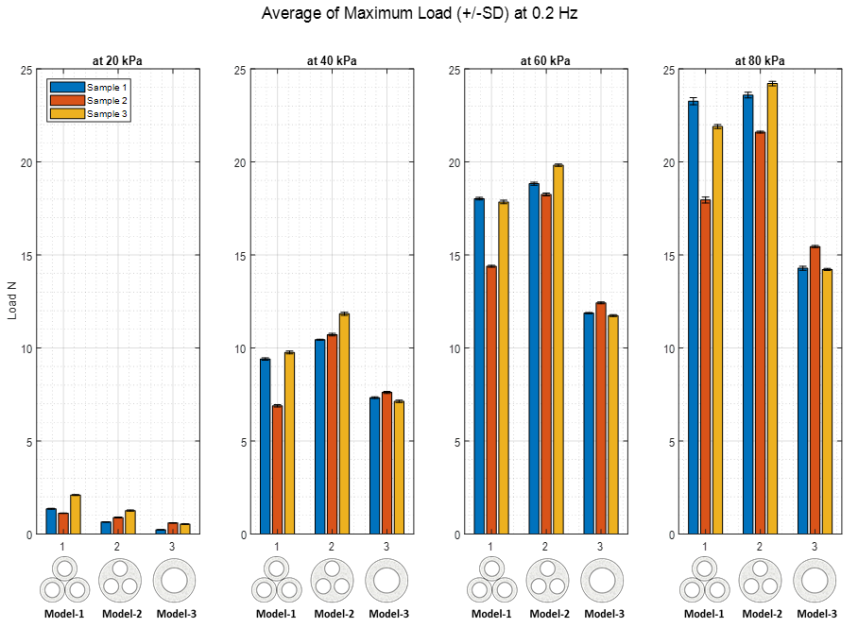


```
clc
clear all

T1S1 = readtable('M1S1_60_02h.xlsx','Sheet','Sheet1','Range','B2:M8');
%%M1S1
T1S1.Properties.VariableNames =
{'Delay','Pre_time','Act_time','Deact_time','Idle_time','Total_time','emp1'
,'tr1','t_act','tp','t_dact','tr2'};
  T2S1 = readtable('M1S1_60_02h.xlsx','Sheet','Sheet1','Range','O1:R9');
  T2S1.Properties.VariableNames =
{'peaks_id','peaks_value_t','peaks_value_p','Peaks_l'};
    T3S1 = readtable('M1S1_60_02h.xlsx','Sheet','Sheet1','Range','S1:S2');
    T3S1.Properties.VariableNames = {'Peak_avg'};
      T4S1 =
readtable('M1S1_60_02h.xlsx','Sheet','Sheet1','Range','T1:U103');
      T4S1.Properties.VariableNames = {'avg','stdev'};
  Delay_1= mean(T1S1.Delay);   Pre_time_1= mean(T1S1.Pre_time); Act_time_1=
mean(T1S1.Act_time);  Deact_time_1= mean(T1S1.Deact_time); Idle_time_1=
mean(T1S1.Idle_time);
  tr1_1= mean(T1S1.tr1); t_act_1= mean(T1S1.t_act); tp_1= mean(T1S1.tp);
t_dact_1= mean(T1S1.t_dact);  tr2_1= mean(T1S1.tr2);

   DelaySTD_1= std(T1S1.Delay);   Pre_timeSTD_1= std(T1S1.Pre_time);
Act_timeSTD_1= std(T1S1.Act_time);  Deact_timeSTD_1= std(T1S1.Deact_time);
Idle_timeSTD_1= std(T1S1.Idle_time);

  %%%%%%%%%%%%%%%%%%%%%%%%%%%%%%%%%%%%%%%%%%%%%%%%%%%%%%%%%%%%%%%%%%%%%%%%
S2
T1S2 = readtable('M1S2_60_02h.xlsx','Sheet','Sheet1','Range','B2:M8');
%%M1S2
T1S2.Properties.VariableNames =
{'Delay','Pre_time','Act_time','Deact_time','Idle_time','Total_time','emp1'
,'tr1','t_act','tp','t_dact','tr2'};
  T2S2 = readtable('M1S2_60_02h.xlsx','Sheet','Sheet1','Range','O1:R9');
  T2S2.Properties.VariableNames =
{'peaks_id','peaks_value_t','peaks_value_p','Peaks_l'};
    T3S2 = readtable('M1S2_60_02h.xlsx','Sheet','Sheet1','Range','S1:S2');
    T3S2.Properties.VariableNames = {'Peak_avg'};
```

```
      T4S2 =
readtable('M1S2_60_02h.xlsx','Sheet','Sheet1','Range','T1:U103');
      T4S2.Properties.VariableNames = {'avg','stdev'};
  Delay_2= mean(T1S2.Delay);   Pre_time_2= mean(T1S2.Pre_time); Act_time_2=
mean(T1S2.Act_time);  Deact_time_2= mean(T1S2.Deact_time); Idle_time_2=
mean(T1S2.Idle_time);
  tr1_2= mean(T1S2.tr1); t_act_2= mean(T1S2.t_act); tp_2= mean(T1S2.tp);
t_dact_2= mean(T1S2.t_dact);  tr2_2= mean(T1S2.tr2);

  DelaySTD_2= std(T1S2.Delay);   Pre_timeSTD_2= std(T1S2.Pre_time);
Act_timeSTD_2= std(T1S2.Act_time);  Deact_timeSTD_2= std(T1S2.Deact_time);
Idle_timeSTD_2= std(T1S2.Idle_time);

%%%%%%%%%%%%%%%%%%%%%%%%%%%%%%%%%%%%%%%%%%%%%%%%%%%%%%%%%%%%%%%%%%%%%%%%%%%%
S3
T1S3 = readtable('M1S3_60_02h.xlsx','Sheet','Sheet1','Range','B2:M8');
%%M1S3
T1S3.Properties.VariableNames =
{'Delay','Pre_time','Act_time','Deact_time','Idle_time','Total_time','emp1'
,'tr1','t_act','tp','t_dact','tr2'};
  T2S3 = readtable('M1S3_60_02h.xlsx','Sheet','Sheet1','Range','O1:R9');
  T2S3.Properties.VariableNames =
{'peaks_id','peaks_value_t','peaks_value_p','Peaks_l'};
    T3S3 = readtable('M1S3_60_02h.xlsx','Sheet','Sheet1','Range','S1:S2');
    T3S3.Properties.VariableNames = {'Peak_avg'};
      T4S3 =
readtable('M1S3_60_02h.xlsx','Sheet','Sheet1','Range','T1:U103');
      T4S3.Properties.VariableNames = {'avg','stdev'};
  Delay_3= mean(T1S3.Delay);   Pre_time_3= mean(T1S3.Pre_time); Act_time_3=
mean(T1S3.Act_time);  Deact_time_3= mean(T1S3.Deact_time); Idle_time_3=
mean(T1S3.Idle_time);
  tr1_3= mean(T1S3.tr1); t_act_3= mean(T1S3.t_act); tp_3= mean(T1S3.tp);
t_dact_3= mean(T1S3.t_dact);  tr2_3= mean(T1S3.tr2);

  DelaySTD_3= std(T1S3.Delay);   Pre_timeSTD_3= std(T1S3.Pre_time);
Act_timeSTD_3= std(T1S3.Act_time);  Deact_timeSTD_3= std(T1S3.Deact_time);
Idle_timeSTD_3= std(T1S3.Idle_time);

%%%%%%%%%%%%%%%%%%%%%%%%%%%%%%%%%%%%%%%%%%%%%%%%%%%%%%%%%%%%%%%%%%%%%%%%%%%%
S4
T1S4 = readtable('M2S1_60_02h.xlsx','Sheet','Sheet1','Range','B2:M8');
%%M2S1
T1S4.Properties.VariableNames =
{'Delay','Pre_time','Act_time','Deact_time','Idle_time','Total_time','emp1'
,'tr1','t_act','tp','t_dact','tr2'};
  T2S4 = readtable('M2S1_60_02h.xlsx','Sheet','Sheet1','Range','O1:R9');
  T2S4.Properties.VariableNames =
{'peaks_id','peaks_value_t','peaks_value_p','Peaks_l'};
    T3S4 = readtable('M2S1_60_02h.xlsx','Sheet','Sheet1','Range','S1:S2');
    T3S4.Properties.VariableNames = {'Peak_avg'};
      T4S4 =
readtable('M2S1_60_02h.xlsx','Sheet','Sheet1','Range','T1:U103');
      T4S4.Properties.VariableNames = {'avg','stdev'};
  Delay_4= mean(T1S4.Delay);   Pre_time_4= mean(T1S4.Pre_time); Act_time_4=
mean(T1S4.Act_time);  Deact_time_4= mean(T1S4.Deact_time); Idle_time_4=
mean(T1S4.Idle_time);
  tr1_4= mean(T1S4.tr1); t_act_4= mean(T1S4.t_act); tp_4= mean(T1S4.tp);
t_dact_4= mean(T1S4.t_dact);  tr2_4= mean(T1S4.tr2);
```

```
  DelaySTD_4= std(T1S4.Delay);   Pre_timeSTD_4= std(T1S4.Pre_time);
Act_timeSTD_4= std(T1S4.Act_time);  Deact_timeSTD_4= std(T1S4.Deact_time);
Idle_timeSTD_4= std(T1S4.Idle_time);

%%%%%%%%%%%%%%%%%%%%%%%%%%%%%%%%%%%%%%%%%%%%%%%%%%%%%%%%%%%%%%%%%%%%%%%%%%%%
S5
T1S5 = readtable('M2S2_60_02h.xlsx','Sheet','Sheet1','Range','B2:M8');
%%M2S2
T1S5.Properties.VariableNames =
{'Delay','Pre_time','Act_time','Deact_time','Idle_time','Total_time','emp1'
,'tr1','t_act','tp','t_dact','tr2'};
  T2S5 = readtable('M2S2_60_02h.xlsx','Sheet','Sheet1','Range','O1:R9');
  T2S5.Properties.VariableNames =
{'peaks_id','peaks_value_t','peaks_value_p','Peaks_l'};
    T3S5 = readtable('M2S2_60_02h.xlsx','Sheet','Sheet1','Range','S1:S2');
    T3S5.Properties.VariableNames = {'Peak_avg'};
      T4S5 =
readtable('M2S2_60_02h.xlsx','Sheet','Sheet1','Range','T1:U103');
      T4S5.Properties.VariableNames = {'avg','stdev'};
  Delay_5= mean(T1S5.Delay);   Pre_time_5= mean(T1S5.Pre_time); Act_time_5=
mean(T1S5.Act_time);  Deact_time_5= mean(T1S5.Deact_time); Idle_time_5=
mean(T1S5.Idle_time);
  tr1_5= mean(T1S5.tr1); t_act_5= mean(T1S5.t_act); tp_5= mean(T1S5.tp);
t_dact_5= mean(T1S5.t_dact);  tr2_5= mean(T1S5.tr2);

  DelaySTD_5= std(T1S5.Delay);   Pre_timeSTD_5= std(T1S5.Pre_time);
Act_timeSTD_5= std(T1S5.Act_time);  Deact_timeSTD_5= std(T1S5.Deact_time);
Idle_timeSTD_5= std(T1S5.Idle_time);

%%%%%%%%%%%%%%%%%%%%%%%%%%%%%%%%%%%%%%%%%%%%%%%%%%%%%%%%%%%%%%%%%%%%%%%%%%%%
S6
T1S6 = readtable('M2S3_60_02h.xlsx','Sheet','Sheet1','Range','B2:M8');
%%M2S3
T1S6.Properties.VariableNames =
{'Delay','Pre_time','Act_time','Deact_time','Idle_time','Total_time','emp1'
,'tr1','t_act','tp','t_dact','tr2'};
  T2S6 = readtable('M2S3_60_02h.xlsx','Sheet','Sheet1','Range','O1:R9');
  T2S6.Properties.VariableNames =
{'peaks_id','peaks_value_t','peaks_value_p','Peaks_l'};
    T3S6 = readtable('M2S3_60_02h.xlsx','Sheet','Sheet1','Range','S1:S2');
    T3S6.Properties.VariableNames = {'Peak_avg'};
      T4S6 =
readtable('M2S3_60_02h.xlsx','Sheet','Sheet1','Range','T1:U103');
      T4S6.Properties.VariableNames = {'avg','stdev'};
  Delay_6= mean(T1S6.Delay);   Pre_time_6= mean(T1S6.Pre_time); Act_time_6=
mean(T1S6.Act_time);  Deact_time_6= mean(T1S6.Deact_time); Idle_time_6=
mean(T1S6.Idle_time);
  tr1_6= mean(T1S6.tr1); t_act_6= mean(T1S6.t_act); tp_6= mean(T1S6.tp);
t_dact_6= mean(T1S6.t_dact);  tr2_6= mean(T1S6.tr2);

  DelaySTD_6= std(T1S6.Delay);   Pre_timeSTD_6= std(T1S6.Pre_time);
Act_timeSTD_6= std(T1S6.Act_time);  Deact_timeSTD_6= std(T1S6.Deact_time);
Idle_timeSTD_6= std(T1S6.Idle_time);

%%%%%%%%%%%%%%%%%%%%%%%%%%%%%%%%%%%%%%%%%%%%%%%%%%%%%%%%%%%%%%%%%%%%%%%%%%%%
S7
T1S7 = readtable('M3S1_60_02h.xlsx','Sheet','Sheet1','Range','B2:M8');
%%M3S1
```

```
T1S7.Properties.VariableNames =
{'Delay','Pre_time','Act_time','Deact_time','Idle_time','Total_time','emp1'
,'tr1','t_act','tp','t_dact','tr2'};
  T2S7 = readtable('M3S1_60_02h.xlsx','Sheet','Sheet1','Range','O1:R9');
  T2S7.Properties.VariableNames =
{'peaks_id','peaks_value_t','peaks_value_p','Peaks_l'};
    T3S7 = readtable('M3S1_60_02h.xlsx','Sheet','Sheet1','Range','S1:S2');
    T3S7.Properties.VariableNames = {'Peak_avg'};
      T4S7 =
readtable('M3S1_60_02h.xlsx','Sheet','Sheet1','Range','T1:U103');
      T4S7.Properties.VariableNames = {'avg','stdev'};
  Delay_7= mean(T1S7.Delay);   Pre_time_7= mean(T1S7.Pre_time); Act_time_7=
mean(T1S7.Act_time);  Deact_time_7= mean(T1S7.Deact_time); Idle_time_7=
mean(T1S7.Idle_time);
  tr1_7= mean(T1S7.tr1); t_act_7= mean(T1S7.t_act); tp_7= mean(T1S7.tp);
t_dact_7= mean(T1S7.t_dact);  tr2_7= mean(T1S7.tr2);

  DelaySTD_7= std(T1S7.Delay);   Pre_timeSTD_7= std(T1S7.Pre_time);
Act_timeSTD_7= std(T1S7.Act_time);  Deact_timeSTD_7= std(T1S7.Deact_time);
Idle_timeSTD_7= std(T1S7.Idle_time);

%%%%%%%%%%%%%%%%%%%%%%%%%%%%%%%%%%%%%%%%%%%%%%%%%%%%%%%%%%%%%%%%%%%%%%%%%%%
S8
T1S8 = readtable('M3S2_60_02h.xlsx','Sheet','Sheet1','Range','B2:M8');
%%M3S2
T1S8.Properties.VariableNames =
{'Delay','Pre_time','Act_time','Deact_time','Idle_time','Total_time','emp1'
,'tr1','t_act','tp','t_dact','tr2'};
  T2S8 = readtable('M3S2_60_02h.xlsx','Sheet','Sheet1','Range','O1:R9');
  T2S8.Properties.VariableNames =
{'peaks_id','peaks_value_t','peaks_value_p','Peaks_l'};
    T3S8 = readtable('M3S2_60_02h.xlsx','Sheet','Sheet1','Range','S1:S2');
    T3S8.Properties.VariableNames = {'Peak_avg'};
      T4S8 =
readtable('M3S2_60_02h.xlsx','Sheet','Sheet1','Range','T1:U103');
      T4S8.Properties.VariableNames = {'avg','stdev'};
  Delay_8= mean(T1S8.Delay);   Pre_time_8= mean(T1S8.Pre_time); Act_time_8=
mean(T1S8.Act_time);  Deact_time_8= mean(T1S8.Deact_time); Idle_time_8=
mean(T1S8.Idle_time);
  tr1_8= mean(T1S8.tr1); t_act_8= mean(T1S8.t_act); tp_8= mean(T1S8.tp);
t_dact_8= mean(T1S8.t_dact);  tr2_8= mean(T1S8.tr2);

  DelaySTD_8= std(T1S8.Delay);   Pre_timeSTD_8= std(T1S8.Pre_time);
Act_timeSTD_8= std(T1S8.Act_time);  Deact_timeSTD_8= std(T1S8.Deact_time);
Idle_timeSTD_8= std(T1S8.Idle_time);

%%%%%%%%%%%%%%%%%%%%%%%%%%%%%%%%%%%%%%%%%%%%%%%%%%%%%%%%%%%%%%%%%%%%%%%%%%%
S9
T1S9 = readtable('M3S3_60_02h.xlsx','Sheet','Sheet1','Range','B2:M8');
%%M3S3
T1S9.Properties.VariableNames =
{'Delay','Pre_time','Act_time','Deact_time','Idle_time','Total_time','emp1'
,'tr1','t_act','tp','t_dact','tr2'};
  T2S8 = readtable('M3S3_60_02h.xlsx','Sheet','Sheet1','Range','O1:R9');
  T2S8.Properties.VariableNames =
{'peaks_id','peaks_value_t','peaks_value_p','Peaks_l'};
    T3S8 = readtable('M3S3_60_02h.xlsx','Sheet','Sheet1','Range','S1:S2');
    T3S8.Properties.VariableNames = {'Peak_avg'};
      T4S8 =
readtable('M3S3_60_02h.xlsx','Sheet','Sheet1','Range','T1:U103');
```

```
      T4S8.Properties.VariableNames = {'avg','stdev'};
  Delay_9= mean(T1S9.Delay);   Pre_time_9= mean(T1S9.Pre_time); Act_time_9=
mean(T1S9.Act_time);  Deact_time_9= mean(T1S9.Deact_time); Idle_time_9=
mean(T1S9.Idle_time);
  tr1_9= mean(T1S9.tr1); t_act_9= mean(T1S9.t_act); tp_9= mean(T1S9.tp);
t_dact_9= mean(T1S9.t_dact);  tr2_9= mean(T1S9.tr2);

  DelaySTD_9= std(T1S9.Delay);   Pre_timeSTD_9= std(T1S9.Pre_time);
Act_timeSTD_9= std(T1S9.Act_time);  Deact_timeSTD_9= std(T1S9.Deact_time);
Idle_timeSTD_9= std(T1S9.Idle_time);

figure(1)
% x = categorical({'Model-1', 'Model-2', 'Model-3'});
% x = reordercats(x,{'Model-1', 'Model-2', 'Model-3'});

y_Pre_time = [Pre_time_1 Pre_time_2 Pre_time_3; Pre_time_4 Pre_time_5
Pre_time_6; Pre_time_7 Pre_time_8 Pre_time_9];
  y_Act_time = [Act_time_1 Act_time_2 Act_time_3; Act_time_4 Act_time_5
Act_time_6; Act_time_7 Act_time_8 Act_time_9];
    y_Deact_time = [Deact_time_1 Deact_time_2 Deact_time_3; Deact_time_4
Deact_time_5 Deact_time_6; Deact_time_7 Deact_time_8 Deact_time_9];
      y_Idle_time = [Idle_time_1 Idle_time_2 Idle_time_3; Idle_time_4
Idle_time_5 Idle_time_6; Idle_time_7 Idle_time_8 Idle_time_9];

% y_Pre_time_STD = [Pre_timeSTD_1 0 0; 0 0 0; 0 0 0];
y_Pre_time_STD = [Pre_timeSTD_1 Pre_timeSTD_2 Pre_timeSTD_3; Pre_timeSTD_4
Pre_timeSTD_5 Pre_timeSTD_6; Pre_timeSTD_7 Pre_timeSTD_8 Pre_timeSTD_9];
subplot(1,4,1)
     a= bar(y_Pre_time, 'grouped')
hold on
% Find the number of groups and the number of bars in each group
[ngroups, nbars] = size(y_Pre_time);
% Calculate the width for each bar group
groupwidth = min(0.8, nbars/(nbars + 1.5));

% errorbar(x1,y_Pre_time,y_Pre_time_STD

% Set the position of each error bar in the centre of the main bar
% Based on barweb.m by Bolu Ajiboye from MATLAB File Exchange
for i = 1:nbars
    % Calculate center of each bar
    x = (1:ngroups) - groupwidth/2 + (2*i-1) * groupwidth / (2*nbars);
    errorbar(x, y_Pre_time(:,i), y_Pre_time_STD(:,i), 'k', 'linestyle',
'none');
end

hold on
% legend('Sample 1', 'Sample 2', 'Sample 3')
 grid on; grid minor;
    title('Pre-Conditioning');
ylabel('Time S'); ylim([0 2.5]);

%%%%%%%%%%%%%%%%%%%%%%%%%%%%%%%%%%%%%%%%%%%%%%%%%%%%%%%%%%%%%%%%%%%%    Act_time
subplot(1,4,2)
y_Act_time_STD = [Act_timeSTD_1 Act_timeSTD_2 Act_timeSTD_3; Act_timeSTD_4
Act_timeSTD_5 Act_timeSTD_6; Act_timeSTD_7 Act_timeSTD_8 Act_timeSTD_9];
     b= bar(y_Act_time, 'grouped')
hold on
```

```
[ngroups, nbars] = size(y_Act_time);
groupwidth = min(0.8, nbars/(nbars + 1.5));
for i = 1:nbars
    x = (1:ngroups) - groupwidth/2 + (2*i-1) * groupwidth / (2*nbars);
    errorbar(x, y_Act_time(:,i), y_Act_time_STD(:,i), 'k', 'linestyle',
'none');
end
hold on

 grid on; grid minor;
    title('Actuation');
  ylim([0 2.5]);
%%%%%%%%%%%%%%%%%%%%%%%%%%%%%%%%%%%%%%%%%%%%%%%%%%%%%%%%%%%%%%%%%%%%Deact_t
ime
subplot(1,4,3)
      y_Deact_time_STD = [Deact_timeSTD_1 Deact_timeSTD_2 Deact_timeSTD_3;
Deact_timeSTD_4 Deact_timeSTD_5 Deact_timeSTD_6; Deact_timeSTD_7
Deact_timeSTD_8 Deact_timeSTD_9];
     c= bar(y_Deact_time, 'grouped')
hold on

[ngroups, nbars] = size(y_Deact_time);
groupwidth = min(0.8, nbars/(nbars + 1.5));
for i = 1:nbars
    x = (1:ngroups) - groupwidth/2 + (2*i-1) * groupwidth / (2*nbars);
    errorbar(x, y_Deact_time(:,i), y_Deact_time_STD(:,i), 'k', 'linestyle',
'none');
end
hold on

 grid on; grid minor;
    title('De-actuation');
 ylim([0 2.5]);
%%%%%%%%%%%%%%%%%%%%%%%%%%%%%%%%%%%%%%%%%%%%%%%%%%%%%%%%%%%%%%%%%%%%Idle_ti
me
subplot(1,4,4)
 y_Idle_time_STD = [Idle_timeSTD_1 Idle_timeSTD_2 Idle_timeSTD_3;
Idle_timeSTD_4 Idle_timeSTD_5 Idle_timeSTD_6; Idle_timeSTD_7 Idle_timeSTD_8
Idle_timeSTD_9];
     d= bar(y_Idle_time, 'grouped')
hold on

[ngroups, nbars] = size(y_Idle_time);
groupwidth = min(0.8, nbars/(nbars + 1.5));
for i = 1:nbars
    x = (1:ngroups) - groupwidth/2 + (2*i-1) * groupwidth / (2*nbars);
    errorbar(x, y_Idle_time(:,i), y_Idle_time_STD(:,i), 'k', 'linestyle',
'none');
end
hold on
 grid on; grid minor;
    title('Idle');
  ylim([0 2.5]);

suptitle('Average Time Intervals of Load Cycles Components')
legend('Sample 1', 'Sample 2', 'Sample
3','Location','EastOutside','Orientation','vertical') %%,'Box','off'
```